INFORMATION TO USERS

This reproduction was made from a copy of a document sent to us for microfilming. While the most advanced technology has been used to photograph and reproduce this document, the quality of the reproduction is heavily dependent upon the quality of the material submitted.

The following explanation of techniques is provided to help clarify markings or notations which may appear on this reproduction.

1. The sign or "target" for pages apparently lacking from the document photographed is "Missing Page(s)". If it was possible to obtain the missing page(s) or section, they are spliced into the film along with adjacent pages. This may have necessitated cutting through an image and duplicating adjacent pages to assure complete continuity.

2. When an image on the film is obliterated with a round black mark, it is an indication of either blurred copy because of movement during exposure, duplicate copy, or copyrighted materials that should not have been filmed. For blurred pages, a good image of the page can be found in the adjacent frame. If copyrighted materials were deleted, a target note will appear listing the pages in the adjacent frame.

3. When a map, drawing or chart, etc., is part of the material being photographed, a definite method of "sectioning" the material has been followed. It is customary to begin filming at the upper left hand corner of a large sheet and to continue from left to right in equal sections with small overlaps. If necessary, sectioning is continued again—beginning below the first row and continuing on until complete.

4. For illustrations that cannot be satisfactorily reproduced by xerographic means, photographic prints can be purchased at additional cost and inserted into your xerographic copy. These prints are available upon request from the Dissertations Customer Services Department.

5. Some pages in any document may have indistinct print. In all cases the best available copy has been filmed.

University Microfilms International
300 N. Zeeb Road
Ann Arbor, MI 48106

8512367

Bougher, Stephen Wesley

VENUS THERMOSPHERIC CIRCULATION

The University of Michigan PH.D. 1985

University
Microfilms
International 300 N. Zeeb Road, Ann Arbor, MI 48106

VENUS THERMOSPHERIC CIRCULATION

by
Stephen Wesley Bougher

A dissertation submitted in partial fulfillment
of the requirement for the degree of
Doctor of Philosophy
(Atmospheric Science)
in The University of Michigan
1985

Doctoral Committee:

Professor Andrew F. Nagy, Co-chairman
Raymond G. Roble, Senior Scientist, National Center for Atmospheric Research, Co-chairman
Robert E. Dickinson, Senior Scientist, National Center for Atmospheric Research
Associate Professor John P. Boyd
Associate Research Scientist Thomas E. Cravens
Professor Chia-Shun Yih

RULES REGARDING THE USE OF

MICROFILMED DISSERTATIONS

Microfilmed or bound copies of doctoral dissertations submitted to The University of Michigan and made available through University Microfilms International or The University of Michigan are open for inspection, but they are to be used only with due regard for the rights of the author. Extensive copying of the dissertation or publication of material in excess of standard copyright limits, whether or not the dissertation has been copyrighted, must have been approved by the author as well as by the Dean of the Graduate School. Proper credit must be given to the author if any material from the dissertation is used in subsequent written or published work.

ACKNOWLEDGMENTS

People at The University of Michigan have made the Space Physics Research Laboratory a great place to be a graduate student! I specifically want to thank Professor Andrew F. Nagy for giving me a start in the department, for suggesting the topic of this thesis, and for his continued support and direction throughout the research. I have greatly enjoyed working with Dr. T. E. Cravens and appreciate our numerous discussions. Thanks also goes to Professors John Boyd and Chia-Shun Yih for their willingness to serve on my committee. NCAR has provided a tremendous environment for me to study. I am especially grateful to Dr. Raymond G. Roble for enabling me to work at NCAR, and for his very timely suggestions and words of encouragement. Thanks also goes to Dr. Robert Dickinson for making time for my questions concerning the dynamical models used. I am greatly indebted to Cicely Ridley, who has been a very patient and willing tutor as I have come to use these models. Special thanks go to Ursula Rosner and my wife, Trish, for typing this manuscript.

I am also grateful to my wife for her support and love which enabled me to continue in the face of discouragement and exhaustion. To my family I extend a warm love and thanks in appreciation for believing in me through years of school. Finally, I praise the Lord for using this thesis to develop my character and to show Himself in my life. The completion of this degree is possible because science does not own me, but Christ does instead.

TABLE OF CONTENTS

ACKNOWLEDGMENTS ii

LIST OF TABLES vii

LIST OF FIGURES viii

LIST OF APPENDICES xii

LIST OF ABBREVIATIONS xiii

CHAPTER

I. INTRODUCTION TO THE PROBLEM OF THE VENUS THERMOSPHERIC CIRCULATION 1

1.1 Motivation for Improved Venus Thermospheric Circulation Models 1

1.2 Goals and Objectives of Thesis 4

II. REVIEW OF AVAILABLE DATA, OBSERVATIONS, AND THEIR DYNAMICAL IMPLICATIONS 7

2.1 Rocket, Mariner, Venera, and Pioneer Venus Observations and Data Sets 7

2.1.1 Brief History of Data Acquisition 7
2.1.2 Review of Best Current Data 9

2.2 Standard Atmosphere Empirical Models 22

2.2.1 ONMS Empirical Model 24
2.2.2 OAD Empirical Model 25

2.3 Summary 27

III. REVIEW OF PREVIOUS MODELLING EFFORTS 28

3.1 Overview of Venus Thermospheric Model Development 28

3.2 Previous Models: Descriptions and Results . . . 30

3.2.1 Introduction 30
3.2.2 One-Dimensional Global Mean Models (Dickinson, 1972, 1976) 30
3.2.3 Two-Dimensional Hydrodynamic Model (Dickinson and Ridley, 1975, 1977) . . 38
3.2.4 One-Dimensional Compositional Model at 60° SZA (von Zahn et al., 1980) 48
3.2.5 One-Dimensional Compositional Model at 150° SZA (Stewart et al., 1980) 50
3.2.6 One-Dimensional Composition Models at 60 and 180° SZA (Massie et al., 1983). . . 52
3.2.7 Three-Dimensional Spectral Model (Mayr et al., 1980) 55

3.3 Shortcomings of Model Predictions 58

3.3.1 Incomplete Models 58
3.3.2 Self-Consistent Hydrodynamic Model . . . 59
3.3.3 Basis for a New Modelling Effort 60

IV. FORMULATION OF AN IMPROVED TWO-DIMENSIONAL HYDRODYNAMIC CODE 63

4.1 Updated Two-Dimensional Model 63

4.1.1 Description of Equations Used 63
4.1.2 New Inputs for a Benchmark Model 69

4.2 Updated Version of the Radiative Transfer Code . 70

4.3 Benchmark Global Mean Calculations 72

4.4 New Physical Parameterizations to be Tested . . 76

4.4.1 Problems To Be Addressed 76
4.4.2 EUV Heating Efficiency Profiles Chosen . 77
4.4.3 Parameterizations Used: Parameters Selected 83

V. SENSITIVITY STUDIES WITH THE UPDATED TWO-DIMENSIONAL MODEL: RESULTS 88

5.1 Procedure 88

5.1.1 Strategy and Fitting Scheme 88

5.2 LO EUV Efficiency Case (2-22%) 92

5.2.1 Qualitative Response of the Model to Eddy Parameterizations 92

5.2.2 Quantitative Sensitivity Study 104
5.2.3 Discussion and Best Tunings 108
5.2.4 Diagnostics 112

5.3 Medium EUV Efficiency Case (10-25%) 114

5.3.1 Establishment of a Correct Dayside Thermal Balance 116
5.3.2 Quantitative Sensitivity Study 120
5.3.3 Discussion and Best Tunings 130
5.3.4 Diagnostics 132

5.4 The High EUV Efficiency Case (18-28%) 132

5.5 Best Model Simulation (7-19%) 135

5.5.1 Assumptions Required 135
5.5.2 Optimization of Adjustments 136
5.5.3 Detailed Comparisons 143
5.5.4 Summary of Adjustments of Parameters . . 147
5.5.5 Diagnostics 148

5.6 Applications of a Best Model Simulation 151

5.6.1 Calculation of Helium 151
5.6.2 Solar Minimum Calculation 160
5.6.3 Time-Dependent Behavior 162
5.6.4 Generalized Rayleigh Friction Scheme for Drag 166

VI. VENUS THREE-DIMENSIONAL MODEL DEVELOPMENT AND RESULTS 172

6.1 Introduction 172

6.1.1 Need for Full Three-Dimensional Code . . 172
6.1.2 Basic VTGCM Goals 173

6.2 Venus TGCM Model Description 173

6.2.1 Adaptation from Terrestrial TGCM 173
6.2.2 Governing Equations 177

6.3 Cases Tested: Results and Comparisons with the Two-Dimensional Model 183

6.3.1 VTGCM Benchmark 183
6.3.2 Two-Reference Temperature 15 μm Cooling . 189
6.3.3 Superrotation Scheme and Model Signatures 197

VII. MODELLING IMPLICATIONS AND DISCUSSION 203

7.1 Summary and Conclusions of Present Research . . 203

7.1.1 Two-Dimensional Model Sensitivity Studies 204
7.1.2 Further Applications 212
7.1.3 VTGCM Model Calculations 214

7.2 Outline of Future Work 217

7.2.1 Venus - TGCM 217
7.2.2 Mars - TGCM 218

7.3 Summary 219

APPENDICES 220

BIBLIOGRAPHY 244

LIST OF TABLES

Table

5.1 Summary of composition and temperature values for the VTS3 and HSYM data sets 91

5.2 Comparison of EUV case model fits: standard deviations 93

5.3 Eddy cooling sensitivity study of the Venus two-dimensional low EUV benchmark 101

5.4 Eddy coefficient sensitivity upon composition 103

5.5 Best parameter adjustments for each EUV efficiency case 110

5.6 K_{CO_2-O} rate sensitivity ranges for various heating efficiency models; (a) dayside mean temperature profile requirements (T_∞ = 280°K), (b) global mean temperature profiles requirements (T_∞ = 208°K) . . . 118

5.7 LO, MED, HI and Best EUV efficiency profiles 138

5.8 Model and empirical data set comparisons at 150 km . 145

LIST OF FIGURES

Figure

2-1 Model number and total mass densities versus altitude in the thermosphere of Venus for the subsolar and antisolar point (from Niemann et al., 1980) 11

2-2 Measurements of CO_2 and O number densities at 170 km taken by the Pioneer Venus orbiter mass spectrometer over nearly three diurnal cycles (from von Zahn et al., 1983) 12

2-3a Diurnal variation of upper atmospheric temperature (from Keating et al., 1980) 16

2-3b Diurnal variation of the exospheric temperature as derived from the number density scale heights measured by the Pioneer Venus orbiter neutral mass spectrometer. The sampling of one diurnal cycle lasted 225 Earth days, the sidereal period of Venus (from von Zahn et al., 1983) 16

2-4 A comparison of Dickinson's theoretical temperature models for the global mean atmosphere with temperature profiles above the clouds measured by the Pioneer small probes (Seiff et al., 1982) . . 18

2-5 A schematic flow pattern for the nightside in the thermosphere of Venus (from Niemann et al., 1980) 23

3-1 Calculated global mean temperature profiles for various model parameterizations. (a) shows the effects of various EUV heating efficiencies, (b) shows the effects of various eddy mixing models (from Dickinson, 1976) 34

3-2a Calculated temperature fields (°K) obtained with the low EUV efficiency model (2-22%) (from Dickinson and Ridley, 1977) 41

3-2b Calculated temperature fields (°K) obtained with the same model except with a 30% efficiency of EUV,

Figure

	$\lambda<1080$, and complete quenching of $O(^1D)$ at longer wavelengths (from Dickinson and Ridley, 1977)	41
3-2c	Horizontal motions (m/sec) calculated for the low EUV efficiency model (from Dickinson and Ridley, 1977)	41
3-2d	Vertical motions (cm/sec) calculated for the low EUV efficiency model (from Dickinson and Ridley, 1977) .	41
3-2e	Relative concentrations (%) of O (given by solid lines) and CO (given by dashed lines) obtained with the low EUV efficiency model (from Dickinson and Ridley, 1977)	42
3-3	The relative magnitude of the various terms in the thermodynamic equation (from Dickinson and Ridley, 1977)	45
3-4	The relative magnitudes of the various terms in the continuity equation for atomic oxygen (from Dickinson and Ridley, 1977)	46
3-5	Comparisons of DRM2 predictions and Pioneer Venus observations	57
4-1	Global mean Venus temperature profiles - radiative transfer tests	73
4-2	Updated two-dimensional benchmark global mean calculations; (a) temperature, (b) composition . . .	75
4-3	EUV heating efficiency profiles	82
5-1a,b	Venus two-dimensional model response to viscous drag tests; (a) T_∞, (b) terminator u(z) profiles	95
5-1c	Venus two-dimensional model response to viscous drag tests; (c) composition	96
5-2	Global mean Venus one-dimensional thermospheric temperature profiles: eddy cooling tests	98
5-3	Venus two-dimensional model temperature response to eddy cooling	99
5-4a	Low EUV case sensitivity study exospheric temperatures	105

Figure

5-4b Low EUV case sensitivity study: winds 106

5-4c Venus two-dimensional model temperatures: low EUV case 111

5-5 Heating and cooling rates 60° and 120°SZA: low EUV case 113

5-6 Term balance plots: low EUV case; (a) [O] composition, (b) [CO] composition 115

5-7 One-dimensional RT model reference temperatures: dayside and nightside mean profiles 119

5-8a MED EUV case sensitivity study exospheric temperatures 122

5-8b MED EUV case sensitivity study: winds 123

5-8c Venus two-dimensional model temperatures: MED EUV case 125

5-9 Production minus loss for O and CO at 60°SZA: MED EUV case 128

5-10 Heating and cooling rates 60° and 120°SZA: MED EUV case 133

5-11 Term balance plots: MED EUV case; (a) [O] composition, (b) [CO] composition 134

5-12 Family of terminator horizontal wind profiles 140

5-13a Venus two-dimensional model temperature: Best EUV case 142

5-13b Venus two-dimensional model composition [O]: Best EUV case 144

5-14 Heating and cooling rates 60° and 120°SZA: Best EUV case 149

5-15 Term balance plots: Best EUV case; (a) [O] composition, (b) [CO] composition 150

5-16 60°SZA model He calculation comparisons 156

5-17 Venus two-dimensional model composition [He]: Best EUV case 159

Figure

5-18 Two-dimensional model time dependent behavior 164

5-19 Generalized Rayleigh friction results; (a) terminator winds, (b) LT = 12 and 24 temperature profiles . . . 169

6-1 T+(u,v) contours on a pressure level slice for benchmark three-dimensional model; (a) z = 5, (b) z = 0, (c) z = -4 185

6-2 Equatorial slices for benchmark three-dimensional model; (a) T, (b) h, (c) u, (d) w 186, 187

6-3 T+(u,v) contours on a pressure level slice for two-reference temperature 15 μm cooling three-dimensional model; (a) z = 5; (b) z = 0, (c) z = -4 . 191

6-4 Equatorial slices for two-reference temperature 15 μm cooling three-dimensional model; (a) T, (b) h, (c) u, (d) w 192, 193

6-5 Heating and cooling rates - 60 and 120°SZA: VTGCM . . 198

6-6 T+(u,v) contours on a pressure level slice for a superrotating three-dimensional model; (a) z = 5, (b) z = 0 200

LIST OF APPENDICES

Appendix

A Contour plots for empirical model fields (1) VTS3, (2) HSYM 221

B Nonlinear temperature-dependent perturbation 15 μm cooling parameterization 226

C Contour plots for two-dimensional cases (1) LO EUV case, (2) MED EUV case, (3) Best EUV case, (4) solar minimum case 229

D Derivation of He molecular diffusion term 239

LIST OF ABBREVIATIONS

BEST	7-19% EUV efficiency case
BNMS	Bus Neutral Mass Spectrometer
DRM1	Dickinson and Ridley (1975)
DRM2	Dickinson and Ridley (1977)
ET	Evening terminator
EUV	Extreme ultraviolet
$\epsilon(z)$	EUV efficiency vertical profile
F10.7	Radio flux at 10.7 cm
HI	18-28% EUV efficiency case
HSYM	Keating et al. (1984) empirical model
IR	Infrared
$K(CO_2\text{-}O)$	CO_2-O rate coefficient
$K_E(z)$	Eddy coefficient vertical profile
KMAX	Maximum value of the eddy coefficient
K_{RA}	Rayleigh friction coefficient
LOW (or LO)	2-22% EUV efficiency case
LT	Local time
MED	10-25% EUV efficiency case
MT	Morning terminator
NCAR	National Center for Atmospheric Research
NLTE	Non-local thermodynamic equilibrium

NT	Night
OAD	Orbiter Atmospheric Drag
OIR	Orbiter Infrared Radiometer
ONMS	Orbiter Neutral Mass Spectrometer
OUVS	Orbiter Ultraviolet Spectrometer
PV	Pioneer Venus
RT	Radiative transfer
STP	Standard temperature and pressure
SZA	Solar Zenith angle
SZAF	Solar Zenith angle factor or variation
TGCM	Thermospheric General Circulation Model (Earth)
UV	Ultraviolet
VTGCM	Venus Thermospheric General Circulation Model
VTS3	Hedin et al. (1983) empirical model
ZPBK	Pressure level of wave-breaking

CHAPTER I

INTRODUCTION TO THE PROBLEM OF THE VENUS THERMOSPHERIC CIRCULATION

1.1 Motivation for Improved Venus Thermospheric Models

A variety of Pioneer Venus observations suggest a global scale day-to-night Venus thermospheric circulation (Mayr et al., 1980; Keating et al., 1980; Stewart et al., 1980; Schubert, 1983.) No direct measurements of wind velocity are available for Venus's upper atmosphere, therefore the circulation of this region must be inferred from indirect observations of its structure (see Chapter II). A particularly prominent feature of Venus's thermosphere is the contrast in temperature between day and nightsides which, to first order, should drive a subsolar-to-antisolar circulation (Seiff et al., 1982). A likely scenario involves dayside upwelling centered on the subsolar point, cross-terminator flow from day to night, and subsidence on the nightside, generally centered on the antisolar point (Stewart et al., 1980; Keating et al., 1980; Schubert, 1982). Very cold nighttime exospheric temperatures are also indicated, a surprising find from the Pioneer Venus data (Niemann et al., 1979).

This type of circulation of the upper atmosphere was qualitatively predicted prior to Pioneer Venus in a series of numerical

studies by Dickinson and Ridley (1972, 1975, 1977). Their most recent two-dimensional coupled chemical-dynamical model correctly predicted the gross characteristics of this mean subsolar-to-antisolar circulation. However, it failed to reproduce the very cold nightside temperatures observed, as well as the phases and number densities of the neutral constituents, most notably atomic oxygen.

Previously neglected chemical or dynamical processes appear to be required to explain the thermal and compositional structure of Venus's upper atmosphere. Several Pioneer Venus instruments, in fact, provided temperature and composition profiles illustrating wave structure (Niemann et al., 1980; Seiff et al., 1980, 1982), which implies that turbulent processes might be operating in the lower thermosphere of Venus. Eddy cooling, eddy or wave drag, and eddy diffusion have all been parameterized in other planetary models as a means to mimic such turbulent processes. However, the works of Dickinson and Ridley (1972, 1975, 1977) have not systematically examined these parameters. In addition, it has been suggested (Dickinson, 1976; Mayr et al., 1980) that observed dayside thermospheric temperatures could be maintained by a more efficient solar EUV heating than used by Dickinson and Ridley (1977), provided that enhanced eddy cooling and/or improved 15 μ radiational cooling processes were invoked. Nightside temperatures could alternatively be lowered by a reduction of terminator winds, thereby isolating the nightside. Light species, particularly He and H, as well as exospheric temperatures, are also seen to display phases not symmetric about the subsolar-to-antisolar axis (Keating et al., 1980; Brinton et al., 1980; Mayr et al., 1980).

Airglow studies by Stewart et al. (1980) furthermore confirmed the existence of a "super-rotating" component of the circulation that needs to be added to the first order subsolar-to-antisolar circulation (Mayr et al., 1980).

A return to Venus thermospheric modelling is certainly appropriate now that the Pioneer Venus observations have become available. Venus modelling is also quite important in its own right because it provides an additional test of our knowledge of terrestrial thermospheric physical processes that are expected to apply to other planetary thermospheres (Mayr and Volland, 1978). In particular, large scale motions are coupled with small scale mixing processes in model calculations of the Earth's thermosphere to give results consistent with observations (Mayr et al., 1978; Dickinson et al., 1984). A similar combination of small and large scale dynamical processes should also control composition in other planetary thermospheres, including Venus. It is also expected that EUV and UV solar heating in the thermosphere of Venus will drive winds which redistribute photodissociated species about the planet, analogous to the terrestrial conditions (Mayr et al., 1978).

Conversely, Venus dynamic modelling will enable a determination to be made of the physical processes which are unique to a thermosphere largely composed of CO_2. Neutral chemistry and airglow processes already suggest a solar EUV heating efficiency much different from that of the Earth (Fox and Dalgarno, 1979, 1981). Furthermore, initial analysis of the Pioneer Venus data indicate a very sluggish response by the Venus thermosphere to solar flux pertur-

bations (Keating et al., 1980; Bauer et al., 1981) unlike the Earth. Some of these questions can be addressed by a sensitivity study whereby solar cycle variations and their effects upon model composition and temperatures can be observed (see Chapters V and VI).

Finally, Venus is in some ways a simpler case study of a planetary thermosphere compared to the Earth. Venus rotation is so slow (243 days per one rotation) that Coriolis terms can be neglected in all equations of motion. As a result, the slow diurnal EUV heating cycle enables a subsolar-to-antisolar circulation to arise as a first-order response by the Venus thermosphere. Ion drag upon the neutrals is also negligible below 200 km (Mayr et al., 1980), a further simplification of the momentum equation. Pioneer Venus instruments have demonstrated that auroral heating is negligible, at best, in Venus' ionosphere and thus will have no influence upon the thermospheric circulation of the neutrals--very different from the terrestrial case (Roble et al., 1982). Thus, some conditions unique to a CO_2 atmosphere can be examined without the additional complications of auroral heating and Coriolis terms.

1.2 Goals and Objectives of the Thesis

The new information obtained from the Pioneer Venus measurements (Chapter II) makes it timely and appropriate to return to comprehensive model studies of the thermospheric circulation of Venus. The principal goal of such a study is to incorporate new theoretical concepts and include new input data to adjust model parameters and obtain a best match of calculated fields to Pioneer Venus

observations. Particular attention can now be given to driving, mixing, and cooling mechanisms which have not yet been examined in the coupled chemical-dynamical model of Dickinson and Ridley (1977). The vast body of upper atmosphere observations now available from several Pioneer Venus instruments provides a framework of model constraints and reference atmospheric fields and parameters vital to the success of such a modelling effort.

This thesis also seeks to identify and quantify physical processes previously neglected in a self-consistent coupled chemical-dynamical model of Venus' thermospheric circulation. Various one-dimensional, two-dimensional and spectral models previously developed for the Venus thermosphere are analyzed to isolate their shortcomings, and to uncover new parameterizations for testing. The two-dimensional symmetric model of Dickinson and Ridley (1977) is primarily utilized as the framework upon which these new model processes--eddy diffusion, eddy cooling, wave drag, and 15 μ radiational cooling--are examined. The formulation of an updated two-dimensional code with new parameterizations appears in Chapter IV. Case studies appropriate to three likely solar EUV heating efficiency profiles were conducted and are presented in Chapter V.

Once a best model simulation of the improved Venus two-dimensional symmetric model of Dickinson and Ridley (1977) is available (giving composition and temperature fields in reasonable agreement with Pioneer Venus observations), the adopted parameter adjustments are applied to a calculation of helium concentrations. The response of the Venus thermospheric circulation to solar cycle variations in

EUV and UV fluxes is also examined. In Chapter VII, the dynamical implications and interpretations of the sensitivity studies are presented. These same parameter adjustments are also applied to the first order Venus version of the terrestrial thermospheric general circulation model (VTGCM) described in Bougher et al. (1981) (Chapter VI). The calculated temperature and wind fields are examined and compared to the previous two-dimensional model results as well as Pioneer Venus observations.

A fully three-dimensional general circulation model for Venus' thermosphere will eventually be required to account for super-rotation of the atmosphere, thereby permitting non-axisymmetric signatures of the observed composition and temperature fields to be modelled. For this purpose, final thesis conclusions are stated and future VTGCM work outlined in Chapter VII.

CHAPTER II

REVIEW OF AVAILABLE DATA, OBSERVATIONS AND THEIR DYNAMICAL IMPLICATIONS

2.1 Rocket, Mariner, Venera, Pioneer Venus Observations

2.1.1 Brief History of Data Acquisition

A large body of observations is now available from which constraints on the dynamics of Venus' thermosphere and reference atmospheric parameters can be obtained. The observed composition and temperatures and their spatial and diurnal variations imply a great deal about dynamical processes acting in Venus's upper atmosphere. This chapter will describe those observations which are important in determining dynamical constraints.

Data has been obtained over the last 50 years by ground-based instruments (primarily spectrometers), sounding rockets, flyby probes, in-situ orbiters, and hard/soft entry-probe landers. Earth-based spectroscopic measurements in the infrared (IR) by 1967 firmly established that CO_2 was the major gas throughout most of the Venus atmosphere (Connes et al., 1967; Belton et al., 1968; Moroz, 1968). Soviet and American flyby missions, beginning in 1962, ushered in a new era of planetary exploration with the Mariner flyby series (5 and 10) and the Soviet Venera series (4-12) to Venus. These flyby,

orbiter and entry-probe landers provided the first glimpses of upper atmosphere composition, temperature, and airglow.

The pioneering work by broad band photometers aboard Venus flybys began with Venera 4 (Kurt et al., 1968) and Mariner 5 (Barth et al., 1967). The hydrogen corona was discovered by measuring the emission rate of Lyman-α on both these missions. Mariner 10 carried the first optical spectrometer to Venus. The grating spectrometer work of Broadfoot et al. (1974) revealed the presence of significant concentrations of He and C atoms in Venus' upper atmosphere. Kumar and Broadfoot (1975), using ultraviolet airglow data, also identified atomic oxygen and helium in the upper atmosphere, and estimated the fractional number density of atomic oxygen at the F1-peak to be >1%.

Venera 9 and 10 orbiters carried two remote sensing instruments: a visible airglow spectrometer and a hydrogen absorption cell. Bertaux et al. (1978) observed the "hot-hydrogen" component by using the absorption cell, and the visible airglow experiment identified and began to map the O_2^* Venus nightglow features corresponding to the Hertzberg II bands of O_2 (Krasnopolsky et al., 1976; Lawrence et al., 1977). The sparse upper atmosphere data provided by these flyby and Soviet orbiter observations prompted a return to the planet to obtain observations over several diurnal cycles with the aid of an orbiter. Accompanying probes would also provide single vertical profiles (Colin, 1980).

In December of 1978, the Pioneer Venus orbiter and its four entry probes and bus began a comprehensive study of the density, temperature, and composition of the upper atmosphere including their

temporal and spatial variations. Numerous airglow features including O_2^*, NO^*, O^* were also observed. Global mapping of composition, temperature, and airglow features revealed asymmetries in a subsolar-to-antisolar thermospheric circulation, not predicted by Dickinson and Ridley (1975, 1977). A cold nightside thermosphere was also discovered. Thus, a substantial body of thermospheric neutral composition and temperature fields over many diurnal cycles is now available for incorporation into a Venus standard atmosphere for altitudes greater than 150 km. (See Table I of von Zahn et al., 1983, for a history of spectroscopic instruments and observations from space probes at Venus.)

2.1.2 Review of Best Current Data

The Pioneer Venus (PV) mission provided the first opportunity to measure the detailed composition of the neutral gases in the upper atmosphere of Venus. CO_2, CO, O, N_2, N, NO, He, and H have been positively identified and their number densities determined. Four PV instruments and their measurements are specifically valuable to the investigation of the neutral upper atmosphere--the ONMS (Orbiter Neutral Mass Spectometer) (Niemann et al., 1979, 1980), the BNMS (Bus Neutral Mass Spectrometer) (von Zahn et al., 1980), the OAD (Orbiter Atmospheric Drag) (Keating et al., 1980), and the OUVS (Orbiter Ultraviolet Spectrometer) (Stewart, 1980; Stewart et al., 1980). The orbiter instruments acquire data in a spin-scanning mode along an orbit inclined 106° to the equator. Periapsis latitude is fixed between 13-17°N for each 24-hour pass about the planet. The sub-

spacecraft periapsis point precesses about the planet so that a complete set of diurnal observations is obtained in 225 Earth days (one Venus sidereal period). The useful low periapsis altitude of 140 km was maintained for about three Venus years. The apoapsis altitude was originally set at 66,900 km. In addition, the bus entry-probe mass spectrometer began taking measurements at about 650 km altitude and continued to do so down to ~130 km, below the turbopause (von Zahn et al., 1980). This multiprobe bus crossed the 200 km level at 37.9°S latitude, at a solar zenith angle (SZA) of 60°.

The most striking feature of the Venus upper atmosphere composition is the diurnal variability of the heaviest constituents--CO_2, CO, N_2, O. Neutral composition measurements by the ONMS instrument span the 140-250 km range and show these heavy constituents to have a density distribution almost symmetric about the subsolar to antisolar axis. This is the likely result of the slow planetary rotation rate (243 days). Maximum values of these densities occur on the dayside because of solar heating and resulting expansion of the dayside thermosphere (see LT=12 model profiles of Niemann et al., 1980 in Fig. 2-1). Low densities on the nightside suggest a very cold atmosphere at thermospheric heights (see LT=24 model profiles of Niemann et al., 1980 in Fig. 2-1). Changes in composition across the terminator are very abrupt and entirely consistent with a contraction of the atmosphere on the nightside (see Fig. 2-2). Such a cold nightside thermosphere is without precedent in the study of planetary thermospheres. In fact, the term "cryosphere" was coined by Schubert et al. (1980) to describe the uniqueness of this nightside temperature

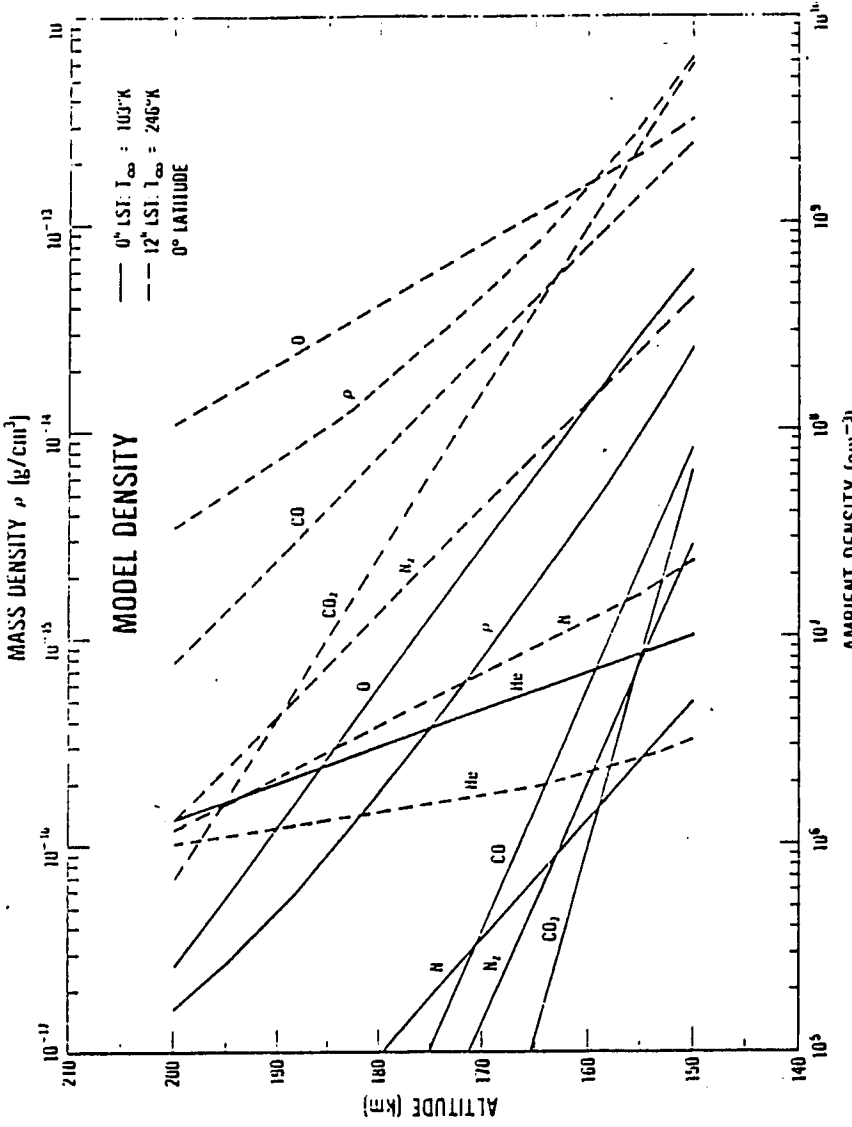


Fig. 2-1 Model number and total mass densities versus altitude in the thermosphere of Venus for the subsolar and antisolar point (from Niemann et al., 1980).

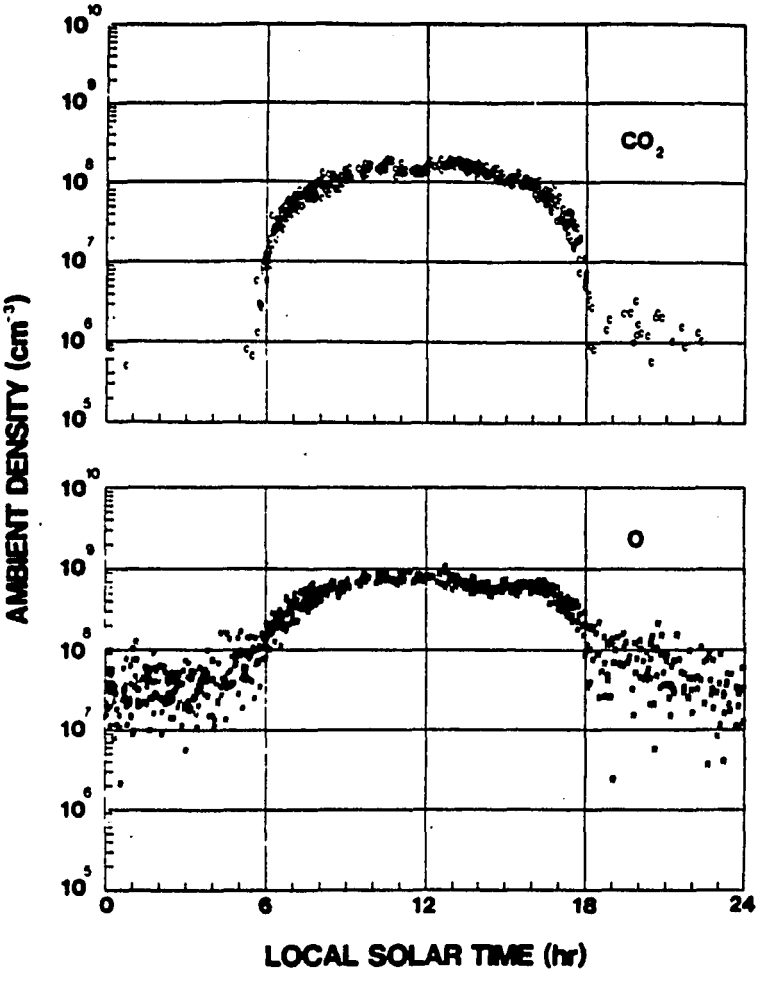


Fig. 2-2 Measurements of CO_2 and O number densities at 170 km taken by the Pioneer Venus orbiter mass spectrometer over nearly three diurnal cycles (from von Zahn et al., 1983).

structure of Venus. Note the large nightside scatter of O densities in Fig. 2-2, corresponding to a fluctuation of roughly 20-25% over several spacecraft passes (Hedin et al., 1983).

Diffusive separation permits the mixing ratio of O to overtake CO_2 at about 155 km on the dayside (see Fig. 2-1). A measure of the photodissociation rate is the $[O]/[CO_2]$ abundance ratio at the ionospheric peak (corresponding to a Chapman layer), which has been measured (Kliore et al., 1981; Cravens et al., 1981) to be in the range of 140-145 km for all SZA. These composition measurements have served as a basis for a number of empirical and one-dimensional models of the upper atmosphere of Venus (von Zahn et al., 1980; Keating, 1980; Hedin et al., 1983; Massie et al., 1983) to be discussed in Chapter III. It is significant at this point to note that all these models indicate an $[O]/[CO_2]$ abundance ratio of 15-20% at the ionospheric peak, which is substantially larger than those previously suggested by observations (Rottman and Moos, 1973; Kumar and Broadfoot, 1975) or modelling (Dickinson and Ridley, 1977). As will be illustrated later, this abundance of O is vital to a proper treatment of the energy budget of the Venus thermosphere (see Chapters V and VI).

Helium and hydrogen, the two lightest constituents, show a diurnal density reversal (opposite to that of the heavy species), with densities higher at night than during the day (Niemann et al., 1980; Brinton et al., 1980). This signature is consistent with their low atomic weights and correspondingly larger scale heights. These properties increase the transport efficiences by the large scale winds for these species, just as for the Earth (Mayr et al., 1978). The

diurnal variation of He at 150 km (Niemann et al., 1980) reveals a distinct bulge at night with a maximum at ~3 hr LST, and decreasing abruptly at the terminator to a nearly constant daytime level (100 × less than the peak nightside value). Results obtained from Brinton et al. (1980) show a similar night-day bulge of H at ~5 hr LST, but now with a day-to-night amplitude enhancement of nearly 400:1 at 165 km. Both these observations of He and H show a SZA asymmetry in the Venus upper atmosphere that suggests a "super-rotating component" of the flow superimposed on the background mean subsolar-to-antisolar thermally driven circulation. In addition, H may also be subject to exospheric escape processes, as detailed in Kumar et al. (1977), von Zahn et al. (1980), and Rodriguez et al. (1984), which would reduce dayside thermospheric H and permit higher night-day H abundance ratios.

Since no measurements of helium exist for the lower atmosphere below 130 km (von Zahn et al., 1983), He has been further examined by extrapolation of BNMS data with the aid of the one-dimensional diffusion model of von Zahn et al. (1980). Basically, BNMS data provided the only in-situ observations throughout the turbopause region at roughly 134 km. Fitting of all helium data from the BNMS up to 200 km gave a predicted He mixing ratio at 100 km of ~12 ppm (see Chapter III for details of von Zahn et al. (1980) one-dimensional model). A large uncertainty (up to a factor of three) remains for the true $[He]/[CO_2]$ ratio in Venus' lower thermosphere (von Zahn et al., 1980, 1983).

Kinetic temperatures are solely inferred from the observed scale heights of the neutral constituents (Niemann et al., 1980; Keating et al., 1980). Figure 2-3a illustrates a plot of exospheric temperatures inferred by Keating et al. (1980) from total mass densities derived from the atmospheric drag effects of the Pioneer Venus orbiter. They are very similar to those derived from the ONMS measurements of number density scale heights (Niemann et al., 1980; von Zahn et al., 1983). It is particularly significant to note that average values for both day and night are lower than predicted (Dickinson and Ridley, 1977, and Chapter III). In addition, changes in temperature across the terminator are very abrupt, with a minimum nightside exospheric temperature of 110-120K seen just beyond midnight. The vertical nightside temperature profile decreases from the ~170°K values observed at roughly 95 km by the orbiter infrared radiometer (Schofield and Taylor, 1982), to ~120°K seen at exospheric heights. This profile shape is remarkably unlike the terrestrial nightside thermosphere. The initial explanation for such cold nightside "cryosphere" temperatures was thought to be found in either an efficient downward heat transport on the nightside caused by turbulence, or possibly lower (Schubert et al., 1983) than predicted horizontal energy transport across the terminator.

Diurnal variation in exospheric temperatures, as illustrated in Fig. 2-3b, is derived from the number density scale heights measured by the ONMS over a complete diurnal cycle (225 Earth days). The scatter of temperatures, particularly of the nightside, is indicative of large nightside variations in density (Niemann et al., 1980;

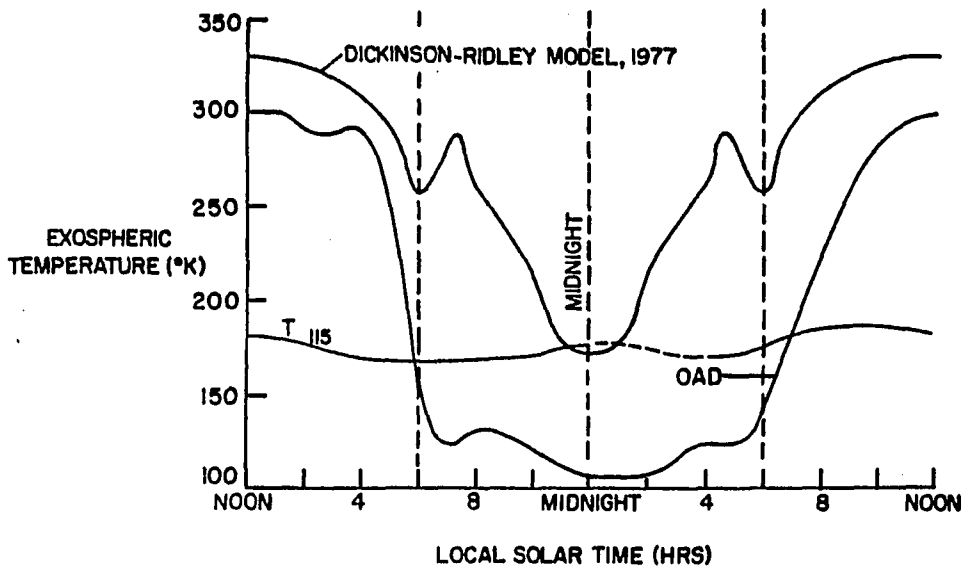


Fig. 2-3a Diurnal variation of upper atmospheric temperature (from Keating et al., 1980).

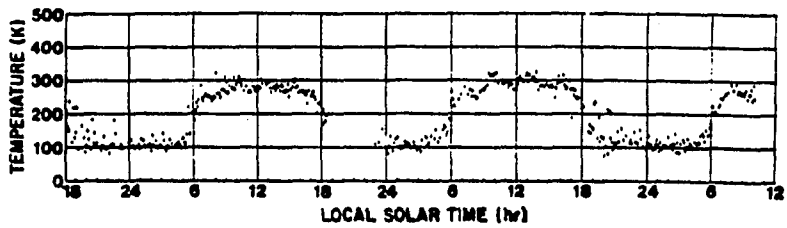


Fig. 2-3b Diurnal variation of the exospheric temperature as derived from the number density scale heights measured by the Pioneer Venus orbiter neutral mass spectrometer. The sampling of one diurnal cycle lasted 225 Earth days, the sidereal period of Venus (from von Zahn et al., 1983).

Keating et al., 1980), presumably due to variability of the thermospheric circulation. Figures 2-2 and 2-3b vividly illustrate the diurnal variability of observed densities and inferred temperatures obtained from PV observations. A description of the mean state of the nightside vertical thermosphere can only be obtained from an average of data sets of many observations over several diurnal cycles. Such a composite standard atmosphere will be described later with the aid of empirical models.

Wavelike perturbations in the height profiles of each of the neutral constituents and of temperature were observed by both orbiter and bus mass spectrometers (ONMS, BNMS) above 120 km. In addition, the Pioneer Venus day and night probes provided measurements of the total mass density below 140 km, upon which strong perturbations were also seen (Seiff et al., 1980, 1982). Hence, there is ample evidence for turbulence or wave motion in the upper atmosphere of Venus (von Zahn et al., 1983) (see Fig. 2-4).

All these observations, however, are snapshots of vertical wave structure, without any information concerning horizontal scales or periods. At present, it is difficult to judge whether the altitude profiles reveal vertical structures of planetary-scale-waves, or of smaller scale waves which propagate upward. However, the vertical wavelengths of these temperature and density perturbations were observed to vary from 5 to 15 km in the altitude range of 120 to 140 km (Seiff et al., 1980, 1982; Schubert, 1983). Smaller scale waves appear to be responsible for the observed structures in temperature and velocity fields at ~120 km, since there appear to be no cor-

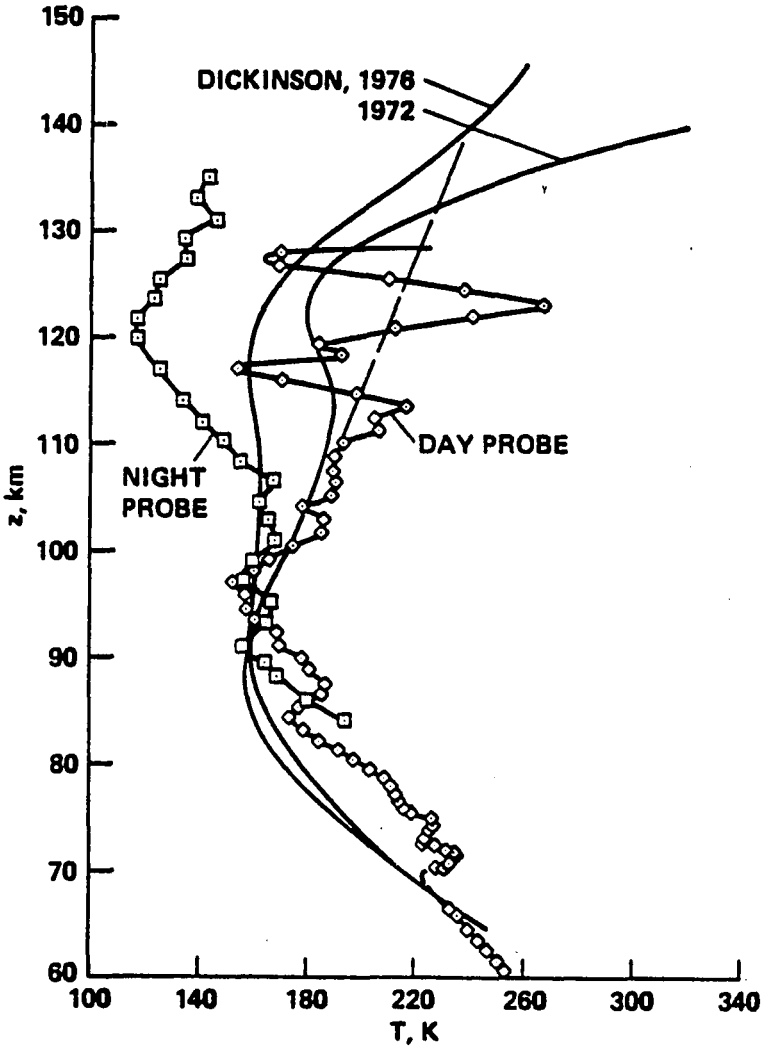


Fig. 2-4 A comparison of Dickinson's theoretical temperature models for the global mean atmosphere with temperature profiles above the clouds measured by the Pioneer small probes (Seiff et al., 1982).

relations in the perturbations among the four entry probe fields, even though they entered the atmosphere simultaneously. Analysis of day-probe temperature profile structure at the terminator also suggests the presence of gravity waves. Seiff et al. (1982) speculated that these day probe oscillations were associated with or excited by large and rapid variations of pressure and density in flow across the terminator.

Several airglow features have also been observed by Pioneer Venus and Venera instruments, including the Hertzberg II emissions of O_2^*, the resonance line of O^* at 1304Å, and the gamma and delta bands of NO^*. The study of the intensity of these emissions and their spatial and temporal variations, is particularly useful in providing information on the photochemistry and dynamics of Venus' upper atmosphere. Observations will be described here only for the $NO^*(0,1)$ delta band and the $O_2^*(c-X)$ emissions, for which a considerable database of spatial and temporal variations has been mapped and interpreted .

The O_2 molecular band system, consisting of several emissions between 4000 and 7000Å, was the first spectra obtained from the visible nightglow of Venus by Krasnopolsky et al. (1976). This band system was subsequently identified by Lawrence et al. (1977) to be part of the Hertzberg II system. Lawrence et al. (1977) conjectured that CO_2 plays a special role in enabling the three-body reaction

$$O + O + CO_2 \rightarrow O_2^* + CO_2 + 5.1 \text{ eV} \qquad (2.1)$$

and subsequent O_2^*(c-X) Hertzberg II emission to occur. The spatial and temporal variations of the oxygen airglow have been examined for the case of the O_2^* (c-X) emissions by Krasnopolsky and Tomashova (1980). The average emission rate across the nightside reaches 2-3 kR (kilo-Rayleighs). The very small variation of this emission with local time implies a transport time for O atoms (from the dayside to the nightside) of approximately one day for altitudes >95 km, which corresponds roughly to the chemical lifetime of these atoms. The diurnal variation of the observed brightness is determined by an average of 25 individual brightness scans across the dark side of Venus. The characteristics of the O_2^* emission include a maximum at 00:30 LST, just beyond the midnight meridian toward the morningside. A significant hemispheric asymmmetry is also seen in the visible nightglow emission, corresponding to a factor of 1.8 brighter intensities at 20°S than at 20°N. Poor timing by the Venera 9 and 10 satellite has degraded vertical resolution, such that reliable information on the altitude position of the maximum volume emission rate is not possible.

OUVS NO^* airglow observations, however, do not suffer from this limitation. UV night airglow of Venus was first detected by Barth et al. (1968) from Mariner 5. This airglow was again detected by the OUVS from Pioneer Venus (Stewart et al., 1979) and identified as the gamma and delta bands of nitric oxide (Feldman et al., 1979; Stewart and Barth, 1980), excited by the radiative association of atoms of nitrogen and oxygen. The emissions in the spectrum of the night airglow that might be expected to accompany the dissociative production of O and N are weak or absent (Stewart and Barth, 1979;

Stewart, 1980). It is evident that the night airglow is a result of the transport of atoms from the dayside by the general circulation of the thermosphere (Stewart 1980). Stewart et al. (1980) conducted a morphological study of the Venus ultraviolet night airglow, for which numerous images of the dark side of Venus showing the spatial and temporal variation of the emission were obtained. A full nightside local time composite map of the $NO^*(0,1)$ band vertical intensity distribution was obtained as the spacecraft orbit precessed in local time. This composite map containing 35 orbits of data on a latitude and hour angle grid shows a bright spot reaching 5 kR located at 2 AM local solar time just south of the equator (see plate 4 of Stewart et al., 1980). Asymmetry about the noon-midnight line is clearly visible, just as for the O_2^* airglow, implying a "super-rotating flow" in addition to the mean subsolar-to-antisolar circulation. A highly variable thermospheric circulation is also implied, based on the observed variability of the peak intensity and position of the nightglow emission (Bougher, 1980). The emitting layer is at 115 ±3 km altitude (Gerard et al., 1981). In short, the OUVS (Orbiter Ultraviolet Spectrometer) instrument provided a valuable study of the NO^* night airglow, from which horizontal (Stewart et al., 1980) and vertical (Gerard et al., 1981) maps were constructed.

Consistency among NO^* and O_2^* airglow maps is not generally expected, since observations were not conducted simultaneously. However, average distributions of these emissions were compiled for several orbital passes to enable a comparison. A noticable discrepancy was observed between the local time dependencies of the NO^* and

O_2^* emissions and the ONMS measurements, which Stewart et al. (1980) attribute to the day-to-day variability of the thermospheric circulation. Despite these problems, the airglow species are a very sensitive tracer of the small and large scale dynamical processes operating in the Venus thermosphere. In particular, these airglow maps provide further evidence of a super-rotating component of the flow, in addition to the mean subsolar-to-antisolar thermally-driven circulation. Any complete model of the thermospheric circulation would seek to incorporate a driving mechanism to mimic this asymmetrical flow (see Fig. 2-5 for a cartoon which illustrates such a circulation).

2.2 Standard Atmosphere Empirical Models

Several empirical composition and temperature models, based on the Pioneer Venus data, have been devised in an effort to describe a standard atmosphere (Niemann et al., 1980; Hedin et al., 1983; Keating et al., 1983). Early ONMS data was expanded in spherical harmonics about the globe to achieve a representative picture of the composition and temperature fields at all latitudes and altitudes. This early model was however found to produce mass densities 60% smaller than those suggested by OAD data of Keating et al. (1980) and BNMS data of von Zahn et al. (1980) at 60°SZA. Ionospheric calculations of Cravens et al. (1981) also suggested that densities higher than those measured by ONMS were needed to fit ionospheric data at low SZA. The F1-ionospheric peak at 140 km required ONMS densities enhanced by roughly a factor of 1.6.

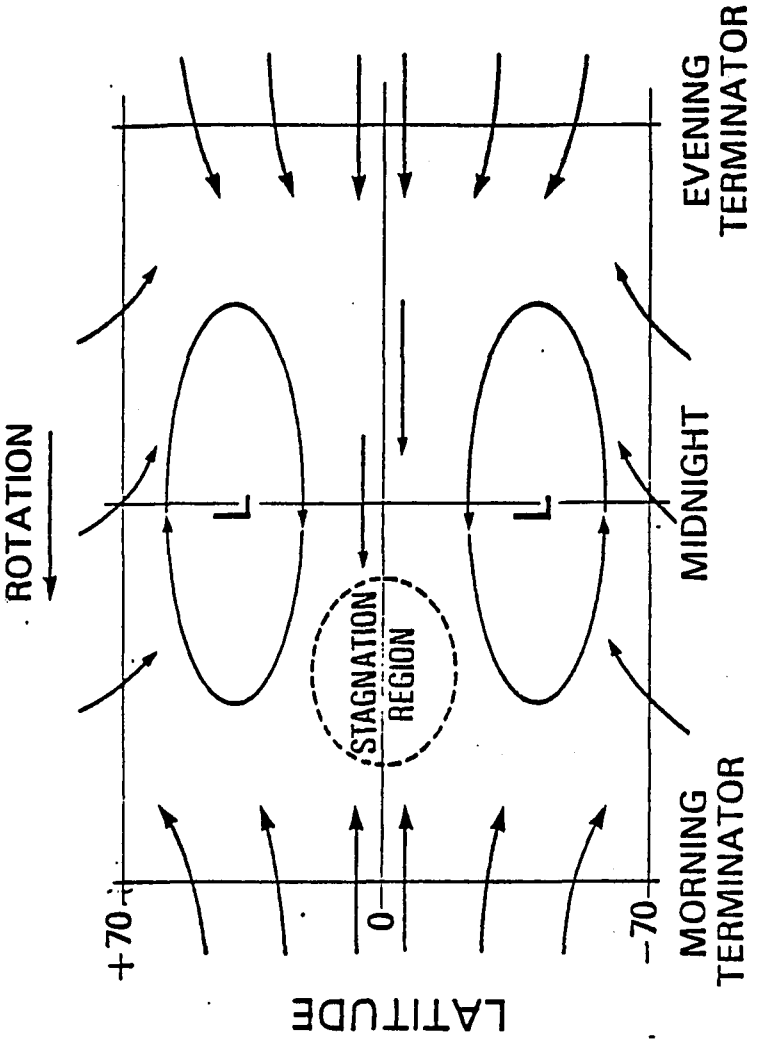


Fig. 2-5 A schematic flow pattern for the nightside in the thermosphere of Venus (from Niemann et al., 1980).

This inconsistency among OAD, BNMS, and ONMS densities prompted the development of the new empirical model of Hedin et al. (1983) (referred to as VTS3). Hedin et al. (1983) suggested that a calibration problem with flow rates may have lead to an underestimation of the densities derived from the mass spectrometer. Laboratory experiments for 5 km/sec flow rates suggested that under the 10 km/sec actual flow conditions, a 1.6 enhancement of densities was quite realistic (private communication, Kasprazak, 1984). The VTS3 empirical model incorporated this 1.6 enhancement factor for all ONMS densities as a means to reconcile conflicting OAD, ONMS, and BNMS density and temperature data. OAD data was later collected to provide an additional empirical model to reconcile conflicting observations (Keating et al., 1984).

2.2.1 ONMS Empirical Model

VTS3 is a global model of the thermospheric temperature and composition data above 100 km which uses a spherical harmonic representation (emphasizing SZA variation) of the ONMS data. Additional information on vertical profiles was provided by entry probe densities above 100 km (Seiff et al., 1980). CO_2 and He data below 180 km was also added from von Zahn et al. (1980). The exospheric temperatures are determined from the altitude variations of atomic oxygen. Density profiles are extended downward to 100 km from the 140 km observational lower boundary (ONMS) by using empirical formulae to provide a transition through the turbopause region. Such empirical formulae prescribe the effects of eddy diffusion and vertical flows, and permit a

match of entry probe density data. The empirical model quantities are approximately symmetric with SZA. Yet, the lowest order sine terms of local time are also included to fit the observed asymmetries. The number of harmonics employed in the current empirical model is limited to five, which somewhat degrades the model fit to the sharp CO_2 and He variations across the terminator. However, all the available data and the model profiles are in reasonable agreement, usually within 10% (dayside) and everywhere within 25% (including nightside scatter of densities) (Hedin et al., 1983). Exospheric temperatures are likewise within 10% of available values inferred from ONMS, OAD, and BNMS measurements.

Hedin et al. (1983) gives tabulations of Venus model calculations at the equator (F10.7 = 200×10^{-22} Wm^{-2} H_z^{-1}) for local noon and midnight. Asymmetries are clearly evident in the model densities and temperatures at 0° latitude, particularly above 150 km. From this data set (VTS3), mixing ratios of O, CO, and N_2 densities, as well as temperatures are contoured on a log-pressure scale for future comparison to theoretical calculations (see Appendix A.1).

2.2.2 OAD Empirical Model

OAD inferred densities and temperatures (which also utilize BNMS data indirectly) have recently been incorporated into an OAD empirical model of the upper atmosphere above 150 km (using F10.7 ≈ 150×10^{-22} Wm^{-2} H_z^{-1}: appropriate at probe descent), referred to as HYSM (Keating et al., 1980). A further extrapolation of densities and temperatures from 150 km to 100 km was made (Keating et al., 1984) by

adopting SZA profiles based on the one-dimensional models of Massie et al. (1983) at 60° and 180°SZA (see Section 3.2.6 for details). Appendix A.2 illustrates mixing ratios of HSYM O, CO, and N_2 densities, as well as contoured temperatures. Again these fields are plotted on a log-pressure scale to facilitate comparison with the VTS3 empirical model and the improved Venus two-dimensional model output fields (see Chapters V and VI).

It is significant to note that dayside densities and temperatures for the HSYM empirical model are lower than those of the VTS3 empirical model. Specifically, HSYM atomic O number densities are ~10% smaller at comparable dayside altitudes above 150 km. This is consistent with the cooler dayside exospheric temperatures of HSYM, which are roughly 20°K lower than those of VTS3. Nightside temperatures of HYSM are also 10°K warmer at exospheric heights. The calibration and interpretation difficulties inherent in OAD and ONMS measurements (upon which these two independent empirical models are based) are partially responsible for this range of empirical model composition and temperature differences. Also, slightly different "average" levels of solar activity are assumed. For our modelling purposes, it is most appropriate to adopt the OAD empirical model composition and temperatures as a lower limit reference or standard atmosphere upon which to base further two-dimensional hydrodynamic model calculations. Likewise, the VTS3 empirical model fields will serve as an upper limit reference for the improved hydrodynamical calculations described in Chapters V and VI.

2.3 Summary

Thus, a multi-dimensional model of the Venus thermosphere needs to predict a thermospheric circulation pattern that consistently explains all the available composition, temperature, and airglow observations. There is a sufficiently large data base now available to permit such a modelling effort. However, present model calculations will likely be limited to simulations of the mean atmosphere, as given by these mean empirical models of Hedin et al. (1983) and Keating et al. (1984).

CHAPTER III

REVIEW OF PREVIOUS MODELLING EFFORTS

3.1 Overview of Venus Thermosphere Model Development

Models of the composition, temperature, and wind structure of the neutral upper atmosphere of Venus have been under development since 1972. Dickinson (1972, 1976) developed a one-dimensional NLTE radiative transfer code that permitted the thermodynamic equation to be solved. The global mean temperature was thus first estimated over the 65 to 200 km altitude range (Dickinson, 1976) (see Fig. 2-4). Subsequently, this global mean temperature, and the corresponding 15μ cooling and infrared heating fields, were incorporated into a two-dimensional hydrodynamical model of the thermospheric circulation (Dickinson and Ridley, 1975, 1977). Composition, momentum, and thermodynamic equations were interactively solved for atomic O, CO, and CO_2, horizontal wind, and temperature fields. Diagnostic vertical velocity and perturbation height fields were also obtained from continuity and state equations. This most recent two-dimensional model (Dickinson and Ridley, 1977 or DRM2) provided the best pre-Pioneer Venus predictions of the composition, temperature, and wind fields based solely on a symmetric subsolar-to-antisolar Venus thermospheric circulation.

Pioneer Venus provided a comprehensive (nearly global) data base of composition and temperatures for the upper atmosphere (see Chapter II). Several one-dimensional empirical model atmospheres were created on the basis of an initial analysis of this Pioneer Venus data, including the measurements of day and nightside airglow. These observations, unfortunately, do not span the entire altitude range between 100 and 200 km. As a result, temperatures and composition below 140 km were obtained by extrapolation of the observations guided whenever possible by these one-dimensional composition models (von Zahn et al., 1980; Stewart et al., 1980; Massie et al., 1983). A more self-consistent scheme was presented by Mayr et al. (1980) for construction of a three-dimensional multi-constituent model describing the solar-diurnal tide in the super-rotating Venus thermosphere. Their spectral model used a mechanistic approach to describe various diurnal characteristics of composition and temperature observed by ONMS.

This chapter identifies the discrepancies present between the Pioneer Venus observations (Chapter II) and the models just discussed. Such a comparison points out the need for a new modelling effort (as described in Chapter I) that seeks to incorporate new physical processes and parameters for an improved match of calculated temperature and composition fields to observations. Improved general circulation models of the Venus thermosphere can be greatly aided by a detailed examination of the successes and failures of these earlier modelling exercises. In particular, what are the shortcomings of these previous model predictions in the light of Pioneer Venus obser-

vations? What specific one-dimensional model parameterizations could be invoked or changed in an improved general circulation model? What additional physical processes seem appropriate for testing that have so far been neglected in one-dimensional and two-dimensional models? The final strategy for developing improved Venus two-dimensional and three-dimensional hydrodynamic models will be guided by these earlier modelling attempts.

3.2 Previous Models: Descriptions and Results

3.2.1 Introduction

Pre-Pioneer Venus models were guided solely by sketchy Mariner 5, 10 and Venera data, whereas post-Pioneer Venus models have had the benefit of comprehensive temperature and composition measurements. More sophisticated and complete models have been developed as a more comprehensive data base has emerged. Such an evolution of Venus thermospheric models, from one-dimensional to two-dimensional and finally three-dimensional general circulation models, closely parallels the development of terrestrial thermospheric models (Dickinson et al., 1975, 1977; Roble et al., 1977; Dickinson et al., 1981; Roble et al., 1982; Dickinson et al., 1983).

3.2.2 One-Dimensional Global Mean Models (Dickinson, 1972, 1976)

Dickinson (1972) set the stage for subsequent Venus upper atmosphere modelling by developing a model to describe the global mean temperature structure from 65 km to 200 km. This first study was

a necessary prerequisite for examining the effects of motions driven by absorption of solar radiation. These calculations incorporated radiative sources and sinks for the Venus upper atmosphere in a self-consistent fashion. The primary goal was to seek a temperature profile for which a global mean balance between radiative sources and sinks, and thermal conduction could be achieved. Subsequently, heating and cooling rates (as a function of SZA) were calculated and parameterized respectively for linkage to the two-dimensional hydrodynamical code (Dickinson and Ridley, 1975, 1977).

Dickinson (1972) chose to concentrate on the radiative transfer of the Venusian mesosphere, where, as for the Earth, a NLTE treatment is required (since relative populations cannot be assumed to be given by a Boltzmann distribution). In particular, the one-dimensional Venus radiative transfer calculation utilized a two-level NLTE formulation for the CO_2 vibrationally-excited states. The primary radiative transfer was assumed to occur only in the 15μ and 4.3μ band systems. Dickinson (1972) pointed out that the ultimate channel for conversion of radiative quanta into heat was the collisional relaxation of the 15μ fundamental band. Hence, the relative populations of the 15μ (and 4.3μ) vibrational levels were needed before the net NLTE radiative heating could be determined.

Dickinson (1972) went to great pains to construct an accurate, yet simplified two-level NLTE treatment of the CO_2 (0, 1, 0) and CO_2 (0, 0, 0) levels. Careful bookkeeping of population-depopulation of all excited vibration levels was done to accurately calculate all important contributions to the above states. To this end, balance

equations were solved for the preceeding ground state and first excited state populations (see Dickinson, 1972, for details). Dickinson (1972, 1976) carefully described the additional model assumptions that permit computations to be carried out. See Chapter IV for additional details of updated assumptions since 1976.

The conduction equation (heat equation) is solved to steady-state for conditions corresponding to a balance of global mean radiative sources and sinks and thermal conduction:

$$c_p \frac{\partial T}{\partial t} - \frac{\partial}{\partial z}\left(K_T \frac{\partial T}{\partial z}\right) = Q_{IR}(z) + Q_{UV}(z) \qquad (3.1)$$

where:

T = temperature

t = time

z = altitude

Q_{IR} = net rate of global mean heating by all infrared processes

Q_{UV} = the rate of absorption of thermal energy due to solar UV radiation

K_T = thermal conductivity coefficient

c_p = specific heat at constant pressure

An iterative approach is necessary since many parameters and terms (i.e., for NLTE source functions and net radiative heating) are temperature dependent.

Dickinson (1972) calculated a global mean temperature profile (see Fig. 2-4) corresponding to an EUV heating efficiency of 30%, sug-

gested by Stewart (1972). Here, all $O(^1D)$ excess energy is assumed to be quenched to heat. Below 115 km, infrared heating approximately balances 15μ cooling. Above 160 km, downward conducted heat (giving rise to cooling) largely balances EUV heating. This conducted heat becomes deposited between 120 to 140 km, and is offset by 15μ cooling. The exospheric temperature calculated is 475°K for this maximum heating efficiency case. Figure 2-4 also shows a temperature minimum (a mesopause) at 122 km corresponding to 180°K.

The relative uncertainty of the EUV heating efficiency, as well as other parameterizations, lead Dickinson (1976) to conduct several sensitivity studies of various model parameterizations including EUV heating efficiency (Fig. 3-1a), eddy mixing (Fig. 3-1b), and collisions of atomic oxygen with CO_2 (for enhanced CO_2 emission).

Studies of Dickinson (1976) and Fox and Dalgano (1981) indicated that the previously assumed EUV efficiency of 30% (Stewart, 1972) was an upper limit. In particular, Dickinson (1976) suggested that the very rapid collisional quenching of $O(^1D)$ is consistent with an assumption that most of the $O(^1D)$ energy is being transferred to CO_2 vibrational-rotational excited states. Such CO_2 vibrationally excited states at low pressures of the Venus thermosphere lose their energy to infrared airglow, rather than being quenched. As such, Dickinson (1976) tentatively concluded that most, if not all, $O(^1D)$ energy in a CO_2 atmosphere is lost to space. Assuming that a significant fraction of the kinetic energy of hot ions, atoms, and molecules is transferred to CO_2 vibrational energy, new heating efficiencies were specified and tested (see Fig. 3-1a).

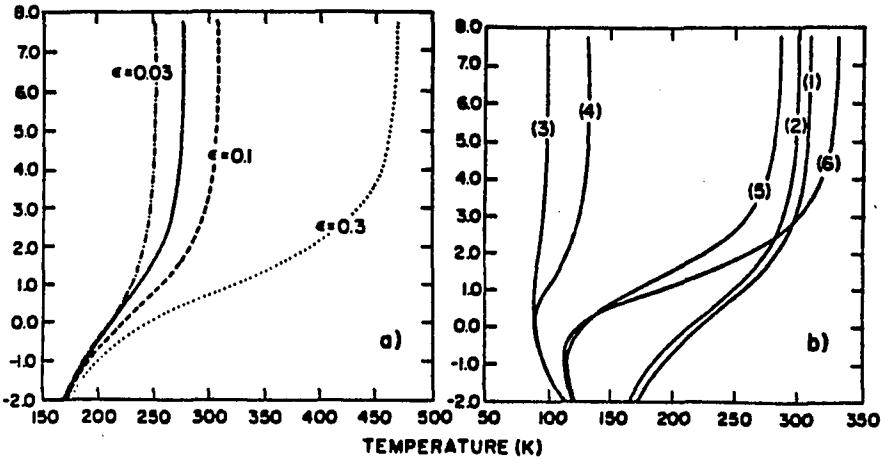


Fig. 3-1 Calculated global mean temperature profiles for various model parameterizations. (a) shows the effects of various EUV heating efficiencies, (b) shows the effects of various eddy mixing models (from Dickinson, 1976)— — (a) the solid line shows the result for $\varepsilon = 0.1$, but with enhanced NLTE excitation of CO_2 by O. (b) Profiles (1) through (4) are calculated for $\varepsilon = 0.1$ EUV efficiency, and profiles (5) and (6) for $\varepsilon = 0.3$. In profile (1) $K = 0$; for all other profiles K is constant between 0 and -4, and the decay is inversely proportional to pressure below $z = -4$. In profiles (2), (3) and (5) K remains constant above $z = -4$, while in profiles (4) and (6) the decay of K is proportional to pressure above $z = 0$. The maximum eddy coefficient is 10^6 for profile (2) and 10^7 cm^2/s for profiles (3) through (6).

Pure CO_2 exospheric temperatures were calculated, ranging from 250 to 475°K corresponding to 2% and 30% constant topside efficiencies. The low EUV efficiency profile (2 to 22%) (Dickinson and Ridley, 1977) was determined as the sum of 2% direct heating and an estimate of that fraction of the solar energy channeled into CO_2 vibrational-rotational states (Stewart, 1972) that is quenched by collisions at the high pressures of the low thermosphere and upper Venusian mesosphere. Dickinson and Ridley (1977) estimated that roughly 50% of the vibrational-rotational excitation goes into excess rotational energy and 50% into vibrational energy, the latter being entirely lost. Hence, the fraction of the vibrational-rotational energy thermalized is given by a quenching factor:

$$f(p) = 0.5/[1 + 1.1 \times 10^{-4}(T/228)^{1/2}/P] \qquad (3.2)$$

where "T" is temperature and "p" is pressure in μbar.

Calculated global mean temperatures were lower in the presence of O atoms (non-pure CO_2 atmosphere), which enhance the collisional excitation of CO_2 vibrations. Available evidence suggested, according to Dickinson (1976), that the relaxation of CO_2 (0, 1, 0) is a factor of ×10 more likely for a collision of CO_2 with O than with CO_2. These estimates were based on extrapolated high temperature studies (Center, 1973) and may be in error by a factor of 3. Exospheric temperatures now ranging from 240 to 400°K (for the same 2 and 30% constant efficiencies) illustrate the effect of a non-pure CO_2 atmosphere upon temperatures. Dickinson (1976) furthermore suggested that future

models of the Venus thermosphere may need to include a detailed parameterization of the enhanced relaxation of CO_2 by atomic O, if O is present in concentrations greater than a few per cent.

The sensitivity of thermospheric mean temperatures to parameterized eddy cooling was also tested. Hunten (1974), Izakov (1978), and others have explained that small scale mixing processes can either give rise to heating of the atmosphere by viscous dissipation, or to cooling due to a redistribution of heat by the vertical motion of convective mixing. Dickinson (1976) chose to assume that all mixing gives rise to cooling, an upper limit assumption, and adopted the Hunten (1974) parameterization:

$$Q_E = \frac{\partial}{\partial z}\left[K_E(z) c_p \rho \left(\frac{\partial T}{\partial z} + \frac{g}{c_p}\right)\right] \qquad (3.3)$$

where:

$K_E(z)$ = eddy coefficient profile

ρ = mass density

c_p = specific heat

g = gravity

Q_E = "eddy conduction" or transport of heat

K_t = maximum eddy coefficient at the turbopause

Generally, $K_E(z) = K_t(P_t/P)$ for $P>P_t$. The z-dependence for $P<P_t$ is described in Fig. 3-1b. It was found (as seen in Fig. 3-1b) that eddy mixing with $K_t = 10^6$ cm^2/sec ($z = \log_e(P_0/P)$ where $P_0 = 5 \times 10^{-6}$ mb), had little or no effect upon thermospheric temper-

atures. For $K_t = 10^7$ cm^2/sec, the effect, however, was drastic with cooling on the order of 100 to 200°K. Furthermore, eddy mixing with $K_t > 10^7$ cm^2/sec could only be consistent with estimated thermospheric temperatures if they were controlled primarily by a balance between heating by viscous dissipation of the mixing motion and cooling by the downward mixing of heat. The most significant effect on temperatures occurs for $z < 0$, particularly around the mesopause at 134 km. Dickinson (1976) also suggested that exospheric temperatures are more sensitive to much smaller values of eddy mixing than is composition, indicating that ad hoc eddy mixing vertical velocities used by one-dimensional models to mimic the effects of large scale circulation would adversely impact temperatures in a self-consistent calculation of composition, winds, and temperature.

This global mean model of the Venus temperature profile suffers from the uncertainties just described: EUV heating efficiency, the effect of eddy mixing, and the unclear role of O in exciting CO_2 vibrations. Such a one-dimensional model is also limited since hydrodynamical terms describing advection and adiabatic convection are not incorporated. Hinteregger's (1970) fluxes that were used for the calculations may also be low by a factor of two, at least for cycle 21 solar maximum conditions appropriate for Pioneer Venus observations. This one-dimensional thermodynamical model does however provide the basis for calculating the radiative sources and sinks as input into a two-dimensional coupled chemical-dynamical code.

3.2.3 Two-Dimensional Hydrodynamic Model (Dickinson and Ridley, 1975, 1977)

Dickinson and Ridley (1975, 1977) made use of the one-dimensional global mean model radiative heating and cooling to formulate a two-dimensional hydrodynamical (DRM) model. The DRM models (DRM1, 1975; DRM2, 1977) were designed to calculate temperature structure, composition, and winds of the mesosphere and thermosphere of Venus using a non-linear time-dependent hydrodynamical code, for which chemistry and dynamics are intimately coupled. Such a model of the large scale thermospheric circulation circumvents the primary limitation of one-dimensional models, which do not use motions calculated from first principles. These winds serve to control the horizontal distribution of temperature and composition. Feedback among composition, temperature, and wind fields can be included for this self-consistent treatment of the multi-component fluid.

The model assumes that all variables depend only on altitude and distance from the subsolar point (two dimensions). The code was designed to solve four time-dependent equations for horizontal motion, temperature, and the distributions of O and CO, as well as the two diagnostic equations for vertical velocity and perturbation height, which represent continuity and hydrostatic balance for the fluid. CO_2 is calculated passively as the remainder of the total density. The winds were driven solely by absorption of EUV and IR radiation, which provided heating of molecules and (for EUV and UV radiation) dissociation of CO_2 into O and CO. IR heating and 15μ cooling were

supplied by the detailed one-dimensional radiative transfer code described in Section 3.2.2.

Details of equations employed by DRM1 and DRM2 are described in Chapter IV. In general, though, each time-dependent equation is solved to steady state. The momentum equation seeks the resulting horizontal wind field that corresponds to a balance of pressure gradient, vertical diffusion, and hydrodynamic advection terms. The thermodynamic equation, at steady state, represents a balance of vertical conduction, EUV and IR heating, adiabatic heating/cooling, 15μ cooling and hydrodynamic advective terms. The coupled mass flux continuity (or composition equation) is solved for each specie, O and CO corresponding to a balance of molecular diffusion, photo-dissociation source, and hydrodynamic advection. Production for O and CO is exclusively due to CO_2 photolysis, whether by direct dissociation or indirect dissociation via CO_2 ionization. An independent prescription for ion chemistry is neglected, except insofar as CO_2^+ production leads to the formation of the O and CO pair. Loss is due to chemical recombination.

The most recent pre-Pioneer Venus two-dimensional model (DRM2) employs adjustable parameterizations tested earlier within the simpler one-dimensional global mean model (Dickinson, 1976). Specifically, a 2-22% "lowest standard" EUV heating efficiency profile is used to estimate that fraction of locally deposited energy that remains as heat (see details in 3.2.2). This profile is notably different from the flat 30% efficiency employed by DRM1. The effect of O on CO_2 collisions in exciting CO_2 vibrational-rotational states is also para-

meterized. Here, O is assumed to excite CO_2 vibrations ten times as rapidly per molecule as do self-collisions. The two-dimensional perturbation 15μ cooling scheme incorporates this multiplicative factor. Finally, DRM1 had previously calculated the departure from a reference cooling (from Dickinson, 1972) with an expression linear in the temperature perturbation (i.e., a Newtonian cooling). Since this linearization was found to be unsatisfactory, particularly in the lower nightside thermosphere, a new parameterization was given (Appendix B) for nonlinear temperature dependencies of the 15μ cooling in a simplified cool-to-space approximation (DRM2). Eddy processes were purposely neglected in the two-dimensional formulation.

This more recent model (DRM2) led to a large scale circulation, consisting of upwelling on the dayside, sinking motion on the nightside, and a day-to-night horizontal flow across the terminator (see the U and W fields of Figs. 3-2c,d). This global mean subsolar-to-antisolar circulation acts to remove the photodissociated species O and CO from the dayside and transports them to the nightside, where sizeable concentrations are realized. Figure 3-2e illustrates the calculated horizontal and vertical distributions of O and CO brought about largely by these thermally driven winds.

DRM1 and DRM2 both predict a wind of several hundred m/s blowing across the terminator, and abruptly weakening to small values on the nightside. This sharp convergence of horizontal winds at the terminator generates a strong tongue of large downward velocities. Adiabatic compressional heating generated by these vertical motions produces the belt of warm air seen nightward of the terminator (see

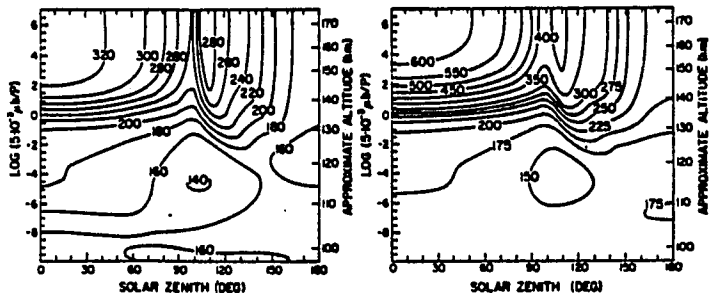


Fig. 3-2a Calculated temperature fields (°K) obtained with the low EUV efficiency model (2-22%) (from Dickinson and Ridley, 1977).

Fig. 3-2b Calculated temperature fields (°K) obtained with the same model except with a 30% efficiency of EUV, $\lambda<1080$, and complete quenching of $O(^1D)$ at longer wavelengths (from Dickinson and Ridley, 1977).

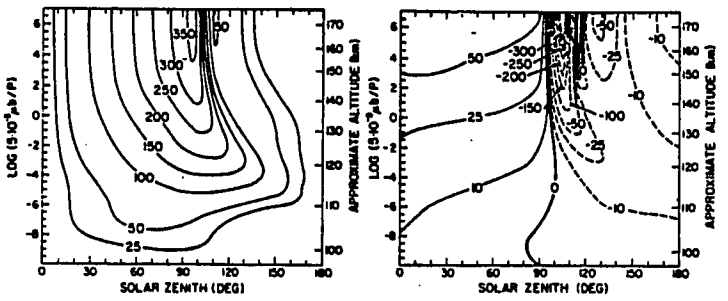


Fig. 3-2c Horizontal motions (m/sec) calculated for the low EUV efficiency model (from Dickinson and Ridley, 1977).

Fig. 3-2d Vertical motions (cm/sec) calculated for the low EUV efficiency model (from Dickinson and Ridley, 1977).

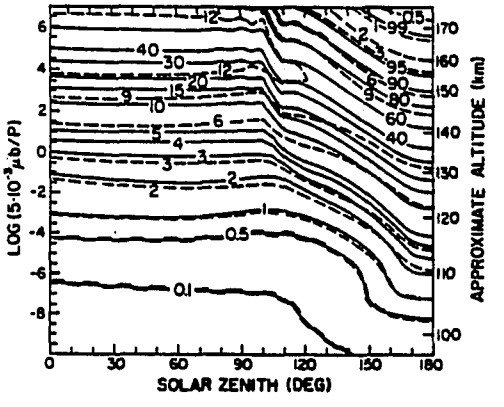


Fig. 3-2e Relative concentrations (%) of O (given by solid lines) and CO (given by dashed lines) obtained with the low EUV efficiency model (from Dickinson and Ridley, 1977).

Fig. 3-2a). A sharp gradient of temperature is also seen across the terminator and downward through the maximum EUV heating region above z = 0 (134 km) on the dayside. Exospheric temperatures on the dayside range from 600°K to 320°K, corresponding to direct heating for separate model runs utilizing constant efficiencies of 30% and 2% respectively (DRM, 1975, 1977). Nightside exospheric temperatures for these same cases drop from 250°K to 180°K (see Figs. 3-2a,b). No notable temperature changes are seen below z = -1 between the two models.

Composition is most easily described by referring to day-night contrast at the F1-ionospheric peak, at roughly 142 km. Dayside atomic oxygen mixing ratios range from 5 to 10% for DRM1 and DRM2, respectively. Correspondingly, nightside values are 60% to 50%. Notice, as in Fig. 3-2e, a large buildup of atomic oxygen on the nightside, due to hydrodynamic advection of photodissociated CO_2 by-products. CO mixing ratios exhibit much less buildup on the nightside, since CO is less readily transported due to its larger molecular weight. Both DRM1 and DRM2 illustrate 5-6% CO mixing ratios at the dayside F1-peak, with 10-12% values present on the nightside.

It is difficult to independently describe the resulting variable fields as calculated, because they are all strongly coupled to one another. Feedback among the composition, temperature, and wind fields is thus quite apparent upon closer inspection of the DRM1 and DRM2 models. For instance, the above comparisons of atomic oxygen at the F1-peak show an increase on the dayside and a decrease on the nightside as the model is changed from DRM1 to DRM2. This "redistribution" of atomic oxygen is caused by a successive weakening

of the day-to-night circulation, as dayside heating is diminished. Von Zahn et al. (1983), in fact, points out that this weakened circulation is also visible in the vertical velocities, which are reduced from 50 to 35 cm/s at 140 km. The implication is that weaker circulation can maintain higher O and CO concentrations on the dayside while reducing the O and CO buildup on the nightside. Of additional importance is the indication from DRM1 and DRM2 that weakened circulation results in cooler nightside temperatures. Balance studies of individual thermodynamic terms suggest that the primary source for nightside heating comes from the circulation, whether by adiabatic compression due to nightside subsidence, or by thermal advection across the terminator. Either way, dynamical processes are very important in controlling the nightside temperatures in Venus' upper atmosphere.

A detailed comparison of the individual terms in each time-dependent equation (at different levels) is important to determine the balances actually operating in the two-dimensional model. Figures 3-3 and 3-4 show such a comparison of terms for the thermodynamic and composition equations respectively. Calculated fields are normalized so that the sum of the absolute values of all terms at a given level is unity. These "balance" plots also provide a measure of convergence in the model as a steady state solution is approached. The integration is continued until the time-tendency terms are <1%, i.e., small compared with the dominant terms in the equations.

Figure 3-3 illustrates the principal balances within the thermodynamic equation at four separate pressure levels over 0 to 180°

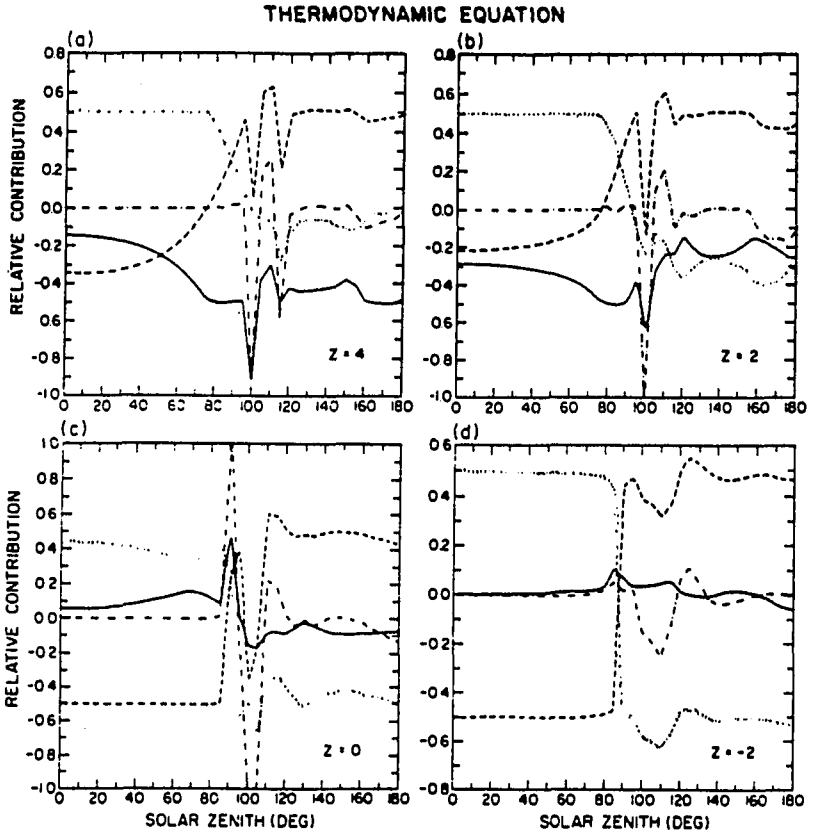


Fig. 3-3 The relative magnitude of the various terms in the thermodynamic equation (from Dickinson and Ridley, 1977). These are normalized so that the sum of their absolute values is unity: _____, heating by molecular conduction; ....., solar heating minus total infrared cooling; -----, net (adiabatic) heating by the horizontal and vertical motion terms; -.-.-, rate of temperature increase minus heating by horizontal diffusion.

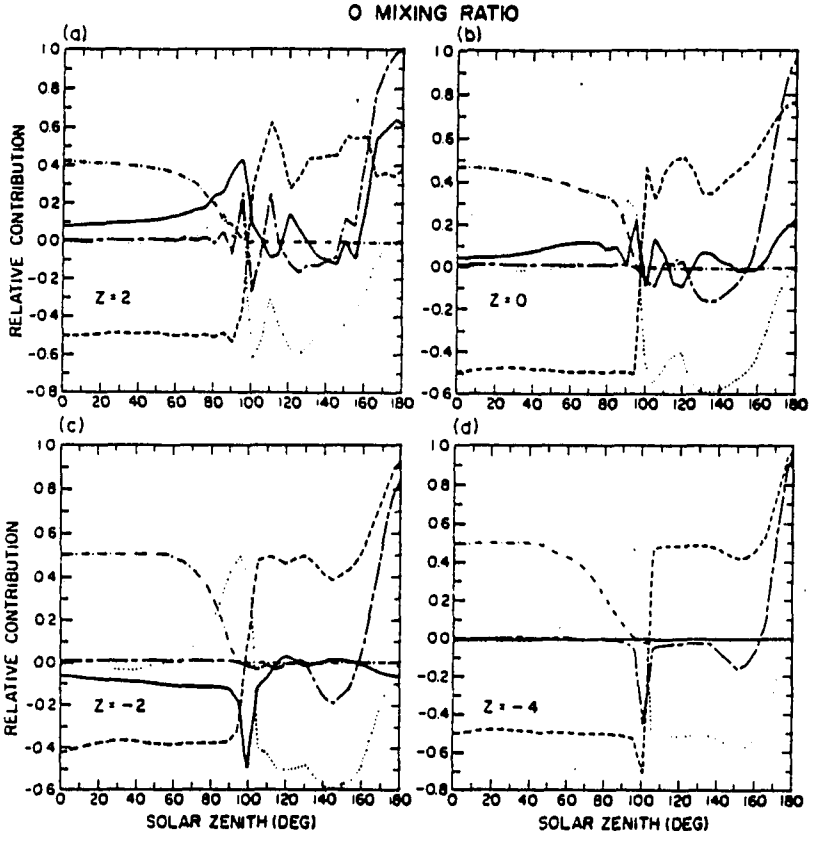


Fig. 3-4 The relative magnitudes of the various terms in the continuity equation for atomic oxygen (from Dickinson and Ridley, 1977). These are normalized as in Fig. 3-3: _____, increase by molecular diffusion; ....., increase by horizontal motion advection; -----, increase by vertical motion advection, -.-.-, photodissociation rate; , time rate of increase minus increase by horizontal diffusion.

SZA. For $z > 2$, net dayside radiative heating balances upwelling adiabatic cooling plus thermal conductive cooling. Conversely, below $z = 0$, net radiative heating is primarily balanced by cooling due to upwelling and horizontal motions. On the nightside, infrared cooling offsets heating by subsidence and horizontal advection from the dayside. It is important to note that dayside cooling and nightside heating are largely determined by the effects of vertical motions. Figure 3-4 illustrates compositional balances for atomic oxygen. Over most of the dayside thermosphere, photodissociation serves as the primary source of O, which is lost by hydrodynamical advection. However, in the upper dayside ($z > 4$), upward molecular diffusion of O is balanced by the same hydrodynamic loss. Over the entire nightside, incoming O, provided by the horizontal winds, is convected downward. Clearly, the presence of O and CO on the nightside is entirely due to its transport from the dayside. Momentum transport by these winds is largely balanced at all levels by the horizontal pressure gradient. Such thermally driven winds are only retarded at low pressures ($z > 2$) by molecular viscosity.

It is often argued that the predictions of detailed hydrodynamical models (such as DRM1 and DRM2) can be represented by one-dimensional eddy mixing models. Dickinson and Ridley (1977) suggest this might be an accurate assumption providing that composition alone is considered. However, feedback among temperature, composition, and winds is shown to be important to the two-dimensional model calculations (DRM1 and DRM2). The problem occurs when the motions hypothesized in a one-dimensional model are strong enough to give good

dayside composition at all altitudes. Then, these eddy motions also drastically alter the global mean thermal structure. Hence, such a coupled chemical-dynamical model is crucial to an accurate simulation of the temperature, composition and wind fields of Venus' thermosphere. The complete lack of eddy diffusion in these two-dimensional models, however, is improper.

3.2.4 One-Dimensional Compositional Model at 60°SZA (von Zahn et al., 1980)

The modelling work of von Zahn et al. (1980) provided a valuable first analysis of the observed dayside composition by fitting calculated fields to BNMS number densities for altitudes above 130 km. Coupled continuity-diffusion equations were numerically integrated upwards from 100 to 225 km to obtain a morningside model at 60°SZA. Chemical production and loss were carefully included above 130 km. It was assumed for computational efficiency, that chemical reactions were of minor importance to O and CO profiles below 130 km. Table 3 of von Zahn et al. (1980) shows the BNMS number densities for He, N_2, CO, O, and CO_2 as calculated by the morningside (MS) model. The model fits BNMS and OAD observations quite well above 130 km. ONMS number densities for He, CO_2, CO, and N_2 are lower than those of the MS model by factors of 1.6, 1.4, 2.4, and 2.5, respectively. The MS model exospheric temperature of 275°K represents the best high-altitude distribution of the BNMS helium and CO_2 data available. Accordingly, the exobase for the major constitutent, atomic oxygen, is established at 190 km for the MS model at 60°SZA.

The success of the MS model fits to BNMS observations is in large part due to the chosen estimate of the altitude dependance of the eddy coefficient profile utilized for eddy diffusion. The analytical representation of the eddy coefficient profile was taken from Lindzen (1971) as $K_E(z) = A/\sqrt{N}$, where N is total number density (cm^{-3}) and A is a tuning factor chosen to be 1.4×10^{13} $cm^{-1/2}/sec$. The He data was in fact used to constrain the eddy profile and provide this specific tuning factor. The upper level cutoff for the maximum eddy coefficient, (KMAX), was set at 5×10^8 cm^2/sec, despite the fact that above the turbopause (where $K_E(z)$ is exceeded by the molecular diffusion coefficient D(z)), unique KMAX is not easily determined. Homopause (or turbopause) altitudes were established at 136, 130, and 134 km for N_2, He, and mean composition, respectively. A density independent eddy coefficient resulted in a worst fit of calculated composition profiles to observations.

Densities were extrapolated below 130 km as good fits to observed BNMS densities above 130 km were achieved. Helium was found to be particularly sensitive to the value of the adopted coefficient profile. The estimated He mixing ratio at 100 km was suggested to be 12 ppm from this MS model. Von Zahn et al. (1980, 1983), however, were careful to point out a considerable uncertainty of this prediction by up to a factor of three.

A one-dimensional model of this type is subject to several limitations, the principal one of which concerns the neglected or improperly parameterized effects of large scale winds of the type modelled by DRM2. Certainly, the eddy diffusion parameterization is a

crude way to mimic vertical velocities and the effects on composition. The scheme is certainly inferior to one that calculates winds from first principles. Furthermore, as stated in von Zahn et al. (1980), it is not yet clear whether the eddy coefficient profile and its altitude dependence assumed for the Venus thermosphere is a genuine signature of small-scale vertical mixing or only a reasonable description of compositional variations brought about by a global-scale circulation cell as in the DRM2 model. Shimuzi (1974) estimates that the composition is likely determined by some combination of large scale winds and small scale eddy mixing. This is a question that an improved two-dimensional model (incorporating eddy diffusion) seeks to answer (see Chapter V).

3.2.5 One-Dimensional Compositional Model at 150°SZA (Stewart et al.,1980)

Stewart et al. (1980) present a one-dimensional model calculation for the nightside thermosphere, as a complement to the von Zahn et al. (1980) MS model. Their nightside model is specifically devised to provide a means to analyze the OUVS NO^* airglow measurements of the emission in the NO(δ) bands. A one-dimensional chemical diffusion model, similar to that employed by Rusch and Cravens (1979) on the dayside, is used to solve for density distributions of CO, N, O, O_2, NO, and O_3 in the Venus mean nightside thermosphere from 70 to 140 km. An attempt is made to estimate downward fluxes of O and N over the nightside, and to tune an adopted eddy coefficient profile for diffusion, to give the observed NO^* emission characteristics. Specifically, the volume emission rate at the peak, its corresponding

altitude, and the integrated average intensity over the nightside were key airglow features simulated.

Nightside downward vertical fluxes are prescribed to mimic the global scale circulation effects upon the nightside composition. It is assumed that the O and N sources are derived solely from transport across the terminator at high altitude. Representative (nightside average) downward fluxes for O and N are specified at the top boundary, and correspond to horizontal fluxes derived from DRM2 across the terminator. Lower altitude recombination was invoked as the principle sink for N and O atoms.

Different profiles of O and N densities were constructed, corresponding to several adjustments of the eddy coefficient, in order to converge on a best fit that simulates a peak volume emission rate at 115 ±3 km, as observed (Stewart et al., 1980; Gerard et al., 1981). The best eddy coefficient profile adjustment giving such a fit required $K_E(z) = 1.4 \times 10^{13}/\sqrt{N}$ and a KMAX of 3×10^8 cm^2/sec at 140 km. This is consistent with the best estimate of the eddy coefficient profile of von Zahn et al. (1980).

It was found that a determination of the altitude at which the NO^* emission rate maximizes is a fairly sensitive indicator of the eddy coefficient. A first order interpretation of the airglow measurements would also suggest that the downward flux of N atoms is directly linked to the NO(δ) band emission, since the peak altitudes for N-density and NO^* emission vary in the same manner with respect to the eddy coefficient. Finally, the integrated vertical intensity of 2.8 kR was calculated by the one-dimensional nightside model. This

is in good agreement with the measured average intensity on the nightside of 2.6 kR (Stewart et al., 1980).

Certainly, the downward nightside fluxes estimated from the DRM2 model are reasonable, and the procedure adopted is the next best to actually calculating winds from first principles. However, the one-dimensional nature of the calculation does not permit advection to be properly described at lower altitudes (see also the nightside model of Massie et al., 1983). Furthermore, the adopted DRM2 fluxes are likely overestimates from a global scale circulation that is somewhat too strong (see comments in Section 3.2.3). However, the eddy parameterization (like that devised by von Zahn et al., 1980) is a reasonable starting point for testing eddy diffusion within an improved version of the two-dimensional DRM2 code. The specifics of the eddy profile are not important above the turbopause.

3.2.6 One-Dimensional Composition Models at 60° and 180°SZA (Massie et al., 1983).

Massie et al. (1983) formulated two one-dimensional composition models for 60° and 180°SZA in an effort to reconcile the available neutral composition data sets of the ONMS, OAD, and BNMS instruments. Their results not only presented alternative density profiles, but also illustrated the sensitivity of the solutions to dayside eddy mixing and nightside vertical fluxes.

Dayside profiles of CO_2, CO, O, N_2, He, and O_2 at 60°SZA were derived by simultaneous solution of the respective continuity-flux equations, which coupled ionospheric and neutral chemistry as well as

the vertical transport processes of molecular and eddy diffusion (see Massie et al., 1983, for details). Ionospheric chemistry (similar to that of Nagy et al., 1980) was employed. The photo-ionization J coefficients were all multiplied by a factor of 1.4 to represent the processes of secondary ionization by photoelectrons (see Nagy et al., 1980). NO, $N(^2D)$, $N(^4S)$ for the dayside were adopted from Rusch and Cravens (1979). Large scale circulation effects were neglected for this dayside calculation.

The same continuity flux equations were integrated for the midnight model, now subject to specified downward vertical fluxes. Such a scheme is very similar to that employed by Stewart et al. (1980) to calculate O and N profiles on the nightside. It was assumed that the nightside composition is maintained by transport processes which include molecular and eddy diffusion, and horizontal/vertical bulk velocities. The specified downward fluxes represent the horizontal velocity convergence on the nightside due to the day-to-night large scale thermospheric flow.

Table 3 of Massie et al. (1983) illustrates the best dayside model density profiles calculated by using the eddy profile (similar to von Zahn et al., 1980 and Stewart et al., 1980) corresponding to $K_E(z) = 1.4 \times 10^{13}/\sqrt{N}$ and KMAX = 5×10^7 cm^2/sec. The mean dayside homopause altitude was located at 134 km. Eddy diffusion was not found to greatly influence the solutions above 140 km. CO_2 and N_2 calculated profiles matched most closely BNMS densities while O and CO profiles provided a closer fit to ONMS densities. The initial implication is that the ONMS observations require a separate correction

factor for each measured specie. Certainly, the chemistry modelled here provides the best description of dayside densities to date. However, there still exist unresolved discrepancies among predictions and observations.

Dayside chemical regions were clearly delineated by comparison of production minus loss terms and the model densities calculated. For altitudes above 140 km, ionospheric reactions were most important, particularly as a net source for O and CO, and correspondingly a principal loss of CO_2. Over 110 to 140 km, CO_2 was lost primarily by photodissociation, also giving rise to O and CO products. Below 110 km, recombination reactions were found to be important for removal of O, CO, and N. Also at the lower boundary (<110 km), the minor chemistry of Yung and Demore (1982) began to be important in altering the O and CO profiles. The dayside He mixing ratio at 110 km was calculated to be 7 ppm. Such a clear description of production minus loss terms and chemical regions will be a useful check for improved Venus two-dimensional model chemistry (see Chapter V).

Calculated nightside model densities are tabulated in Table 8 of Massie et al. (1983) for which a slightly stronger eddy profile was used ($K_E(z) = 2 \times 10^{13}/\sqrt{N}$). An exospheric temperature of 115°K was favored as a result of the density profiles and corresponding scale heights. It is very clear from the Massie et al. (1983) midnight model, that downward fluxes for N, O, CO, He, and N_2 are crucial to the calculation of a reasonable nightside neutral thermosphere (see also Stewart et al., 1980).

3.2.7 Three-Dimensional Spectral Model (Mayr et al., 1980)

Mayr et al. (1980) used a mechanistic-type spectral model to describe solar diurnal tides in the rotating Venus atmosphere. Their primary goal was to interpret the available ONMS data with the aid of a three-dimensional multi-constituent model and to infer dynamic properties of the thermosphere. The model specifically illustrates how atmospheric rotation and eddy diffusion affect the global scale diurnal variations of the thermospheric composition. Such a description of the Venus upper atmosphere is a useful precursor to a full three-dimensional general circulation model, which will eventually be required to properly describe the temperature, composition, and wind fields of the Venus thermosphere.

The three-dimensional tidal model was designed first to reproduce the fundamental diurnal mode, which describes the first order day-night variations of the heavier species (CO_2, CO, N_2, and O) and temperature. However, nonlinear coupling, whereby wind-induced diffusion dominates, is important for the lighter species He and H, and to describe the small asymmetrical signature seen in the temperatures. Thus, P_2^2 and P_3^3 higher order modes were calculated. The theoretical results of the tidal model were compared directly with the corresponding terms from the spherical harmonic representation of the ONMS data (according to Niemann et al., 1980).

All atmospheric species were assumed to be in diffusive equilibrium, and subject to eddy diffusion corresponding to an eddy coefficient independent of height ($K_E(z) = 3 \times 10^7$ cm^2/sec). Eddy

heat conduction was neglected in the description of net heating. Source amplitudes for the fundamental mode were also adjusted so that the model heating reproduced the observed temperature variations. Furthermore, models of infrared heating and 15μ cooling were adopted from Dickinson (1972).

Model calculations corresponding to the lowest order harmonic suggested that the day-night contrast of composition and temperature is associated with wind velocities $\lesssim$200 m/s (see Fig. 3-5d). Mass exchange with the mesosphere (as parameterized by downward eddy diffusion) seems to be necessary to buffer the strong horizontal advection provided by these large scale winds, so as to maintain the observed dayside O bulge. The analysis provided by the incorporation of higher order modes furthermore suggested that super-rotating winds, superimposed upon the mean subsolar-to-antisolar circulation, are necessary to give the proper phases and amplitudes of the lighter species He and H about the planet. Specifically, retrograde winds in excess of 50 m/s are required at the equator to give He and H density maximum toward the dawn terminator as observed by ONMS data. Exospheric (return) flow was also parameterized and determined to have a significant effect upon the H distribution. However, thermally-driven mass advection seems to be the dominant dynamical process affecting He. Finally, ion-drag was shown to have a negligible effect upon the calculated wind fields below 200 km.

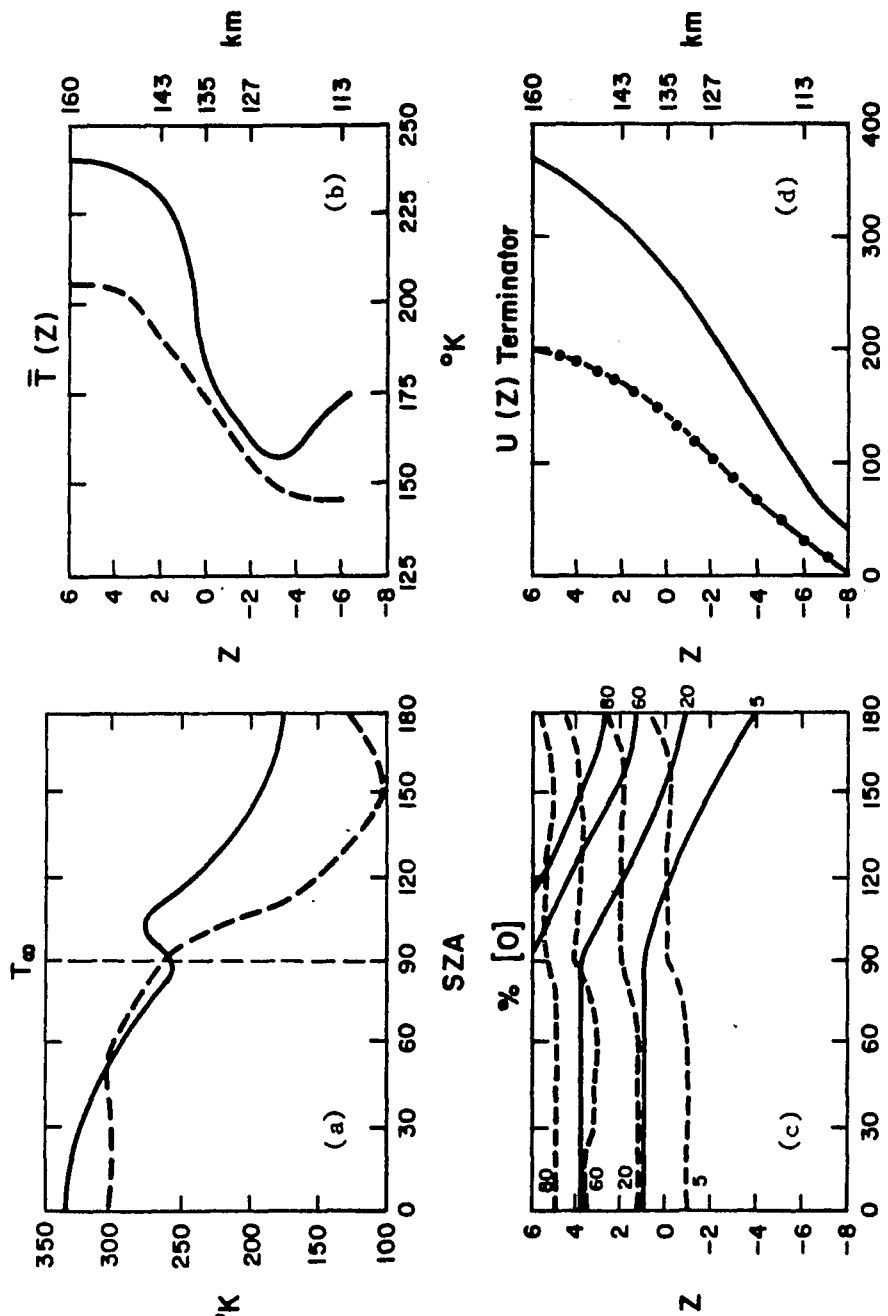


Fig. 3-5 Comparisons of DRM2 predictions and Pioneer Venus observations (_____ DRM2; ----- PV; .-.-. Mayr et al., 1980).

3.3 Shortcomings of Model Predictions

3.3.1 Incomplete Models

In general, the one-dimensional composition models (Stewart et al., 1980; von Zahn et al., 1980; Massie et al., 1983) have been very successful in calculating selected SZA density profiles that match available observations (above 140 km). All these models employ a very similar form of eddy diffusion as parameterized by a pressure-dependent eddy coefficient. Yet, each fails to properly describe the effects of large scale winds, particularly at lower altitudes (below 130 km) where predictions of densities are made. Chapter V will describe just how important vertical bulk velocities are in determining density profiles.

The lack of self-consistently calculated winds makes it quite difficult to expand the one-dimensional calculations beyond mean dayside and nightside models. Terminator estimates of horizontal fluxes are currently used to estimate average downward fluxes and source terms for the transported species over the nightside (Stewart et al., 1980; Massie et al., 1983). Only a full horizontal and vertical wind calculation could improve the nightside neutral atmosphere. It is also important to point out that none of these one-dimensional models calculate temperature profiles coincident with the composition. As suggested by DRM1 and DRM2, there is likely to be significant feedback among the temperature, composition, and wind fields, such that the calculation of any field independently may be improper.

A reasonable alternative has been the spectral model approach of Mayr et al. (1980). An analysis of fundamental and higher order tidal modes has revealed the diurnal characteristics of the major (CO_2, CO, O, N_2) and minor (He and H) species. Asymmetries are clearly seen, and a possible explanation is proposed whereby a particular combination of eddy diffusion and super-rotating winds act to modify the mean subsolar-to-antisolar flow to give proper phases of densities and temperatures about the planet. The model, however, is only a diagnostic examination of the observed composition and temperature fields, from which reasonable winds are estimated. Since temperatures are not entirely calculated from first principles, a degree of inconsistency remains. Implications for dynamical constraints are provided, with the hope that a full three-dimensional self-consistent model will eventually be developed.

3.3.2 Self-Consistent Hydrodynamic Model

The best alternative to these one-dimensional and spectral models has been the DRM2 code. As described in Section 3.2.3, the self-consistent hydrodynamical two-dimensional code has permitted the effect of winds on composition and temperatures to be examined. Strong feedback has indeed been uncovered. Calculated fields, however, are strikingly different from Pioneer Venus observations (see Fig. 3-5). Dayside densities are considerably below that observed (by 40% for O) while nightside densities are correspondingly larger (see Fig. 3-5c). Nightside temperatures are calculated to be 50-70°K too warm (Keating et al., 1980). The major problems with the DRM2 two-dimensional code thus include:

(1) an inability to reproduce the observed day-night temperature contrast, and specifically the very cold nightside temperatures,

(2) failure to properly redistribute the transported species (O and CO) about the planet with strong large-scale winds,

(3) lack of a proper global mean thermal balance for a reasonable (and more efficient) EUV heating efficiency, and

(4) lack of eddy diffusion effects on composition.

3.3.3 Basis for a New Modelling Effort

The apparent discrepancy between DRM2 predictions (Section 3.3.2) and actual observations has been puzzling (see Chapter II). Large scale circulation and its effects on composition and temperature are accurately modelled by DRM2. However, small scale mixing processes (inferred from wave signatures; see Chapter II) are not incorporated. Conversely, one-dimensional models of von Zahn et al. (1980), Stewart et al. (1980), and Massie et al. (1983) properly examine the influence of eddy mixing on composition, but neglect any proper incorporation of large scale dynamical effects. Mechanistic models, furthermore, do not start from first principles, and (as with one-dimensional models) cannot examine the likely feedback among temperature, wind, and compositional fields.

A new modelling effort (as outlined in Chapter I) is needed that makes use of a large-scale circulation scheme like DRM2 to exa-

mine the role of small-scale mixing processes in the Venus thermosphere. Several parameterizations are thus suggested for use in the development of an improved hydrodynamical model. Eddy diffusion and eddy cooling have been found to have a significant effect on composition and temperatures, respectively. The details of the eddy coefficient parameterizations among each of the compositional models presented (von Zahn et al., 1980; Stewart et al., 1980; Massie et al., 1983) are surprisingly similar. A consistent picture of the eddy coefficient has emerged, implying globally uniform mixing. These earlier eddy coefficient parameterizations will serve as a starting point for testing small scale mixing processes (diffusion and cooling) in an improved version of the Venus hydrodynamical code (see Chapters V and VI).

The radiative transfer models of Dickinson (1972, 1976) and the subsequent two-dimensional cases (Dickinson and Ridley, 1975, 1977) have implied that the dayside thermospheric temperatures can be maintained by a more efficient solar EUV heating, provided that additional cooling processes are invoked. Since atomic O is present in the Venus upper atmosphere as the major constituent (above 150-160 km), the enhancement of 15μ cooling by collisions of O with CO_2 will likely be very important to the thermal balance. Improved 15μ cooling parameterizations will be tested within the two-dimensional hydrodynamical code. Ionospheric EUV heating efficiencies, ranging from 2 to 20%, will also be examined.

There is also a clear indication that a global circulation system weaker than DRM2 predicts is required (see Section 3.2.3).

This permits a reduction in the buildup of nightside densities (and temperatures), while retaining more O and CO on the dayside. An improved hydrodynamical code needs to uncover a plausible "drag" parameterization to provide such a reasonable momentum balance and a redistribution of composition and heat about the planet. Terrestrial mesopause "wave breaking" models serve as a guide for possible "momentum drag" schemes (see Chapters IV and V).

A three-dimensional extension of the DRM2 model will eventually be required to provide a self-consistent and thorough quantitative description of the Venusian thermosphere. The important role of "super-rotating" winds (Mayr et al., 1980) can then be examined.

CHAPTER IV

FORMULATION OF AN IMPROVED TWO-DIMENSIONAL HYDRODYNAMICAL CODE

4.1 Updated Two-Dimensional Model

4.1.1 Description of Equations Used

The hydrodynamical system solved consists of four prognostic equations for motion, temperature, and the distributions of O and CO, with two additional diagnostic equations representing continuity and hydrostatic balance (Dickinson and Ridley, 1977). New terms are incorporated to represent those new physically motivated parameterizations introduced briefly in Section 3.3. Section 4.4 will describe these new parameterizations in detail.

The equation of motion is essentially that given by DRM1, modified now by a drag term proportional to u:

$$\frac{\partial u}{\partial t} = \underbrace{\frac{ge^z}{p_0}\frac{\partial}{\partial z}\left(\frac{\mu}{H}\frac{\partial u}{\partial z}\right)}_{A} - \underbrace{\left[\frac{u}{r}\frac{\partial u}{\partial \theta} + w\frac{\partial u}{\partial z}\right]}_{B} - \underbrace{\frac{1}{r}\frac{\partial \Phi}{\partial \theta}}_{C} - \underbrace{\{K_{RA} * u\}}_{D} \qquad (4.1)$$

where:

z = vertical coordinate defined to be log pressure, measured from the P_0 pressure level; i.e., $z = \log_e(P_0/P)$

P_0 = reference pressure = 5×10^{-3} microbars

t = time

r = vertical position from the center of the planet (6200 km)

θ = solar zenith angle (SZA)

H = scale height

m = mean mass

μ = viscosity (laminar)

g = gravity

u = horizontal velocity

w = vertical velocity parameter (dz/dt)

Φ = geopotential

K_{RA} = coefficient for Rayleigh or generalized Rayleigh friction (sec^{-1})

$K_E(z)$ = eddy diffusion coefficient (also SZA dependence)

{ } = terms added to DRM2 code

[ ] = nonlinear, inertial terms

The terms above represent:

A = molecular viscosity

B = nonlinear hydrodynamical advection/convection

C = geopotential gradient force

D = wave or viscous eddy drag

Similarly, the equation determining CO and O concentrations is essentially that given by DRM1. Eddy diffusion is added for testing, so that:

$$\frac{\partial \underline{\psi}}{\partial t} = \underbrace{(-e^{z}\tau^{-1})\frac{\partial}{\partial z}\left(\frac{m}{m_{CO_2}}\left(\frac{T_{00}}{T}\right)^{0.25}\underline{\alpha}^{-1}\underline{L}\underline{\psi}\right)}_{E}$$

$$\underbrace{-\left[\frac{u}{r}\frac{\partial \underline{\psi}}{\partial \theta} + w\frac{\partial \underline{\psi}}{\partial z}\right]}_{F} + \underline{S}$$

$$\underbrace{+\left\{e^{z}\frac{\partial}{\partial z}\left(\frac{K_E(z)}{H^2}e^{-z}\frac{\partial \underline{\psi}}{\partial z}\right)\right\}}_{G} \qquad (4.2)$$

where:

"T_{00}" = reference temperature at terrestrial STP,

"τ" = molecular diffusion time scale,

"$\underline{\alpha}^{-1}$" = matrix operator of diffusion coefficients,

"$\underline{L}$" = operator specifying the importance of diffusive equilibrium ($L_{ij} \equiv \delta_{ij}(\partial/\partial z - 1 + m_i/m + 1/m\ \partial m/\partial z)$)

$\underline{\psi}$ = mass mixing ratio for O and CO ($\psi_1 = O$, $\psi_2 = CO$)

and:

E = molecular diffusion term

F = advective and convective terms

G = eddy diffusion term,

$\underline{S}$ = O and CO net source term per unit mass, derived from direct (or indirect) CO_2 photodissociation and recombination.

To calculate temperature, the following variation of the DRM1 thermodynamic equation is solved, now incorporating eddy cooling:

$$\frac{\partial T}{\partial t} = \underbrace{\frac{ge^z}{p_0 c_p}\frac{\partial}{\partial z}\left(\frac{K_T}{H}\frac{\partial T}{\partial z}\right)}_{H} + \underbrace{\left\{\frac{ge^z}{p_0 c_p}\frac{\partial}{\partial z}\left(K_E(z) c_p \rho\left(\frac{1}{H}\frac{\partial T}{\partial z} + \frac{g}{c_p}\right)\right)\right\}}_{I}$$

$$- \underbrace{\left[\frac{u}{r}\frac{\partial T}{\partial \theta} + w\left(\frac{\partial T}{\partial z} + \frac{R^* T}{c_{p_m}}\right)\right]}_{J} + \underbrace{\left(Q_{EUV} + Q_{IR} - Q_{15\mu m}^{mean}\right)/c_p}_{K}$$

$$- \underbrace{\left\{Q_{15\mu m}^{perturbation}\right\}}_{L} \qquad (4.3)$$

where:

H = vertical molecular heat conduction: "K_T" is the coefficient of the thermal conductivity, "c_p" is the specific heat at constant pressure

I = eddy heat conduction term: "ρ" is the mass density and $K_E(z)$ is the eddy diffusion coefficient

J = advective and convective adiabatic heating or cooling terms: "R^*" is the universal gas constant

K = net heating term, as the sum of EUV, UV and IR heating minus reference mean 15μ cooling

L = nonlinear temperature dependent 15μ perturbation cooling term, which is calculated about the reference mean temperature profile(s) given with the mean 15μ cooling profile(s).

Two diagnostic equations were also solved at the conclusion of each time step. The following hydrostatic equation is integrated upwards from the bottom to get geopotential height from T:

$$\frac{\partial \Phi}{\partial z} = \frac{R^* T}{m} \qquad (4.4)$$

for which altitude "h" is related differentially to "Φ" according to:

$$dh = d\Phi/g(h) \qquad (4.5)$$

Likewise, the vertical and horizontal velocities are related by the continuity equation, which is integrated downward from the upper boundary for w:

$$\frac{1}{r \sin\theta} \frac{\partial}{\partial \theta} (u \sin\theta) + e^z \frac{\partial}{\partial z} \left(e^{-z} w\right) = 0 \qquad (4.6)$$

The above code requires the solution of a series of one-dimensional equations about the planet for each set of four coupled time-dependent equations, using a "block-tridiagonal" solver. Adjacent SZA bins communicate by means of the hydrodynamic terms. The calculation is run to steady-state, which is determined by a pre-defined convergence criterion for each of the four fields (see Section 3.2.3). For fixed winds, the composition is generally expected to reach a steady-state in approximately one Earth day (DRM1). However, the distribution of composition near the lower boundary and the composition and temperatures deep on the nightside

appear to take the longest to adjust to equilibrium values. Suitable numerical approximations were incorporated by DRM1 and DRM2 to achieve a stable and convergent time integration of these four (unmodified) equations. To avoid rapidly growing "linear instability," it was found necessary to use a time-step no larger than ~300 sec. However, a slow instability attributed to the nonlinear hydrodynamic terms remains. DRM2 used a "smoothing" scheme to remove this instability, such that a nonlinear horizontal eddy diffusion term is defined from finite-differences.

Geometric and physical boundary conditions are specified in the model based on preliminary assumptions about the physical processes operating. At the top, no diffusive transports of heat, momentum, or relative mass concentrations are permitted. At the subsolar and anti-solar points, continuity within this two-dimensional model framework requires that u, $\partial T/\partial\theta$ and $\partial\psi/\partial\theta$ vanish. The boundary conditions at the bottom are more specialized for the Venus circulation and chemistry. For upwelling regions (primarily the dayside), $T = \bar{T}$, $u = 0$, and $\underline{\psi} = 0$. At the present time, the influence of return flow (below the model boundary) upon mass mixing ratios at the lower boundary is neglected. Conversely, for $w < 0$ (primarily the nightside), forms of the time-dependent composition, momentum, and thermodynamic equations without the vertical diffusion terms are used. This permits the "convection" of heat, momentum and composition out of the lower boundary.

DRM1 and DRM2 EUV fluxes were taken from Hinteregger (1970), and longer UV solar fluxes were adopted from Widing et al. (1970).

These data sets correspond to cycle 20 solar conditions most appropriate to F10.7 ≈ 140×10^{-22} Wm^{-2} Hz^{-1}. Cross sections chosen for CO_2 were identical to those used by Dickinson (1972), except for the updated Shemansky (1972) values available for $\lambda > 1700$Å. Cross sections for CO and O in the EUV were taken from Sun and Weissler (1955) and Dalgarno et al. (1964), respectively.

The rate of EUV energy absorption is calculated, as before, by calculating the energy locally absorbed and multiplying that value by an efficiency profile similar to the 2-22% profile from DRM2 (see Section 3.2.2). UV airglow loss by the CO Cameron bands and atomic O (6300 and 5577Å) has been parameterized to modify the heating efficiency longward of 1080Å. Finally, the spatial variation of infrared heating and the global mean 15μ cooling were provided by the output of the Dickinson (1976) one-dimensional radiative transfer model calculations. Section 3.2.2 describes the EUV efficiency and eddy cooling sensitivity studies applied to this code.

4.1.2 New Inputs for a Benchmark Model

In the course of bringing up the two-dimensional code for sensitivity study calculations, it was found that a new benchmark calculation is required that makes use of the best current model inputs. Better cross sections and more appropriate solar fluxes are but two of the available updated inputs for incorporation into a new benchmark two-dimensional model. The N_2 density, in fact, can now be specified empirically from Hedin et al. (1983) for a more complete model atmosphere.

A decision was made to adopt solar fluxes appropriate to the conditions at Venus during the early Pioneer Venus observations. The Torr et al. (1979) EUV fluxes shortward of 1050Å were thus utilized for day 78348, corresponding to an average F10.7 cm flux of 206 x 10^{-22} Wm^{-2} Hz^{-1}. These values are representative of "average" solar maximum conditions for cycle 21. Likewise, Torr et al. (1980) Schumann-Runge continuum fluxes over 1350 to 1750Å were adopted for the same date. Rocket data of Donnely and Pope (1973) was scaled to provide solar maximum fluxes for wavelengths >1900Å. Fluxes used by Nagy et al. (1980) were also used to specify the contribution by Lyman-α and other specific lines not given by Torr et al. (1979, 1980). For those regions where binning is not comparable or fluxes are not otherwise available (1750 < λ < 1900Å), Heroux and Hinteregger (1978) fluxes (74113) are scaled for solar maximum conditions.

Weighted photoionization and photoabsorption cross sections for CO and CO_2 are taken from Torr et al. (1979) for λ < 1050Å. These binned and weighted values were derived from CO and CO_2 cross sections from Cook et al. (1965, 1966); Cairns and Samson (1965, 1966); Watson et al. (1975); and Lee et al. (1975). O ionization and N_2 absorption cross sections are also adopted from Torr et al. (1979). All cross sections utilized are quite similar to those of Nagy et al. (1980).

4.2 Updated Version of the Radiative Transfer Code

As described in Chapter III, the radiative-transfer code developed and tested by Dickinson (1972, 1976) is available to provide mean 15μ cooling and SZA dependent infrared heating fields for usage

in the two-dimensional model. These calculations, however, are conducted external to the two-dimensional model, and require that these fields (as well as the mean temperature profile) be linked to the code as inputs. Perturbation 15μ cooling is then explicitly calculated within the two-dimensional model, thereby providing a consistent damping of the temperature perturbations.

The improvements to the two-dimensional model inputs (see Section 4.1.2) must now be applied to the one-dimensional radiative transfer code in order that compatible 15μ cooling and slant IR heating fields can be obtained. Identical fluxes and cross-sections are thus adopted for the one-dimensional model. A further improvement is provided by the incorporation of Pioneer Venus global mean composition from Hedin et al. (1983). In particular, the fractional number density of atomic O at the F1-peak is taken to be 18%. A more realistic non-pure CO_2 atmosphere is now available for calculating the radiative-equilibrium temperature. This development of a new benchmark calculation is also used as an opportunity to improve several assumptions within the one-dimensional code. For instance, isotopic exchange between CO_2 isotopes is now estimated rather than neglected (Dickinson, 1976). Also, the effect of atomic O collisions upon $CO_2(0,1,0)$ de-excitation is increased by two, to give a new rate corresponding to 20 x the effect of CO_2-CO_2 collisions. Measurements justifying these new O-CO_2 rate coefficients will be described in Section 4.4.3.

4.3 Benchmark Global Mean Calculations

The new benchmark versions of the previous two-dimensional (DRM2) and one-dimensional (Dickinson, 1976) models for Venus' upper atmosphere were run to equilibrium. These new calculations serve as a reference upon which eddy parameterizations, rate coefficients, and EUV efficiency profiles can be tested in a sensitivity study analysis (see Chapter V). Global mean fields are singled out for comparison here to show the inconsistencies present among these one- and two-dimensional model calculations, and observations.

Figure 4.1 illustrates several global mean Venus temperature profiles from 65 to 160 km. The Hedin et al. (1983) profile corresponds to actual ONMS data above ~140 km, and is a reasonable extrapolation below 140 km (see Chapter II). The day probe of Seiff et al. (1982) provides an experimental profile, showing considerable wave structure. It is apparent that the Dickinson (1976) one-dimensional radiative-equilibrium temperature profile is significantly warmer (75°K) than the empirical profiles above z = -2. The updated version of this same code lowers the mean exospheric temperature to 240°K from 275°K. Somewhat warmer temperatures over z = -12 to z = -6 correspond to the isotopic exchange corrections described above. For this low EUV efficiency case, additional external cooling above z = 0 is required for the radiative-equilibrium temperature profile to more closely match the empirical profiles. Such an improved thermal balance is needed specifically in the region where EUV heating is dominant.

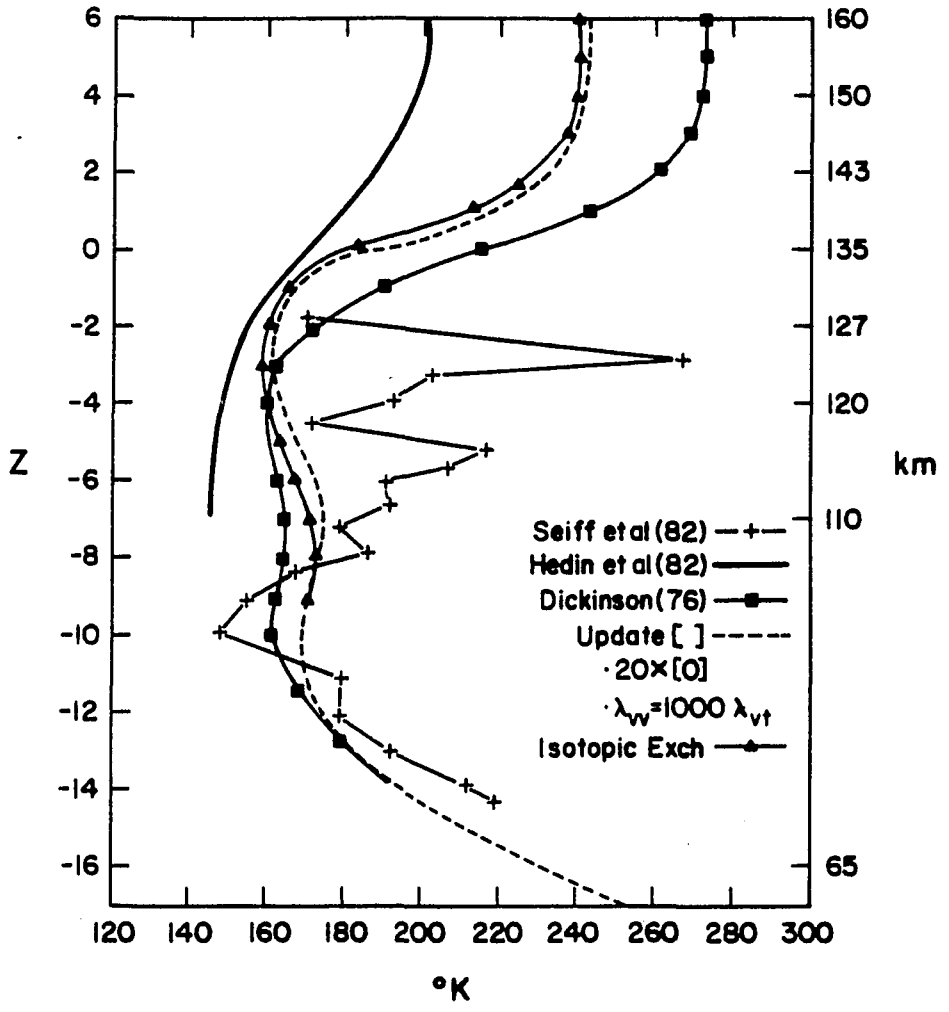


Fig. 4-1 Global mean Venus temperature profiles - radiative transfer tests.

The response of the two-dimensional fields is very similar to that of DRM2. Specifically, exospheric temperatures range from 330°K (dayside) to 145°K (nightside), with a very strong compressional heating signature evident on the nightside. The strong circulation ($U \lesssim 418$ m/s) again reveals a sharp downflow just nightward of the terminator. It also gives rise to an improper redistribution of composition, for which dayside % [O] is depleted, and a considerable nightside bulge arises contrary to observations. Nightside temperatures are calculated to be 30°K warmer than observations (Hedin et al., 1983; Keating et al., 1984; Massie et al., 1983). Figures 4.2a and 4.2b show results of the two-dimensional benchmark calculation for global mean temperature and O and CO fractional number densities. These global mean plots also reflect a portion of this two-dimensional problem of the redistribution of heat and composition about the planet. Discrepancies among the calculated fields and the empirical data sets are striking.

Of particular note is the fact that the global mean composition employed by the new one-dimensional code (from Hedin et al., 1983) does not resemble that calculated by the two-dimensional benchmark (4.2b). Likewise, the one-dimensional global mean temperature profile is markedly different from that calculated by the hydrodynamic model. These inconsistencies suggest that an improper link is present between the two-dimensional and one-dimensional codes. This incompatability is fundamental to the inability of the two-dimensional model to reproduce empirical model temperatures. The development of a reasonable global mean radiative transfer model is a first step in

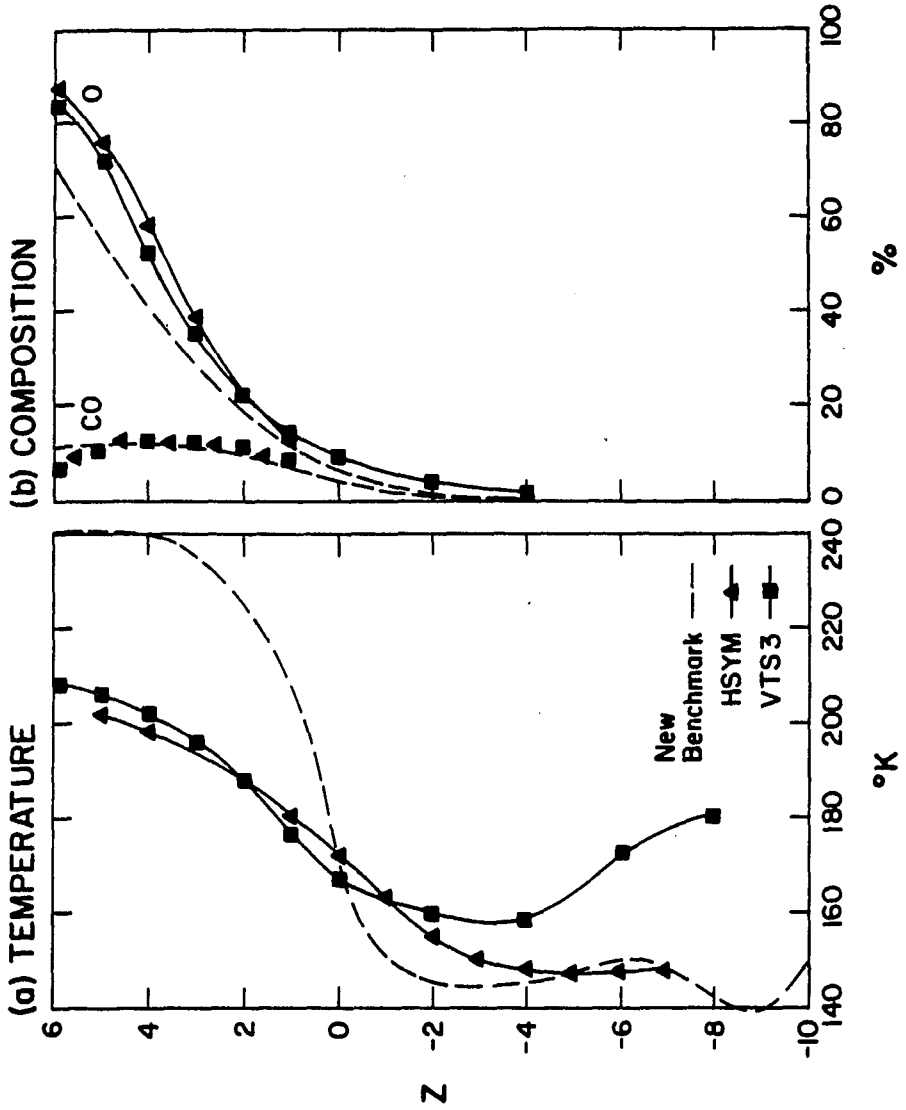


Fig. 4-2 Updated two-dimensional benchmark global mean calculations; (a) temperature, (b) composition.

establishing a correct link to the two-dimensional code. Once the cooling mechanisms are established for the global mean case, the compatible two-dimensional improvements will enable reasonable total 15μ cooling to be calculated.

4.4 New Physical Parameterizations To Be Tested

4.4.1 Problems To Be Addressed

Section 3.3 has carefully described the shortcomings of previous model calculations and uncovered several likely physical parameterizations for testing. Those updated global mean calculations outlined in Section 4.3 suggest similar problems that an improved hydrodynamic model must address. Specifically, the role eddy processes serve in modifying or controlling composition, temperatures and winds in a hydrodynamic code must be examined. Eddy diffusion, eddy cooling, and eddy drag parameterizations will be used to approximate these processes. The manner in which CO_2 vibration-rotation states are excited by collisions with atomic-O is important for providing enhanced 15μ cooling. Reasonable limits of the $k(CO_2\text{-}O)$ rate coefficient will be defined. Updated external cooling will enable an improved thermal balance to be derived for the dayside, giving reasonable temperatures for a range of adopted EUV heating efficiency profiles. It is hoped that a consistent specification of these eddy, cooling and EUV efficiency parameterizations will enable the nightside temperatures to be reduced to observed levels, and permit the composition to be redistributed properly about the planet.

4.4.2 EUV Heating Efficiency Profiles Chosen

Three representative EUV heating efficiency profiles are chosen to examine the range of external cooling parameters required to calculate observed dayside temperatures. The designation of an ultraviolet heating efficiency--$\varepsilon(z)$--(or that fraction of the total solar energy that is deposited locally as heat) is an efficient means to parameterize heating in large-scale dynamical models of the type used by DRM1 and DRM2. As previously suggested in Chapter III, $\varepsilon(z)$ remains an adjustable parameter for Venus due to several assumptions that must be made concerning metastable species and CO_2 rotation-vibration states (see Sections 3.2.2 and 3.2.3.). Estimates of $\varepsilon(z)$ between 10% and 30% have been made by Stewart (1972), Stewart et al. (1972), Dickinson (1976), Dickinson and Ridley (1975, 1977), and Fox and Dalgarno (1981). The general consensus is that $\varepsilon(z)$ almost certainly exceeds 10%, so that an additional external cooling mechanism must be invoked to explain the observed dayside exospheric temperatures (Fox and Dalgarno, 1981).

Stewart et al. (1972) derived an $\varepsilon(z)$ of roughly 30% for $\lambda <$ 1080Å. It was assumed that an ion-electron pair is produced for every 36 eV of EUV energy absorbed as follows:

$$
\begin{aligned}
&(a) \qquad CO_2 + h\nu \rightarrow CO_2^+ + e \\
&(b) \qquad CO_2^+ + O \rightarrow O_2^+ + CO + 1.7eV \\
&(c) \qquad O_2^+ + e \xrightarrow{90\%} O + O(^1D) + 5.1eV \\
&(d) \qquad \xrightarrow{10\%} O + O(^1S) + 2.9eV
\end{aligned} \tag{4.7}
$$

6.6 eV per ionization (or 18%) of the solar EUV energy goes into kinetic energy of O_2^+ (the dominant ion), plus O and CO. The complete quenching of $O(^1D)$ (10%) was also assumed, thereby raising the combined efficiency to ~30%. Other metastable states addressed (from dissociative recombination of CO_2^+ and O_2^+) include CO (a-X) and $O(^1S)$, which radiate in the Cameron bands and at 5577Å, respectively. All photo-electron energy was also permitted to be lost to CO_2 vibrations, which result in cooling-to-space. Overall, 70% of the incoming solar energy (EUV) was assumed lost to: the breaking of CO_2 bonds (40%), UV airglow (20%), and CO_2 vibration from photoelectron excitation (10%).

Dickinson and Ridley (1977) take exception with several of the Stewart et al. (1972) assumptions for $O(^1D)$ and the hot particles. Section 3.2.2 and 3.2.3 describe the development of a "lowest" EUV efficiency profile for which $\epsilon(z)$= 2-22%. The 2% direct heating at the top assumes that 80% of the net chemical heating of reactions (a)-(d) and all $O(^1D)$ energy is lost to excitation of CO_2 vibration-rotation states. CO_2 vibration is thereafter lost to space by re-radiation. Collisional quenching is assumed to thermalize CO_2

rotational energy at higher pressures (see f(p) quenching factor in Section 3.2.3). Thus, roughly half of the available CO_2 excitation is assumed to be partitioned each to rotational and vibrational degrees of freedom. Such an efficiency profile was shown to give a fairly good thermal balance for the Venus dayside, without additional external cooling (see Section 3.2.3). However, DRM2 points out that these extreme assumptions for $O(^1D)$ and the hot particles require that this 2-22% case be a "lowest limit" $\epsilon(z)$ model. As a result, this profile will serve only as a reasonable starting point for thermal balance calculations within an improved two-dimensional model.

An improved medium (MED) EUV case is constructed from the sum of ~10% direct heating, plus a new estimate of CO_2 rotation quenching by collisions at low altitude. Fifty percent of the topside chemical energy (reactions (a)-(d)) is thermalized, with the remainder lost to CO_2 vib-rot excitation. Half of the available 30% excess energy diverted to vibrational-rotational excited states (from hot particles, photoelectrons, and $O(^1D)$ species) is now quenched by collisions to provide a 25% heating efficiency at the bottom. This estimate of an efficiency profile is similar to that suggested by Seiff et al. (1982). However, topside heating is nearly a factor of two smaller than the lowest Model C profile of Fox and Dalgarno (1981).

Fox and Dalgarno (1981) made a detailed assessment of the heating of the neutral and ionized components of the Venus atmosphere arising from the absorption of solar ultraviolet radiation. They adopted a model atmosphere based on that of Liu and Donahue (1975), and made use of the solar fluxes of Hinteregger (1976) scaled for

Venus. Ultraviolet airglow loss is carefully described for several excited species, including CO (a-X) Cameron bands, O(^{1}S): 5577Å, CO_2^+ Fox-Diffendack-Barker and ultraviolet doublet bands, CO-4th positive bands, O(^{1}D): 6300Å, and the excited states of N_2 and N_2^+. Calculated heating rates and efficiencies for three different models are provided on the basis of different assumptions about the fraction of energy converted to CO_2 vibrational excitation. At high altitudes, vibrationally-excited CO_2 molecules are assumed to lose their energy by radiation. Quenching at higher pressures is a viable mechanism to thermalize the CO_2 rotation energy, but it was neglected.

Subsequent calculations were performed using the preliminary ONMS empirical model atmosphere (Hedin, 1981, private communication) for different levels of solar activity (Fox, 1981, private communication). The heating efficiency profiles were largely unchanged as a function of solar activity. However, above ~130 km the new model atmosphere permitted slightly ($\leq$4%) more efficient EUV heating to be calculated for 18°SZA.

Model A and C profiles from Fox and Dalgarno (1981) and Fox (1981, private communication), respectively, are reproduced in Fig. 4.3 for which:

A: 10% Excess Energy (CO_2 vib-rot, cool-to-space)
90% Excess Energy (thermalized)

C: 50% Excess Energy (CO_2 vib-rot, cool-to-space)
50% Excess Energy (thermalized)

Model A (30%) is a probable upper limit to the heating efficiency, for which $O(^1D)$ excess energy is largely thermalized. Model C (24-12%), however, is a lower limit profile making use of similar $O(^1D)$ assumptions for cooling-to-space employed by DRM2. In practice, the increased efficiency of rotational quenching collisions at low altitudes will tend to lessen the decrease in heating efficiency. The drop in $\varepsilon(z)$ below 135 km for model C will thus likely not occur (see Fig. 4.3). Use of the improved Hedin et al. (1983) empirical model atmosphere may also alter the heating efficiency, particularly above ~130 km.

A high (HI) EUV efficiency (18-28%) profile is now specifically constructed to closely mimic Model C (above) at high altitude, and also to provide a reasonable improved quenching mechanism for CO_2 rotational states at low altitude. Roughly 70% of the topside chemical energy is assumed to be thermalized with the remainder being lost to CO_2 vibration-rotation. $O(^1D)$ restrictions are also relaxed to permit 50% of its excess energy to be thermalized at high altitude. At lower altitudes (high pressures), half of the available 20% excess energy (diverted to CO_2 vibration-rotation) is quenched to give an efficiency of 28%, quite similar to that of Model A (Fox and Dalgarno, 1981). This HI EUV case thus serves as an improved version of the Model C profile.

Figure 4.3 illustrates a comparison of the heating efficiency profiles (A and C) previously calculated, and the three newly adopted cases (LOW, MED, HI) for the Venus two-dimensional sensitivity studies. The topside heating efficiency gradually approaches that of

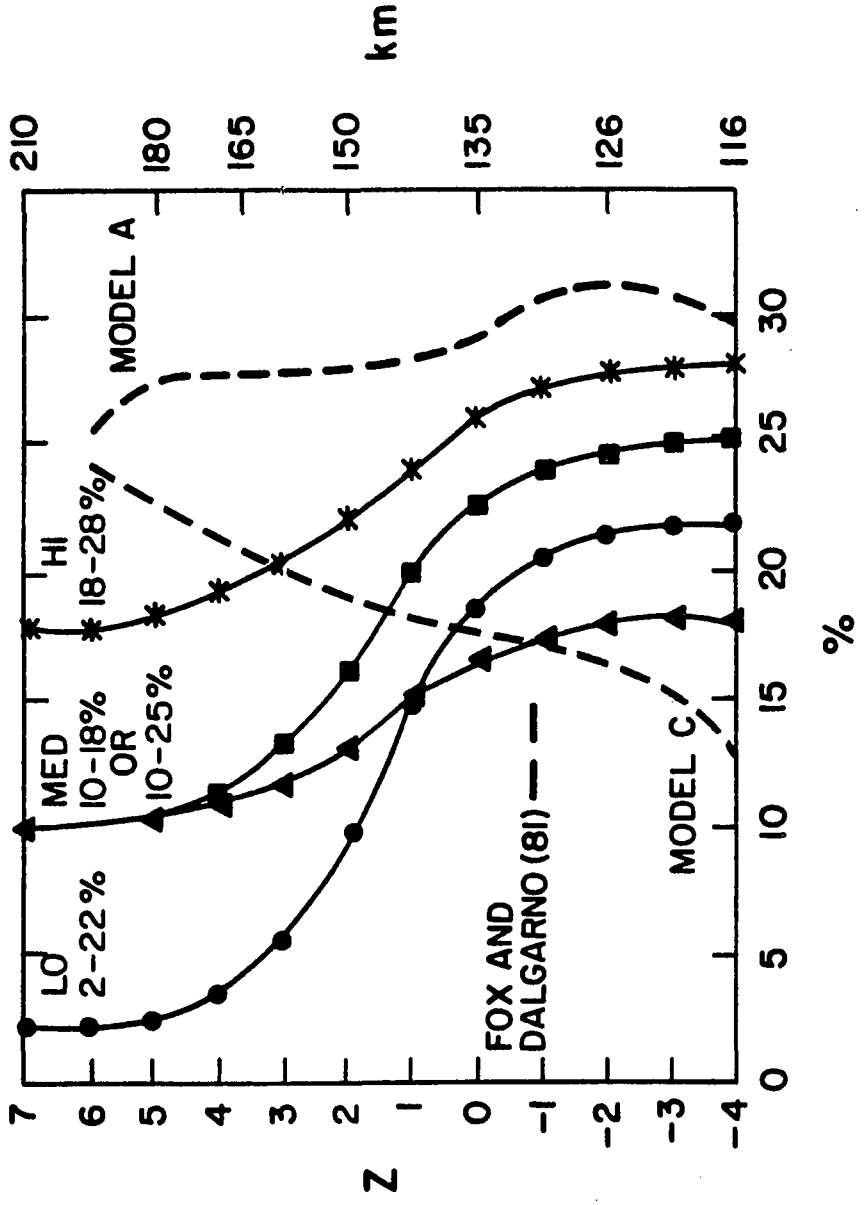


Fig. 4-3 EUV heating efficiency profiles.

Model C with the HI case (18-28%). The MED and HI cases are notably in excess of the 10% lower limit suggested by Fox and Dalgarno (1981). An optimal $\varepsilon(z)$ profile will become apparent as restrictions upon eddy cooling and the $k(CO_2\text{-}O)$ rate coefficient are uncovered (see Sections 5.2-5.6).

4.4.3 Parameterizations Used: Parameters Selected

Equation (4.3) incorporates the eddy cooling term used by Hunten (1974) (transformed to log pressure coordinates), for which all mixing gives rise to cooling. This is an upper limit assumption, similar to that made by the one-dimensional sensitivity tests conducted earlier by Dickinson (1976). Its systematic application in a two-dimensional hydrodynamic code will help specify the SZA dependence of the eddy coefficient, $K_E(z)$, which is used. $K_E(z)$, in fact, will be the key adjustable parameter linking all the eddy parameterizations.

Previously developed one-dimensional models (Chapter III) will serve as a starting point for deriving an eddy coefficient profile and its SZA variation. KMAX (the upper limit cut-off), ZPBK (the breaking level altitude above which $K_E(z)$ = KMAX) and SZAF (specifying SZA variation) are parameters selected for adjustment. These parameters are chosen for ease of comparison with previous one-dimensional model work. In addition, the profile shape ($K_E(z) = A/\sqrt{N}$), suggested by Lindzen (1971) (and used by all three one-dimensional compositional models described in Chapter III), will be employed. This "mixing length" approach to small scale overturning is dynamically unsatis-

factory, but it is an expedient scheme to mimic such processes in a large scale hydrodynamic model. $K_E(z)$ is roughly equivalent to isotropic and time averaged diffusivity D_{ZZ}, described in Weinstock (1983).

Equation (4.2) incorporates an additional eddy diffusion parameterization similar to that used by Dickinson et al. (1984). This log-pressure form again makes use of the same $K_E(z)$ profile as eddy cooling. The scheme is also similar to that employed by von Zahn et al. (1980); Stewart et al. (1980); and Massie et al. (1983) models for one-dimensional composition. Now however, large scale winds and small scale mixing processes are acting in concert to control composition. $K_E(z)$ will likely be some fraction of the one-dimensional model values used earlier (as suggested by Shimizu, 1974).

Equation (4.1) uses a wave or viscous drag term to crudely simulate the effects of wave breaking on the mean flow. A Rayleigh friction scheme is initially adopted (as previously used for early terrestrial mesopause calculations) for improved momentum balance (Schoeberl and Strobel, 1978; Holton and Wehrbein, 1980; Lindzen, 1981). An appropriate drag time scale (K_{RA} in sec^{-1}) is derived independent of height to determine the magnitude of wave-momentum deposition required. A profile shape similar to that of $K_E(z)$ is next utilized to fine tune the drag provided by Rayleigh friction. Finally, a more satisfying generalized Rayleigh friction method is tested that links the drag time scale to $K_E(z)$ and vertical wave number (K_z) via the parameterized drag scheme of Weinstock (1982):

$$K_{RA} = 2 K_z^2 \left(\frac{K_x}{K_h}\right)^2 K_E(z) \quad . \qquad (4.8)$$

Here, (K_x/K_h) is the ratio of zonal wave number to horizontal wave number.

Weinstock (1982) suggests that the momentum deposition flux and vertical diffusion caused by "saturated" gravity waves are related by the above simple expression. Section 2.1.2. describes the explicit evidence for small scale wave activity in the low thermosphere nightward of the terminator. It has generally been convenient to treat momentum deposition and diffusion separately as if they were independent of one another. However, from a turbulence point of view, it is reasonable that the same short scale fluctuations that cause one process should cause the other. When a wave "saturates," it is converted into random waves or fluctuations which cause diffusion and deposition. The magnitudes of the two processes are thus closely related according to the above expression. This relation determines the friction coefficient in terms of the diffusion coefficient and the vertical wave number, K_z, of a single gravity wave.

K_{RA} is now referred to as a generalized Rayleigh friction coefficient, because it is based on a more general scheme than the ordinary Rayleigh friction, but having the same dimensions (sec^{-1}). K_x/K_h is easily estimated to be $1/\sqrt{2}$ (isotropic assumption) and K_z is taken from Seiff et al. (1982) (see Chapter II). SZA variation of drag is now directly linked to the same variation of $K_E(z)$

used in eddy cooling and eddy diffusion. A degree of consistency among all the eddy parameterizations is thus possible through $K_E(z)$.

The final parameter for adjustment is the rate coefficient for deactivation of $CO_2(0,1,0)$ by collisions with atomic-O :

$$CO_2(0,1,0) + O \rightarrow CO_2(0,0,0) + O + h\nu \qquad (4.9)$$

The poorly known rate coefficient for this reaction has been estimated by several authors over the last decade. Dickinson (1976) refers to high (shock tube) temperature studies of Center (1973) and the CO_2 4.3μ work of Cramp and Lambert (1973) to estimate that the relaxation of $CO_2(0,1,0)$ is a factor of ten more likely for a collision of CO_2 with O than with CO_2 (see Section 3.2.2). This corresponds roughly to a $k(CO_2\text{-}O)$ rate coefficient of 5×10^{-14} cm^3/sec.

Fifteen μ band data acquired recently from scans of the Earth's limb (Stair et al., 1978) clearly suggests the need for a collisional excitation process in excess of N_2 and O_2 collisions with CO_2 in the lower thermosphere. Analysis of SPIRE (Spectral Infrared Rocket Experiment) data by Kumer (1981) and Sharma and Nadile (1981) strongly implies that CO_2-O collisions are a responsible mechanism for excitation of $CO_2(0,1,0)$. An improved estimate for this rate coefficient was presented by Sharma and Nadile (1981). Their inferred rate of 5×10^{-13} cm^3/s was based on a rocket measurement of CO_2 emission limb radiance above 100 km and an assumed concentration of atomic oxygen. This 300°K rate has also been used by Apruzese and Strobel (1984) for thermal budget calculations of the terrestrial

middle atmosphere. Gordiets et al. (1982), however, adjusted their rate coefficient to give good agreement between their thermospheric temperature distribution and the Jacchia (1977) empirical thermospheric reference model values:

$$k(CO_2\text{-}O) = 1.5 \times 10^{-11} * \exp(-800/T) \text{ cm}^3/\text{sec} \quad . \qquad (4.10)$$

This rate is nearly 10^{-12} cm^3/sec at 300°K, which is roughly a factor of two faster than SPIRE data allow.

Venus two-dimensional model work will establish a range of acceptable rate coefficients giving 15μ cooling appropriate to the three EUV efficiency profiles just proposed. The goal will be to derive a thermal balance for which observed temperatures can be calculated. The ability of this CO_2 deactivation to serve as an effective cooling mechanism in the Venus thermosphere will be limited by the requirements of the terrestrial thermospheric heat budget, and the sparse data available.

The five previous parameters described ($K_E(z)$--via ZPBK and KMAX, SZAF, K_{RA}, EUV efficiency and $k(CO_2\text{-}O)$) are the fewest number presently possible for specification in a series of two-dimensional model sensitivity studies. It is not known a priori whether a unique combination of these parameters will give a best match of calculated fields to observations. However, the next chapter will present a strategy to approach such a fit if it exists. Those case studies most appropriate for establishing the ranges of the above parameters will be singled out for discussion.

CHAPTER V

SENSITIVITY STUDIES WITH THE UPDATED TWO-DIMENSIONAL MODEL: RESULTS

5.1 Procedure

5.1.1 Strategy and Fitting Scheme

As previously stated in Chapter IV, a systematic scheme is needed for the development of model sensitivity studies, whereby a unique best fit to observations can be derived. The five adopted parameters for adjustment are $K_E(z)$, K_{RA}, $K(CO_2\text{-}O)$, SZAF and $\varepsilon(z)$ (EUV efficiency). KMAX and ZPBK are both specified for a given $K_E(z)$ profile. Can a unique combination of these be employed for a best match of calculated fields to observations?

In the process of examining the EUV heating efficiency cases described in Section 4.4.2 (LO: 2-22%; MED: 10-25%; and HI: 18-28%), the initial objective is to (1) adjust those parameters that specify external cooling to give a proper dayside thermal balance and bring calculated temperatures into agreement with observations. Thereafter, (2) wave drag parameterizations need to be invoked for a proper redistribution of composition and heat about the planet. Finally, (3) eddy diffusion is added for fine-tuning of composition as its role is kept to a minimum. This is consistent with the overall goal to con-

fine the influence of eddy processes to the minimum required to augment the present role of the large scale circulation (see Section 3.1). Calculations cycle through these series of tests until a best fit for a given heating efficiency case is achieved. The last parameter, specifying SZA variation of $K_E(z)$, (SZAF), is examined in two stages. Calculations are first performed for (1) no SZA variation of $K_E(z)$ and later improved with (2) the best possible SZA variation of $K_E(z, \theta)$. The goal is to obtain an overall best match of calculated fields to observations for a single $\epsilon(z)$ case using all five parameters.

This same scheme is applied to each of three EUV heating efficiency cases (see Section 4.4.2), so that the ranges of the needed parameters can be properly established. A closer inspection of these parameters and a realistic estimate of their best or mean values are used to develop a best model simulation. The maximum EUV heating efficiency possible is incorporated. This final two-dimensional model calculation is subject to additional applications (see Section 5.6), which provide a means for further tuning of the model parameters.

A least squares fitting scheme (similar to that described by Gerard et al., 1981) is used to quantify the degree of fit of the calculated two-dimensional output fields to the empirical model reference observations. In particular, a "best" model simulation is designated as one derived by adjusting the five parameters discussed in Chapter IV, such that the normalized standard deviation (s) over the chosen set of observation points is minimized:

$$s = \left\{ \frac{1}{N} \sum_{i=1}^{N} \frac{(d_i - f_i)^2}{f_i} \right\}^{1/2} \qquad (5.1)$$

Twenty-four (N) observation points (d) are used to sample the temperature and the % O and % CO composition fields over the region for which Pioneer Venus observations are available. Root-mean-squared fits (RMSF) are calculated at LT = 12 and 24 hours for pressure levels corresponding to z = 0, 1, 4, and 7. This roughly spans the dayside region from 135 to 210 km and the nightside from 130 to 160 km. The VTS3 and HYSM empirical reference atmospheres (see Chapter II) provide the "d" standard points against which the estimation of a good fit, "f," is made. Table 5.1 summarizes composition and temperature values of the VTS3 and HSYM data sets for LT = 12 and 24 hours and global mean conditions.

Weights are also incorporated to provide a bias toward closest fits in those regions for which data contains the least scatter, and is therefore most accurate. The VTS3 empirical model was in fact created to reconcile all available Pioneer Venus data sets (ONMS, BNMS, OAD, and probes) in the thermosphere (Hedin et al., 1983). This model is used to provide an estimate of the scatter of the available data over SZA. VTS3 composition on the dayside matches all available data sets to within ~10%, while the highly variable nightside thermosphere requires a range of 25% or more. Exospheric temperature is subject to a scatter of ~5% for the dayside and 10% near the anti-solar point. These stated ranges are used to specify weights

Table 5.1

Summary of Composition and Temperature Values
for the VTS3 and HSYM Data Sets

HSYM

	LT = 12			Global Mean			LT = 24		
Z_p	T	%[O]	%[CO]	T	%[ ]	%[CO]	T	%[O]	%[CO]
7	288	.89	.044	208	.875	.038	127	.86	.032
6	287	.85	.071	207	.835	.062	127	.82	.053
5	284	.73	.114	206	.720	.100	127	.71	.085
4	276	.54	.147	202	.520	.123	127	.50	.098
3	265	.36	.150	196	.350	.121	127	.34	.092
2	247	.23	.134	188	.225	.105	128	.22	.076
1	224	.129	.104	176	.140	.081	128	.15	.058
0	206	.079	.077	167	.090	.059	128	.10	.040
-1									
-2	190	.032	.040	160	.043	.031	129	.054	.022
-3									
-4	181	.0167	.0198	157	.017	.015	132	.017	.011
-5									
-6	178	$\leq$.01	$\leq$.01	174	$\leq$.01	$\leq$.01			
-7									
-8	186	$\leq$.01	$\leq$.01	181	$\leq$.01	$\leq$.01	176	$\leq$.01	$\leq$.01
					VTS3				
7	308	.930	.046	203	.920	.038	121	.890	.034
6	307	.880	.084	202	.868	.069	118	.820	.060
5	305	.780	.130	201	.750	.107	119	.640	.082
4	299	.640	.180	199	.575	.132	119	.420	.080
3	290	.470	.200	195	.382	.130	120	.240	.062
2	273	.300	.180	188	.217	.105	125	.130	.042
1	248	.170	.130	180	.118	.070	127	.063	.026
0	222	.084	.078	171	.056	.042	132	.030	.015
-1	206	.038	.042	163	.026	.022	136	.014	$\leq$.01
-2	200	.016	.020	155	.011	.011	138	$\leq$.01	
-3	190	$\leq$.01	$\leq$.01	150	$\leq$.01	$\leq$.01	140		
-4	187			148			145		
-5	182			147			148		
-6	180			147			150		
-7	179			146			152		
-8									

which give particular emphasis to a good dayside fit. Geometric (i.e., latitudinal) weighting factors are not necessary at this time, since two-dimensional model calculations effectively model conditions about the equator.

Model calculations are now described for three likely EUV heating efficiency cases. The usefulness of the chosen fitting strategy is illustrated by a comparison of the individual normalized standard deviations for each EUV case (see Table 5.2). A "best" model simulation is eventually obtained, and largely based on this fitting procedure.

5.2 LO EUV Efficiency Case (2-22%)

5.2.1 Qualitative Response of the Model to Eddy Parameterizations

Testing of the 2-22% heating efficiency case begins with a qualitative examination of the way in which eddy drag, eddy cooling, and eddy diffusion independently influence the composition, temperature, and wind fields. Trends are particularly sought which suggest (according to von Zahn et al., 1983) that increased dayside densities, depleted nightside densities, and colder nightside temperatures with respect to DRM2 are possible. Coupling of these processes will be addressed later.

Several different time scales for wave drag are first tested with the aid of the Rayleigh friction parameterization (Section 4.4.2) in order to estimate what possible magnitude of momentum-deposition (via wave breaking) is necessary. An improved momentum balance is

Table 5.2

Comparison of EUV Case Model Fits:
Standard Deviations

Curve	LO (2-22%)		MED (10-25%)		BEST (7-19%)	
VTS3 Reference	S	S/S_{Best}	S	S/S_{Best}	S	S/S_{Best}
A	6.10	9.38	1.45	2.23	-	-
B	1.39	2.14	0.65	1.0	-	-
Optimal	0.68	1.05	0.81*	1.25	0.65*	1.0
HSYM Reference						
Optimal	1.4	1.2	0.97*	0.82	1.18*	1.0

Note: Generally, the VTS3 reference atmosphere enables a better model fit to the chosen data points. However, as total number densities and columns were examined (*), composition was more nearly reproduced by a departure from minimum "S" (recall that "S" is derived from calculated mixing ratios, not individual number densities).

sought (as suggested by von Zahn et al., 1983), that gives wind velocities similar to those of Mayr et al. (1980). It is crudely assumed (in Figs. 5.1 a, b, and c) that wave drag is linearly proportional to horizontal velocity and otherwise constant with altitude. Time scales ranging from 5×10^{-5} sec^{-1} to 2×10^{-4} sec^{-1} are initially chosen for study. The resulting terminator winds for 5×10^{-5} sec^{-1} and 7×10^{-5} sec^{-1} are selected for comparison in Fig. 5.1b with results from the benchmark two-dimensional model (Section 4.3). Note that it is possible to reduce terminator winds by roughly 40% to 240 m/s at the top.

This terminator wind reduction has a very striking effect on exospheric temperatures about the equator. Figure 5.1a illustrates that the day-night temperature contrast is enhanced by wave drag, whereby dayside temperatures increase and nightside temperatures decrease. It is seen that the nightside "warming" feature (due to compressional heating) in the benchmark model exospheric temperatures is eliminated by drag (for a time scale of 5×10^{-5} sec^{-1}). Nightside temperatures are reduced to values as low as 110°K by a drag time scale of 7×10^{-5} sec^{-1}. Wave drag does not, however, greatly alter global mean temperature, giving only a partial answer to improved thermal balance. Certainly, dayside heat is isolated from the nightside with slower winds, giving colder nightside temperatures.

Figure 5.1c shows that day and night composition improves tremendously with slower winds (according to Fig. 5.1b), particularly for $K_{RA} = 1\times10^{-4}$ s^{-1}. Dayside [0] is beginning to increase toward VTS3 reference model values, while nightside [0] is reduced. More of

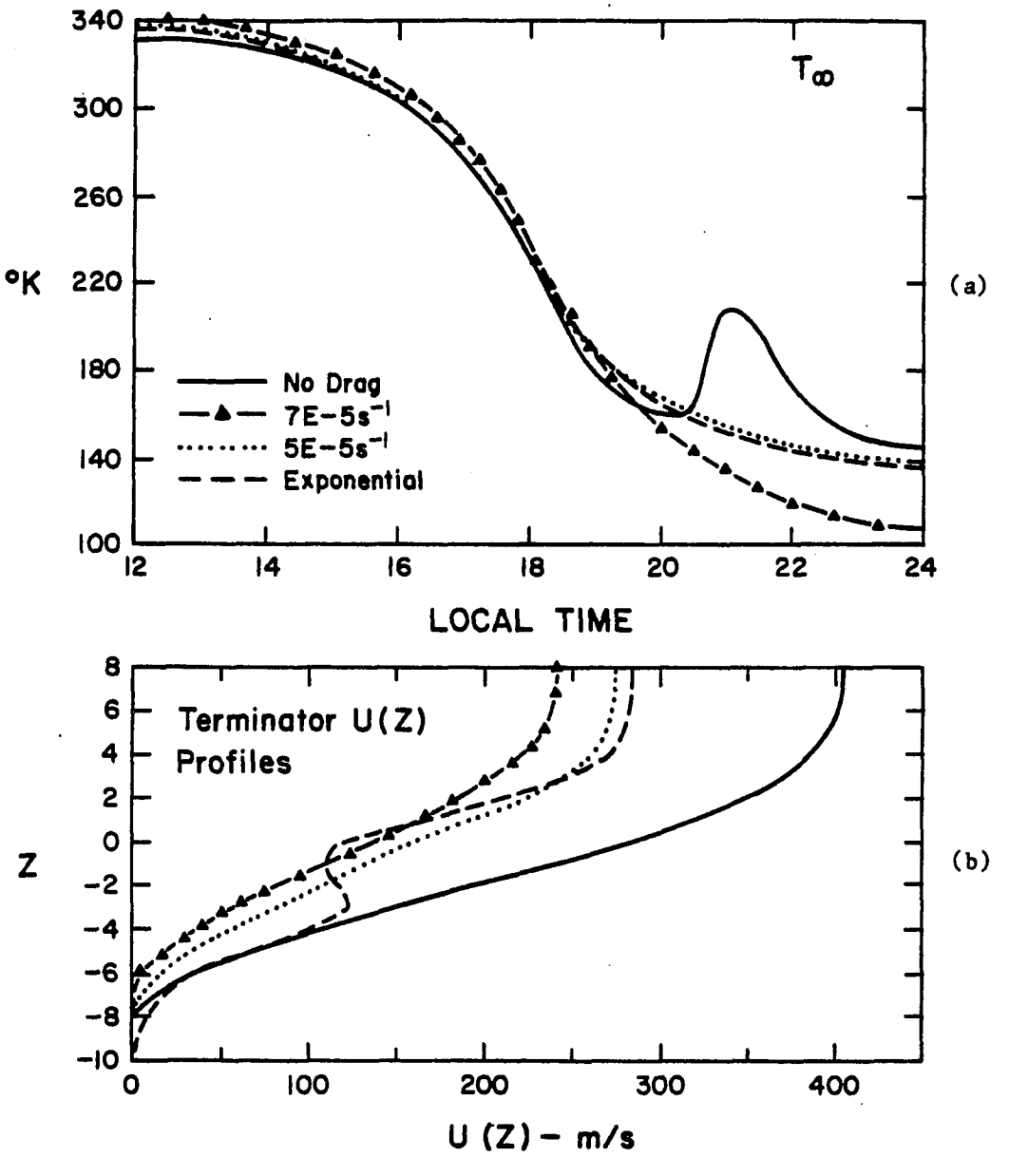


Fig. 5-1a,b Venus two-dimensional model response to viscous drag tests; (a) T_∞, (b) terminator u(z) profiles.

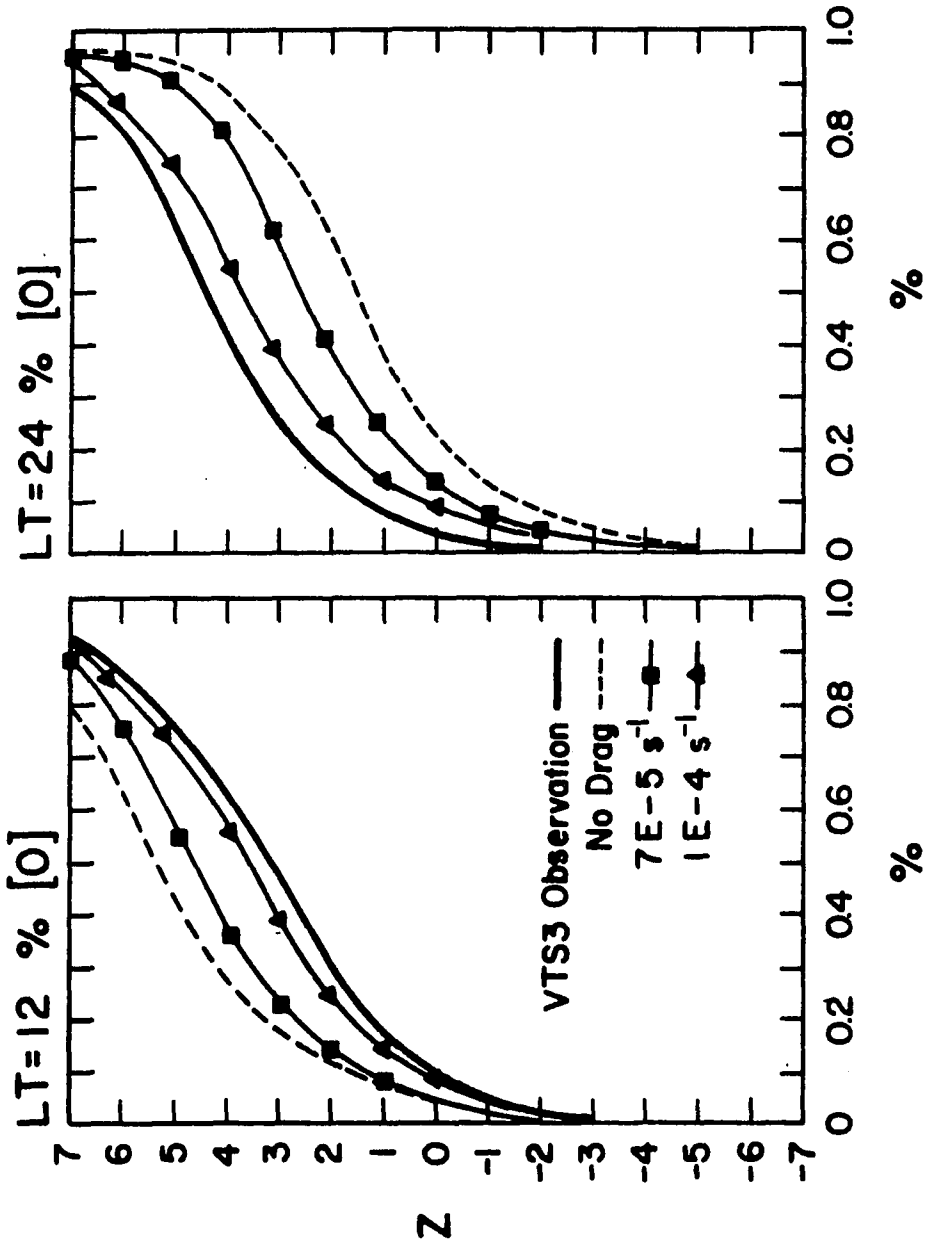


Fig. 5-1c Venus two-dimensional model response to viscous drag tests; (c) composition.

the photodissociated O and CO is being retained on the dayside. This is the same type of improvement noticed earlier by von Zahn et al. (1983), resulting from the development of slower winds in the progression from DRM1 to DRM2. This trend suggests that a proper redistribution of composition can be achieved provided that a sufficient eddy drag parameterization can be applied for an improved momentum balance. One promising improvement is given by an "exponential" profile shape of the type adopted for the $K_E(z)$ parameterization (see Sections 5.2.3 and 5.3.2 for details).

Realistic dayside temperatures are seen to require additional external cooling, particularly in the face of wave drag described above. Eddy cooling is now examined as a possible mechanism for this purpose. The Hunten (1974) parameterization is first applied in the one-dimensional radiative transfer code, updated according to Section 4.2. $K_E(z)$ is assumed to have a shape $1/\sqrt{N}$, just as previously used by the one-dimensional composition models of Chapter III. Figure 5.2 illustrates several global mean temperature profiles and their input parameters for comparison with the derived global mean profile from Hedin et al. (1983). The $K_E(z) = K = 0$ profile represents the benchmark results described earlier in Section 4.2.1. A reasonable fit is possible for ZPBK = 0 and a turbopause value of $K_E(z) = 1\text{-}1.5\times10^7$ cm^2/s. ($K_E(z)$ above ZPBK = 0 remains constant.) Notice also that temperatures in the vicinity of z = 1 are somewhat cooler than the suggested VTS3 mean temperatures.

The identical eddy cooling parameterization is now invoked in the hydrodynamic code over all SZA. Figure 5.3 illustrates the two-

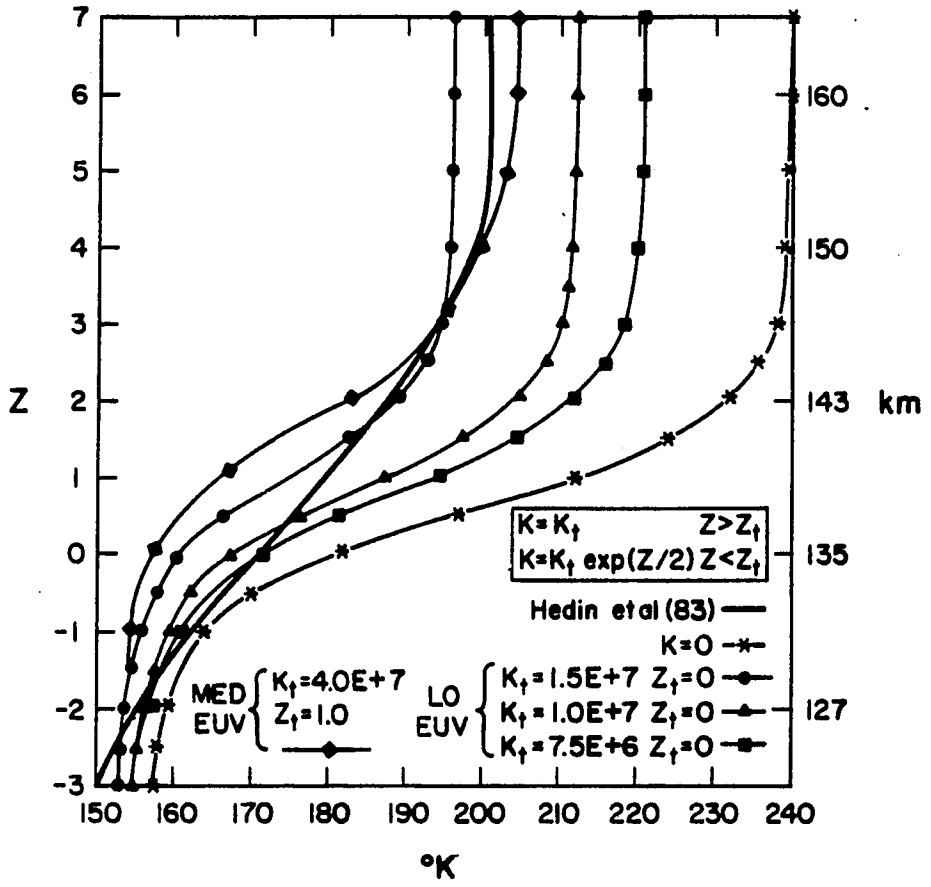


Fig. 5-2 Global mean Venus one-dimensional thermospheric temperature profiles: eddy cooling tests.

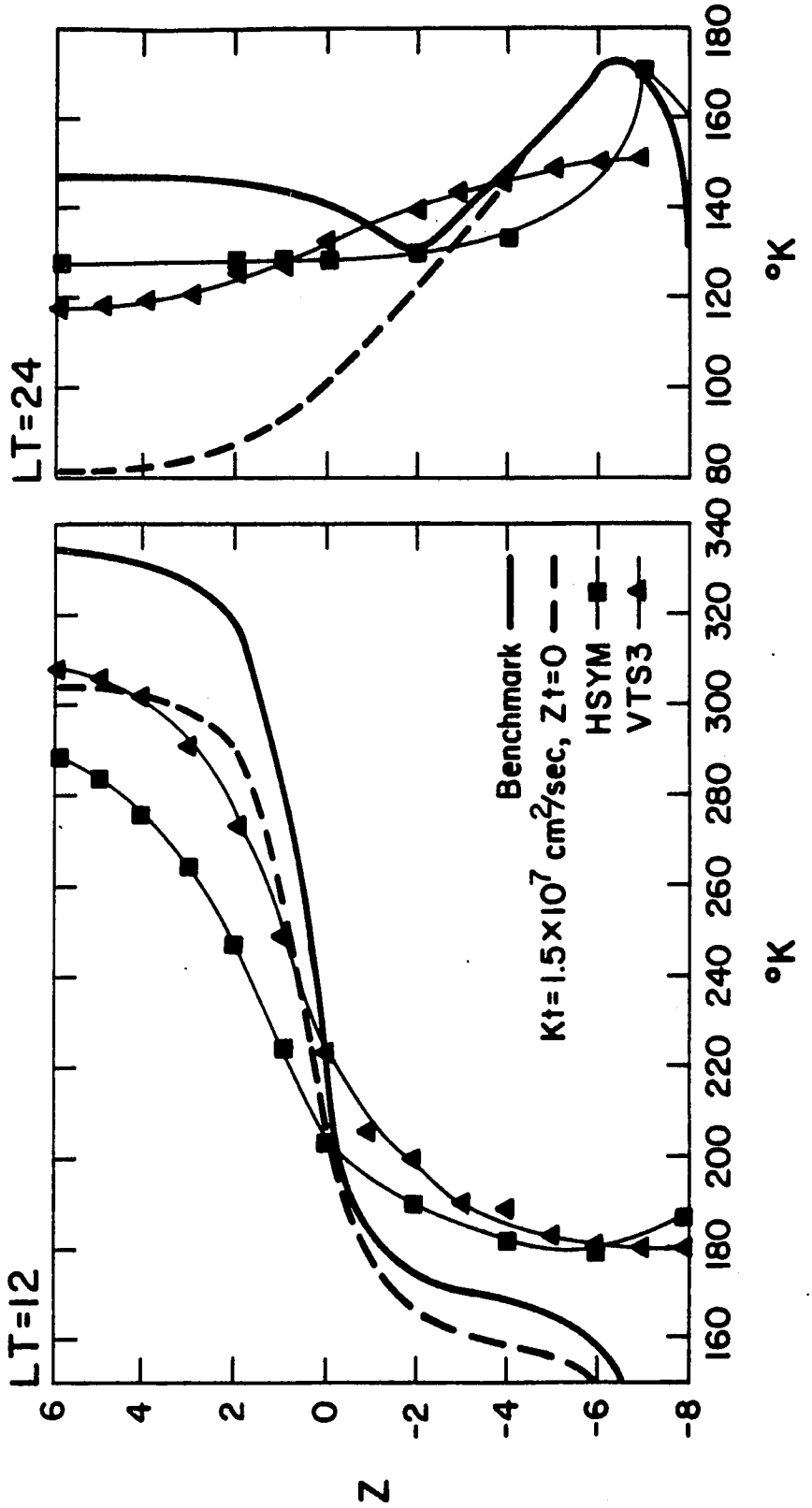


Fig. 5-3 Venus two-dimensional model temperature response to eddy cooling.

dimensional model response to eddy cooling at LT = 12 and 24. The dayside exospheric temperatures are seen to drop nearly 27°K to 300°K, bringing the calculated temperature structure into much better agreement with VTS3 and HSYM observations (than the previous two-dimensional benchmark). This is entirely consistent with the one-dimensional model calculations just described. Nightside eddy cooling, however, has a much stronger response for the same $K_E(z)$ profile, and causes exospheric temperatures to decline 60°K to 80-90°K. SZA variation of mass density $\rho(z)$ at a single pressure level is primarily responsible for this strong temperature decrease.

Table 5.3 summarizes a series of eddy cooling sensitivity studies conducted upon the benchmark model case. A range of $K_E(z)$ profiles is examined for which $2.0\times10^6<KMAX<1.5\times10^7$ cm^2/s, and the turbopause level spans z = -4 to 0. It is significant to point out that dayside values of $K_E(z)<5\times10^6$ cm^2/sec provide a very small amount of external cooling, certainly less than 10°K. Exospheric temperatures can only begin to approach dayside values (for this 2-22% case) for $K_E(z) = 1 - 1.5\times10^7$ cm^2/sec. Also, nightside eddy cooling is roughly ×2 more effective. This could cause problems resulting in extremely cold nightside temperatures, if eddy drag is invoked simultaneously.

A comparison of one-dimensional composition and hydrodynamic models (Section 3.3) suggests that large-scale winds and eddy diffusion should operate simultaneously to control the composition. Those previous eddy diffusion parameterizations (Sections 3.2.4-3.2.6) are now used as a starting point for testing in the two-dimensional

Table 5.3

Eddy Cooling Sensitivity Study of the Venus Two-Dimensional Low EUV Benchmark

ZPBK	ZKM	KMAX	ΔT(°K) Cooling
Dayside			
0	135	1.5×10^7	27°K*
		7×10^6	10-15°K**
		5×10^6	6-10°K**
-2	126	3×10^6	3-5°K**
-4	117	2×10^6	1-2°K**
Nightside			
0	125	1.5×10^7	≥60°K*
		1.0×10^7	≥50°K
-2	119	7×10^6	≥25°K
-4	113	5×10^6	≥16°K

* One-dimensional dayside eddy cooling requirements for low EUV case

**Eddy cooling compatible with K(z) needed for dayside eddy diffusion

code. The current best eddy drag case (K_{RA} = 1×10^{-4} sec^{-1} constant with altitude) is now combined with an examination of needed eddy diffusion. Table 5.4 contains the results from a series of eddy diffusion tests covering a range of KMAX from 2.0×10^{6} to 1.7×10^{7} cm^2/s and ZPBK from -4 to 1.0, for various profile shapes.

The most obvious trend indicates that eddy diffusion (and correspondingly $K_E(z)$) must be roughly a factor of ×2 stronger on the nightside. Since the large-scale winds very effectively control upper dayside composition (Section 3.3), eddy diffusion cannot be of help in maintaining the dayside O and CO bulges observed (Section 2.1.2). Thus a dayside "threshold" value of $K_E(z)$ is obtained, for which eddy diffusion has an insignificant impact on dayside composition. $K_E(z)$ values for dayside eddy diffusion are shown for $2.0\times10^{6}<KMAX<7.0\times10^{6}$ cm^2/s as ZPBK is adjusted from -4 to +1.0. Sufficient nightside eddy diffusion requires $KMAX<1.5\times10^{7}$ cm^2/s for ZPBK = 0 to give composition within the bounds set by the VTS3 and HSYM empirical data sets. It is significant that the dayside requirements for $K_E(z)$ giving eddy diffusion ($KMAX\leq5\times10^{6}$ cm^2/s) are incompatible with the corresponding needs of eddy cooling ($KMAX\geq1-1.5\times10^{7}$ cm^2/s) for this LO EUV case. The preliminary indication is that eddy cooling is not a viable mechanism to provide dayside thermal balance. A consistent picture (for all eddy processes) awaits a quantitative assessment of a coupling of all three eddy parameterizations.

Table 5.4

Eddy Coefficient Sensitivity Upon Composition

Nightside

ZPBK	KM	KMAX(*)	KMAX(**)
1	128	1.5E + 7	1.7E + 7
0	125	1.0E + 7	1.2E + 7
-2	119	7.0E + 6	9.0E + 6
-4	113	5.0E + 6	7.0E + 6

Dayside

ZPBK	KM	KMAX(*)	KMAX(**)
1	140	7E + 6	
0	135	5E + 6	same
-2	126	3E + 6	(threshold)
-4	117	2E + 6	

Note: for $K_E(z) \leq$ KMAX

$$K_E(z) = \text{KMAX} \exp\left(-\frac{\text{ZPBK}-z}{2}\right) \quad (*)$$

$$K_E(z) = \text{KMAX} \exp\left(-(\text{ZPBK}-z)\right) \quad (**)$$

5.2.2 Quantitative Sensitivity Study

External cooling, eddy drag, and eddy diffusion are now progressively incorporated into the two-dimensional model according to the scheme outlined in Section 5.1.1. Figures 5.4a and b illustrate the LO EUV case two-dimensional model responses by the temperature and wind fields, respectively, for each significant stage in the development of a "best" LO EUV model fit. The benchmark case and the VTS3 and HSYM field values are also plotted for comparison. Initial parameter estimates are guided by the independent parameter values established in Section 5.2.1.

Curve (A) in Fig. 5.4a assumes no SZA variation of $K_E(z)$, thereby requiring that all eddy parameterizations have parameter adjustments uniform about the globe. KMAX is set to 5.0×10^6 cm^2/s at ZPBK = 0 for eddy diffusion. Eddy cooling uses KMAX = 1.0×10^7 cm^2/s at ZPBK = 0 (corresponding to the earlier one-dimensional model requirements). $K_{RA} = 1.25\times10^{-4}$ s^{-1} for constant eddy drag. Notice the extremely poor fit, particularly for the nightside temperatures. Eddy cooling and eddy drag cannot be invoked simultaneously to lower nightside temperatures. Additional nightside eddy cooling is unnecessary since slower winds appear to "isolate" the nightside from the dayside sources of heat. Also, it is preferred that $K_E(z)$ be applied identically for all eddy processes. Nevertheless, the value of $K_E(z)$ required by eddy cooling to achieve good dayside tempera- (KMAX = $1\text{-}1.5\times10^7$ cm^2/sec) is incompatible with the corresponding needs for dayside eddy diffusion (KMAX$<5.0\times10^6$). Eddy cooling en-

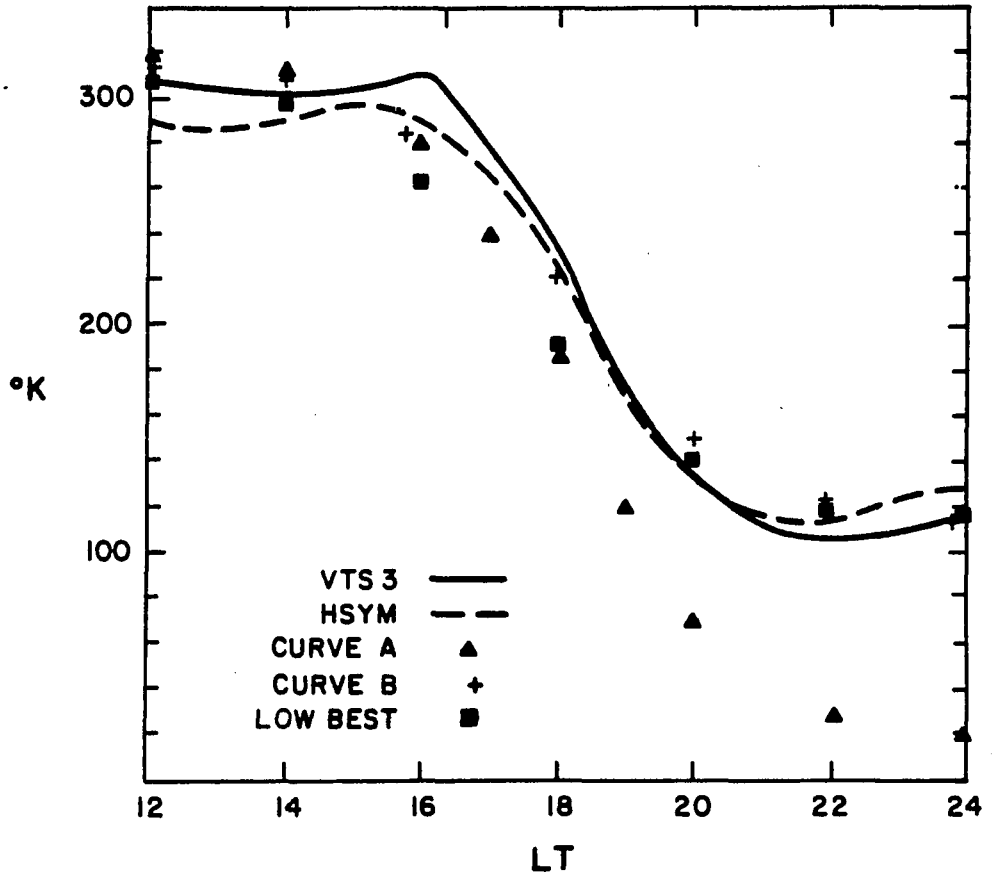


Fig. 5-4a Low EUV case sensitivity study exospheric temperatures.

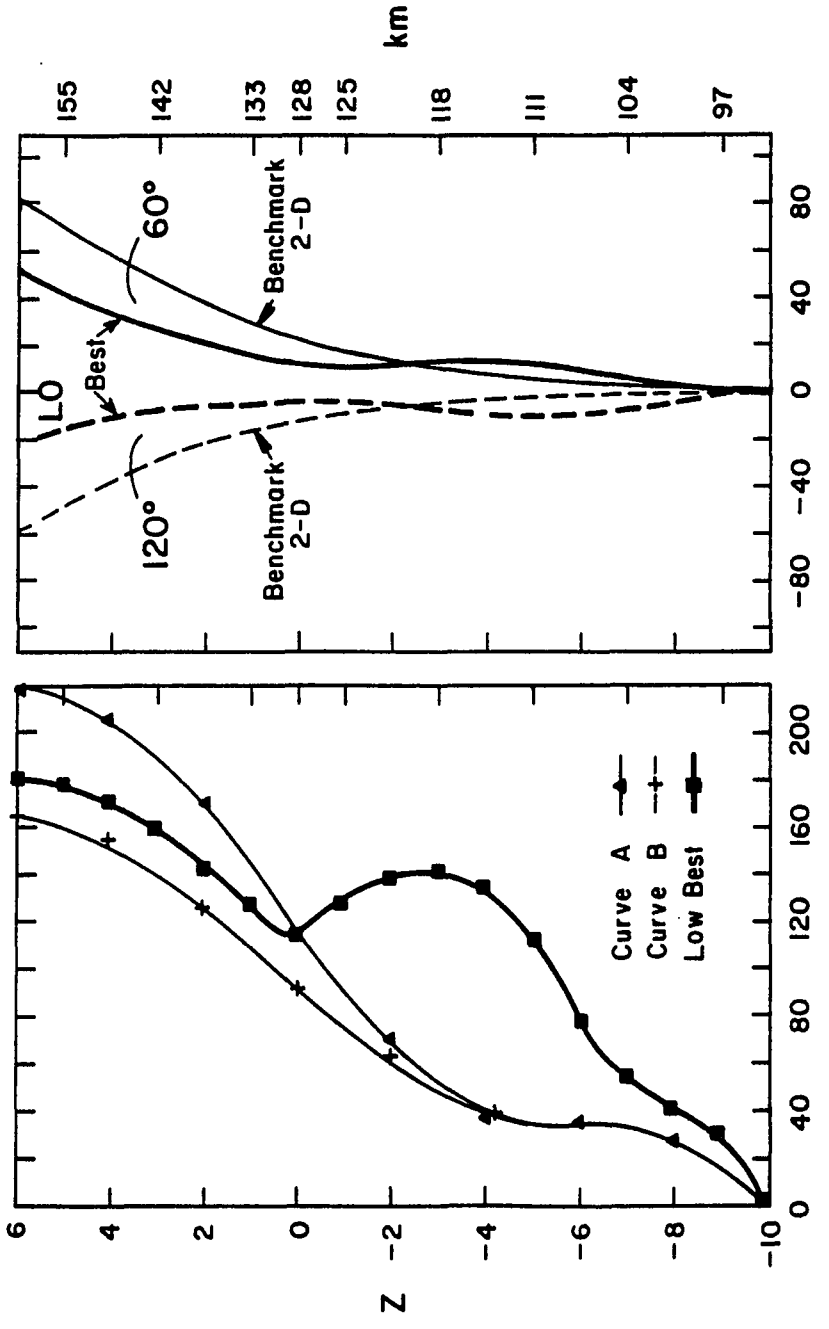


Fig. 5-4b Low EUV case sensitivity study: winds

counters severe problems globally in its ability to provide cooling for a better thermal balance. Another cooling mechanism is needed that provides a good dayside thermal balance consistent with eddy diffusion, without destroying the reasonable nightside temperatures derived by wave drag (see Section 5.3.1).

The day-night thermal balance problem is temporarily addressed by permitting eddy cooling to be relaxed for dayside application only, using KMAX = 1.0×10^{7} cm^2/s. Curve (B) now specifically adopts the SZA variation of eddy diffusion recommended by the independent parameter values established in Section 5.2.1. Nightside eddy diffusion is given for KMAX = 1×10^{7} cm^2/s, while dayside KMAX is retained at 5×10^{6} cm^2/s. Both use ZPBK = 0 and give a SZAF of two. Eddy drag is again set at $K_{RA} = 1.25\times10^{-4}$ s^{-1}. The nightside temperature profile is seen to improve tremendously (Fig. 5.4a), suggesting that the isolation necessary to retain O and CO on the dayside is also sufficient to reduce heat transport to the nightside. Strong nightside eddy diffusion also has an effective role in pumping O downward (reducing O toward observational levels), while leaving CO virtually unchanged. Nightside atomic-O densities can now be maintained (within 15% of observations) with this strong eddy diffusion, even in the face of strong terminator winds (see Fig. 5.4b). Calculated thermospheric winds appear to be most suited to observed composition and temperatures for $u \leq 180$ m/s.

However, it appears that as the drag is selected to optimize agreement of the calculated and observed dayside composition (weakened winds), then too little nightside CO is calculated, with corre-

spondingly colder (10-15°K below observations) nightside temperatures. Nightside atomic-O is also reduced by stronger drag. Conversely, faster winds (not shown) raise nightside O and CO and temperatures at the expense of depleting dayside composition. Apparently, eddy drag is crucial to the day-night distribution of calculated composition and temperatures, and requires a more precise prescription. Eddy diffusion, however, seems important only for the nightside [O] distribution.

5.2.3 Discussion and Best Tunings

Several feedback signatures are visible among the coupled composition, temperature and wind fields as model eddy parameters are adjusted. Slower winds (with respect to DRM2) cannot provide proper composition about the planet alone, without the additional incorporation of eddy diffusion. It is true, however, that drag is the only conceivable mechanism leading to good dayside composition, requiring minimal application of dayside diffusion. Such diffusion is helpful, though, to fine-tune nightside atomic-O, which is very efficiently pumped downward. Drag that is too strong ($K_{RA}>1.25\times10^{-4}$ s^{-1}) will further improve dayside composition, but at the expense of reducing nightside CO and temperatures.

Drag also has an effect on low altitude temperature structure. Calculated temperatures at 100 km are seen to depart substantially from OIR observations, which are approximately horizontally constant at 175°K (Taylor et al., 1980). Calculated dayside temperatures are 30°K warmer, and nightside temperatures 30°K cooler than ob-

servations. This appears to be an artifact of the adopted crude Rayleigh friction scheme, which currently uses a drag time-scale constant with altitude. Clearly, faster low altitude winds are needed to allow the redistribution of heat about the planet at the 100 km level (for little day-night temperature contrast). Here a new profile shape for K_{RA}, similar to $K_E(z)$, may be useful.

These feedback and low altitude considerations are helpful in establishing a "best" set of parameters necessary to give an optimal match of calculated fields to Pioneer Venus observations. A "best" LO EUV case model is now derived, making use of the realistic range of LO EUV parameter values established according to Table 5.5. A new profile of drag is also adopted (similar to the exponential profile used for $K_E(z)$), where $K_{RA} = 1\times10^{-4}$ s^{-1} at ZPBK = 0 and above. An $e^{(Z-ZPBK)/2}$ shape is invoked below the specified turbopause or breaking level (ZPBK). Notice also that the rate coefficient for CO_2 (0, 1, 0) collisionally excited 15 μm cooling is set at $k(CO_2\text{-}O) = 2\times10^{-13}$ cm^3/s, providing nearly ×4 the $O\text{-}CO_2$ cooling used in DRM2 (see Section 3.2.2). No eddy cooling is used.

Figure 5.4c presents LT = 12 and 24 profiles of calculated temperature for this best LO EUV case run. Dayside model temperatures are seen to match the VTS3 profile quite well. Calculated temperatures near 150 km are noted to be somewhat warmer than observations ($\leq$15°K). Nightside temperatures, however, are 20-25°K cooler than both reference atmospheres over $-4<z<0$. Appendix C.1 illustrates the contour plots of T, u, %[O], %[CO] over SZA (on a log pressure scale) for this improved LO EUV case. Note that % [O] is now largely flat

Table 5.5

Best Parameter Adjustments for Each EUV Efficiency Case

Parameter	Low (2-22%)	Medium (10-25%)	High (18-28%)	Best (7-19%)
Eddy Cooling				
DY: Kmax/ZPBK	$1.0\times10^{7}/0$ (NG)	$4\times10^{7}/0$ (NG)	-	none
15 μm Cooling				
$k(CO_2\text{-}O)$	2×10^{-13}	7.5×10^{-13}	1.75×10^{-12}	5×10^{-13}
Eddy Drag				
K_{RA}	$1\text{-}1.25\times10^{-4}s^{-1}$	$1\text{-}1.2\times10^{-4}s^{-1}$	-	$1.2\times10^{-4}s^{-1}$
ZPBK	0	0→1	-	2.0
Eddy Diffusion				
DY: K_{max}/ZPBK	$<5\times10^{6}/0$	none	-	none
NT: K_{max}/ZPBK	$1\text{-}1.5\times10^{7}/0$	$7\times10^{6}/0$	-	$7.5\times10^{6}/\phi$
SZAF	2.0	$\geq$2.0	-	$\geq$2.0
Efficiency Profile Shape				
$\varepsilon(z)$	0.02+0.4*f(p)	0.10+0.3*f(p)	0.18+0.2*f(p)	0.07+0.24*f(p)
f(p)	$0.5/\left(1.+\frac{1.05\times10^{-3}}{p}\right)$	$0.5/\left(1.+\frac{1.05\times10^{-3}}{p}\right)$	$0.5/\left(1.+\frac{1.05\times10^{-3}}{p}\right)$	$0.5/\left(1.+\frac{4.73\times10^{-4}}{p}\left(\frac{T}{200}\right)^{0.55}\right)$
ε_{Top}	2%	10%	18%	7%
ε_{Bot}	22%	25%	28%	19%

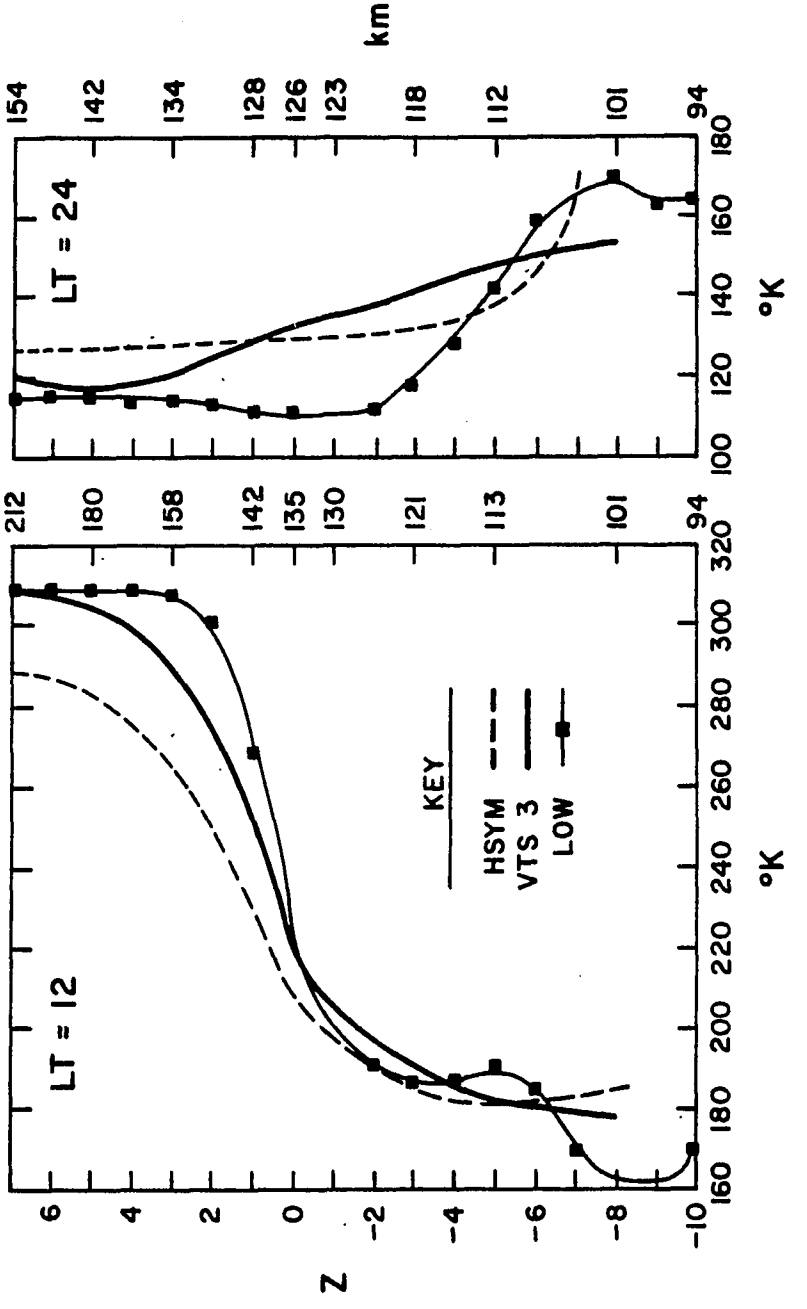


Fig. 5-4c Venus two-dimensional model temperatures: low EUV case

over SZA, contrary to DRM2 predictions. Section 5.3 will describe in detail sensitivity tests examining (O-CO_2) rate coefficients and various drag profile shapes that have been used to make this best LO EUV case possible. Further fine-tuning of the drag parameterization will be conducted for the MED EUV case in Section 5.3.

5.2.4 Diagnostics

Diagnostic plots are provided for use in examining the thermal, momentum and compositional balances for this optimal LO EUV case run. Figure 5.5 shows heating/cooling balances at 60 and 120°SZA, representing average dayside and nightside conditions. As with DRM2 on the dayside, upper level EUV heating ($z>1$) approximately balances downward molecular conduction and 15μ cooling. Lower altitude infrared heating ($z<0$) is primarily offset by 15μ cooling. It is important to note that the LO EUV case heating and 15μ cooling are both ~2.0× previous dayside DRM2 model values. This is primarily due to improved 15μ cooling and the incorporation of solar maximum fluxes for heating. Nightside balance is primarily between adiabatic compressional heating and 15μ cooling, with additional high altitude cooling resulting from conduction. Slower winds require that the heat source available for the nightside be reduced. This is particularly evident above $z = -1$, where newly calculated adiabatic compressional heating is reduced by as much as a factor of three from average nightside DRM2 values. Similarly, thermal advection (and the role of the large-scale winds in diminishing day-night thermal contrast) is nearly reduced by half. The improved 15μ cooling calculation also provides

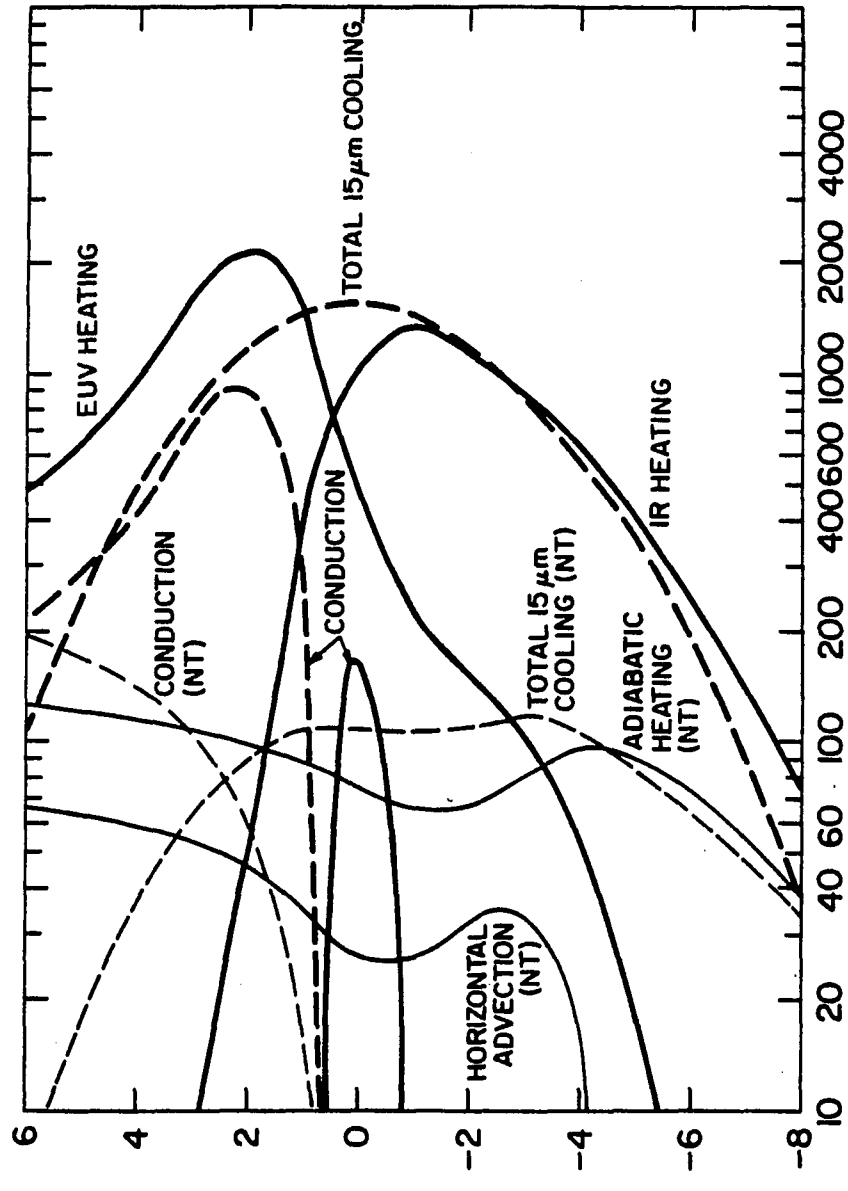


Fig. 5-5 Heating and cooling rates 60° and 120°SZA: low EUV case.

diminished longwave cooling (from a factor of 1.65 to 2.0). The net result is an average nightside thermal balance that gives rise to cooler temperatures than calculated by DRM2. Reduced adiabatic heating also appears to be a major contributor to cooler nightside temperatures above z = 2.

Isolation of the nightside is not only important to a proper thermal balance, but also to a reasonable distribution of composition about the planet (see Section 5.4). Figures 5.6a and b show term balances for %[O] and %[CO] at all SZA for z = 0 and 6. Comparison with the previous DRM2 term balance plot (see Fig. 3.4) reveals the dominant role diffusion has for nightside composition (z>0). The transport source terms for O and CO are also smaller, giving additional cause for diminished nightside O and CO. This redistribution of composition about the planet is the result of wave drag, which now provides a great deal of control over u-momentum balance, particularly for z>0. Here, eddy and laminar viscosity give rise to drag which largely balances the pressure gradient term.

5.3 Medium EUV Efficiency Case (10-25%)

The LO EUV case parameter adjustments have been very helpful in obtaining a good match of calculated fields to observations. Now, a more realistic EUV efficiency profile will be tested (10-25%) that is derived from reasonable assumptions about the fate of $O(^1D)$ and hot particle energies (see Section 5.2.2). In this section, parameter changes will be discussed primarily for external cooling and wave drag. However, all parameters are subject to change for this new heating efficiency case.

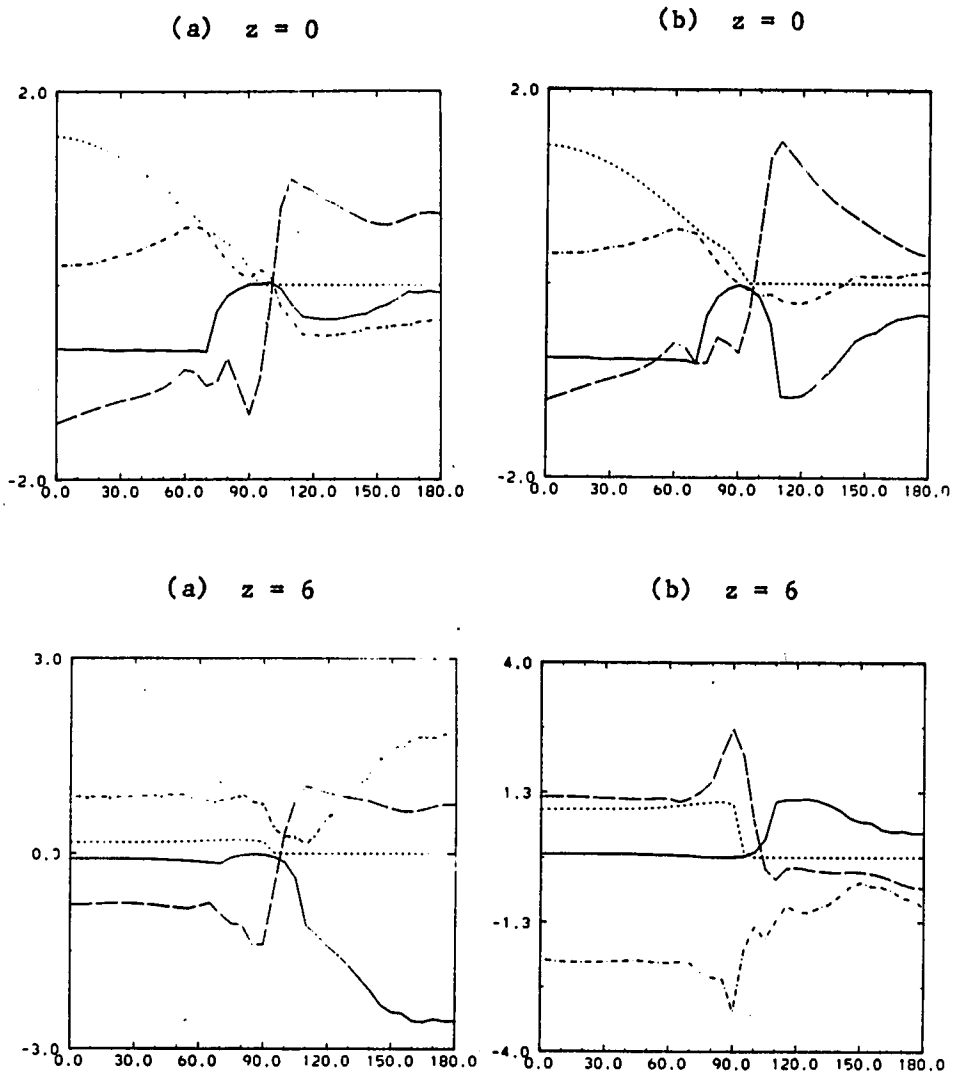


Fig. 5-6 Term balance plots: low EUV case; (a) [O] composition, (b) [CO] composition.
.--.-- molecular diffusion
_____ eddy diffusion
------ advection
..... photodissociation source

5.3.1 Establishment of a Correct Dayside Thermal Balance

Additional external cooling is immediately required with the incorporation of a more efficient EUV heating profile (10-25%). Previously, the LO EUV case made use of eddy cooling to give a proper dayside thermal balance. KMAX was set at 1×10^7 cm^2/s at ZPBK = 0 to provide sufficient cooling. Figure 5.2 also illustrates the effects of eddy cooling upon the one-dimensional global mean temperature calculation for the MED EUV case. Adequate cooling now makes use of an even stronger $K_E(z)$ profile (KMAX$\geq 4\times10^7$ cm^2/s). The upper limit eddy diffusion requirement for dayside $K_E(z)$ (see Section 5.2.3) falls far short of that needed for MED EUV eddy cooling. In fact, sufficient cooling now demands that $K_E(z)$ be tuned even beyond the one-dimensional estimates described in Sections 3.2.4-3.2.6. From this requirement it is possible to conclude that eddy cooling is generally insufficient (beyond the LO EUV case) to provide the external cooling needed to incorporate more efficient EUV heating.

The possibility of using collisionally excited CO_2 (0, 1, 0) to enhance external 15μ cooling was discussed earlier in Section 4.4.3. Terrestrial mesopause and low thermosphere calculations have shown that CO_2 15μ cooling is crucial for determining a proper thermal balance. Atomic-O collisions are especially efficient in exciting CO_2 (0, 1, 0). Observations (Chapter II) showing significant Venus thermospheric atomic-O densities (above 150 km) suggest that increased 15μ cooling is also a mechanism worth investigating for Venus (see DRM2).

The range of collisional excitation rates ($k(CO_2\text{-}O)$) required to reproduce good dayside and global mean temperatures is examined in Table 5.6 a,b for several EUV heating efficiency cases. Dayside mean temperatures (T_∞ = 275-280°K) for MED EUV heating require $k(CO_2\text{-}O) = 7.5\times10^{-13}$ cm^3/s, which is the upper limit of the realistic range of values from presently available rocket observations and lab measurements. A distinctly different rate coefficient is required for the calculation of one-dimensional global mean (T_∞ = 210°K) temperatures: $k(CO_2\text{-}O) = 1.25\times10^{-12}$ cm^3/s. This rate is outside the error bars currently specified according to Table 5.6. It appears that a 15 μm cooling scheme based on dayside and nightside mean reference temperatures would enable reasonable values of $k(CO_2\text{-}O)$ (for MED EUV heating) to be used. Realistic rate coefficients ($k(CO_2\text{-}O) = 5\pm3\times10^{-13}$ cm^3/s) also seem to confine the topside heating efficiencies to $\leq$10%. (Section 5.4 will provide additional detail.)

Total 15 μm cooling can now be calculated within the two-dimensional model based upon updated values of this rate coefficient and corresponding reference calculations for mean dayside and nightside conditions. The radiative transfer code (see Section 4.2) is redesigned to calculate reasonable dayside and nightside mean temperature profiles using MED EUV heating and $k(O\text{-}CO_2) = 7.5\times10^{-13}$ cm^3/s (see Fig. 5.7). A nonlinear temperature-dependent damping parameterization is used to interactively calculate total 15μ cooling at other temperatures based upon this externally supplied reference cooling. Perturbation temperatures are defined about these reference dayside and nightside profiles, and are generally less than 60°K. By compa-

Table 5.6

K_{CO_2-O} Rate Sensitivity Ranges
For Various Heating Efficiency Models

(a) Dayside Mean Temperature Profile Requirements ($T_\infty \approx 280°K$)

Model	Efficiency (EUV)	K_{CO_2-O} Rate Required (cm^3/s)	Comments
LO	2-22%	3×10^{-13}	~Measured lab rate
MED_1	10-18%	6×10^{-13}	~Rocket rate of Sharma and Nadile (1981)
MED_2	10-25%	7.5×10^{-13}	75% Gordiets et al. (1982)
HI_1	14% flat	1×10^{-12}	Gordiets et al. (1982) rate
HI_2	18-28%	1.75×10^{-13}	175% Gordiets et al. (1982)
Best	7-19%	5×10^{-13}	Sharma and Nadile (1981) rocket rate

(b) Global Mean Temperature Profile Requirements ($T_\infty \approx 208°K$)

LO	2-22%	5×10^{-13}	Sharma and Nadile (1981) rate
MED_1	10-18%	1.0×10^{-12}	Gordiets et al. (1982) rate
MED_2	10-25%	1.25×10^{-12}	NG
HI_1	14% flat	1.67×10^{-12}	NG
HI_2	18-28%	2.92×10^{-12}	NG
Best	7-19%	8.33×10^{-13}	Upper limit of range

Best Estimate of Actual K_{CO_2-O} Rate
$2E\text{-}13 \leq K_{CO_2-O} \leq 8E\text{-}13\ cm^3/s$
$K_{CO_2-O} = 5 \pm 3E\text{-}13\ cm^3/s$

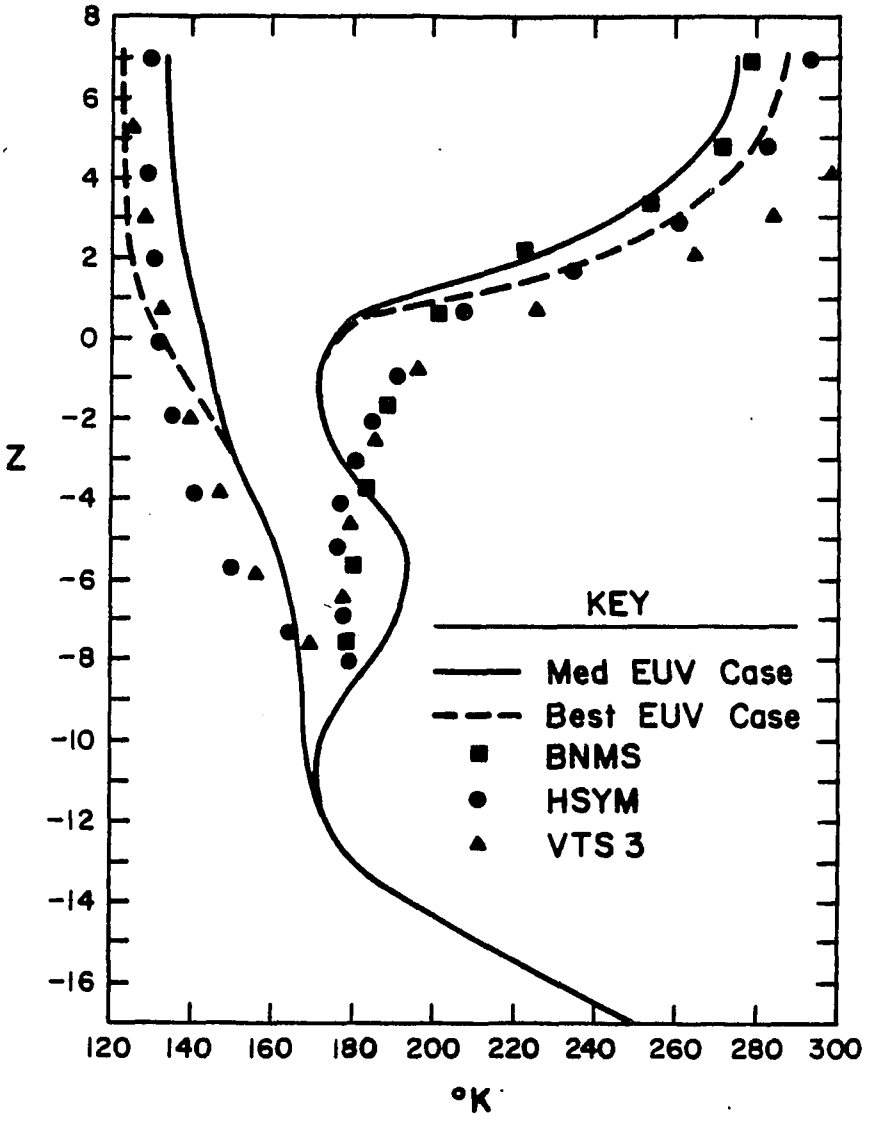


Fig. 5-7 One-dimensional RT model reference temperatures: dayside and nightside mean profiles.

rison, total 15μm cooling based upon a global mean prescription for reference cooling and temperatures requires that larger temperature perturbations ($\Delta T \leq 120°K$) be damped (see DRM2). This improved "two-reference" temperature 15μm cooling scheme is a closer approximation to that given by a series of exact one-dimensional radiative transfer calculations at each SZA bin about the planet. Accuracy will improve for total 15μm cooling as such an ideal (and expensive) procedure is approached.

Appendix B outlines the coding changes necessary to incorporate this new "two-reference temperature" 15 μm cooling scheme in the two-dimensional model. The explicit ratio of $k(CO_2\text{-}O)$ and $k(CO_2\text{-}CO_2)$ is now calculated, for which temperature dependencies are taken from Sharma and Nadile (1981) and Simpson et al. (1977), respectively.

5.3.2 Quantitative Sensitivity Study

A two step approach is used to confirm that the two-reference temperature 15μm cooling scheme is a valuable improvement over the global mean reference temperature formulation used by DRM2. First, eddy cooling is entirely eliminated in favor of enhanced 15μm cooling, which uses $k(CO_2\text{-}O) = 1.25\times10^{-12}$ cm^3/s consistent with global mean reference temperature 15μm cooling. Drag is retained (constant $K_{RA} = 2.00\times10^{-4}$ s^{-1}) to give maximum horizontal winds <180 m/s. Compatibility of the one-dimensional and two-dimensional codes is now examined by a consistency check which compares the one-dimensional calculations at the SSP (subsolar point) and the ASP (antisolar point) with the corresponding two-dimensional model temperature profiles.

Curve (A) of Figs. 5.8a and b shows the model response to these parameter adjustments. Dayside temperatures match Keating et al. (1984) values quite well. Notice, however, that cold nightside temperatures are calculated ($\leq$100°K), which are not reproduced in the one-dimensional results. This suggests first that the nightside thermal balance is skewed by inappropriately large perturbation 15μ cooling, even though the dayside balance is quite good. The calculated terminator exospheric temperatures are also 40-60°K cooler than the reference empirical models. The global mean reference temperature prescription for 15μm cooling appears to be inadequate to closely reproduce both dayside and nightside observed temperatures. For this run, an upper limit to drag requiring u<180 m/s (weakest possible winds) is also established (see Fig. 5.8b). These winds are roughly half of the previous updated model values (Section 4.3).

Curve (B) (see Figs. 5.8a and b) specifically addresses two important improvements to the two-dimensional model: two-reference temperature 15μ cooling and a vertical profile of drag. The newly calculated one-dimensional temperature profiles (see Fig. 5.7) and their corresponding 15μ cooling are now employed with $k(O\text{-}CO_2) = 7.5\times10^{-13}$ cm^3/s to comprise step two of our testing of global cooling schemes. Low altitude winds are also permitted to blow uninhibited by using a drag profile that grows toward $K_{RA} = 1\times10^{-4}$ sec^{-1} at ZPBK = 0:

$$z < 0 \qquad \text{Drag} = K_{RA} \exp(z/2)$$

$$z > 0 \qquad \text{Drag} = K_{RA} = 1\times10^{-4} \text{ sec}^{-1} \qquad (5.2)$$

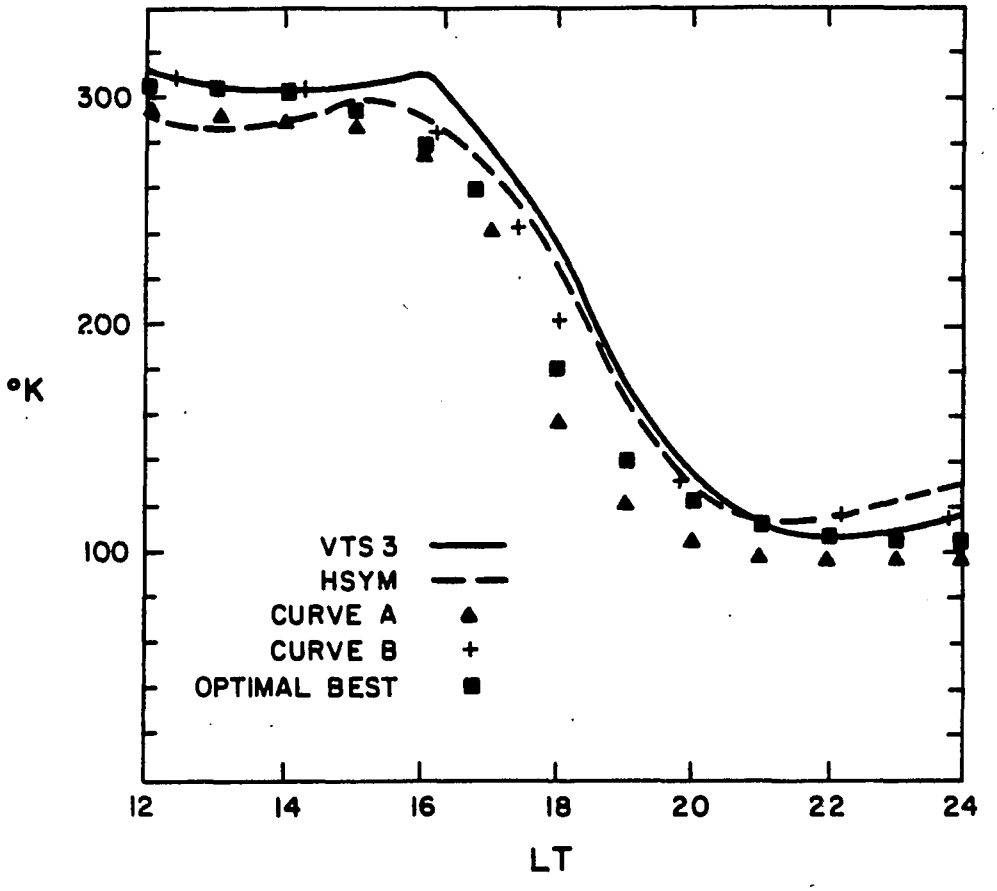


Fig. 5-8a MED EUV case sensitivity study exospheric temperatures.

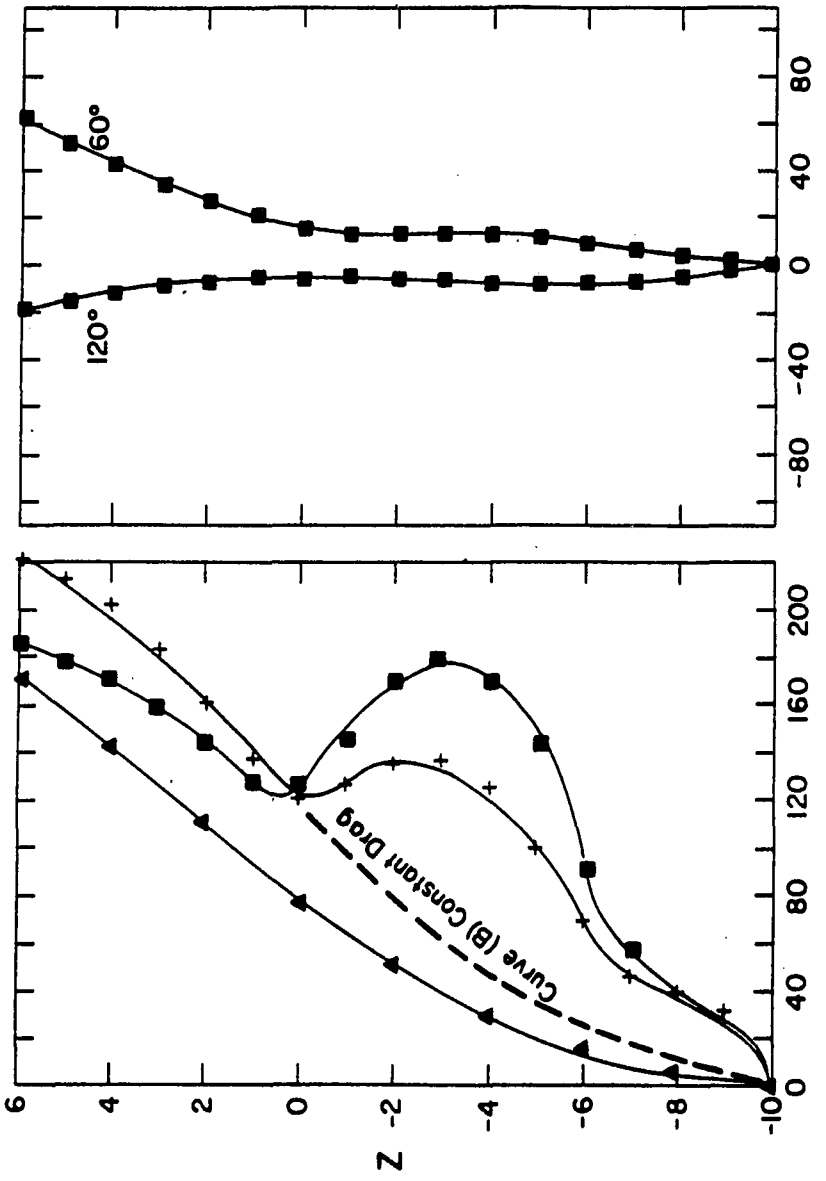


Fig. 5-8b MED EUV case sensitivity study: winds

This vertical variation of drag is similar to that used for parameterizations of $K_E(z)$. Eddy diffusion is essentially identical to the previous best LO EUV case model prescription.

The improvements to global temperatures and composition are striking. Nightside exospheric temperatures are seen to rise 10-15°K to 115°K at midnight. At the same time, global mean and dayside exospheric temperatures rise toward VTS3 values (285°K and 311°K, respectively) (see Fig. 5.8a). Terminator exospheric temperatures are 40°K warmer, now just 20-30°K short of HSYM and VTS3 values of 220 and 230°K. Clearly, much better day-night temperature variations and global mean temperatures are possible with this improved two-reference temperature 15μ cooling scheme.

Largely uninhibited low altitude winds are also crucial to the development of an expanded and warmer nightside column. Temperatures at 100 km are observed to approach 165-170°K over all SZA (see Fig. 5.8c), in contrast to LO EUV case lower boundary values of 190°K and 150°K for day and night, respectively. A redistribution of heat now seems to be occurring at low altitudes about the planet. Nightside temperatures ($z<-2$) are also warmer by 10-20°K due to these stronger low altitude winds. The warmer nightside column also serves to alter the nightside composition (the % of [O] and [CO] at midnight rises). High altitude winds are also somewhat faster than possible for constant drag ($U\leq 220$ m/s) (see Fig. 5.8b). This enhances thermal advection to the nightside and contributes to the warmer nightside upper thermosphere temperatures. Dayside composition does not change appreciably, since the largest increase in winds occurs at altitudes

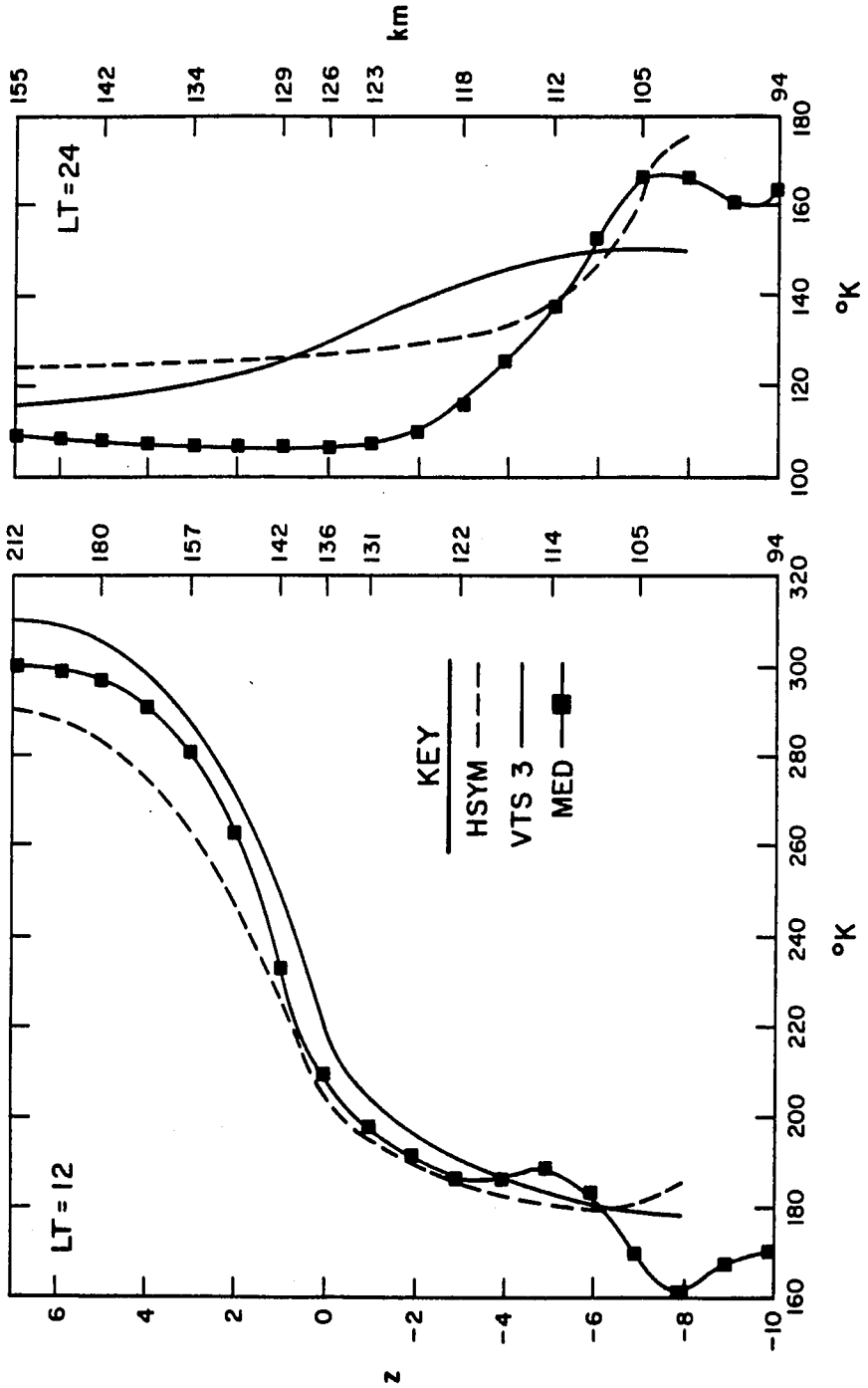


Fig. 5-8c Venus two-dimensional model temperatures: MED EUV case

below z = 0, where the transported species O and CO are minor compared to CO_2.

One of the primary limitations of the present fitting scheme involving drag, diffusion, and external cooling parameters is that no feasible mechanism other than drag seems sufficient to retain O and CO on the dayside at levels close to observations. The drag necessary to do this restricts the ability of the large scale winds to transport CO and O to the nightside and to provide an adequate heat source to maintain a sufficiently warm nightside column.

The parametrically-prescribed chemistry of the two-dimensional model may in fact be inferior to the more realistic and complete formulation provided by Massie et al. (1983) (Section 3.2.6.). It is useful to check the model dayside production and loss (P-L) terms for O and CO. An attempt is made to match P-L terms at 60°SZA, given by Massie et al. (1983), with those calculated by the two-dimensional model. Enhanced dayside O and CO sources would enable stronger winds to blow with no further damage to dayside composition. The nightside column, however, would be improved.

Several changes in the two-dimensional model parameterized chemistry were made, which reduce (to within 20%) the discrepancies between the (P-L) terms of the two-dimensional model and Massie et al. (1983) at 60°SZA. N_2, O, and CO photo-ionization rates are calculated, providing additional sources of CO_2^+ by ion-molecule (atom) interchange. This can be important, since CO_2^+ eventually recombines to produce one O and CO pair. These additional sources of O and CO production are augmented furthermore by 40% (as in Massie et al.,

1983) to represent the effects of secondary ionization. Similarly, the multiple dissociation possible via CO_2^+ is parameterized in a fashion according to DRM2. Now, however, the threshold wavelength for 100% yield is raised to λ = 475Å, which is midway between that suggested by Torr et al. (1979) (λ_{crit} = 600Å) and that previously used by DRM2 (λ_{crit} = 388Å). Recombination effects, due to $O+O+CO_2$, are also included over the planet at low altitudes. Seventy-five percent of the resultant excess energy is permitted to be thermalized in the two-dimensional code, with the remainder lost via $O_2(^1\Delta)$ airglow.

The [O] source terms from the two-dimensional model are compared with the Massie et al. (1983) values at 60°SZA for calculations before and after the model improvements to dayside chemistry. Previous calculations (as well as those of DRM2) are largely given by the I_{CO_2} and J_{CO_2} source terms. From Fig. 5.9, it is evident that the ionization sources from O, CO and N_2 provide an enhancement of nearly a factor of two (over previous DRM2 values) in the total source term above 160 km. The CO_2^+ ionization source is dominant, yet it changes very little as a result of the improvements in chemistry described above. Below 138 km, ionization gives way to direct CO_2 dissociation as the principal source of O and CO and is also largely undisturbed. Below 110 km, $O+O+CO_2$ recombination begins to offset the dissociation source. Finally, below 100 km, minor species chemistry is needed (as suggested by Yung and Demore, 1982) for a proper formulation of O (and CO) production and loss. With the above improvements to the two-dimensional model, the DRM2 chemistry is now in excellent agreement

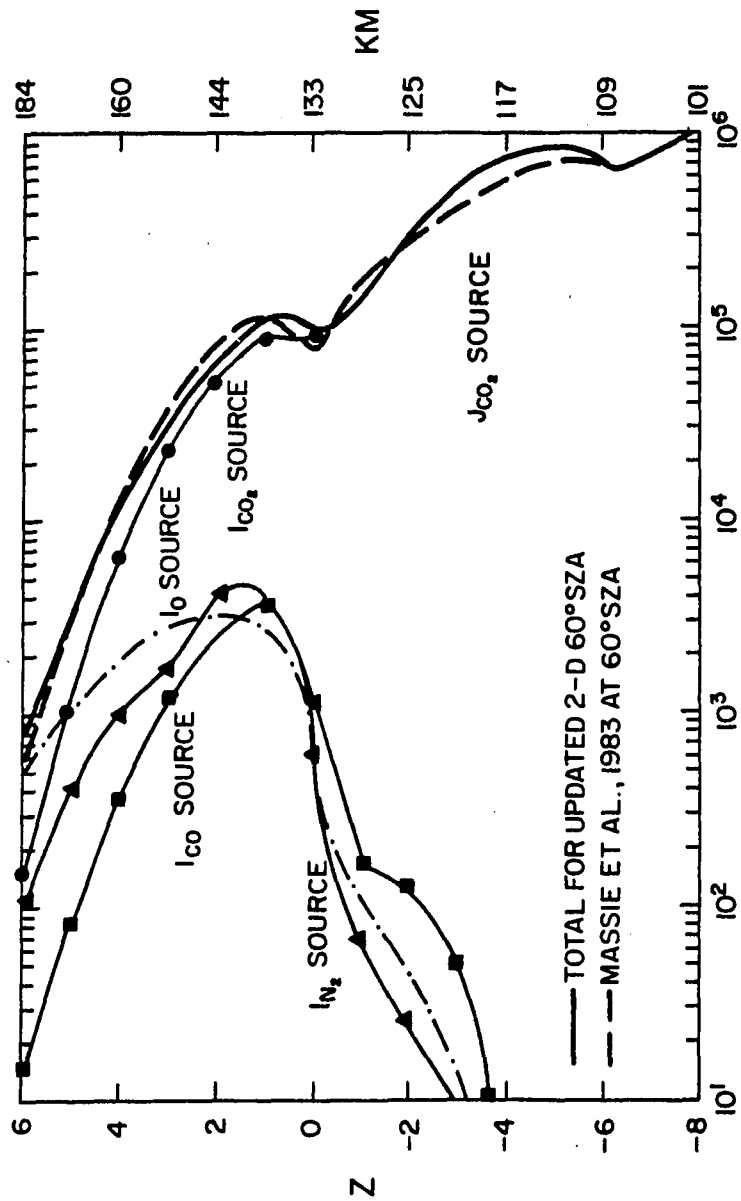


Fig. 5-9 Production minus loss for O and CO at 60°SZA: MED EUV case.

with the chemistry of Massie et al. (1983) for altitudes above 100 km.

The MED EUV "optimal best" curve now shows that improved dayside source terms for chemistry enable stronger low altitude ($z<0$) winds to blow and still maintain good dayside composition. An improved version of the drag profile is also used, for which $K_{RA} = 1.2\times10^{-4}$ sec^{-1} and ZPBK = 1.0. This is the result of a series of tests for which ZPBK and K_{RA} have been adjusted to achieve the best possible dayside composition and nightside temperatures. Dayside % [O] is now maintained at values near 48% at z = 4. This is an example of the dayside [O] levels that are crucial to good dayside thermal balance. Nightside composition is also improved from these stronger winds, giving % [CO] = 6% at z = 4. Exospheric temperatures now reach 305°K for the dayside, with nightside values near 110°K (see Figs. 5.8a and c).

The fitting scheme described in Section 5.1 samples specific fields at particular pressure levels at LT = 12 and 24. It is also instructive to examine total number densities and the heights of the column at various pressure levels. One hundred and fifty kilometers is chosen as a useful reference altitude (noon and midnight) for comparison of calculated fields and the VTS3 and HSYM empirical models. From Fig. 5.8c, it is apparent (for MED EUV optimal conditions) that the nightside column is considerably "collapsed" or cooler than observations. The 150 km altitude occurs at a much lower pressure level than observations. As a result, the number densities for [O], [CO], [CO_2], [N_2] are all reduced below observed nightside values by factors

of 2 to 3. Also the model upper boundary at z = 7 for midnight corresponds to 155 km, which is 5 km below that given by Pioneer Venus observations. The thermal balance of the nightside thermosphere is not yet consistent with all available observations. The dayside column, however, matches very closely VTS3 temperatures and HSYM total number densities at 150 km.

Figures 5.8a, b, and c show also that raising ZPBK above 0 is very effective for building up the nightside column. Such a "breaking level" for the waves might now be considered a transition region above which molecular diffusion processes damp any further growth of gravity wave perturbations. The resulting faster low altitude winds permit thermal advection and adiabatic compression to raise nightside temperatures toward VTS3 and HSYM values. Apparently, some combination of strong low altitude winds smoothly tapering off to constant upper altitude winds is necessary, and ZPBK is crucial for parameterizing this transition.

5.3.3 Discussion and Best Tunings

Optimal parameter adjustments used for this case are summarized in Table 5.5. Figure 5.8c shows that the dayside calculated temperatures now fall between the HYSM and VTS3 values. This is primarily a result of good dayside thermal balance now possible by enhanced 15μ cooling provided by $K(CO_2\text{-}O) = 7.5\times10^{-13}$ cm^3/s within a two-reference temperature formulation. Notice also that maximum terminator winds are restricted to be $u<220$ m/s, which is roughly half of the two-dimensional (DRM2) model values (see Section 4.3). This

requires that eddy drag be invoked, utilizing ZPBK>0.0 and $10^{-4}<K_{RA}<1.2\times10^{-4}$ sec^{-1}. Stronger winds (u>220 m/s) certainly do enhance nightside temperatures and drive composition much closer to empirical model values. Yet, day atomic-O is seriously depleted below that acceptable by the lower limit HSYM empirical reference, even with improved dayside chemistry. It also appears that nightside [CO] is highly sensitive to winds, as is the response of the entire nightside column (total number densities and temperatures). Eddy diffusion does not, however, have as strong an effect on nightside [CO] as [O]. Presently, KMAX = 7.5×10^{6} cm^2/s at ZPBK = 0 is acceptable (with the strongest possible winds) to restore nightside [O] to observed levels. Dayside eddy diffusion is best neglected or limited to values of KMAX<5×10^{6} cm^2/s at ZPBK = 0.

Appendix C.2 illustrates this best MED EUV case by showing log-pressure contour plots of T, u, % [O], and % [CO] over SZA. The lower boundary has very little temperature variation as required by OIR data. Day-night contrast for temperatures is characterized by a sharp drop across the terminator. The thermal gradient across the dayside z = 0, +1 level is also quite strong, corresponding to a peak in the EUV heating. Winds are smooth at high altitude, but clearly indicate a sharp transition over z = -2 to 2 due to the adopted exp(z/2) vertical profile structure. Composition is quite flat over SZA (in log pressure coordinates), but is shown to give rise to slight nightside O and CO bulges.

5.3.4 Diagnostics

Heating/cooling balance for the best MED EUV case is presented for 60 and 120°SZA in Fig. 5.10. Dayside EUV heating is roughly 1.7× as large as the LO EUV case, with correspondingly enhanced 15μ cooling. Nightside heating (via adiabatic compression and thermal advection) is largely unchanged, primarily due to similar winds. Notice that nightside 15μ cooling, now calculated via the two-reference temperature scheme, is 0.6× the former value of the global mean 15μ cooling scheme (see Curve A of Fig. 5.8a).

Term balances of % [O] and % [CO] for all SZA at z = 0, and +6 are presented in Figs. 5.11a and b. It is significant to note that the nightside advective source terms for O and CO are slightly enhanced over the LO EUV case values. This corresponds to several improvements that have been incorporated into the model to better maintain the nightside temperatures and composition (see Section 5.4.2). The dayside photo-source terms for O and CO are also increased as a result of the improved dayside chemistry (see Section 5.4.2). These balances make it quite clear how the model fields respond to the significant changes made in the tuned parameters.

5.4 The High EUV Efficiency Case (18-28%)

Section 5.2 describes the motivation for attempting a high EUV case sensitivity study. Such a profile is a reasonable match to the Model C EUV heating case (Fox, 1981, private communication). However, raising the topside heating efficiency to 18% immediately requires

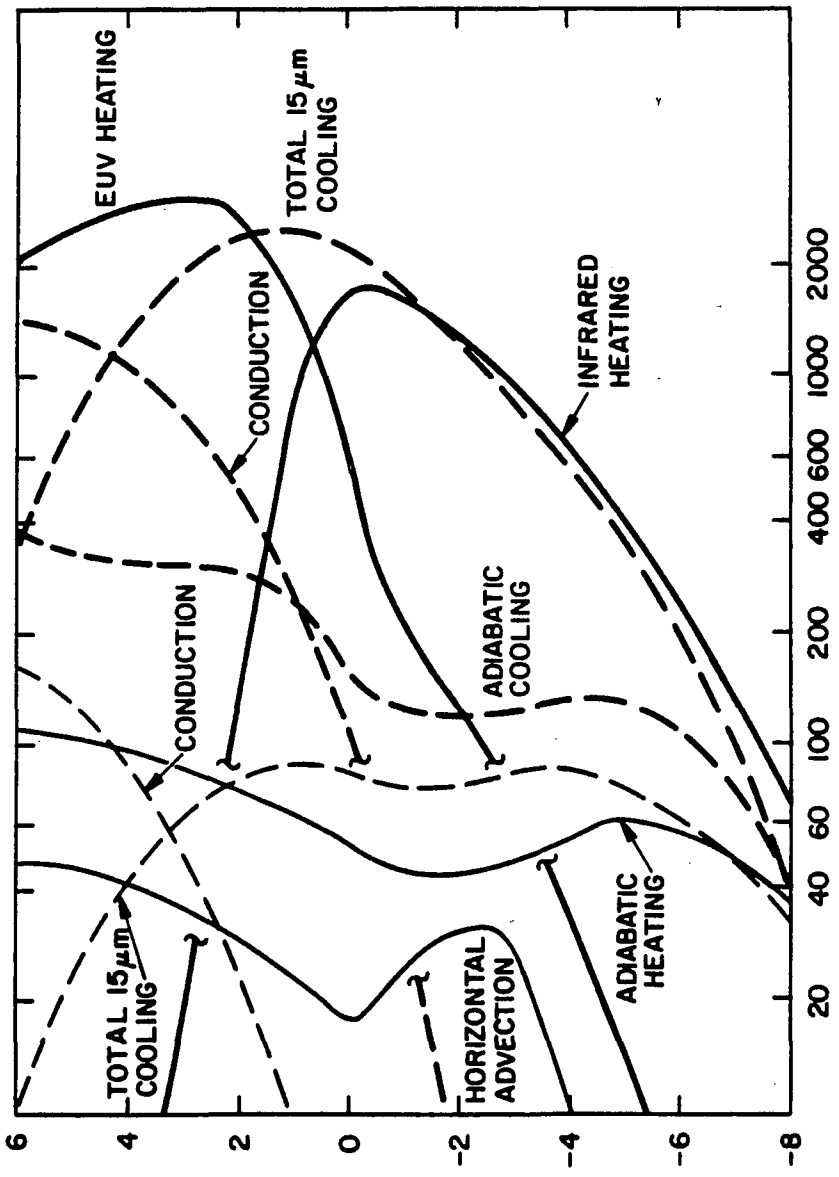


Fig. 5-10 Heating and cooling rates 60° and 120°SZA: MED EUV case.

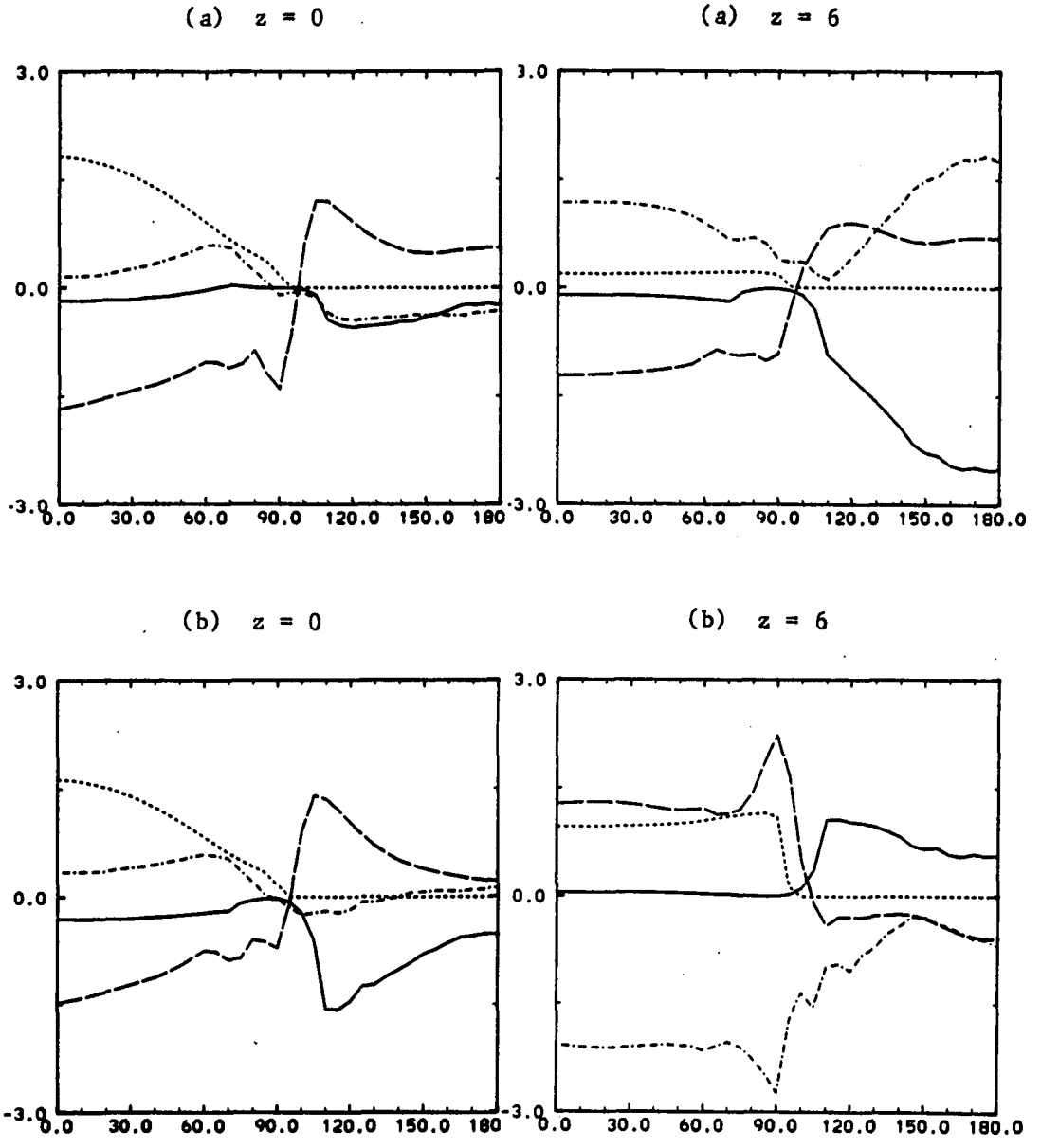


Fig. 5-11 Term balance plots: MED EUV case; (a) [O] composition, (b) [CO] composition

.--.-- molecular diffusion
_____ eddy diffusion
------ advection
..... photodissociation rsource

that additional external cooling be invoked (above MED EUV case levels) for a proper dayside thermal balance and temperatures.

Table 5.6 is again cited to show the external cooling requirements by CO_2 (0, 1, 0) excitation (through collisions with atomic-O) for various $\varepsilon(z)$ profiles. Note that this high EUV case requires $k(CO_2\text{-}O) = 1.75\times10^{-12}$ cm^3/s (for good dayside mean temperatures), which is clearly outside the realistic range for rate coefficients given earlier (see Table 5.6). The large value used by Gordiets et al. (1982), in fact, can only provide sufficient cooling for a topside heating efficiency of 14%. At this time, no conceivable external cooling mechanism is sufficient to warrant the use of a topside efficiency as large as 18%. As a result, the HI EUV efficiency profile cannot presently be used to calculate observed dayside temperatures. Two-dimensional calculations are not conducted for this HI EUV efficiency case.

5.5 Best Model Simulation (7-19%)

5.5.1 Assumptions Required

A best model simulation is constructed for optimal parameters selected from the previous LO and MED EUV case studies. In particular, a mean rate coefficient of $k(CO_2\text{-}O) = 5\times10^{-13}$ cm^3/sec is adopted as the best currently available, based on the rocket data of Sharma and Nadile (1981). A corresponding adjustment of the EUV efficiency is now required to achieve a proper dayside thermal balance. An additional objective of a final adjustment of model parameters is

to improve the nightside column composition and temperatures while maintaining good dayside composition. For this purpose, a smoother drag profile is sought that gives a better transition from low to high altitude wind regions.

5.5.2 Optimization of Adjustments

Optimal tunings of the five model parameters described in Section 4.4.3 are designated as those which:

(1) utilize mean values of these parameters which are within the range of acceptable limits established by LO and MED EUV cases (see Table 5.5)

(2) confine the global output fields (T, [O], [CO], [CO_2]) to remain within the scatter established by the VTS3 and HSYM empirical model observations

(3) limit the $K_E(z)$ adopted to that minimum profile, which can sufficiently supplement the effects of the large scale winds.

It is not known a priori that adjustment of the five model parameters can meet all these criteria, yet that is the objective. Additional parameters may in fact be required that a two-dimensional model is not capable of examining (i.e., super-rotation).

The successful incorporation of the new ($k(O\text{-}CO_2) = 5\times10^{-13}$ cm^3/s) rate coefficient demands the adoption of a new EUV heating efficiency ($\varepsilon(z)$) profile. The one-dimensional radiative transfer model is again utilized to test for an appropriate $\varepsilon(z)$ profile under dayside mean conditions. A proper thermal balance between 15μ cooling

and EUV heating is achieved for a 7% topside EUV efficiency (giving an exospheric temperature of 285°K). Figure 5.7 presents the new dayside and nightside mean temperature profiles for comparison. Notice that the temperature profile structure changes only for the EUV heating region ($z>0$). Somewhat warmer dayside exospheric temperatures are calculated for this optimal case than for the previous MED EUV case conditions.

New assumptions for the quenching of CO_2 rotation states were also made in the construction of an optimal EUV efficiency profile shape. Table 5.7 compares the LO, MED, and HI EUV efficiency profile values over $-5<z<7$. It is particularly significant to note the change of the EUV efficiency for the three cases at $z = 1$, (ε = 15%, 20%, and 24%) and $z = 7$ (ε = 2%, 10%, and 18%). These pressure levels correspond roughly to the maximum EUV heating and exobase regions, respectively. A better balance of heating and cooling might be possible if the maximum EUV heating (at $z = 1.0$) is reduced, requiring that less CO_2 rotation quenching occur at lower altitudes. A new quenching factor is adopted, whereby 50% of the available CO_2 rotation-vibration energy is now realized as heat below 125 km:

$$f(p) = 0.5/\left[1.+(4.73\times10^{-4}/p)(T/200)^{0.55}\right] \qquad (5.3)$$

giving rise to an optimal $\varepsilon(z)$ profile:

$$\varepsilon(z) = 0.07+0.24*f(p) \qquad (5.4)$$

Table 5.7

Lo, Med, HI and Best EUV Efficiency Profiles

ZP	LO (2-22%)	Med (10-254%)	HI (18-28%)	Best (7-19%)
7	.02	.10	.18	.071
6	.023	.102	.181	.073
5	.026	.105	.183	.077
4	.036	.112	.188	.087
3	.058	.129	.199	.107
2	.098	.159	.219	.138
1	.147	.196	.240	.166
0	.185	.224	.260	.180
-1	.206	.239	.273	.186
-2	.214	.246	.277	.190
-3	.218	.248	.279	.190
-4	.220	.250	.280	.190
-5	.220	.250	.280	.190

The EUV efficiency now spans 7 to 19%, with ~17% efficiency at z = 1.0. The maximum EUV heating is reduced to a level midway between that calculated previously for the LO EUV and MED EUV cases. A thermal balance appropriate for reasonable dayside thermospheric temperatures is now achieved, for $\varepsilon(z)$ = 7-19% with $k(O\text{-}CO_2) = 5\times10^{-13}$ cm^3/sec.

One possible mechanism for "pumping up" a more realistic nightside thermospheric column is a stronger and smoother wind structure. A sensitivity test is now devised to estimate the best values of ZPBK and K_{RA} in the construction of a smooth and sufficiently improved terminator wind profile. Various combinations of ZPBK ($0<z<4.0$) and K_{RA} (10^{-4} to 1.4×10^{-4} s^{-1}) are tested with the aid of a new pressure dependent Rayleigh drag term in the equation of motion:

$$\text{Drag} = K_{RA} \frac{2}{1 + (P/P0)^{1/2}} \qquad (5.5)$$

This drag approaches K_{RA} as $P = P_0$ and vanishes as $P>P_0$. Figure 5.12 illustrates a family of terminator wind profiles that result from these adjustments. Generally, as ZPBK is raised, low altitude winds are enhanced, thereby weakening the day-night temperature contrast below z = -4. The new pressure dependence of the drag term effectively smoothes out the transition from the low to high altitude winds by prescribing that the (negative) momentum be deposited more gradually over a wider altitude region. The high altitude winds, shown in

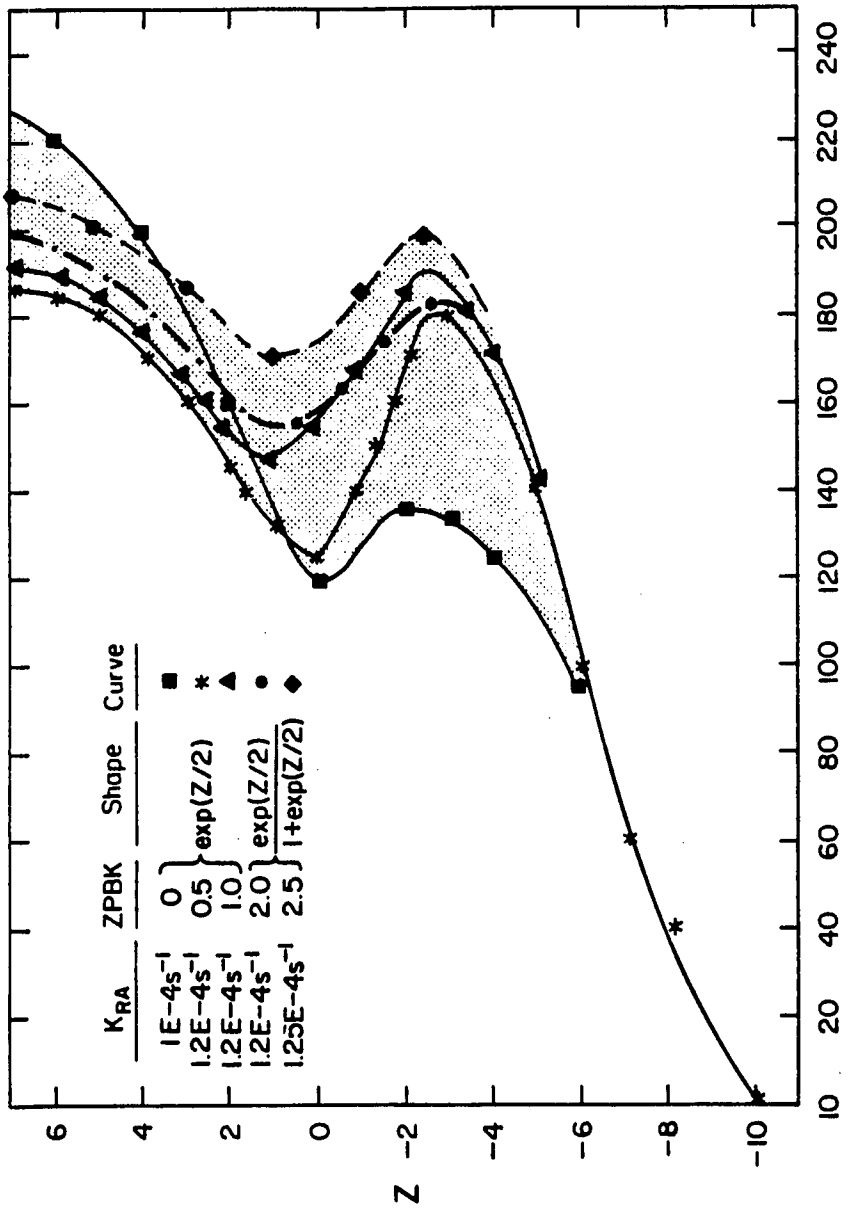


Fig. 5-12 Family of terminator horizontal wind profiles.

Fig. 5.12, are seen to span the range ($180<U<220$ m/s), established earlier in LO and MED EUV case studies. Smoother and more reasonable wind profiles are obtained with the new parameterization of Eq. (5.5). A best drag profile is adopted ($K_{RA} = 1.2\times10^{-4}$ sec^{-1} at ZPBK = 2) using the "smoothed" profile shape, giving $U\leq200$ m/s (see Fig. 5.12).

These new parameter changes result in the best two-dimensional model simulation presently available. Calculated temperature profiles for noon and midnight are compared with the VTS3 and HSYM empirical model values in Fig. 5.13a. The calculated dayside profile corresponds closely to VTS3 temperatures above z = -8 (100 km), giving a dayside exospheric temperature of 311°K. Nightside temperatures are also seen to rise toward empirical model temperatures, resulting in the expansion of the entire nightside column. The midnight exospheric temperature is now 111°K, which is quite close to VTS3 and Massie et al. (1983) values of 118° and 115°K, respectively. The intermediate profile temperatures ($-4<z<4$) are however 10-20°K cooler. Lower boundary temperatures, particularly on the dayside, are also 10-15°K cooler than OIR observations. The lack of sufficient recombination (chemical) heating below 100 km is likely responsible. A better and probably fairer comparison would be obtained by considering nightside and dayside horizontally averaged temperatures profiles above 100 km (see Section 5.5.4).

The improved nightside column is also partially due to a new designation for the reference lower boundary altitude at z = -10, which is presently set to 94.5 km. This is the best representative

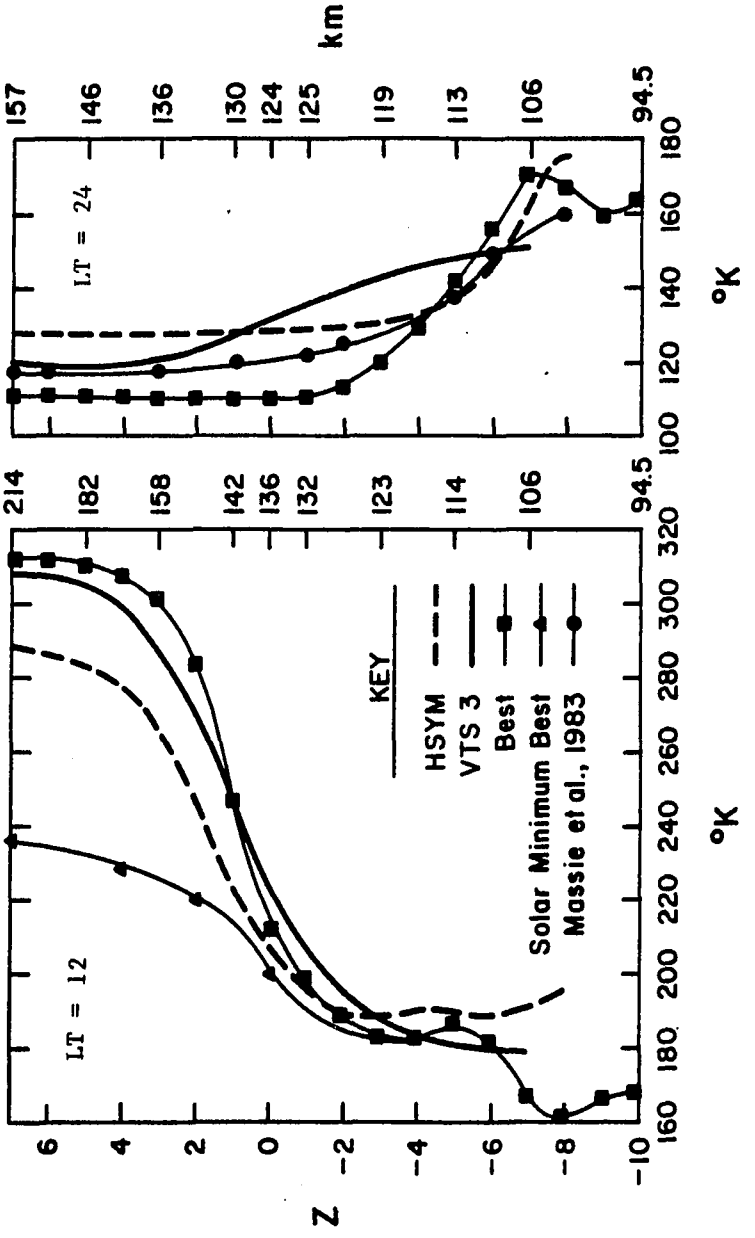


Fig. 5-13a Venus two-dimensional model temperature: Best EUV case.

average (over all SZA) of the values available from the probe data sets of Seiff et al. (1982), the OAD (Keating et al., 1984) and ONMS (Hedin et al., 1983) empirical data sets, the one-dimensional composition models of Massie et al. (1983), and the improved one-dimensional dayside and nightside mean radiative-transfer model calculations. Formerly, this lower boundary was set at 94.0 km.

Improvement of the nightside column must not be developed independently of the dayside composition, which primarily relies upon the drag to regulate O and CO transport to the nightside. Figure 5.13b presents a comparison of the LT = 12 and 24 calculated composition profiles corresponding to this improved terminator wind profile (Fig. 5.12). It is shown that dayside [O] composition is slightly depleted (particularly at z = 4) and that nightside [O] composition is enhanced with respect to VTS3 reference values. As all of the sensitivity studies have shown, there is a delicate balance to be met in the proper global redistribution of the different species and heat.

5.5.3 Detailed Comparisons

Table 5.8 compares number densities ([O], [CO], [CO_2], [N_2], [O], [He], N total) and temperatures at 150 km for the best model simulation with the HSYM and VTS3 reference atmospheres. This level is chosen since it represents the lower boundary (periapsis altitude) of many of the orbiter generated data sets (OAD, ONMS, etc.). An examination of number densities provides a useful check of the character of the entire vertical column, or integrated temperature structure. Dayside and nightside averages are specifically compared (as suggested in Section 5.5.2), rather than profiles at LT = 12 and 24.

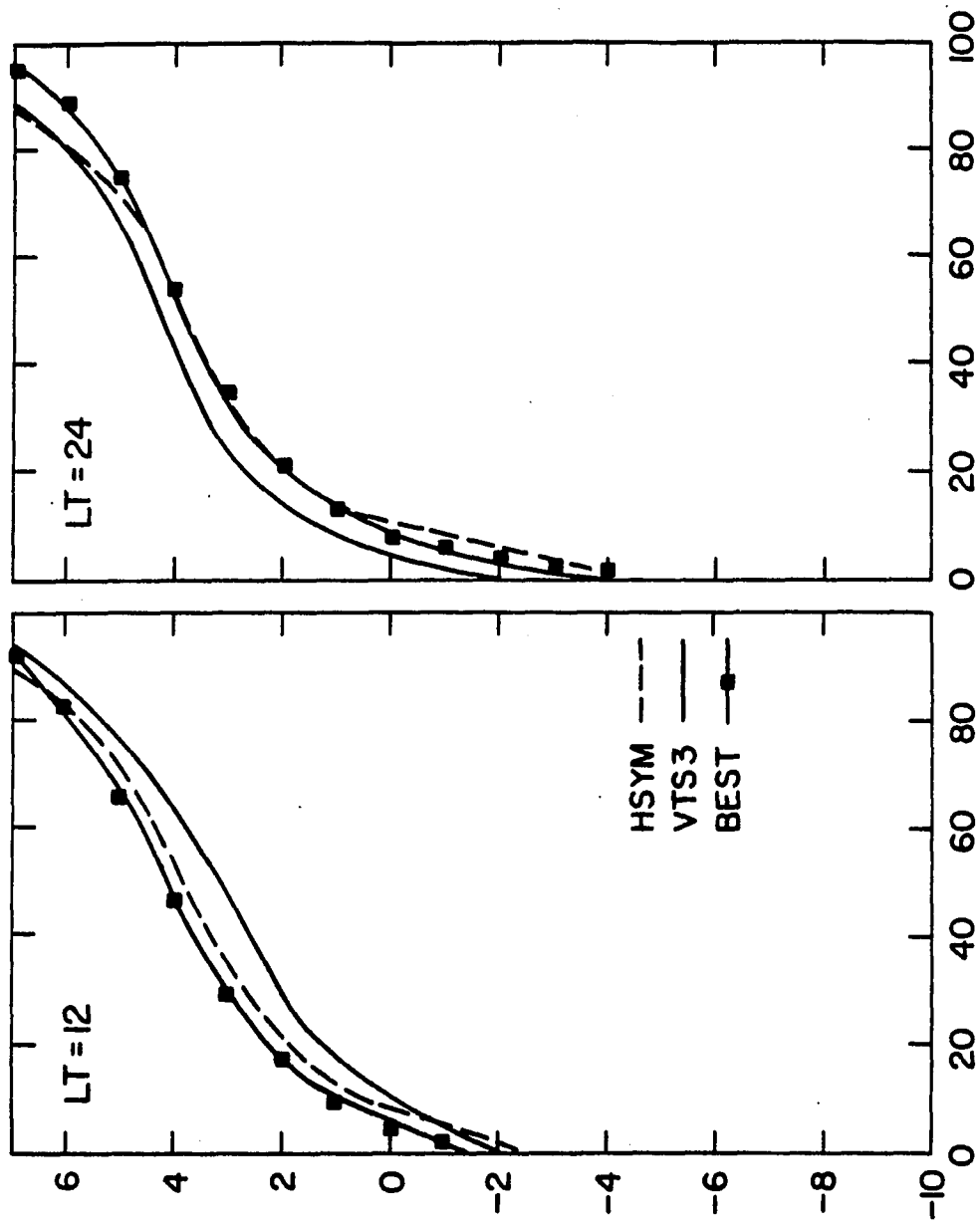


Fig. 5-13b Venus two-dimensional model composition [O] ; Best EUV case.

Table 5.8

Model and Empirical Data Set Comparisons at 150 km

	Hedin et al. (1983) H	H/2D	Keating et al. (1984) K	K/2D	H/K	2-D Model 6/84
Averages Over Dayside (LT = 12-16 hr)						
η_T	1.39(10)	1.01	1.36(10)	0.99	1.02	1.38(10)
η_O	4.70(9)	1.74	3.56(9)	1.32	1.32	2.70(9)
η_{CO}	2.32(9)	1.05	1.80(9)	0.82	1.29	2.20(9)
η_{CO_2}	5.82(9)	0.77	7.13(9)	0.95	0.82	7.52(9)
η_{N_2}	1.01(9)	1.11	1.04(9)	1.15	0.97	9.06(8)
η_{He}	6.39(6)	1.73	4.57(6)	1.24	1.40	3.70(6)
T	271.3	0.97	252.5	0.90	1.07	280
Averages Over Nightside (LT = 19-24 hr or 0-5 hr)						
η_T	1.43(9)	1.15	1.39(9)	1.12	1.03	1.24(9)
η_O	1.12(9)	1.14	1.03(9)	1.05	1.09	9.80(8)
η_{CO}	1.10(8)	1.26	1.09(8)	1.25	1.01	8.73(7)
η_{CO_2}	9.70(7)	0.89	9.90(7)	0.91	0.98	1.09(8)
η_{N_2}	7.63(7)	1.17	9.74(7)	1.50	0.78	6.51(7)
η_{He}	4.41(7)	0.41	3.11(7)	0.29	0.48	1.08(8)
T	119.3	0.98	129.8	1.06	0.92	122.1

It is significant to point out that the Keating et al. (1984) densities are generally more closely matched by the best two-dimensional simulation than the Hedin et al. (1983) empirical model. In particular, the calculated nightside column compares quite well with the HSYM midnight column, for which the z = 7 pressure level rises to 157 km (which is quite close to the HSYM height of 160 km). These average nightside densities ([O], [CO], [CO_2])are within 25%. However, the adopted [N_2] is somewhat smaller than HYSM values suggest. The calculated [He] is also enhanced above observed values. [He] is specifically discussed in Section 5.7.1. Calculated dayside densities are all within 25% of the Keating et al. (1984) reference, except for [O] which lies ~30% below observational levels. The model is apparently being strained to calculate good dayside composition and warmer nightside temperatures simultaneously.

Notable discrepancies are also apparent between the two-reference atmospheres. VTS3 dayside average densities for [O], [CO], and [He] are generally 30-40% larger than those for HSYM. This is consistent with the lower average temperatures exhibited by Keating et al. (1984) on the dayside. The comparison of nightside average densities is quite good for N, [O], [CO], and [CO_2]. [He], however, is roughly 50% of HSYM empirical values. Discrepancies are also present for [N_2]. The Keating et al. (1984) average nightside temperatures are nearly 10°K warmer than the Hedin et al. (1983) values. Contours of the T, u, w, % [O], and % [CO] fields for the best two-dimensional model simulation (on a log-pressure scale) are displayed in Appendix C.3.

5.5.4 Summary of Adjustments of Parameters

Temperature and composition fields in good agreement with Pioneer Venus observations were obtained by careful adjustment of a number of chosen parameters in the two-dimensional model. Table 5.5 outlines the parameter values adopted for the "best" two-dimensional model simulation. The assumed EUV heating efficiency varies from a value of 7% at the highest altitudes, up to 19% at the model lower boundary. An eddy diffusion coefficient <20% of the previous one-dimensional model requirements (see Chapter III) is adopted for the nightside (KMAX = 7.5×10^{6} cm^2/s). However, very little eddy diffusion was found to be necessary for the dayside; a "threshold" level roughly 10% of one-dimensional model values ($K_E(z)$ = 4×10^{6} cm^2/sec) seems appropriate, giving a factor of two variation of $K_E(z)$ from day-to-nightside. The role of eddy diffusion is significantly reduced in the best two-dimensional model simulation compared with the one-dimensional model requirements. Evidently, large scale winds are primarily responsible for controlling composition in the two-dimensional code (see Section 7.3). External cooling appropriate to derive reasonable dayside temperatures is obtained by employing enhanced 15μ cooling from collisionally excited CO_2 (0, 1, 0). A rate coefficient of $k(O\text{-}CO_2)$ = 5×10^{-13} cm^2/sec is adopted. No eddy cooling is incorporated in the "best" model simulation. A Rayleigh friction scheme is also used to parameterize the effects of gravity-wave breaking on the momentum budget of the thermosphere. An exponentially growing drag is specified below a breaking level (ZPBK = 2) at which a time scale for drag (K_{RA} = 1.2×10^{-4} sec^{-1}) is prescribed.

5.5.5 Diagnostics

Figure 5.14 illustrates thermal balance plots for the best two-dimensional simulation at 60° and 120°SZA. The general balances of the contributing terms are quite similar to those of the MED EUV case (see Fig. 5.10). Notice, however, that the absolute magnitudes of the terms are somewhat different. Dayside EUV heating for instance, is nearly 10% smaller at the peak (z = 2) than the MED EUV case value. Fifteen μ cooling is correspondingly weakened to maintain a thermal balance. The principal nightside heating term is still adiabatic compression. Both it and hydrodynamic advection are now increased, particularly at low altitude. This corresponds to the smoother and stronger low altitude generated wind profile, which provides increased warming of the lower nightside thermosphere. The improvement is most visible when the profile shape for the hydrodynamic term (120°SZA) is contrasted between Figs. 5.10 and 5.14.

Figure 5.15 shows % [O] and [CO] term balances over all SZA at z = 0 and 6. Results are quite similar to the MED EUV case values of Fig. 5.11. The hydrodynamic transport source for % [CO] is notably increased on the nightside over earlier LO and MED case levels. This is largely the result of stronger day-to-night winds, now possible due to improved dayside chemistry (Section 5.4.3), and an improved profile for drag.

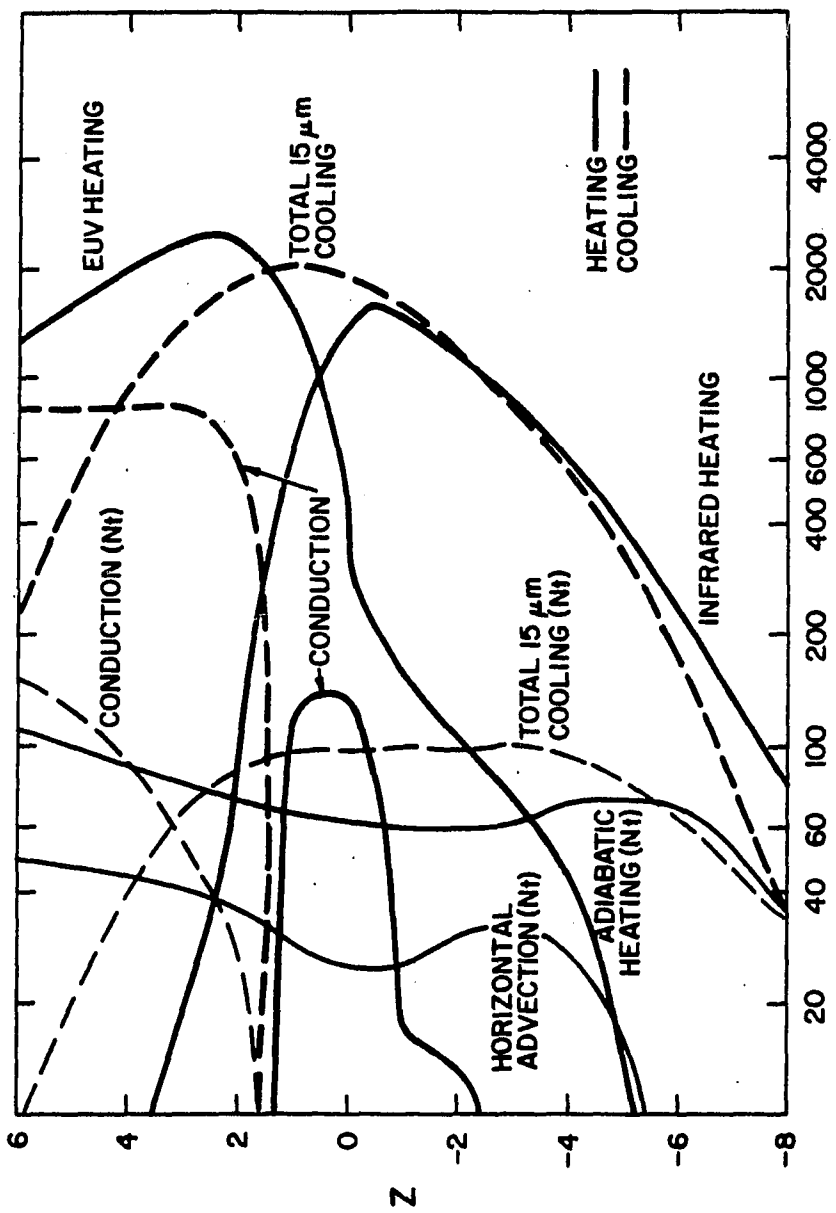


Fig. 5-14 Heating and cooling rates 60° and 120°SZA: Best EUV case.

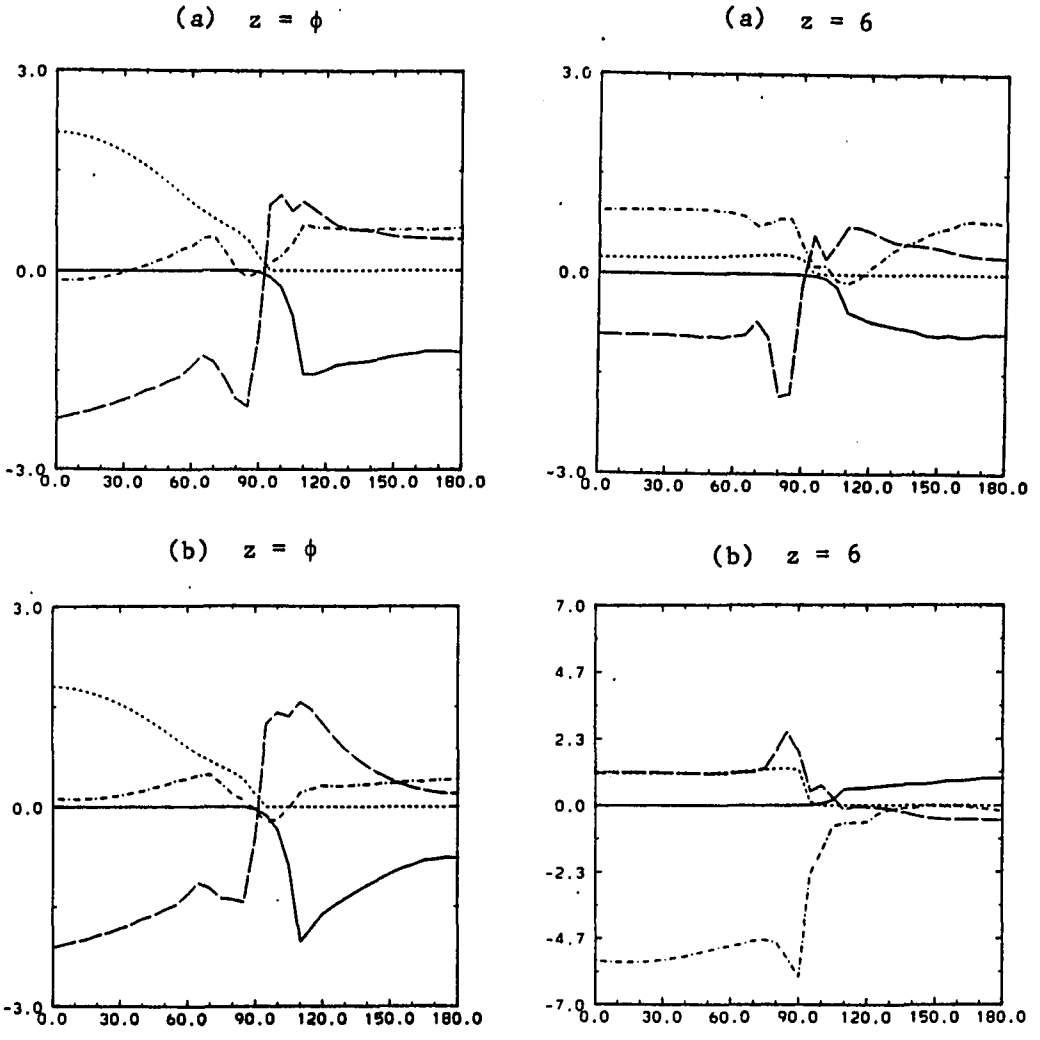


Fig. 5-15 Term balance plots: Best EUV case; (a) [O] composition, (b) [CO] composition.
.--.-- molecular diffusion
_____ eddy diffusion
------ advection
..... photodissociation source

5.6 Applications of a Best Model Simulation

It is appropriate to extend the current best two-dimensional model simulation to study the model time-dependent behavior and to examine its effect in establishing the distribution of a minor neutral species such as helium. An improved generalized Rayleigh friction scheme for drag is also tested. Such tests are useful to provide a further validation of the model's ability to reliably simulate the Venus thermospheric parameters. Predictions are also made as to the character of the thermospheric circulation for various levels of solar activity.

5.6.1 Calculation of Helium

A subroutine has been developed to investigate the time-independent transport of passive scalars using the model-generated wind system and background O, CO, N_2 (empirical), and CO_2 composition. The subroutine has been applied to modeling the vertical and SZA distribution of helium. No chemical sources or sinks are provided for helium within the model. Rather, a density lower boundary condition is specified for the dayside. Correspondingly, a flux lower boundary condition is provided on the nightside (just as for the two-dimensional code) so that material may properly flow out of the bottom.

A reformulated steady state continuity-diffusion equation is solved for the vertical distribution of He, one for each SZA. The nonlinear transport terms provide a communication between the adjacent columns to give a full two-dimensional calculation:

$$\underbrace{\left[\frac{u}{r}\frac{\partial\psi_3}{\partial\theta} + w\frac{\partial\psi_3}{\partial z}\right]}_{M} =$$

$$\underbrace{\left(-e^{z}\tau^{-1}\right)\frac{\partial}{\partial z}\left(\frac{m}{m_{CO_2}}\left(\frac{T_{00}}{T}\right)^{0.25}\left\{\beta_{33}\langle-(C_{11}L_{11}\psi_1 + C_{22}L_{22}\psi_2) + L_{33}\psi_3\rangle\right\}\right)}_{N}$$

$$+ \underbrace{e^{z}\frac{\partial}{\partial z}\left(e^{-z}\frac{K_E(z)}{\bar{H}^2}\frac{\partial\psi_3}{\partial z}\right)}_{O} \qquad (5.6)$$

where:

$\psi_{1,2,3,4}$	=	ψ_{O,CO,He,CO_2} (mass mixing ratio)
z	=	log-pressure vertical coordinate
θ	=	SZA
r	=	distance from center of planet (6200 km)
u	=	horizontal velocity
w	=	vertical velocity (dz/dt)
τ	=	molecular diffusion time scale
m	=	mean mass
m_{CO_2}	=	CO_2 mean mass (44)
T_{00}	=	273°K (at STP for Earth)
$K_E(z)$	=	eddy diffusion coefficient
$\bar{H}$	=	mean scale height

Specific terms are denoted as follows:

$\beta 33\langle\ \rangle$	=	"effective" molecular flux of He through a

moving background gas (see Appendix D for details)

M = hydrodynamic advection

N = molecular diffusion

O = eddy diffusion

[ ] = nonlinear terms

{ } = new code for He

This equation for determining He is developed in a fashion similar to that for O and CO (Dickinson and Ridley, 1972). It is necessary to calculate the flux of a minor species (He) through a moving background gas. A general vertical flux equation for He is needed, for which no assumptions are required concerning the background gas (i.e., the identity of the major specie and its relative flux within the gas must remain unspecified). This is particularly important for Venus' thermosphere, in light of the dominance of [O] above and [CO_2] below 155 km (see Chapter II). Generally, O, CO and CO_2 frictional effects on He are assumed important, and the frictional effects of He on these "major" species are negligible. A general vertical flux equation for the i^{th} specie gas through all the other components of a multi-component fluid is given in Dickinson and Ridley (1972) (Eq. 2.1 from Chapman and Cowling, 1970, p. 344). This general formulation and its nomenclature are now used to develop a molecular diffusion term for He. The "effective" molecular diffusion coefficient matrix ($\underline{\alpha}^{-1}$), and the diffusive operators (L_{ii}) and coefficients (C_{ii}) found in Eq. (5.6) are described in Appendix D.

The minor constituent assumptions made in this simplified derivation limit the calculation of He to those regions where $\psi_3 << \psi_1$ and ψ_2. This is certainly the case for the dayside empirical values (according to Hedin et al., 1983, and Keating et al., 1983). Nightside % [He] values reach 10% at z = +7 at LT = 3. The CO number density is comparable, yet it is of minor importance in its "frictional" effect upon He diffusion. Atomic O, rather, is the major constituent at these nightside levels, and satisfies the above restriction. This permits a time-independent calculation (based on the equilibrium composition and wind fields from the two-dimensional model) to be made. The linear dependence of molecular diffusion on ψ_3 is now possible, due to the expansion of α^{-1}. An implicit calculation results, for which a Crank-Nicholson scheme with upstream horizontal differencing is employed. Terms involving ψ_1 and ψ_2 are known and can be treated explicitly as forcing terms. The He calculation has no effect on mean mass, heating, winds, major composition or any model generated input quantities. The background composition and winds are thus used to drive a calculation of He with no feedback whatsoever on the previous two-dimensional model fields or inputs. Diffusive equilibrium is assumed at the top.

The linear model formulated above responds directly to changes in the dayside lower boundary condition. It will be shown that helium densities can be calculated to match dayside empirical values above 150 km by the adjustment of this He lower boundary condition. A better indicator of model fitting to empirical model data is instead found in the day-night He ratio at a specific altitude (i.e., 150

km). Such a ratio is independent of the dayside lower boundary condition, and is easily derived for empirical model data. It analyzes the ability of the background circulation and molecular and eddy diffusion to simulate the observed day-night distribution of He.

Horizontal diffusion (previously used in the DRM2, two-dimensional code to provide "smoothing" and stability), is not employed in this He calculation. This permits a linear calculation (in ψ_3) to be maintained. However, a slow instability due to nonlinear hydrodynamic advection remains. Its effects are particularly evident near the anti-solar point (ASP) where horizontal velocities are constrained to vanish. Dickinson and Ridley (1972) encountered similar ASP problems due to the lack of horizontal diffusion required for composition balance. Hence, it will be necessary to disregard He values nightward of 165°SZA. Alternatively, values can be used by mechanically smoothing the output from 165°SZA to midnight.

The hydrodynamic model calculations for He are first examined for the profile at 60°SZA, which can easily be compared to previous one-dimensional model profiles (von Zahn et al., 1980; Massie et al., 1983). Data for He densities are available above 140 km ($z = 1$). Notice (in Fig. 5.16) that both one-dimensional profiles and the two-dimensional calculation agree for the diffusion controlled region above $z = 1$. Lower boundary % [He] values (at 100 km) are, however, much different: 7 ppm (Massie et al., 1983); 12 ppm (von Zahn et al., 1980); 40 ppm (1984 two-dimensional code). This suggests, first of all, that the vertical velocities provided by the two-dimensional

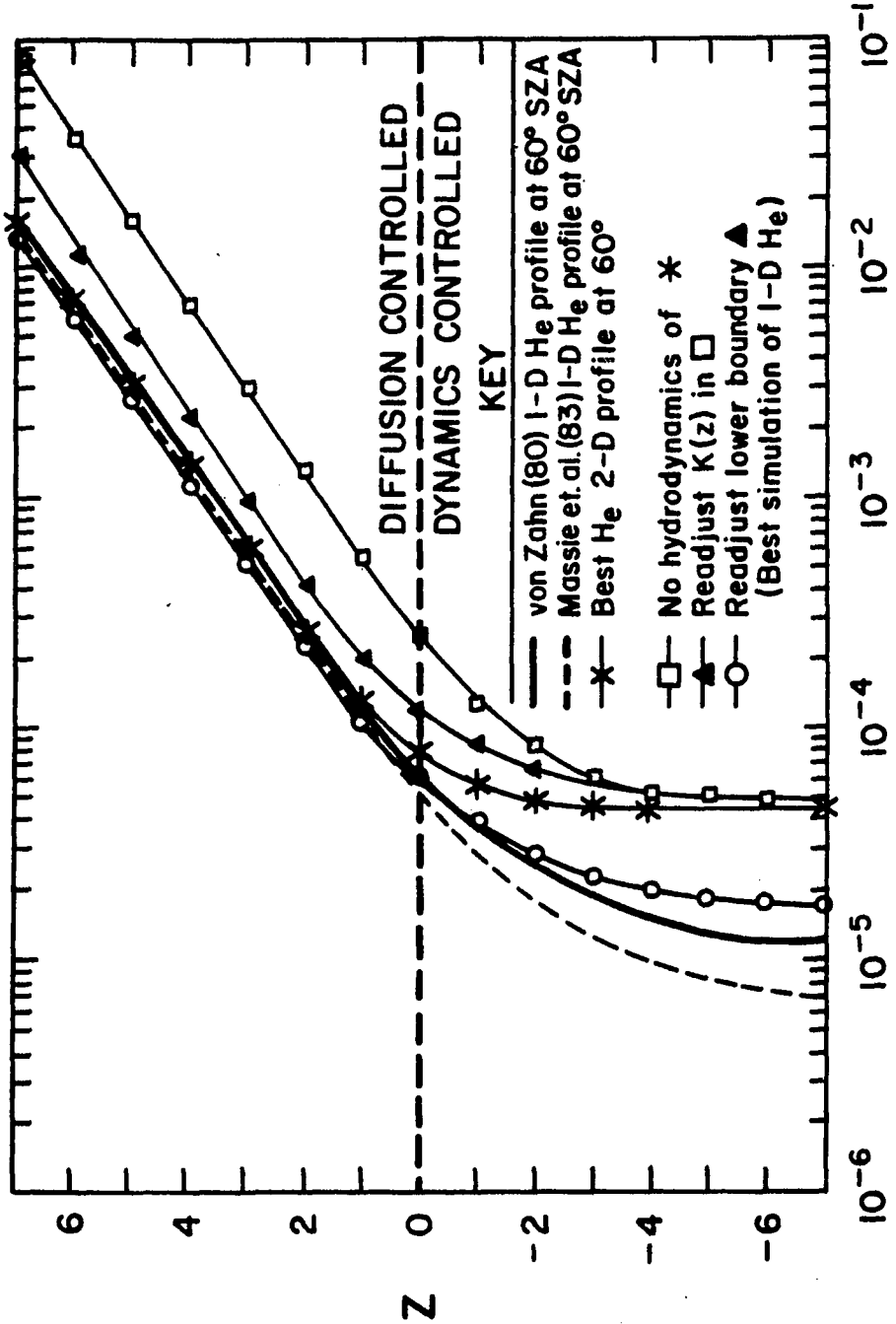


Fig. 5-16 60°SZA model He calculation comparisons.

model give a much different He profile (below z = 0) than the one-dimensional parameterized vertical velocities.

Proof of this fact is illustrated in a series of tests (also shown in Fig. 5.16) which enable the hydrodynamic code to be altered to incorporate earlier one-dimensional model parameterizations for "dynamics." The two-dimensional code winds are first turned off, which causes the upper thermosphere [He] to rise (predictably) by a factor of five. Certainly, large-scale winds are very effective in removing dayside He from the upper thermosphere. Next, the eddy diffusion coefficient is replaced with the parameterization of the Massie et al. (1983) dayside model (see Section 3.2.6). KMAX is now set at 5×10^7 cm^2/s at ZPBK = 0 (134 km). Downward pumping is seen to deplete upper thermosphere He by nearly a factor of three. Finally, resetting the lower boundary to %[He] = 17 ppm lowers the upper thermosphere He to match these earlier one-dimensional model profiles.

These large-scale winds provide a much different compositional structure for He within the dynamically controlled region (below z = 0) than does eddy diffusion. The fact that the two-dimensional code can be reformulated to reproduce the one-dimensional He profiles is a further confirmation of this effect. He is the most sensitive (of all the species so far modeled) to large-scale wind effects. Yet, O and CO should also respond similarly below z = 0. The most important implication of this short study at 60°SZA is that self-consistently calculated winds are indispensible for a proper calculation of transported species, even on the dayside. Nightside compo-

sition has previously been shown to be dominated by this day-to-night transport (DRM1; Stewart et al., 1980; Massie et al., 1983).

Two-dimensional model He profiles at LT = 12 and 23 hours are shown in Fig. 5.17. Recall that He values at the ASP are not valid in this linear model calculation. Values at 165°SZA are instead employed to represent near midnight conditions. Furthermore, the nightside comparisons are made with HSYM and VTS3 empirical profiles, at the "morningside peak" at LT = 3 A.M. It is assumed that the two-dimensional geometric boundary condition applied at midnight (requiring that horizontal winds vanish) corresponds closely to those actual atmospheric conditions at the He peak, where the horizontal flow stagnates (see Fig. 3.9). A more appropriate comparison of calculated and empirical He profiles near midnight is thus obtained.

Figure 5.17 illustrates a very good comparison of calculated and empirical model He fractional number densities for dayside conditions above z = 0. VTS3 and HSYM values at the top range from 1% to 1.7%, respectively. The calculated profile generally falls between these two limits above z = 0, with a slight depletion near z = 2 (150 km). The calculated He profile below z = 0 departs markedly from the VTS3 empirical model predictions. Recall that eddy diffusion is also employed in the derivation of low altitude VTS3 empirical model values (below ONMS observations). The influence of the large scale winds in the two-dimensional code maintains a much different He composition profile in the dynamically controlled region below z = 0, than does the eddy diffusion parameterization used by Hedin et al. (1983).

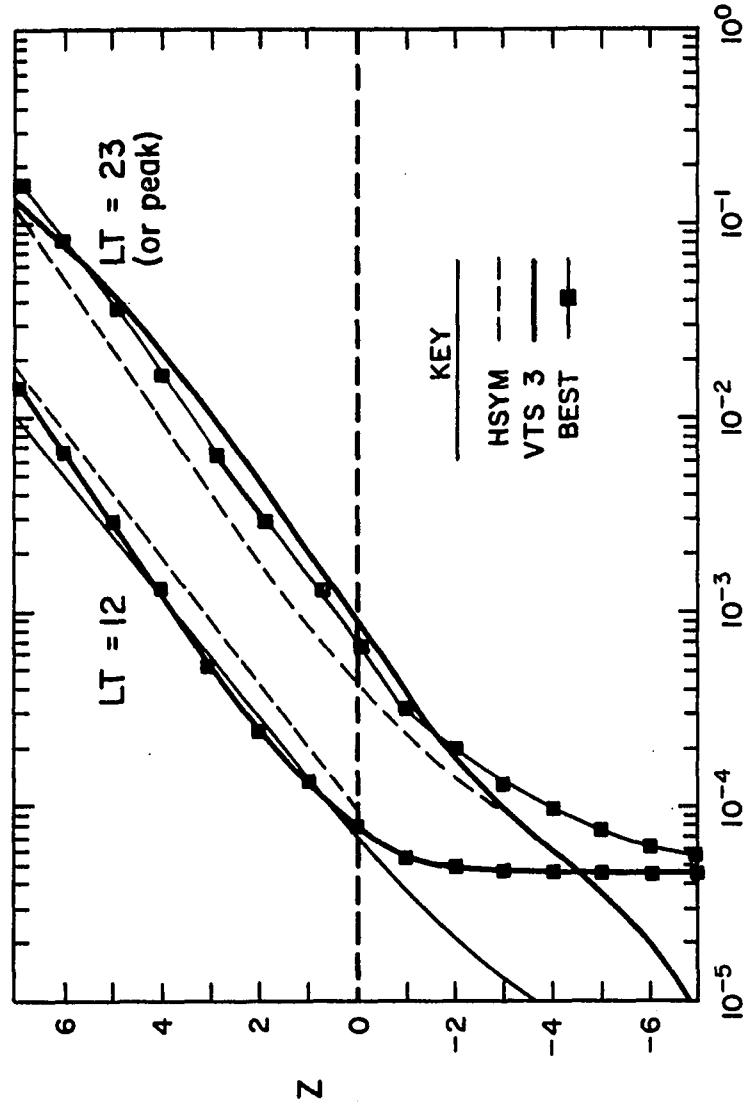


Fig. 5-17 Venus two-dimensional model composition [He]: Best EUV case.

The calculated nightside mixing ratio profile does match the VTS3 reference in the upper thermosphere quite well. However, the day-night ratio of [He] at 150 km is calculated to be 250:1, while the VTS3 and HSYM density ratios are approximately 100:1 (more than a factor of two smaller). Thus, a larger nightside [He] bulge is calculated than is realized in the actual thermosphere. Slower wind profiles (adopted from two-dimensional cases other than the best model simulation) would reduce this day-night ratio slightly at the expense of seriously cooling the nightside column. Evidently, reasonable large-scale winds are simulated, yet other processes are needed to improve the nightside He calculation. Exospheric transport (returning He to the dayside) was not found to be important (Mayr et al., 1980). The observed nightside He bulge suggests that a super-rotation of the upper atmosphere winds is necessary for the calculation of the proper phase (and possible amplitude) of the observed [He] peak at LT = 3 A.M. (Mayr et al., 1980). The two-dimensional model cannot adequately deal with this problem. These and other suggestions will be addressed in Chapters VI and VII.

5.6.2 Solar Minimum Calculation

Mariner 10 observations for Venus temperatures are presently available for solar minimum conditions (solar cycle 20). It is thus useful to explore the two-dimensional model response of the T, u, w, % [CO], %[O], and % [He] fields to variations in solar cycle. The primary solar cycle changes are assumed to occur in the EUV fluxes shortward of 2000Å. All other inputs and eddy or cooling parameteri-

zations are retained as before. Heroux and Hinterregger (1978) fluxes (similar to values of DRM1 and DRM2) are now adopted for the specific examination of solar minimum conditions (F10.7 = 80×10^{-22} Wm^{-2} Hz^{-1}). The best two-dimensional model simulation (Section 5.5) will be used as a reference for comparison with solar maximum conditions.

The incorporation of these solar minimum fluxes results in the reduction of EUV heating by approximately a factor of two. IR heating, important below z = 0, remains virtually unchanged. Corresponding 15μ cooling is also reduced (to 80% of previous model values) in order to drive the thermal budget toward radiative equilibrium. Appendix C.4 illustrates equilibrium contours of composition, temperature, and wind fields calculated for this solar minimum test. Notice (see also Fig. 5.13a) that dayside exospheric temperatures approach 240°K at LT = 12, which is a reduction of nearly 70°K. The rest of the dayside (z > 0) is also cooled. These newly calculated values fall within the range of exospheric temperatures specified from Mariner-10 Lyman-α data (Anderson et al., 1975). The temperature gradient across the z = 1 dayside region and across the terminator is considerably weakened compared to the solar maximum case.

The alteration of the dayside temperature structure results in a new global wind and composition distribution, giving a slightly different nightside thermosphere. A new equilibrium thermal balance about the planet also occurs. Specifically, cooler dayside temperatures drive weaker day-to-night winds, which are reduced by nearly 30-35 m/s at the terminator. This has the effect of further isolating the nightside, for which less dayside heat is transported and night-

side adiabatic heating is diminished. Nightside exospheric temperatures are seen to be reduced by 6°K to 105°K. The corresponding nightside column collapses to approximately 155 km at z = 7.0 (a reduction of 2 km). Atomic-O on the nightside is also reduced (<2%) due to the diminished winds. Overall, the response of the nightside composition and temperature is quite small.

Generally, the thermal structure remains unchanged below z = 0, with the maximum response instead felt by dayside temperatures above z = 0 where EUV heating dominates. Nightside fields are seen to change very little. This is likely the result of the confinement of changes in the heating to the upper thermosphere. It appears that composition is largely transported at lower altitudes along streamlines for which the wind structure does not greatly change. Such a signature is also revealed by a new helium calculation based on the background composition and temperature fields for this solar minimum case. A day-night helium ratio at 150 km is now calculated to be 200:1, which is very similar to the the previous best model simulation. Apparently, the Venus thermospheric circulation is only slightly changed by a factor of two reduction in EUV heating. CO_2 15μ cooling may be an effective buffer against temperature perturbations. More will be said concerning this rather weak thermospheric response to solar cycle variability in Chapter VII.

5.6.3 Time-Dependent Behavior

The time-dependent behavior of the two-dimensional code is now examined, with particular attention given to the response of the out-

put fields to a perturbation heating event. A solar flare event (or sudden increase in the solar EUV flux) is crudely simulated by an instantaneous application of the solar maximum fluxes within the previously described solar minimum run. It is useful to watch the temporal development of the calculated composition, wind and temperature fields to learn which fields achieve their equilibrium values most rapidly. This examination is also a diagnostic tool to further study the details of the feedback operating among the temperature, composition, and wind fields.

A progression of dayside temperature profiles is examined over 30-minute intervals for the first three hours of model integration (see Fig. 5.18). It is observed, from comparison of all model output fields, that the upper dayside temperatures approach their equilibrium values the fastest. The heating responsible subsequently drives terminator horizontal winds that come to equilibrium within the same three-hour period. These winds, in turn, control the nightside temperature distribution by regulating the importance of thermal transport and adiabatic compression. Eventually it becomes apparent that time scales on the order of one Earth day are required for the nightside temperatures to come to equilibrium.

Earlier LO, MED, and best model simulation cases indicate that the redistribution of composition slows down the above temperature-wind equilibrium process. Increasing nightside composition (for stronger winds) occurs in concert with increasing nightside temperatures. The subsequent effect is to reduce the terminator winds that may have given rise to the expanding nightside column just described.

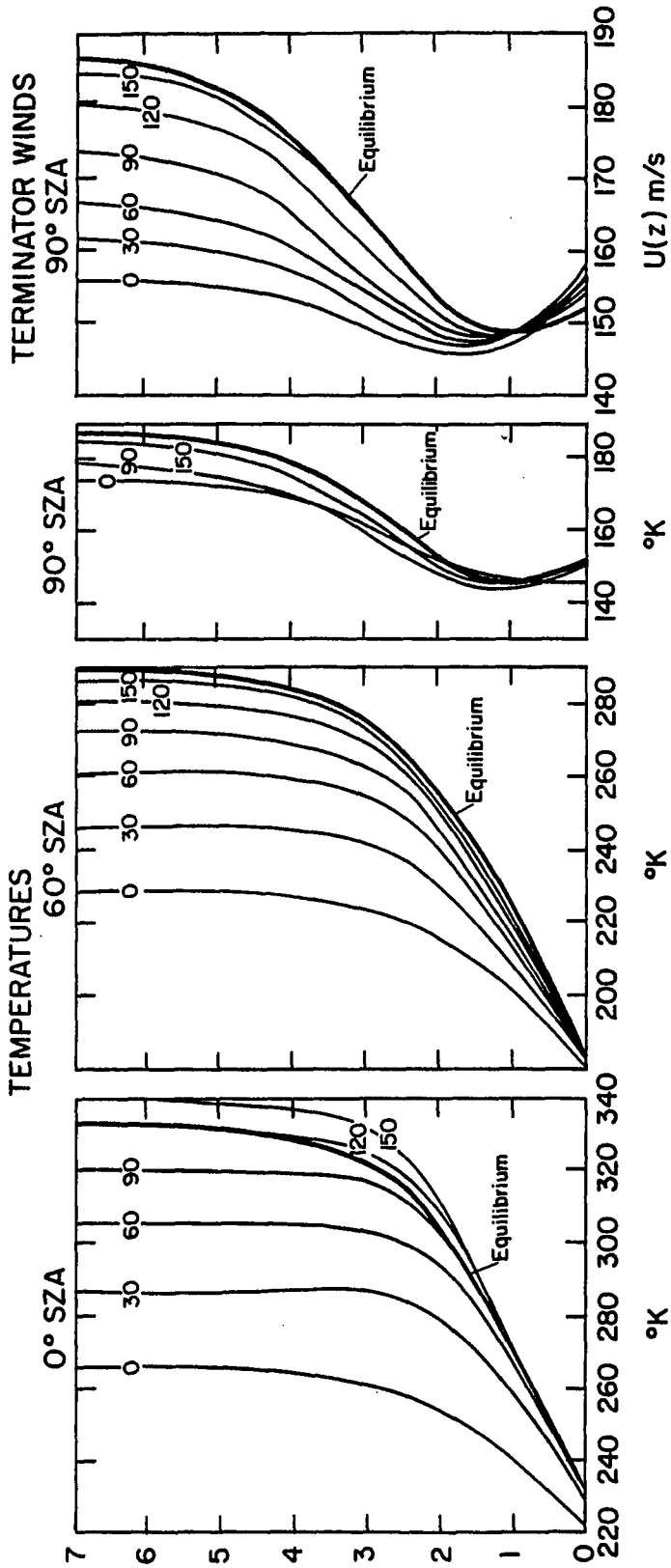


Fig. 5-18 Two-dimensional model time dependent behavior

Conversely, decreasing nightside composition and temperatures (for slower horizontal winds) strengthens the terminator winds, in an effort to restore the nightside column and hydrodynamic balance. Reduced dayside O (due to stronger winds) will initially be seen with diminished dayside temperatures. These changes will operate to weaken the day-to-night circulation to bring about equilibrium. However, with depleted dayside O, 15μ cooling is also reduced. This gives rise to warmer temperatures, an expanded dayside column, and a restoring of stronger terminator winds. The familiar cooling effect of stronger winds on dayside temperatures is mitigated by the warming effect of weakened $O\text{-}CO_2$ cooling. Generally, stronger winds reduce dayside composition and build up nightside composition.

Equilibrium at low altitudes (100 km) is approached very slowly (>>1 Earth day). The "turn-on" of solar maximum fluxes does not greatly alter low altitude winds ($z<0$) or temperatures. However, earlier drag tests were specifically conducted to observe changes in temperatures and composition as low altitude winds were permitted to blow uninhibited (Section 5.5). Recall that heat was redistributed over all SZA by these winds, and resulted in the development of nearly horizontally constant thermal structure at 100 km. Composition was very slowly readjusted and was particularly influential in building up the nightside column. These case runs were integrated for 5-6 Earth days before near equilibrium values could be identified. Feedback among composition, temperature and winds fields is thus tied to the time scale for hydrodynamics at each pressure level.

5.6.4 Generalized Rayleigh Friction Scheme for Drag

Formerly, in the "best" model simulation of Section 5.5, a vertical profile of Rayleigh friction was derived to establish an appropriate time-scale for needed momentum deposition (caused by breaking gravity waves). Calculated composition and temperature fields were derived to closely match Pioneer Venus observations, thereby constraining the wind fields. However, no real mechanism was advanced to permit such an interaction of breaking gravity waves with the mean flow.

An improved scheme for wave-drag is now investigated, which adopts parameters specifically related to gravity wave characteristics. Weinstock (1982, 1983) described a plausible connection between momentum-deposition and small-scale diffusion for the terrestrial mesosphere, where dissipation by turbulence generally exceeds molecular dissipation of gravity waves. Section 4.4.3 presents a parameterization that makes use of this connection, where K_{RA} is now proportional to K_Z and $K_E(z)$. The parameterization of Eq. (4.8) is easily incorporated into large-scale circulation models of the type used by DRM1 and DRM2 for the Venusian mesosphere (below 140 km).

Its application now requires a careful examination of a few needed assumptions. Breaking gravity waves "saturate" when they are converted into random waves or fluctuations. These small-scale fluctuations then cause diffusion and momentum deposition. Such a process is very complicated and highly nonlinear, unless a single wave is considered. Weinstock (1982) limits his parameterization to a

linear model describing a single wave. This requires that a single gravity wave (averaged over space and time) most representative of all the wave-like structures so far observed be adopted for Venus' thermosphere. The scheme is applicable only above a "saturation" or breaking level (turbopause), above which the wave amplitude ceases to grow. Exponential decay below that level, of the type used in development of the $K_E(z)$ profile, is acceptable. In addition, incompressibility constrains the vertical wavenumber (or vertical wavelength λ_z) ($K_z = 2\pi/\lambda_z$) such that $2K_zH>>1$. Finally, $K_E(z)$ is approximately equivalent to isotropic and temporally-averaged vertical diffusivity, D_{ZZ}, which must be less than 10^7 cm^2/sec.

The previously prescribed SZA variation of $K_E(z)$ needed for eddy diffusion is now combined with an adjustment of K_z (subject to the above restrictions) in order to derive K_{RA} similar to that of the "best" model simulation. The goal is to find if reasonable K_z values, corresponding to Seiff et al. (1982) probe observations, can be used to provide sufficient drag. Recall that these probe observations, which were generally confined to the high altitude wave-like perturbations, had vertical scales of roughly 5-15 km. Two-dimensional model studies have so far indicated that the turbopause is in the region $0<z<+2$. Dayside mean scale heights in this region are approximately 4-5 km, which requires that $\lambda_z<<50$ km. Likewise for the nightside, $H \approx 3$ km, so that $\lambda_z<<38$ km is required. Weinstock's (1982) requirements for K_z (or λ_z) are compatible with Pioneer Venus observations.

λ_z is specifically adjusted to give reasonable drag for a proper redistribution of composition and heat about the planet. It is assumed first that λ_z is constant with SZA. There is no restriction, however, that would prohibit different scales of gravity waves on the day and nightsides. Thus, a second test is made for a SZA variation of λ_z.

Figure 5.19 shows LT = 12 and 24 profiles for temperature (as well as corresponding terminator wind profiles) for the above two assumptions for λ_z. Specific vertical wave scales are chosen to give K_{RA} values close to those previously derived by the Rayleigh friction parameterization. Uniform K_z is given (curve A) for $\lambda_z \approx 16$ km. Notice that dayside drag is reduced, permitting quite strong winds (U > 220 m/s) at the terminator. Once onto the nightside when KMAX = 7.5×10^6 cm^2/sec, drag is nearly doubled (K_{RA} = 1.25×10^{-4} sec^{-1}) for which winds are quickly diminished. A sharp gradient in horizontal winds across the terminator is generated. From the temperatures profiles at LT = 12 and 24, it is evident that the isolation of the nightside is still largely maintained without considerable warming of the upper dayside thermosphere. However, dayside composition is strongly depleted below HSYM observed values by the strong dayside winds (not shown).

An improvement for the dayside-to-nightside wind structure is possible if λ_z = 12.5 km on the dayside and $\lambda_z \tilde{=}$ 16 km on the nightside. This suggests that larger amplitudes are possible on the nightside, possibly due to a smaller static stability. The amount of additional forcing needed to drive unstable waves (breaking) and drag

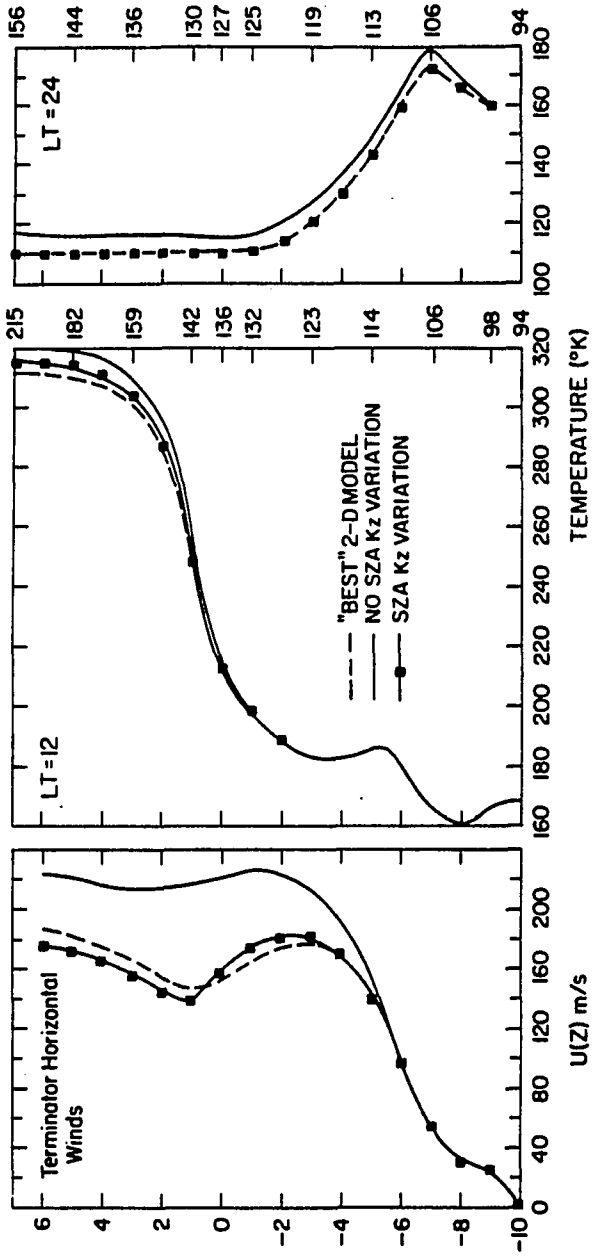


Fig. 5-19 Generalized Rayleigh friction results; (a) terminator winds, (b) LT = 12 and 24 temperature profiles.

is conceivably reduced for the nightside, such that a SZA variation of λ_z is possible. It is significant to see that terminator winds similar to those derived for the "best" model simulation are reproduced ($U \leq 210$ m/s), which permit sufficient O and CO to be retained on the dayside. Such winds also enable thermal advection and nightside adiabatic heating to be reduced, thereby lowering upper nightside temperatures toward observations.

The Generalized Rayleigh Friction scheme is preferable to the Rayleigh friction parameterization used earlier to estimate wave drag. Certainly, a degree of consistency is now present among all eddy-related parameterizations, since similar $K_E(z)$ values are adopted for all. This is possible for drag, now that the Weinstock (1982) hypothesis linking small-scale diffusion and momentum-deposition is adopted. Notice that $\lambda_z \leq 16$ km is required for the development of a reasonable eddy drag parameterization giving a good match of calculated composition and temperature fields to observations. This representative wave scale is probably large enough to permit propagation up to $z = 0$ without significant frictional dissipation. Generalized Rayleigh friction is a useful first step in the development of a realistic parameterization for wave-mean flow interaction in Venus' mesosphere.

This parameterization, however, is limited to a single wave for which nonlinear interactions are neglected. Its application to the Venus mesosphere ($z \leq 0$) is certainly an oversimplification. Further improvements in the development of gravity-wave breaking models for Venus' thermosphere awaits the acquisition of measured wind

profiles over 60-150 km, as well as specific wave phase speeds and length scales. Schubert and Walterscheid (1984) establish that static stability and wind structure are critical parameters to determine the vertical propagation of ground-generated and cloud-generated gravity waves into the Venus thermosphere. Present estimates of horizontal winds above 60 km are insufficient to warrant the development of a detailed gravity-wave breaking model at this time. Wave drag may also arise from in situ instability of the mean flow, independent of gravity waves propagating upward from below.

CHAPTER VI

VENUS THREE-DIMENSIONAL MODEL DEVELOPMENT AND RESULTS

6.1 Introduction

6.1.1 Need for Full Three-Dimensional Code

The need for a fully self-consistent three-dimensional coupled chemical-dynamical model of the Venus thermospheric circulation has been suggested earlier by Pioneer Venus observations (Chapter II) and modelling work (Chapters III and V). It is apparent that asymmetric signatures in composition (He, H), temperatures, and airglow require that a super-rotating zonal wind component (in addition to the mean subsolar-to-antisolar flow) be incorporated into the global scale circulation. Retrograde winds in excess of 50-75 m/s (independent of latitude and altitude) are estimated to account for the observed phases and amplitudes of species and temperatures (Mayr et al., 1980, 1984).

The two-dimensional model (described and used previously in Chapters V and VI) is not capable of examining such asymmetries, since it uses an altitude-SZA dependent geometry that explicitly defines a symmetric circulation. Lateral boundary conditions are also invoked to artificially require that horizontal flow vanish at noon and midnight. Such a geometry is somewhat specialized to the unique sub-

solar-to-antisolar circulation of Venus that is dominant. A more general code and model geometry is needed.

6.1.2 Basic VTGCM Goals

The treatment of the Venus thermospheric circulation in this thesis using the Venus TGCM (VTGCM) is of limited scope. The principal goal is to reproduce the symmetric two-dimensional model fields calculated previously in the "best" model simulation. This is accomplished by using a "symmetric" version of the terrestrial TGCM (Dickinson et al., 1981, 1984) adapted for Venus. Two-dimensional model composition, model inputs, new parameterizations, and new rate coefficients are incorporated into the VTGCM. The primary purpose of using an independent model is to validate the two-dimensional model calculations, and to establish a three-dimensional benchmark for further model development. Further studies designed to simulate observed asymmetries in temperature and composition fields will then be possible, once a self-consistent scheme for calculating composition is developed for the VTGCM. However, super-rotation effects on temperature are examined using the present VTGCM code.

6.2 Venus TGCM Model Description

6.2.1 Adaptation from Terrestrial TGCM

The NCAR TGCM has been used to study the terrestrial thermospheric structure and circulation, and is based on the pressure coordinate primitive equations of lower-atmosphere dynamic meteorology.

The physical processes incorporated into the model, however, are those appropriate to thermospheric dynamics (Dickinson et al., 1981). Specifically, the basic framework of the NCAR fourth-order general circulation model (Washington and Williamson, 1977) is modified to account for fast vertical diffusion of heat and momentum at thermospheric heights.

The Dickinson et al. (1981) TGCM was first developed on a 5°×5° grid in latitude and longitude, with 24 constant pressure surface layers in the vertical (z = -7 to z = +5) extending from approximately 90 to 500 km altitude. Independent variables are t (time), ϕ (latitude), λ (longitude), and log pressure ($z = \log_e(P_0/P)$). Three prognostic (thermodynamic, eastward momentum, and northward momentum) equations are solved to obtain steady-state solutions for the following dependent variables: u (eastward velocity), v (northward velocity) and T' (perturbation temperature). Diagnostic hydrostatic and continuity equations are also solved for Φ' (perturbation geopotential) and w (vertical motion) following each model time step of 5 minutes. The model requires nearly 10 minutes of CRAY 1 computer time per simulated Earth model day.

This early version of the TGCM (Dickinson et al., 1981) required that composition be specified at each pressure level, latitude, and longitude. Those relative number densities of the different chemical species were obtained from the MSIS (mass spectrometer and incoherent scatter) empirical model of Hedin et al (1977a,b). Mean molecular mass was thus obtained for the hydrostatic equation, and used to define the gas mixture molecular conductivity, viscosity, spe-

cific heat and mean scale height. This model also calculated temperature departures from the MSIS reference global mean temperature profile, specified for particular geophysical conditions. Such a mean profile was assumed to be representative of a first-order balance between global mean vertical heat conduction and net radiative heating. Other parameterizations are incorporated into the model to describe ion drag and auroral (high latitude) heat and momentum processes.

One of the primary goals of this early TGCM code (Dickinson et al., 1981) was to make comparisons with the results of earlier two-dimensional models (Dickinson et al., 1975, 1977; Roble et al., 1977) for identical or similar geophysical conditions and inputs. Such a study not only enabled the two-dimensional model behavior to be validated, but it also provided a necessary framework upon which further TGCM model runs could be built. Magnetospheric convection (Roble et al., 1982) and self-consistently calculated composition (Dickinson et al., 1984) were later incorporated.

The Dickinson et al. (1981) TGCM, employing empirical composition, is now adapted for Venus conditions to simulate the circulation and temperature structure of the Venusian thermosphere. The basic computational framework of the TGCM is retained, which enables large scale winds and three-dimensional fields to be calculated. However, new inputs (including solar EUV and UV fluxes, cross sections, and heating efficiency rates) and physical processes (eddy drag, 15 μm cooling) are incorporated into the model to reproduce the Venus two-dimensional symmetric fields previously calculated by the "best" model

simulation (see Chapter V). VTGCM symmetry is specified by means of model inputs (about the equator and with respect to the noon-midnight axis) to match two-dimensional model geometry.

An input data set is supplied to the VTGCM code that provides all the externally calculated fields and parameters, including perturbation heating, composition, viscosity, specific heat, thermal conductivity, and mean 15 μm cooling and mean reference temperatures. Solar maximum fluxes (corresponding to the 78348 day reference for F10.7 ≈ 200 Wm^{-2} Hz^{-1}) and updated cross sections, according to the two-dimensional model (Section 4.2), are also employed by the VTGCM. The scheme for EUV and UV heating is that used by Nagy et al. (1980), now modified to incorporate EUV efficiency (7-19%), UV efficiency, and airglow loss as specified earlier for the two-dimensional model (Sections 4.2 and 5.5). Wavelength bins are defined for broader intervals in the three-dimensional code, making the model heating quite similar, but not identical to the "best" two-dimensional case. Slant IR heating, however, is identical, since it is adopted from the same IR data set (Section 5.5). Various constants, including the reference pressure (P_0 = 5×10^{-3} μbar), gravity (g = 840 cm^2/s), specific heat (c_p), molecular viscosity (K_M), and thermal conductivity (K_T), are now prescribed for Venus. K_T and K_M values for CO and CO_2 corresponding to temperatures $\leq$300°K are interpolated from the tables of Hilsenrath (1961). A slightly different mixed gas prescription for K_T and K_M (according to Banks and Kockarts, 1973) is used for the three-dimensional code. Finally, %[O] and %[CO_2] (from the two-dimensional code) are explicitly buffered to the VTGCM to

facilitate the proper incorporation of the compositional dependence of the 15 μm cooling parameterization.

The physical parameterizations added to the model include eddy drag, 15 μm cooling, and EUV efficiency. Parameters of the "best" two-dimensional model simulation (see Table 5.5) are used. However, eddy diffusion is neglected, since empirical composition is invoked in lieu of a self-consistent calculation of composition. The VTGCM model is now limited to a calculation of T, u, v, w, and Φ fields.

Other processes and inputs unique to the terrestrial thermosphere are neglected. In particular, ion drag terms are all eliminated, since Mayr et al. (1980) established that the effect of such drag upon the neutrals was unimportant for altitudes below 200 km. Coriolis terms are also negligible, due to the extremely slow planetary rotation rate (see Chapter I). Presently, solar heating alone is used to drive large scale winds. The terrestrial code pertaining to auroral heating is thus removed. This is possible due to the distinctly different Venus energetic particle environment that is the result of its very weak magnetic field (Russell et al., 1979). As a result, no external momentum forces are prescribed upon the neutrals (i.e., magnetospheric convection). The VTGCM code is thus set for calculations similar to the two-dimensional ones, using nearly identical inputs and parameterizations.

6.2.2 Governing Equations

The Venus time-dependent equations for T', u, and v (which are solved to steady state) are outlined below. Primes denote departures from global mean reference values.

T': Thermodynamic Equation

$$\frac{\partial T'}{\partial t} = \underbrace{\frac{ge^z}{P_0 c_p}\frac{\partial}{\partial z}\left(\frac{K_T}{H}\frac{\partial T'}{\partial z}\right)}_{A} - \underbrace{w\left(S + \frac{RT'}{C_{p_m}} + \frac{\partial T'}{\partial z}\right)}_{B}$$

$$\underbrace{- [\underline{V}\cdot\underline{\nabla}T']}_{C} + \underbrace{\frac{Q'}{c_p}}_{D} - \underbrace{\frac{C'}{c_p}}_{E} \qquad (6.1)$$

where:

z = log pressure ($z \equiv \log_e(P_0/P)$)

P_0 = 5×10^{-6} mbar (reference pressure)

ϕ = latitude

λ = longitude

h = altitude ($h \equiv 100$ km + h')

Φ = geopotential

T_0 = global mean reference temperature

T' = perturbation temperature

T = total temperature ($T \equiv T' + T_0$)

r = radial distance to center of planet (~6200 km)

u = zonal velocity

v = meridional velocity

w = vertical motion (dz/dt)

g = acceleration of gravity (840 cm/s^2)

c_p = specific heat at constant pressure

K_T = thermal conductivity

K_M = viscosity

S = static stability ($\partial T_0/\partial z + RT_0/c_p m$)

H = mean pressure scale height

R = universal gas constant

m = mean molecular mass

Q' = perturbation heat source (erg/gm s)

C' = perturbation 15 μm cooling (erg/gm s)

K_{RA} = Rayleigh friction (or generalized Rayleigh friction) coefficient (sec^{-1})

The terms above represent:

A = thermal diffusion

B = adiabatic heating/cooling

C = hydrodynamic advection

D = IR and EUV heating (perturbation)

E = 15 μm cooling (perturbation

$\underline{V}\cdot\underline{\nabla}$ = $u/r\cos\phi\ \partial/\partial\lambda + v/r\ \partial/\partial\phi$

u: Momentum Equation

$$\frac{\partial u}{\partial t} = \underbrace{\frac{ge^z}{P_0}\frac{\partial}{\partial z}\left(\frac{K_M}{H}\frac{\partial u}{\partial z}\right)}_{F} + \underbrace{\frac{uv}{r}\tan\phi}_{G}$$

$$- \underbrace{\left[\underline{V}\cdot\underline{\nabla}u + w\frac{\partial u}{\partial z}\right]}_{H} - \underbrace{\frac{1}{r\cos\phi}\frac{\partial\Phi'}{\partial\lambda}}_{I} - \underbrace{K_{RA}\cdot u}_{J} \qquad (6.2)$$

where:

F = molecular diffusion

G = curvature term

H = hydrodynamic advection terms

I = geopotential gradient force

J = wave or eddy drag

v: Momentum Equation

$$\frac{\partial v}{\partial t} = \underbrace{\frac{ge^z}{P_0}\frac{\partial}{\partial z}\left(\frac{K_M}{H}\frac{\partial v}{\partial t}\right)}_{K} - \underbrace{\frac{u^2}{r}\tan\phi}_{L}$$

$$- \underbrace{\left[\underline{V}\cdot\nabla v + w\frac{\partial v}{\partial z}\right]}_{M} - \underbrace{\frac{1}{r}\frac{\partial \Phi'}{\partial \phi}}_{N} - \underbrace{K_{RA}\cdot v}_{O} \qquad (6.3)$$

where:

K = molecular diffusion

L = curvature term

M = hydrodynamic advection

N = geopotential gradient force

O = wave on eddy drag

A leap-frog scheme is used to transform these equations into a set of difference approximations for each latitude slice at a particular altitude. Vector operations on the CRAY 1 permit computation over all

longitude bins simultaneously. Spherical geometry is again prescribed within this discrete 5×5° grid, to provide uniformity in latitude and longitude. The log-pressure scale is set to cover z = -7 to z = +5.

Total temperature is derived as the sum of the adopted global mean reference temperature profile and calculated perturbation temperatures. Hydrostatic and continuity equations appropriate to this model are as follows:

Hydrostatic:

$$\frac{\partial \Phi'}{\partial z} = \frac{R(T' + T_0)}{m} = \frac{RT}{m} \qquad (6.4)$$

where

$$d\Phi' = g(h)dh'$$

Continuity:

$$\frac{1}{r\cos\phi}\frac{\partial}{\partial \phi}(v\cos\phi) + \frac{1}{r\cos\phi}\frac{\partial u}{\partial \lambda} + e^{z}\frac{\partial}{\partial z}\left(e^{-z}w\right) = 0 \qquad (6.5)$$

The preceding equations and computational scheme require that certain filtering, smoothing and time step assumptions be invoked for numerical stability. Centered finite-difference approximations give rise to linear instability, unless the Courant-Friedrich-Levy criterion is satisfied. The time step is thus limited by the least time required for a disturbance to travel between any two grid

points. At present, a time step of ≈300 sec is found to be adequate. Likewise, instability is also a problem at the poles, where the distance between longitudinal grid points becomes increasingly small. The resulting small time step required in the polar regions is prohibitively expensive. Filtering of the shorter wavelength, fast-moving waves of the prognostic variables in the polar regions by Fourier analysis is able to alleviate this problem, and restore the use of the large 300 sec time step. Only very low wavenumber components of the T', u, and v fields are retained at high latitudes. Nonlinear instabilities, giving rise to a time computational mode, are also commonly encountered in the nonlinear time-dependent hydrodynamic equations solved by finite-difference (without the use of "horizontal diffusion"). Smoothing, using the frequency filter originally designed by Robert (1966), is added in the VTGCM to control this time computational mode.

Identical parameterizations and parameter tunings from the "best" model simulation (Section 5.5) cannot be immediately applied. It has been discovered that the 15 μm cooling parameterization (as used in the two-dimensional code) gives rise to such strong forcing in the VTGCM that instability arises for a time step greater than ~150 sec. A shorter integration for a simulated model day is possible (and stable) with the separation of the nonlinear temperature-dependent 15 μm cooling parameterization into two terms. The total 15 μm cooling parameterization is expanded in a Taylor series about a reference mean temperature profile taken from the two-dimensional

model. An implicit term is given by the second-order term of this expansion that is proportional to perturbation temperature (linear). It is subtracted from the forcing and added to the left-hand side (interior) difference approximation terms in the thermodynamic equation. The explicit term is now the reduced forcing. Such a delineation of explicit and implicit 15 μm cooling terms enables stability to be restored for a 300 sec time step. Perturbation 15 μm cooling is finally derived by subtracting an appropriate global mean cooling (see 6.3.2).

6.3 Cases Tested: Results and Comparisons with the Two-Dimensional Model

Results will now be described for three separate three-dimensional model runs. The present objective is to compare VTGCM T, u, w and Φ (or height) fields at the equator with those of the two-dimensional model for comparable inputs and parameters.

6.3.1 VTGCM Benchmark

The input data set described in Section 6.2.1 is now modified to provide EUV and UV heating, IR heating, and 15 μm cooling consistent with the two-dimensional benchmark of Section 4.3. Specifically, the 2-22% "lowest limit" EUV efficiency is used in concert with slant IR heating (based on the updated one-dimensional calculation of Section 4.2) to give nearly identical input heating as before (Section 4.3). The 15 μm cooling parameterization is identical to that used earlier in DRM2. An internally consistent global mean temp-

erature profile (from the two-dimensional benchmark) is now used within the three-dimensional model. Other global mean quantities (EUV and IR heating, 15 μm cooling) are derived from the VTGCM model itself. Net perturbation heating and temperatures result. Finally, composition previously calculated by the two-dimensional benchmark is adopted for use by the VTGCM.

Figures 6.1 and 6.2 provide latitude-longitude slices (at z = 5, 0, -4) and equatorial cross sections corresponding to this new benchmark. Very strong terminator winds (u $\leq$480 m/s) are again simulated, much like those of the two-dimensional benchmark. A very sharp gradient in horizontal wind (at 120°SZA) gives rise to significant subsidence on the nightside, with downward velocities approaching -3.9 m/s. As seen earlier in DRM2 and the two-dimensional benchmark, these strong descending winds are a large source of nightside compressional heating, particularly near 150°SZA. Total temperatures plotted are ~60-70°K warmer than the nightside average. Dayside exospheric temperatures rise to nearly 334°K, while midnight temperatures are close to 140°K. Symmetry of the fields about noon-midnight is clearly maintained.

The T (total temperature), u, w and h fields shown are similar to those of the two-dimensional benchmark, yet not identical. VTGCM horizontal winds are slightly enhanced ($\leq$50 m/s) over comparable upper thermosphere two-dimensional benchmark values. However, the day-night distribution and structure of the horizontal winds in these two models matches quite well, particularly for the sharp gradients derived near 120-150°SZA. Here, VTGCM vertical descending winds are somewhat

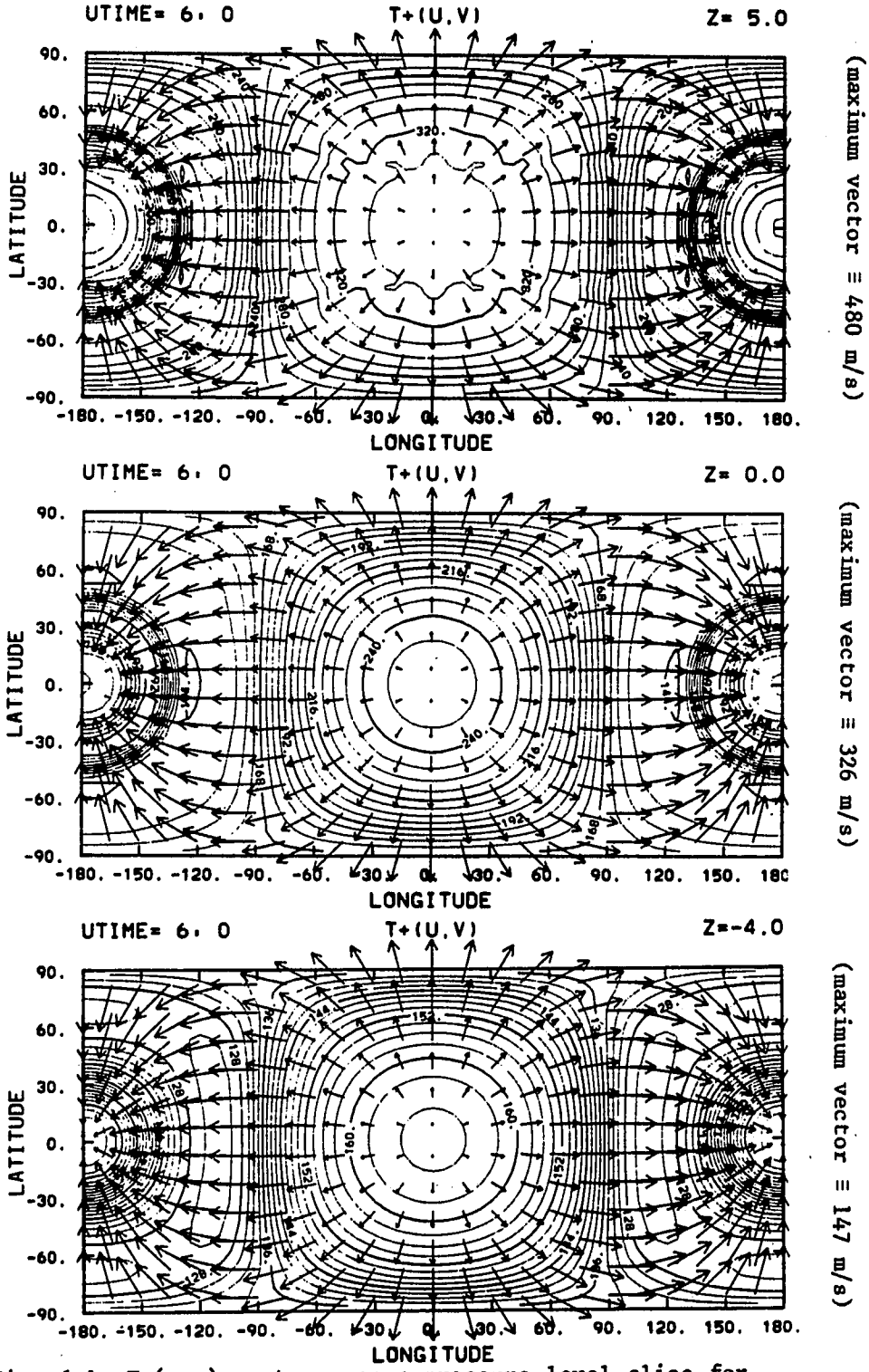


Fig. 6-1 T+(u,v) contours on a pressure level slice for benchmark three-dimensional model; (a) z = 5, (b) z = 0, (c) z = -4.

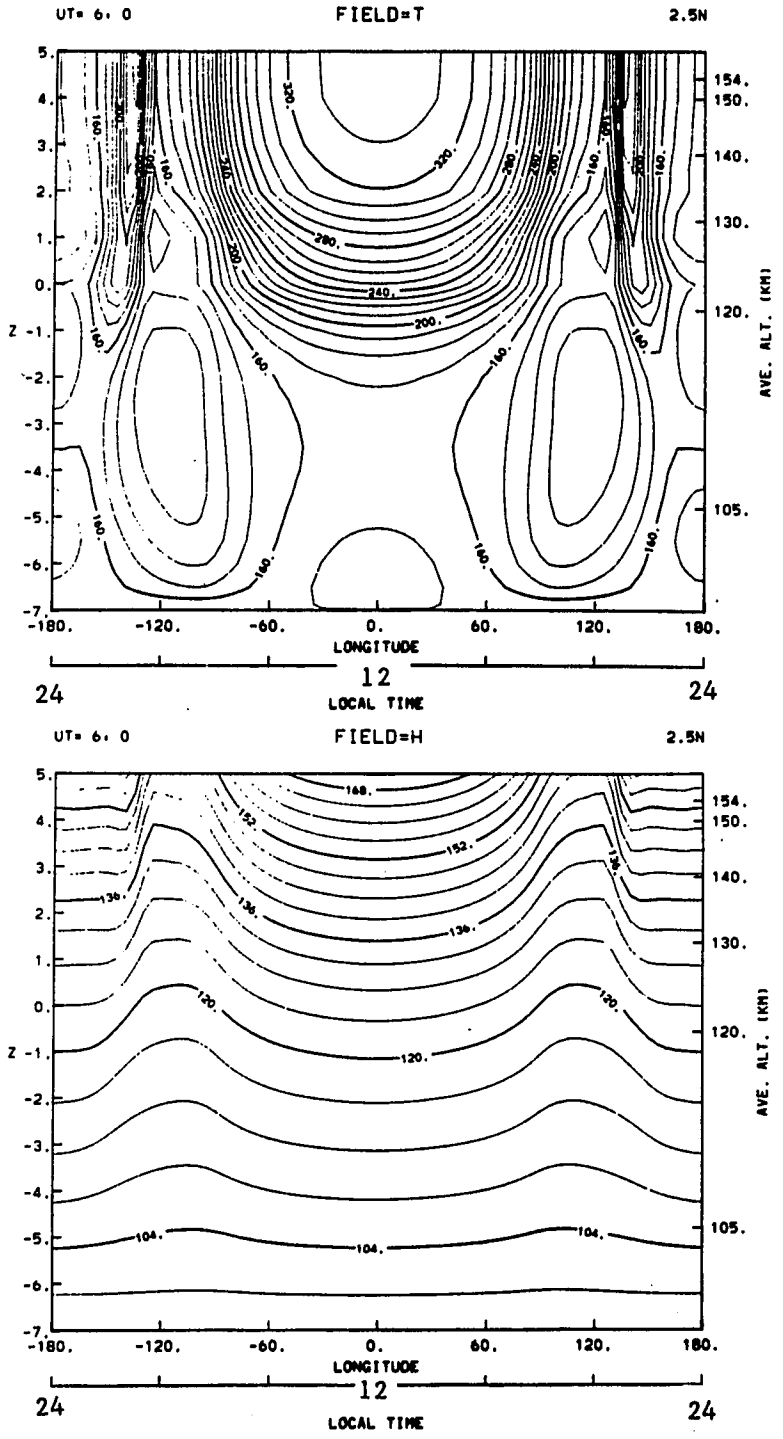


Fig. 6-2 Equatorial slices for benchmark three-dimensional model; (a) T, (b) h (in km).

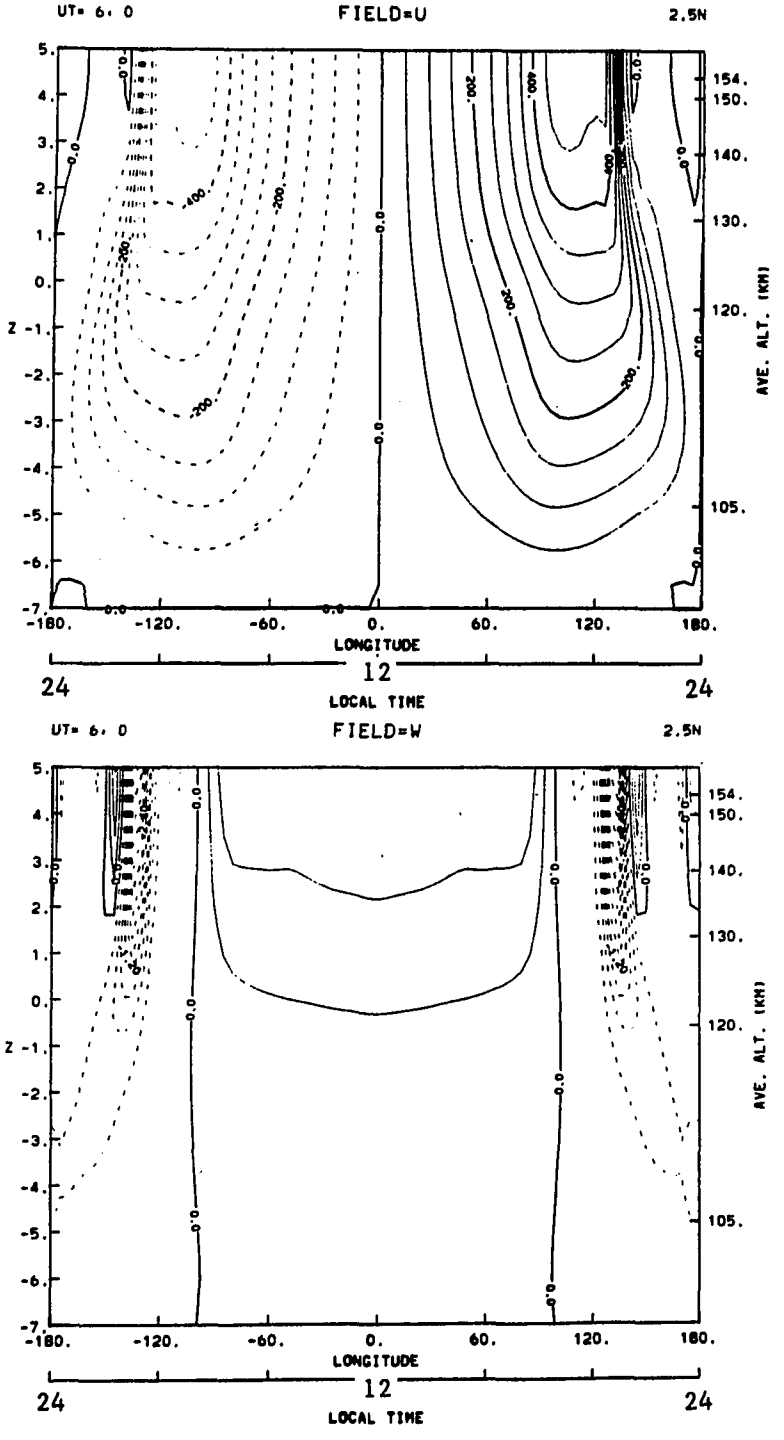


Fig. 6-2 Equatorial slices for benchmark three-dimensional model; (c) u (m/s), (d) w (m/s).

faster ($w \leq -3.9$ m/s), giving a nightside temperature anomaly that is roughly ~20°K warmer than the two-dimensional counterpart. The generally stronger VTGCM horizontal winds are a result of slightly warmer dayside temperatures, particularly above z = 1. The discrepancy is at most 10°K. Midnight temperatures are somewhat cooler ($\Delta T \leq 8$°K), which suggests that the stronger "back-pressure" present in the VTGCM model serves to "isolate" the deep nightside from being considerably warmer. The lower boundary temperatures of the two models are also different. Here, the VTGCM benchmark prescribes a global mean temperature, with dayside values (z = -7) approximately 10-15°K warmer than the two-dimensional model.

These discrepancies between the benchmark models occur as a result of a number of constructional differences between the two-dimensional and VTGCM codes. Total temperature is provided by the VTGCM model from the sum of a reference global mean temperature profile and calculated perturbation temperatures. The two-dimensional model calculates total temperature directly. The specification of a consistent global mean atmosphere between the VTGCM and two-dimensional codes may yet require fine tuning. The two models also extend over slightly different vertical regimes, such that the application of identical lower boundary conditions at somewhat different pressure levels is not consistent. Presently, composition is externally specified for the VTGCM while a self-consistent atmosphere is calculated for the two-dimensional model. Decoupling of composition should strongly alter the feedback among the calculated fields, as well as the final equilibrium solutions. Vertical resolution is also

coarser for the VTGCM code, which degrades the calculated fields, particularly in regions of strong gradients.

Despite these minor discrepancies and the lack of self-consistently calculated composition, the VTGCM benchmark corresponds quite well with the previous two-dimensional benchmark. All the outstanding departures of the calculated fields from Pioneer Venus observations are reproduced, especially the lack of a cold nightside thermosphere. A reasonable VTGCM is thus established.

6.3.2 Two-Reference Temperature 15 μm Cooling

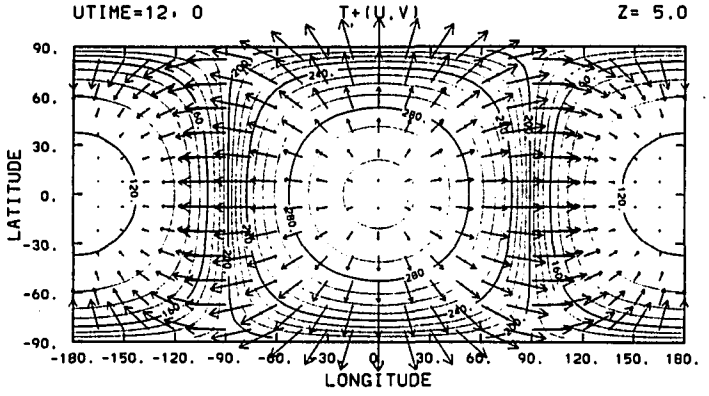
The establishment of a consistent VTGCM benchmark (with respect to the earlier two-dimensional benchmark) giving very similar T, u, w and h fields, is a first step toward the construction of a Venus TGCM capable of calculating fields that closely match Venus observations (Chapter II). It is evident that additional parameterizations providing external cooling, eddy drag, and more efficient EUV heating are now required for the VTGCM, just as previously described for the two-dimensional code (Section 4.4).

Those sensitivity study tests of Chapter V leading to a "best" model simulation are now used to prescribe identical model parameters for incorporation into the VTGCM. The "best case" K_{RA}, $\varepsilon(z)$ and K_{CO_2-O} parameters of Table 5.5 are specifically used. Eddy diffusion is abandoned until a calculation of composition is available. Total 15 μm cooling is provided by the more accurate two-reference temperature scheme used by the latest two-dimensional model simulation. The dayside and nightside mean temperature profiles from the

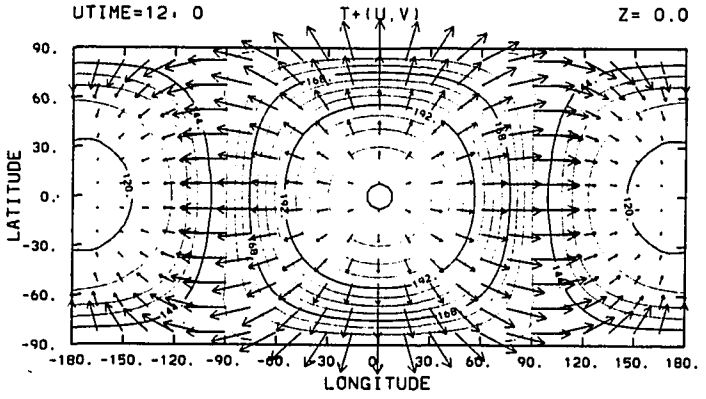
"best" model calculation are adopted for use by the VTGCM. From these, a global mean temperature profile and corresponding global mean 15 μm cooling are derived to facilitate the calculation of internally consistent perturbation temperature and net heating. Also, global mean IR and EUV heating are externally specified at ~60°SZA and subtracted from total heating. Stability is now possible, due to the explicit-implicit prescription provided for 15 μm cooling (see Section 6.2.2). The present goal is to derive improved day and nightside temperatures and integrated columns (with respect to the three-dimensional benchmark) closer to Pioneer Venus observations, and similar to the "best" two-dimensional model simulation.

A two-day integration giving new T, u, v, w and h fields is illustrated by similar vertical and equatorial two-dimensional slices (Figs. 6.3 and 6.4). Wave drag is seen to reduce terminator winds by nearly a factor of two, to $u \leq 205$ m/s. A much smoother distribution of horizontal winds is also derived, with no signature of sharply decelerating winds near 120°SZA. Likewise, a much weaker distribution of day and nightside vertical winds is calculated, with upwelling of ≤ 0.45 m/s and subsidence of ≤ -0.60 m/s. The sharp tongue of downward winds near 120°SZA seen by the VTGCM benchmark is no longer visible. Notice, however, the apparent increase in vertical descending winds near midnight ($w \leq -0.24$ m/s). This is a significant departure that should be visible in the signatures of other fields.

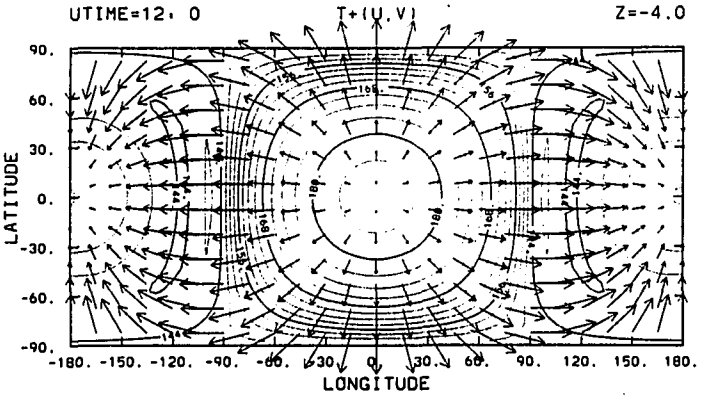
These calculated winds are consistent with a new balance of heating and cooling terms, resulting in dayside exospheric temperatures approaching 309°K, and nightside temperatures near 114°K. Such



(maximum vector ≡ 206 m/s)



(maximum vector ≡ 169 m/s)



(maximum vector ≡ 140 m/s)

Fig. 6-3 T+(u,v) contours on a pressure level slice for two-reference temperature 15 μm cooling three-dimensional model; (a) z = 5; (b) z = 0, (c) z = -4.

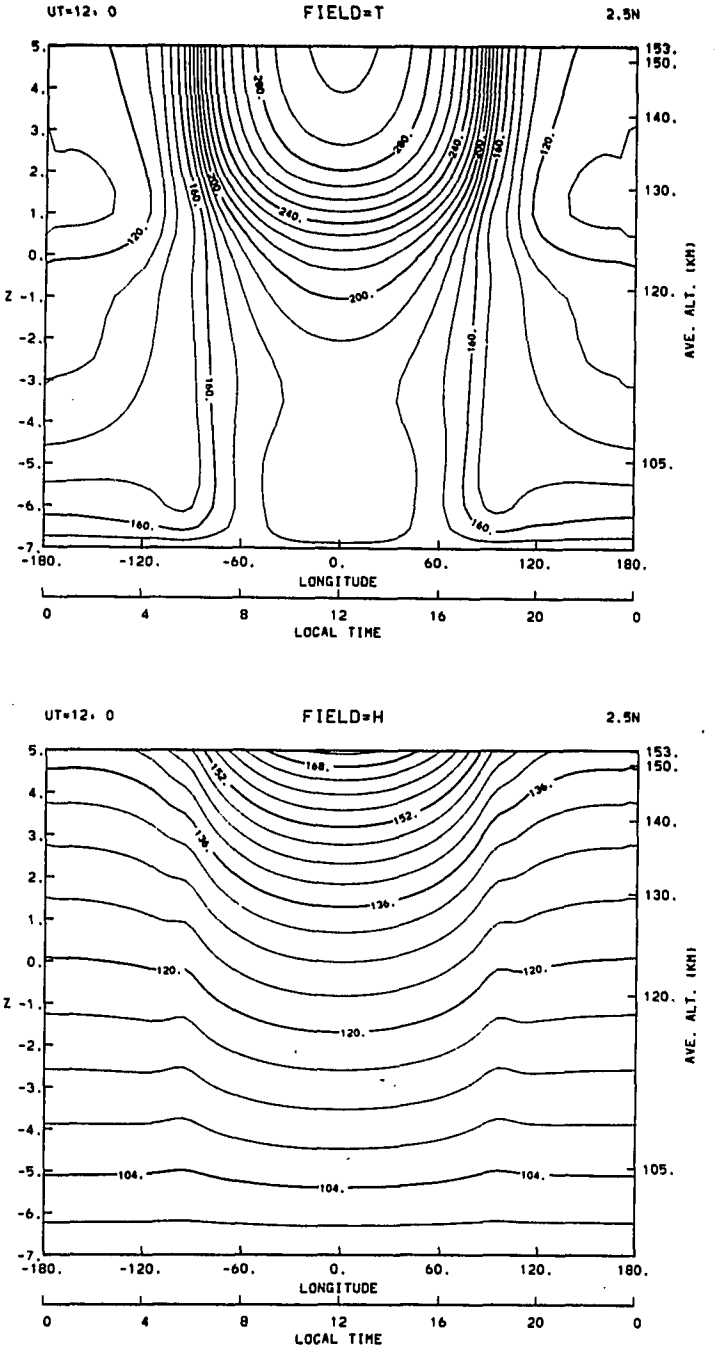


Fig. 6-4 Equatorial slices for two-reference temperature 15 μm cooling three-dimensional model; (a) T, (b) h (in km).

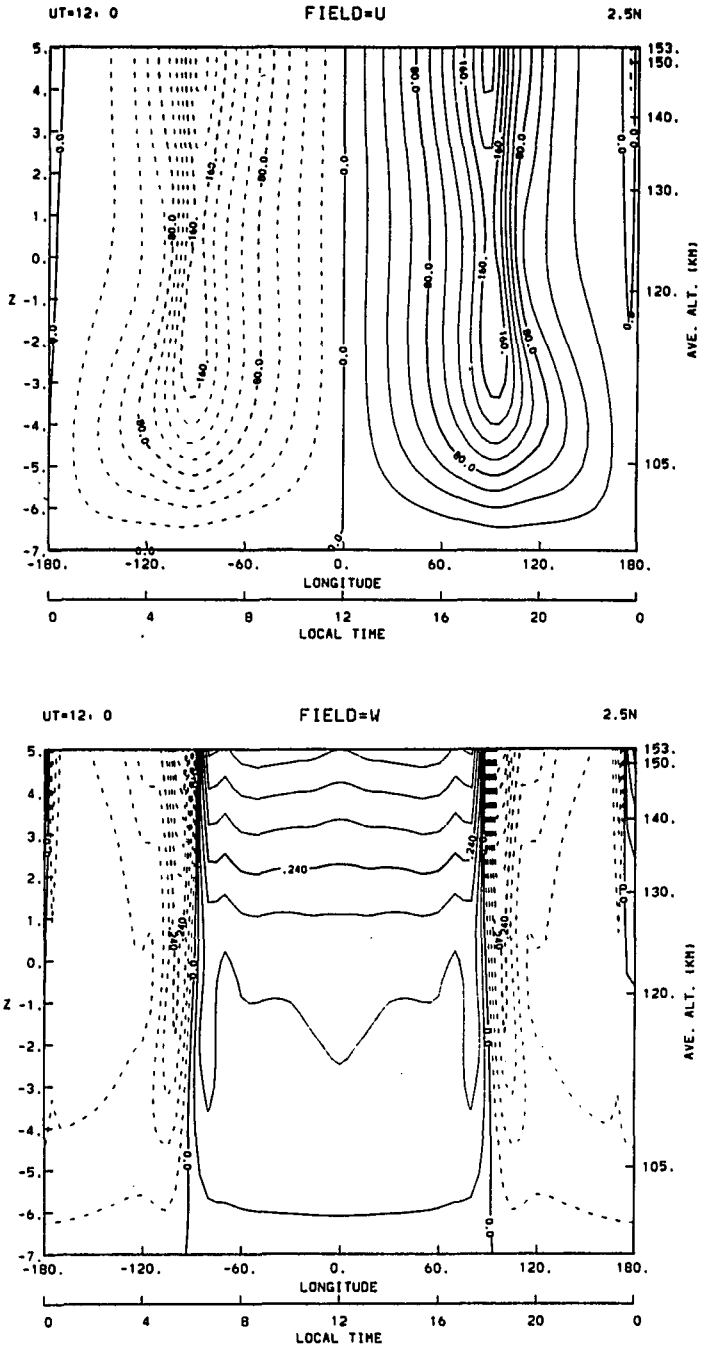


Fig. 6-4 Equatorial slices for two-reference temperature 15 μm cooling three-dimensional model; (c) u (m/s), (d) w (m/s).

midnight temperatures are consistent with the compressional heating (provided by subsidence) and 15 μm cooling present. A very sharp gradient in temperatures still remains across the terminator. Nightside temperatures are now much smoother, with no "compressional heating" signature at 120°SZA. Notice that the nightside column rises to 153 km at z = +5, which is consistent with Pioneer Venus observations. It is clear that model convergence to steady state is nearly obtained for this two-day integration. Deep nightside winds and temperatures, however, are still fluctuating by ±5%.

It is important to compare these VTGCM symmetric model fields to those of the two-dimensional "best" model simulation (Section 5.5). Dayside thermospheric temperatures ($z \geq -5$) are seen to correspond very closely to two-dimensional model values, with minor discrepancies of less than 6°K. This is consistent with the close correspondence of dayside EUV and IR heating fields between the two models. Dayside exospheric temperatures are very similar, approaching ~310°K for both model calculations. However, lower boundary temperatures ($z \leq -6$) are somewhat warmer (≤ 11°K) for the VTGCM, and require explanation.

The comparison of the nightside temperatures is not so close. Upper level temperatures ($z \geq 0$) again match two-dimensional model values quite well ($\Delta T \leq 6$°K). However, lower altitude temperatures ($-3 < z < -1$) are 10-15°K warmer. As a result of this nightside warming, the VTGCM has a slightly smaller day-night temperature gradient throughout the thermosphere, particularly at altitudes below 135 km.

Lower boundary temperatures are quite close to two-dimensional model values.

It is not surprising to find, therefore, that upper and lower level winds are somewhat different between the two-dimensional and three-dimensional models. Terminator VTGCM winds above $z = 0$ are ≤ 10 m/s slower, which is consistent with the slightly reduced day-night pressure gradient. Lower altitude winds are ≤ 20 m/s slower, and show a mild increase or "jet" at the $z = -3$ level, which is visible in the two-dimensional U-fields. This occurs because of the identical drag parameterization used in the two models. Upper level vertical winds over the day and nightsides compare very well between the two models. Yet, the lower altitude vertical winds (particularly those nightward of the terminator) are 30% weaker for the VTGCM code. This is consistent with the overall reduction of winds below $z = 0$. Symmetry is obtained about the equator and with respect to the sun-Venus axis for the three-dimensional model, a necessary requirement for comparisons between the two circulation models.

The most noteable discrepancy between the two model results is found in the lower nightside temperatures and corresponding winds. Dynamical-compressional heating, as evidenced by the stronger nightside (LT = 24) descending winds, appears to be responsible for the warmer temperatures in the VTGCM. "Lateral" boundary conditions at noon and midnight ($u = 0$) are virtually the same between the two models, as might be expected for a symmetric model circulation. However, horizontal wind gradients are sufficiently different to alter the resultant vertical velocities calculated in the VTGCM model,

particularly near local midnight. Feedback among temperature and u, v, and w fields now alters adiabatic heating to account for the expanded and warmer nightside column.

Minor differences in model fields also result from computational differences between the two Venus codes. Specifically, the vertical resolution is much coarser ($\Delta z \approx 0.5$ or roughly 0.5 H) for the VTGCM, as opposed to the two-dimensional model ($\Delta z \approx 0.125$ or 0.2 H). Also, upper and lower boundary conditions for T, u, v, w, and Φ are identical, but set at slightly different levels (z(bottom) = -10 and z(top) = 7 for the two-dimensional model vs z(bottom) = -7 and z(top) = +5 for the VTGCM). It may be necessary to extend the three-dimensional calculations to z = -10 (where T' = 0, u = 0, v = 0 and Φ' = 0, just as for the two-dimensional code) to reconcile lower boundary temperatures. Also, it is significant that VTGCM total temperatures are obtained by adding calculated perturbation temperatures to the specified global mean reference temperature profile. A more accurate and consistent approach would be to calculate VTGCM total temperatures independent of a separate designation of global mean quantities. Finally, the two-dimensional model is entirely self-consistent in its formulation of composition, temperatures and winds. The adoption of empirical composition is a significant deficiency of the VTGCM model that likely alters the feedback operating among the calculated fields.

It is clear that a very close reproduction of the "best" model simulation T, u, w, and h fields is provided by the VTGCM. Nightside

temperatures are notably closer to the HSYM and VTS3 model atmospheres. Thermal balances (shown in Fig. 6.5) illustrate that enhanced nightside adiabatic heating is primarily responsible for these warmer nightside temperatures. Heat conducted up from below also provides warming. A foundation is now set for asymmetrical model studies using the VTGCM.

6.3.3 Superrotation Scheme and Model Signatures

The physical mechanism necessary to actually drive a superrotating Venus thermospheric flow is not well known. Estimates by several authors (Schubert and Walterscheid, 1984) indicate that some remnant of the stratospheric four-day superrotating flow should remain at high altitude ($\geq$100 km). Suggested ~100 km supperrotating velocities range from 0-100 m/s, depending upon cloud top retrograde velocities chosen. Cyclostrophic balance is generally adopted to calculate winds from meridional temperature gradients.

Mayr et al. (1980, 1984) have chosen to assume a retrograde, superrotating velocity of the entire thermosphere ($\geq$100 km) and to determine the effects on the model calculated fields. Current VTGCM work circumvents the question of the generation of the superrotating flow to observe its effects on large scale fields. To fully examine asymmetrical model signatures to a superrotating flow, a self-consistent calculation of composition must be considered for the VTGCM. However, as a first approximation, it is possible to study superrotating effects on the overall circulation and temperatures while still adopting empirical composition.

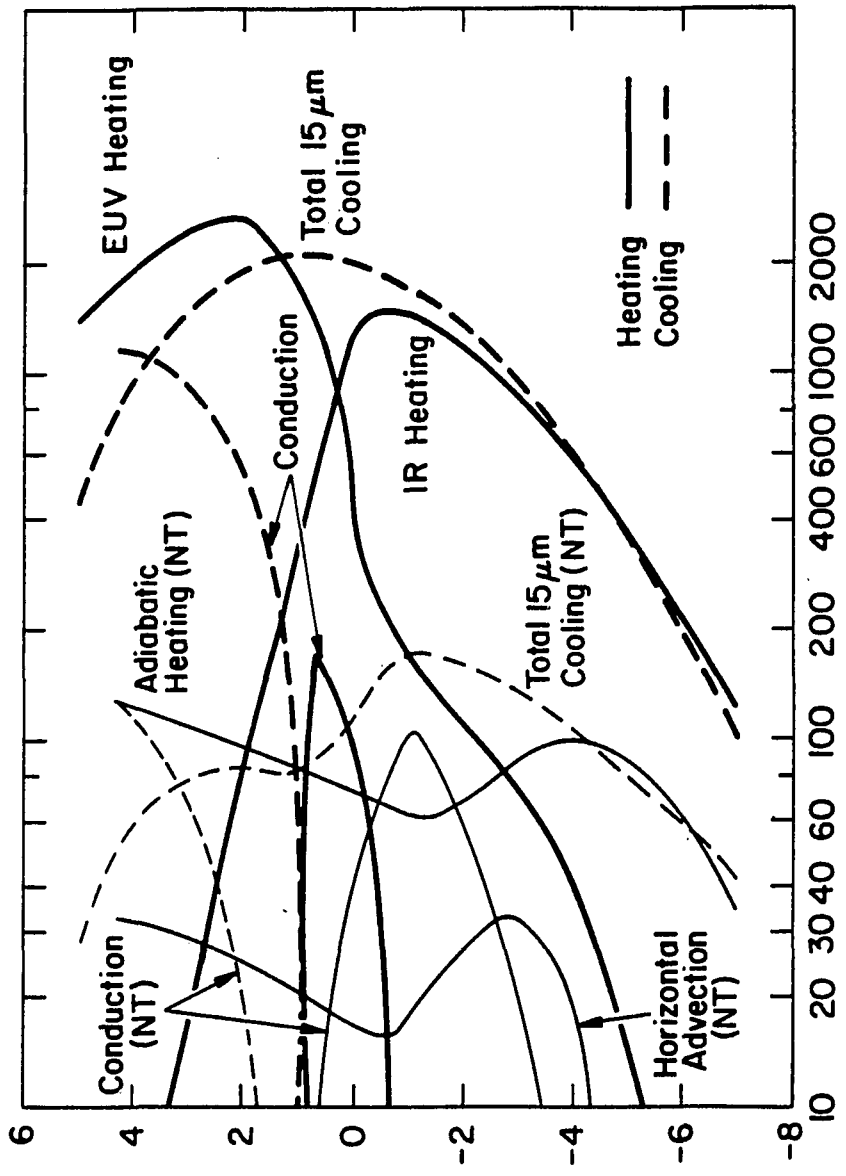
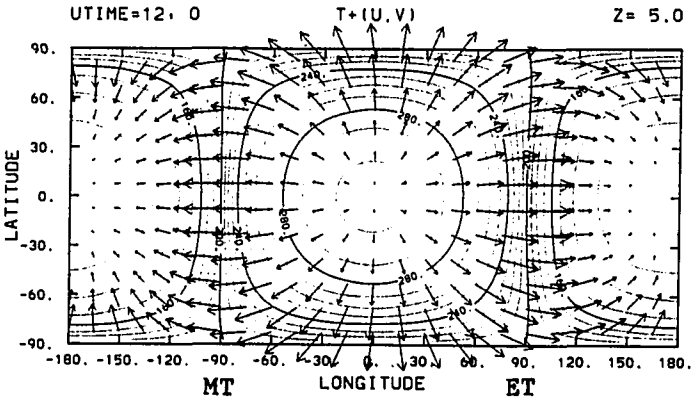


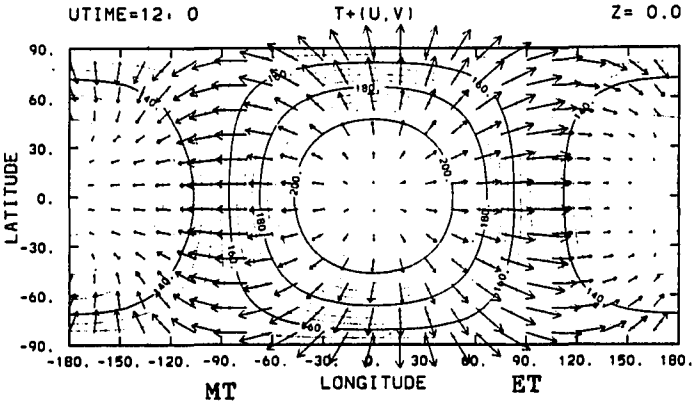
Fig. 6-5 Heating and cooling rates - 60 and 120°SZA: VTGCM.

The updated VTGCM (from Section 6.3.2) is now altered to contain an assumed retrograde superrotation of the entire thermosphere. The reference frame is prescribed to rotate with an Ω corresponding to an equatorial velocity of 75 m/s. This solid body rotation (from midnight toward the morning terminator--the same direction as planetary rotation) is identical to that employed by the three-dimensional spectral model of Mayr et al. (1984). Upon that background, the coupled equations of energy and momentum are solved. Horizontal velocities are now computed relative to the superrotating thermosphere. Model integration is specifically conducted for one Earth day, which corresponds to the dynamical time constant of the upper atmosphere ($z \geq 0$). Resulting trends showing asymmetrical responses by the atmosphere ($z \geq 0$) can now be estimated. Lower boundary conditions are left unchanged, and should have negligible influence upon the model fields for $z > 0$.

A useful comparison between VTGCM runs with and without superrotation can now be made. Figure 6.6 illustrates the resulting superrotating circulation for two pressure-level slices at $z = 0$ and $z = 5$. Total temperature is shown. It is immediately apparent that the horizontal winds (calculated with respect to the rotating thermosphere) now converge after midnight at $\gtrsim$1 AM L.T., rather than precisely at the anti-solar point. Zonal winds (u) are correspondingly 20-30 m/s faster across the evening terminator (ET) than at dawn. This corresponds roughly to a one-hour shift of the circulation pattern toward the morning terminator (MT). Vertical (descending)



(maximum vector ≡ 202 m/s)



(maximum vector ≡ 175 m/s)

Fig. 6-6 T+(u,v) contours on a pressure level slice for a superrotating three-dimensional model; (a) z = 5, (b) z = 0.

velocities are likewise enhanced nearest the morning terminator, consistent with the post-midnight stagnation of the horizontal winds. These phase shifts in the circulation should be similar to those possible for a parameterized (actual) superrotating circulation in a more rigorous calculation.

Current upper level temperatures, however, do not greatly change. Figure 6.6a also shows exospheric temperatures now calculated about the planet. The distribution is rather symmetrical about noon-midnight, and the differences are relatively small between dawn and dusk. This suggests (as demonstrated by Mayr et al., 1984) that superrotation is not important for exospheric temperatures. Temperatures down to z = 0 are similarly undisturbed.

These preliminary results for a superrotating Venus thermosphere are only suggestive of the complete atmospheric response possible. Composition is not self-consistently calculated, and therefore feedback among temperature, composition, and wind fields cannot be complete. The current scheme (that assumes a thermospheric rotation period of six Earth days) neglects a proper lower boundary condition, for which height and wind fields should be compatible. Fields are thus reliable only for the upper thermosphere ($z \geq 0$) at a distance sufficiently removed from the lower boundary. Despite these caveats, the asymmetrical response by the VTGCM T, u, v, and w fields is qualitatively similar to that seen by Mayr et al. (1984) for a similar superrotation scheme.

Such a calculation raises many more questions than it answers. What physical mechanism can be utilized to drive these

superrotating winds? Are the empirical model responses characteristic of the feedback possible with a calculation that also includes calculated composition? How do the lightest species (He, H) and the heavier species (CO_2, CO, O) respond differently to superrotating flow? These and other problems associated with further use of the VTGCM code will be addressed in Chapter VII.

CHAPTER VII

MODELLING IMPLICATIONS AND DISCUSSION

7.1 Summary and Conclusions of Present Research

This thesis research has sought to identify and quantify new physical processes previously neglected in a self-consistent coupled chemical dynamical model of the Venus thermospheric circulation. The two-dimensional symmetric model of Dickinson and Ridley (1977) was utilized as the primary framework upon which these new model processes--eddy diffusion, eddy cooling, wave drag, and 15μ radiational cooling--were parameterized and tested. The experience gained from this symmetric two-dimensional model has been used to develop a first-order Venus version of the three-dimensional TGCM (VTGCM), which includes these new Venus physical parameterizations and inputs. Tests indicate that these two models calculate very similar output fields at the equator. A strong foundation has thus been laid for further modelling using the VTGCM code. This chapter discusses the present research, and outlines how the thesis work can now be incorporated into the fully self-consistent three-dimensional models that are planned for the thermospheres of Venus and Mars.

7.1.1 Two-Dimensional Model Sensitivity Studies

The previously developed Venus two-dimensional symmetric hydrodynamical model of Dickinson and Ridley (1977) has thus been revised and improved in light of the Pioneer Venus observations, to give temperature and composition fields that compare quite well with the empirical model atmospheres of Hedin et al. (1983) and Keating et al. (1984). Such a correspondence is the result of a series of sensitivity tests which were undertaken to examine eddy and 15μ cooling parameterizations with respect to three estimates of EUV heating efficiency profiles. These exercises not only restricted the range of chosen (adjustable) parameters, but also gave a great deal of insight into the feedback mechanisms operating among the temperature, wind and composition fields which could only be examined by a coupled chemical dynamical code.

Initially, a sensitivity exercise was conducted whereby EUV heating was balanced against enhanced eddy cooling and 15μ radiational cooling to give observed Venus dayside thermospheric temperatures. EUV efficiencies in excess of 10% were sought, according to the recommendation of Fox and Dalgarno (1981) and others. It was found that eddy cooling is not a viable mechanism to provide external cooling sufficient to enable a topside EUV efficiency greater than 2% to be used. An attempt was made to link all eddy processes consistently to one another using the same eddy coefficient profile. As a result, eddy cooling does not appear to be an important cooling mechanism because it requires an eddy coefficient much larger than that appropriate for dayside eddy diffusion.

More efficient EUV heating is however possible with the application of enhanced 15 μm cooling. Atomic-O collisions with CO_2 are assumed to excite CO_2 vibrational-rotational states much more efficiently than CO_2, CO or N_2 collisions. A 7-19% EUV profile heating now seems to be best suited to give a good dayside thermal balance and temperatures. The cooling required is in general agreement with the best rocket-laboratory rate coefficient of Sharma and Nadile (1981): $k(CO_2\text{-}O) = 5\times10^{-13}$ cm^3/s. The high heating efficiency profile, Model C, estimated by Fox (1981, private communication), cannot presently be used with any conceivable cooling mechanism for Venus. In fact, the maximum topside EUV efficiency permitted from the two-dimensional model studies is generally less than 10%. This is notably smaller than the values suggested by Fox and Dalgarno (1981). Greater certainty in a reliable and sufficient 15 μm cooling scheme would be possible if the $k(CO_2\text{-}O)$ rate coefficient was more precisely measured over a 100-300°K temperature range.

Wave drag was found to be a crucial addition to the momentum balance needed for a more realistic Venus thermospheric circulation. Terminator winds are only consistent with observed temperature and composition fields about the planet if maximum horizontal winds are <220 m/s. Such a reduction of winds by nearly a factor of two from DRM2 calculations was accomplished by parameterizing a wave drag within the horizontal momentum equation. These slower winds permit more dissociation fragments and light species to remain on the dayside and less to be carried to the nightside, giving O, CO, CO_2 and newly modelled He mixing ratios closer to Pioneer Venus observations. This

increasing "isolation" also serves to enhance the day-night temperature contrast, for which dayside temperatures increase and nightside temperatures decrease. Slower winds are primarily responsible for reducing the nightside adiabatic compressional heating--the dominant source of nightside heating--which largely balances 15 μm cooling to give the calculated temperatures (which closely match nightside observed values).

Presently, no mechanism other than drag seems sufficient to retain O, CO and He on the dayside at levels close to observations. The necessary drag restricts the ability of the large-scale winds to transport species to the nightside and to provide an adequate heat source to maintain the observed nightside temperatures. Low altitude return flow not currently parameterized (i.e., below the bottom boundary) could be of help in pumping up dayside densities while permitting stronger winds and a better nightside distribution of temperatures and integrated heights. Measurements of horizontal winds over the 100-200 km altitude range would be ideal, which then could be used to constrain the drag and validate the presently inferred circulation based on observations of its structure.

Two-dimensional model sensitivity tests have also examined model parameters specifying eddy diffusion. Its control over composition (and indirectly, temperatures) is secondary to the advection effects provided by the global winds. Eddy diffusion was adjusted to give improved day and nightside composition not otherwise possible by modifying the momentum drag. The application of eddy diffusion was also kept to a minimum, corresponding to just that required to aid the

self-consistently calculated winds. It was found that very little eddy diffusion is needed on the dayside (KMAX $\leq 5\times10^6$ cm^2/s). Conversely, the nightside composition required KMAX = 8.0×10^6 cm^2/s These maximum eddy coefficient values are also calculated to be 10-20% of the previous one-dimensional model values for the day and nightside (see Chapter III). This indicates that the "mixing" that actually occurs in the Venus two-dimensional hydrodynamical code is partitioned between small-scale turbulent processes and large-scale winds. An application of the two-dimensional model to the calculation of He confirms this significant role of vertical velocities in controlling composition. It is conceivable that eddy diffusion not only affects the amplitudes of the specie densities, but their phases about the globe as well. Such a response would be visible in an asymmetrical circulation of the type planned for the expanded VTGCM (see Section 7.2).

The Rayleigh friction scheme currently used is a useful method to determine the time scales for momentum deposition (or drag) necessary to reduce horizontal winds to give a reasonable distribution of composition and temperatures about the planet. An assumed altitude profile for drag, similar to that used by the $K_E(z)$ parameterization, is incorporated. This enables a constant time scale (K_{RA} = $1.2 \pm0.2\times10^{-4}$ sec^{-1}), comparable to that of the pressure gradient term, to be approached at a turbopause or "breaking level" (ZPBK = 0). However, Rayleigh friction is not a physically derived (or fundamentally developed) parameter. It is basically an ad-hoc method to incorporate wave-breaking effects on the mean flow.

Yet, the sparse data available concerning the observed wave structures is not sufficient to piece together a reasonable theory for wave generation and propagation into the thermosphere.

A reasonable alternative has been to make use of the Weinstock (1982) parameterization for momentum deposition, which is proportional to $K_E(Z)$ and K_z. This new approach assumes that internal gravity wave (IGW) breaking is the same mechanism that gives rise to eddy diffusion (small-scale mixing) and drag (negative momentum deposition) upon the mean flow. The adopted scheme is limited to a single wave, and requires certain restrictions upon wave scales and $K_E(z)$. Yet, it still gives a time scale (sec^{-1}) for specifying a drag term proportional to "u." The improvement lies in the fact that the parameterization is now based on wave scales and the previously defined eddy diffusion coefficient. An effective strategy has been to use this parameterization to construct a K_{RA} profile similar to that needed previously. From specifying the "best" model values of $K_E(z)$, it is possible to learn what vertical wave scales are required. Waves having $\lambda_z<16$ km are needed to derive a wind structure very similar to the "best" model simulation. Such vertical scales meet all the restrictions posed by the Weinstock (1982) scheme, and they are generally consistent with the vertical wave structure currently seen in the temperature data (λ_z = 5-10 km) (Seiff et al., 1982). Certainly, single wave models are very crude, and the absence of nonlinear wave interaction is a major deficiency. However, it does seem possible to link eddy diffusion and momentum deposition via a common eddy coefficient to give drag comparable to Rayleigh friction. Further refinement of this parameterization is needed.

State-of-the-art wave-breaking models--such as those of Garcia and Solomon (private communication, 1983), Holton (1982, 1983), and Schubert and Walterscheid (1984)--are not warranted at this time for Venus' mesosphere. Propagation of gravity waves is strongly dependent on the structure of the atmosphere, particularly the static stability and horizontal winds. Present knowledge of the thermosphere and mesosphere structure of Venus (below 140 km) is very limited. Measured wind velocities are first needed to estimate the possible influence of low altitude (<60 km) generated internal gravity waves upon the thermosphere.

It is significant to note that all eddy-related parameterizations can be tied together with the use of a single reference eddy coefficient profile. This consistency maintains the aeronomical practice of consolidating all turbulent terms into a single, prescribable coefficient based on mixing length theory. However, it remains to derive an internal consistency between the large scale fields, (T, u, w, Φ, %[O], %[CO]) and the eddy coefficient (or diffusivity). The incorporation of these eddy processes presently means a loss of internal consistency for the two-dimensional model (von Zahn et al., 1983). Any internally consistent prescription must evolve from a much better understanding of the sources of wave activity.

The possible role of thermospheric level gravity wave sources from below is not well understood (Schubert and Walterscheid, 1984). However, a useful diagnostic tool is available to examine the character of the mean flow to determine its potential for instability and wave breaking. The Richardson number is a non-dimensional parameter

calculated from the ratio of bouyancy to the vertical shear of horizontal winds. Values less than 0.25 indicate a tendency toward instability. This parameter is used for Venus to ascertain what region of the thermosphere has the most potential for instability, thereby requiring very little additional external forcing (tidal or gravity wave) for overturning to occur. The two-dimensional benchmark atmosphere is specifically tested, since no eddy or external cooling parameterizations are incorporated. Results indicate that the flow is potentially unstable downwind of the terminator, where a Richardson number as small as 1.6 is seen over $-6<z>-2$ (roughly 110 to 125 km). This region therefore has the greatest potential for wave breaking and turbulence, and is the site of the strongest vertical wind shear and the weakest static stability. Symmetry about the terminator is not indicated by this diagnostic analysis. Instead, wave breaking should be most prevalent downwind of the terminator and onto the nightside. The development of improved and internally consistent parameterizations for eddy processes may make use of such a non-dimensional parameter. An additional Richardson number component must also be derived for the turbulent or small-scale structure that one desires to include.

It is useful to compare the two-dimensional finite-difference model scheme adopted in this thesis to that used for the spectral model calculations of Mayr et al. (1980, 1984). Aside from the obvious differences in calculation technique (grid point vs spectral) described in Chapter III, these two codes are seen to bring about a reasonable day-night distribution of composition and temperatures

using different physical parameterizations. The finite difference approach has been to reduce horizontal winds (by eddy viscous drag) to a level where the dayside thermosphere is sufficiently isolated from the nightside to give dayside bulges of O, CO and CO_2, and cold nightside temperatures. It was discovered that a fraction of the previous one-dimensional model levels of eddy diffusion were required to aid the large-scale winds. Conversely, the spectral model approach has been to retain very strong ($u \approx 300$-400 m/s) horizontal winds without the application of eddy viscous drag. Instead, very large horizontal and vertical eddy diffusion were used at altitudes below 135 km to restore a realistic day-night distribution of composition and temperatures. The principal effect of such a large anisotropic eddy coefficient (and the resulting strong horizontal diffusion) is to smear out any horizontal contrast caused by the large scale winds. The lower atmosphere was calculated to be largely homogeneous over all SZA. Above 135 km, horizontal and vertical diffusion were relaxed to permit the large-scale wind effects on composition and temperatures to dominate.

The finite-difference model strategy using reduced winds and minimal eddy diffusion is preferred. This calculation is based upon the primitive equations which are modified as little as possible. Balances closer to the terrestrial thermosphere are retained, whereby large-scale winds (not eddy diffusion) are dominant in the control of composition. Wave (eddy viscous) drag is also a physically-motivated process that has been successfully parameterized for the terrestrial mesopause for an improved momentum balance. Wave breaking models for

the Earth (at the turbopause) are prototypes for the Venus wave drag parameterization. Large horizontal eddy diffusion can be estimated from scaling arguments based on mixing length theory. However, it is not generally used in global models of the terrestrial mesosphere/thermosphere due to recent advances in gravity-wave breaking theory and models (Holton, 1983). The range of values for the horizontal eddy coefficient is also not clearly defined. Finite difference models already make use of limited horizontal eddy diffusion to eliminate subgrid scale perturbations that can lead to numerical instability. Any attempt to parameterize a physically-motivated large horizontal eddy diffusion would be confused with this "smoothing" procedure.

7.1.2 Further Applications

Several applications of the "best" model simulation were undertaken, not only to validate the two-dimensional model behavior and parameter adjustments, but also to provide additional model predictions. Helium calculations in particular reveal the importance of vertical velocities in controlling composition profiles. This is especially evident when comparing profiles at 60°SZA, corresponding to hydrodynamic and one-dimensional composition model calculations. Eddy diffusion and large-scale winds are found to have a similar effect upon composition above $z = 0$, for which He is depleted from the dayside. However, their effects on composition below $z = 0$ are quite different. A much larger lower boundary value of He (~40 ppm) is predicted by the hydrodynamical code to derive a He profile above $z = 0$ that closely reproduces available observations. This is im-

portant since there are no available measurements for comparison with calculations below 130 km (von Zahn et al., 1983). Helium is the most sensitive of all the transported species examined, and should respond most strongly to these individual schemes for parameterizing eddy and large-scale vertical velocities. This discrepancy is thus significant, and confirms that one-dimensional models are deficient in their ability to properly account for hydrodynamic effects on composition. Fully self-consistent chemical-dynamical models are clearly required, as suggested earlier for the nightside composition (Stewart et al., 1980, and Massie et al., 1983). However, the same is now shown to be true for the dayside densities, especially for the dynamically-controlled regime below z = 0 (roughly 134 km). Measurements of O, CO, CO_2, N_2 and He densities over 100-150 km would be invaluable.

Helium is also an additional check on the parameter adjustments previously used for the "best" model simulation. Good dayside He densities resembling observations (>140 km) can be obtained. However, the nighttime He peak densities are calculated to be 2-3× the reference atmosphere values (near 150 km). Apparently, He is subject to additional physical processes that do not significantly affect O and CO. Specifically, superrotation and eddy diffusion may interact to determine amplitudes and phases of densities, especially He. The time scales of these two terms affecting composition should be analyzed once a fully self-consistent VTGCM code is available. This may show that a "smearing" of the nightside He peak is possible, thereby reducing helium densities toward observations (Mayr et al., 1984).

Solar minimum calculations were also made for identical physical parameterizations and inputs (other than reduced fluxes). It was discovered that the Venus thermosphere is quite insensitive to solar cycle (primarily EUV flux) variations. Dayside temperatures ($z>0$) are reduced by roughly 70°K, giving an exospheric temperature of 240°K at noon. In contrast, solar cycle variations result in terrestrial exospheric temperature changes of as much as 1200°K. Bauer et al. (1982) noticed this weak Venus response during their investigation of the effects of the 27-day solar flux periodicity. Two explanations are possible. The generally adopted (and time-dependent) EUV efficiency for the Earth (Torr et al., 1980b,c) is larger than that used by the Venus "best" model simulation. Also, Venusian cooling is dominated by CO_2 15 μm cooling throughout the thermosphere, unlike the Earth. Less efficient heating and much stronger 15 μm cooling both permit solar perturbations to be effectively "buffered" for Venus. Clearly, planetary thermospheres dominated by CO_2 have significantly different thermal properties than the Earth.

7.1.3 VTGCM Model Calculations

The "best" two-dimensional model simulation parameter adjustments (see Table 5.5) are tested within the first order Venus version of the three-dimensional TGCM described earlier in Bougher et al. (1981). Such a symmetric version of the VTGCM is necessary to validate the three-dimensional model behavior, and to compare the two model responses to the same tuned parameters. The temperature, height, and wind fields compare quite favorably between the two models. However, the correspondence is not exact.

The VTGCM "best" simulation T, u, w, and h fields calculated near the equator differ somewhat from those previously given by the "best" two-dimensional model. Dayside temperatures match quite well for the two model calculations. However, the most notable discrepancy lies in the nightside temperatures and winds. Three-dimensional temperatures over $-3 \leq z \leq 0$ are 10-15°K warmer as a result of enhanced compressional adiabatic heating near midnight. Lateral boundary conditions ($u = 0$) are nearly identical within the VTGCM and two-dimensional models. Yet a somewhat different momentum balance (and heating) appears on the nightside for the VTGCM calculations. The reduced day-night pressure gradient causes slower terminator winds to be calculated for the VTGCM throughout most of the atmosphere. Differences in the two model specifications of vertical resolution and total temperature may be significant enough to account for some of these discrepancies. Also, the designation of the lower boundary is set at different pressure levels between the two codes, and results in slightly different lower boundary temperatures. Most importantly, the VTGCM does not include self-consistently calculated composition, but rather the final "best" two-dimensional model atmosphere. As a result, feedback among composition, temperature and wind fields is not complete for the VTGCM, and could have a significant effect on the final fields calculated.

Nevertheless, the comparison is sufficiently close to validate the three-dimensional model behavior for identical parameterizations (eddy, drag, and cooling) and very similar geophysical inputs. It is also shown that the two-reference temperature scheme is a valuable im-

provement to perturbation 15 μm cooling, regardless of which code is used. Such a correspondence between the two- and three-dimensional models enables a new benchmark to be set for further VTGCM model studies. It is now possible for the symmetric subsolar-to-antisolar circulation to be altered by the addition of a superrotating component of the day-to-night flow.

To properly examine asymmetrical model signatures to a superrotating flow, a fully self-consistent calculation of composition must be included in the VTGCM. However, it is possible to study superrotating effects on temperatures while still adopting empirical composition. A new superrotating reference frame is specified, upon which the subsolar-to-antisolar winds are driven. A 75 m/s retrograde rotation of the entire thermosphere is assumed, identical to that of Mayr et al. (1984). A very small effect in exospheric temperatures is seen, with a phase shift of $<<1$ hour in the direction of superrotation. This is quite similar to that calculated by Mayr et al. (1984). However, the phase shift of horizontal and vertical winds is significant. Nightside horizontal winds converge after midnight at LT = 1-2, toward the morning terminator. This response by the circulation suggests that composition (particularly He) will be strongly affected by these superrotating winds. A solid motivation for the incorporation of VTGCM self-consistently calculated composition is now given.

7.2 Outline of Future Work

7.2.1 Venus - TGCM

The Venus two-dimensional and preliminary three-dimensional models have so far sought to describe the first order structure of the Venus thermospheric circulation--its symmetric composition, temperature and wind fields. Future work would however be focused on new modelling to calculate the observed asymmetrical signature of the above fields with the Venus three-dimensional TGCM described earlier. Such a project would build upon the experience gained by the sensitivity studies conducted within the Venus two-dimensional code. The crucial improvement to the VTGCM will be a coupling of composition into the calculation, just as developed in Dickinson et al. (1984), but specifically designed to calculate CO_2, CO, O and He. The observed asymmetrical nature of the thermospheric flow can only be properly addressed with this coupling of composition. Mayr et al. (1980, 1984) suggest that a particular combination of superrotation (with retrograde winds in excess of 50-75 m/s) and large eddy diffusion could produce phases and magnitudes of composition, temperature and airglow in reasonable agreement with observations. Currently, it is thought that superrotation could be parameterized by allowing the lower boundary of the model to attain an appropriate retrograde velocity with respect to the solid planet. Such a perturbation to the mean wind field might be physically motivated by a pole-to-equator pressure gradient that could be imposed to give rise to a cyclo-

strophic type wind. The principal goal of this VTGCM modelling work would be to fine-tune all previously tested parameters plus super-rotation to produce composition and temperature fields which closely match the asymmetrical description of Hedin et al. (1983).

7.2.2 Mars - TGCM

A second possibility for future research would be to adapt the Venus TGCM and the basic physical processes applicable to a CO_2 atmosphere to a Mars thermospheric circulation model. Such a model calculation is motivated partly by a possible Mars climatology mission that is slated to visit the planet during the 1990s. A preliminary Mars model would be derived from the VTGCM, and altered to contain those physical parameters unique to Mars. It is fully anticipated that very similar physical processes should be operating within the Venusian and Martian thermospheres, principally since both planetary atmospheres are largely composed of CO_2.

Available Viking, Mariner, and Soviet thermospheric Mars data are very sparse, creating the immediate need for coupled composition studies within the more general TGCM code. Such a first-order model for Mars will be highly predictive in nature, just as the Venus two-dimensional model of Dickinson and Ridley (1977) prior to Pioneer Venus. CO_2-O rate coefficients, eddy drag, 15 μm cooling, and eddy diffusion parameterizations similar to the VTGCM will initially be invoked. However, the temperature of the upper atmosphere of Mars is strongly affected by processes not directly related to solar activity (Stewart et al., 1972; McElroy et al., 1977). Heating by dissipation

of atmospheric gravity waves (tides) and cooling by turbulent heat transport are obvious possibilities. Excitation of these waves in fact should be favored when Mars is closest to the sun and may be enhanced by additional dust present in the atmosphere during dust storms (Gierasch and Goody, 1971). This suggests that a preliminary three-dimensional model for Mars without eddy and tidal processes will likely be inadequate. A new scheme for lower boundary tidal forcing, similar to that currently being tested for the Earth (Fesen, private communication, 1984), may be required.

7.3 Summary

In conclusion, future research would seek to build upon the multi-dimensional model work already completed for this thesis. In particular, the continued development of an improved Venus version of the TGCM is planned. Eventually, a comparison of the terrestrial and Venusian thermospheric circulations will be made (composition, winds and temperatures) once analogous three-dimensional coupled chemical-dynamical models for each planetary thermosphere are available. The physical processes common to Earth and Venus can then be discussed. Conversely, those physical processes unique to a CO_2 atmosphere will be isolated. A natural extension of thermospheric modelling of CO_2 atmospheres is also planned with a preliminary model of the Martian thermospheric circulation. It is hoped that such modelling work on the Martian and Venusian planetary atmospheres will provide valuable insight into the terrestrial thermospheric research already underway.

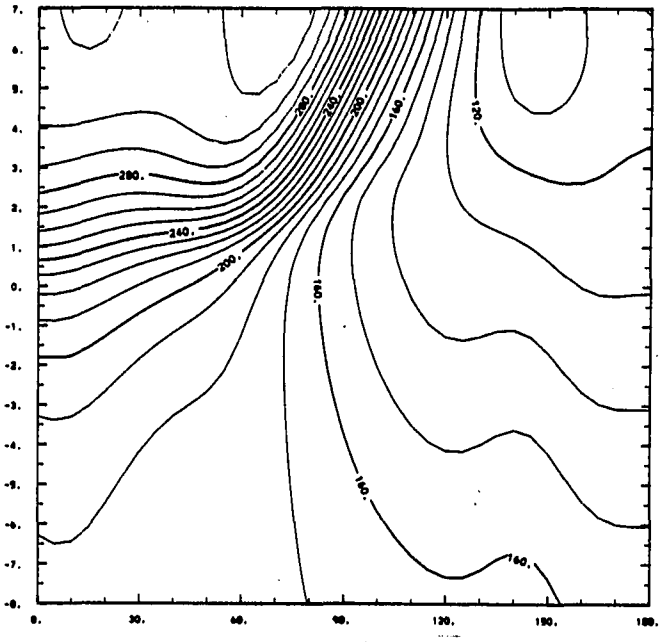
APPENDICES

APPENDIX A

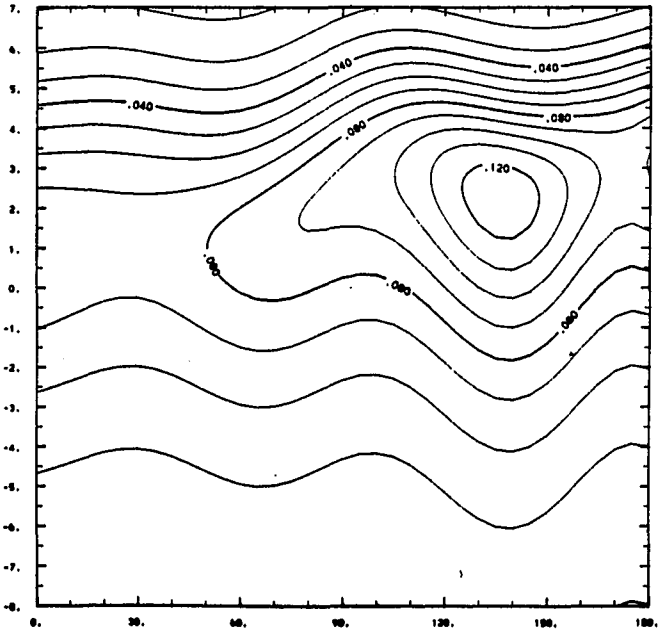
CONTOUR PLOTS FOR EMPIRICAL MODEL FIELDS

Appendix A.1 VTS3

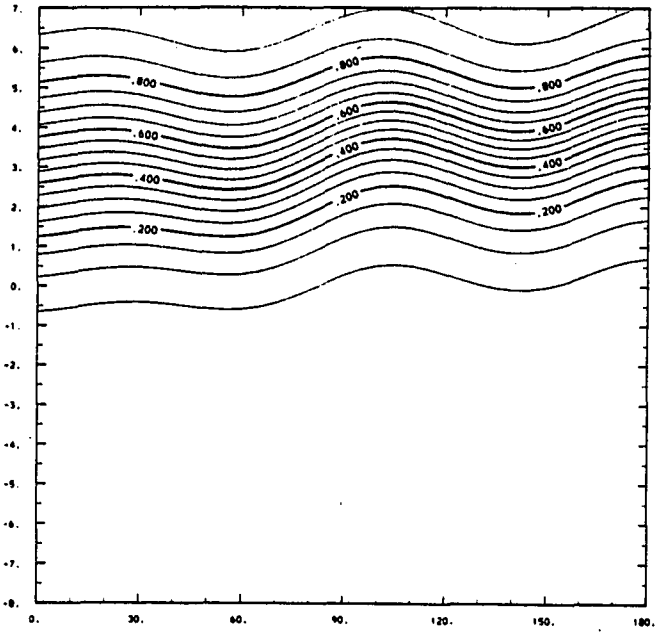
Total Temperature



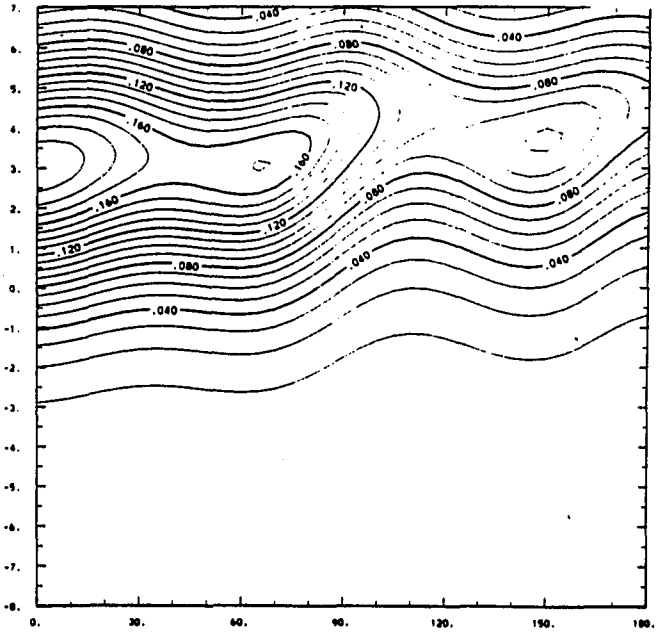
Fractional Number Density of N_2



Fractional Number Density of O

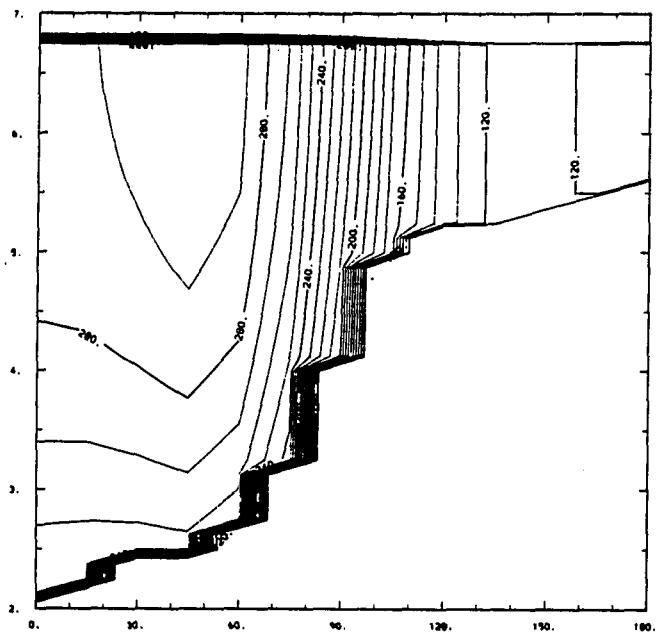


Fractional Number Density of CO

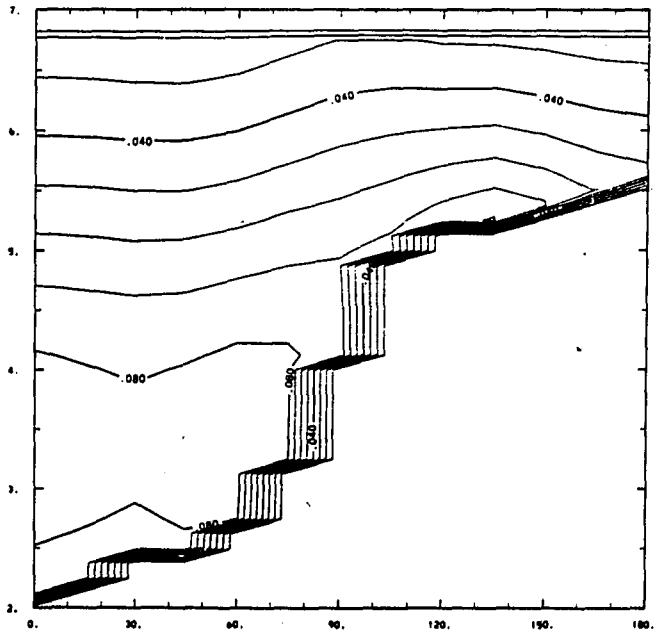


Appendix A.2 HSYM

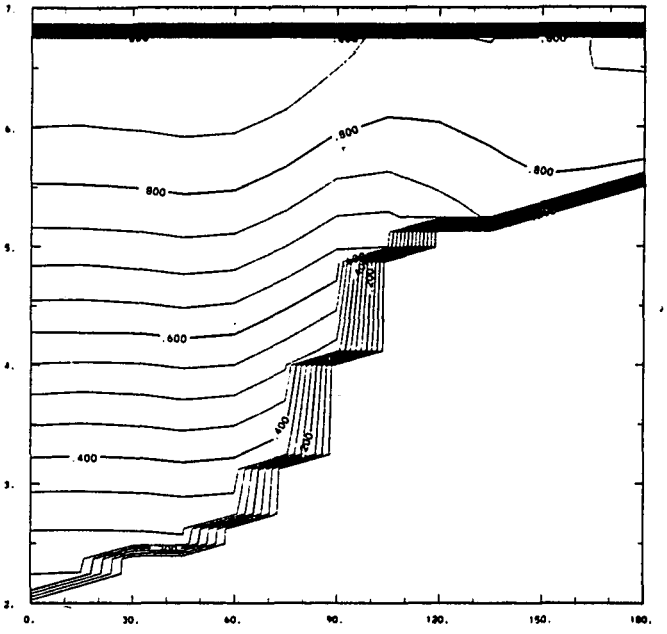
Total Temperature



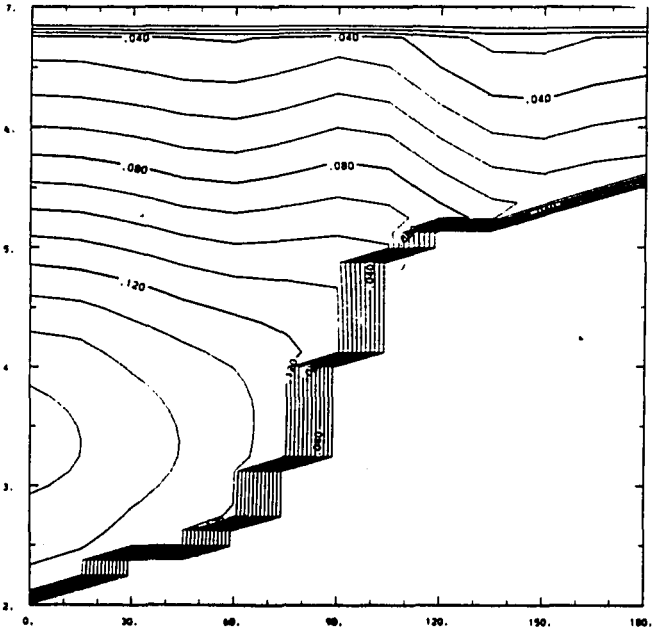
Fractional Number Density of N_2



Fractional Number Density of O



Fractional Number Density of CO



APPENDIX B

NONLINEAR TEMPERATURE DEPENDENT PERTURBATION 15μ COOLING PARAMETERIZATION

1. Perturbation Cooling (DRM2)

$$Q_{15}[T,p,n(0)] = Q_{15}[T_0,p,n(0)_{ref}]*(R-1)$$

$$R = \frac{F[p,T,n(0)]}{F[p,t_0,n(0)_{ref}]}$$

$$F[p,T,n(0)] = \frac{\exp(-960/T)}{1+g[p,T,n(0)]}$$

$$g[p,T,n(0)] \hat{=} \exp(z+1.5)*$$

$$\exp\left[40.6\left(\frac{1}{T_0^{1/3}} - \frac{1}{T^{1/3}}\right)\right]*$$

$$\left(\frac{n(CO_2) + n(0)}{n(CO_2) + 10n(0)}\right)$$

where

$Q_{15}[T_0,p,n(0)_{ref}]$ = global mean 15μ cooling (corresponding to mean temperature "T_0" and reference O-density "$n(0)_{ref}$"

$Q_{15}(T,p,n(0))$ = perturbation cooling

z = log pressure

T_0 = mean temperature

T = total temperature

$n(CO_2)$ = number density of CO_2

$n(0)$ = number density of 0

ref = reference quantities corresponding to the global mean conditions

Alternatively:

$$Q_{15}[T,p,n(0)] = Q_{15}[T_0,p,n(0)_{ref}]*(R-1)$$

$$R = \exp\left(960\left(\frac{1}{T_0} - \frac{1}{T}\right)\right)*$$

$$\frac{1 + e^{z+1.5}*[\ \ ]ref}{1 + e^{z+1.5}*[\ \ ]*EXPT}$$

$$EXPT = \exp\left(40.6\left(\frac{1}{T_0^{1/3}} - \frac{1}{T/^{1/3}}\right)\right)$$

$$[\ \ ]_{ref} = \frac{n(CO_2) + n(0)ref}{n(CO_2) + 10n(0)ref}$$

$$[\ \ ] = \frac{n(CO_2) + n(0)}{n(CO_2) + 10n(0)}$$

2. Improved Perturbation Cooling (2-D Code, 1984)

$$Q_{15}[T,p,n(0)] = Q_{15}[T_0,p,n(0)_{ref}]*(R-1)$$

$$R = \exp\left(960\left(\frac{1}{T_0} - \frac{1}{T}\right)\right)*$$

$$\frac{1 + e^{z+1.5*[\ ]^{new}_{ref}}}{1 + e^{z+1.5*[\ ]^{new}*EXPT}}$$

$$EXPT = \exp\left(40.6\left(\frac{1}{T_0^{1/3}} - \frac{1}{T^{1/3}}\right)\right)$$

$$[\ ]^{new}_{ref} = \frac{n(CO_2) + n(0)ref}{n(CO_2) + ROCO_2*n(0)ref}$$

$$[\ ]^{new} = \frac{n(CO_2) + n(0)ref}{n(CO_2) + ROCO_2M*n(0)ref}$$

$$ROCO_2 = \frac{k(CO_2\text{-}0)*AMAXI(1,\ T/300)}{k(CO_2\text{-}CO_2)*(1+2\times10^{-3}*(T-220)*T/273.3)}$$

$$ROCO_2M = \frac{k(CO_2\text{-}0)*AMAXI(1,\ T_0/300)}{k(CO_2\text{-}CO_2)*(1+2\times10^{-3}*(T_0-220)*T_0/273.3)}$$

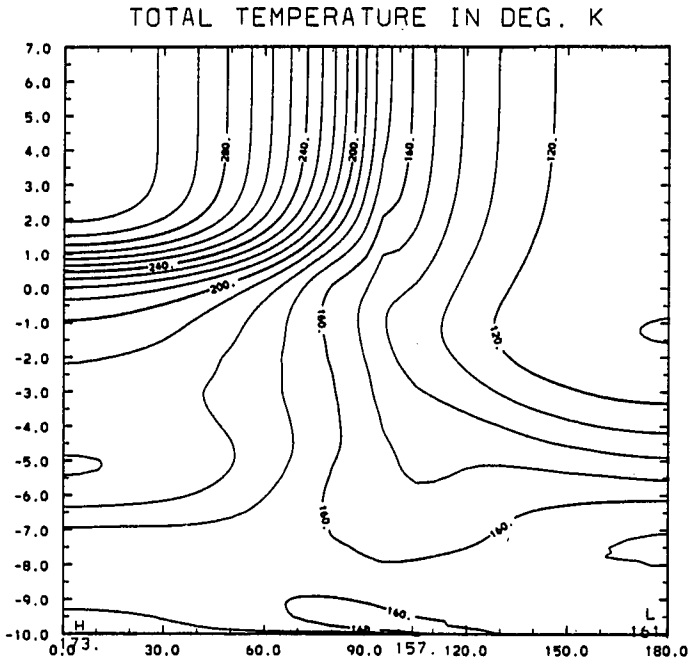
$$k(CO_2\text{-}0) = 2\times10^{-13} \text{ to } 1\times10^{-12}\ cm^3/sec$$

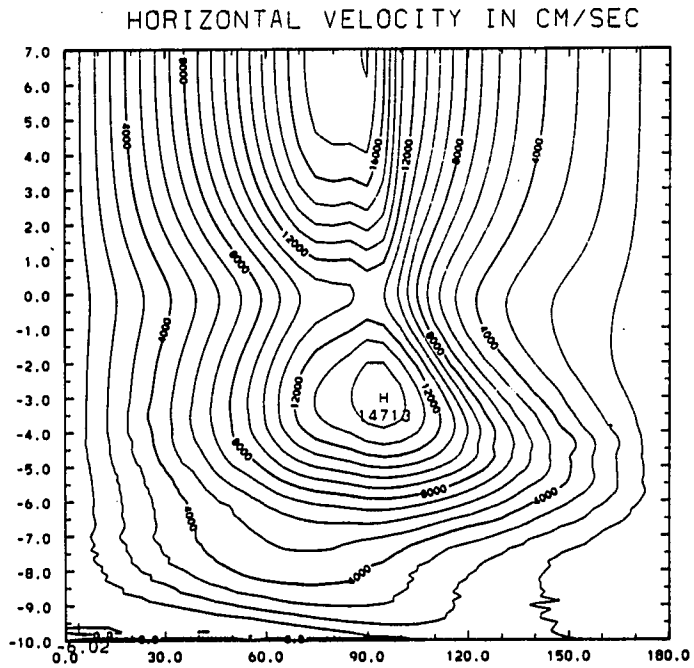
$$k(CO_2\text{-}CO_2) = 5.2\times10^{-15}\ cm^3/sec$$

APPENDIX C

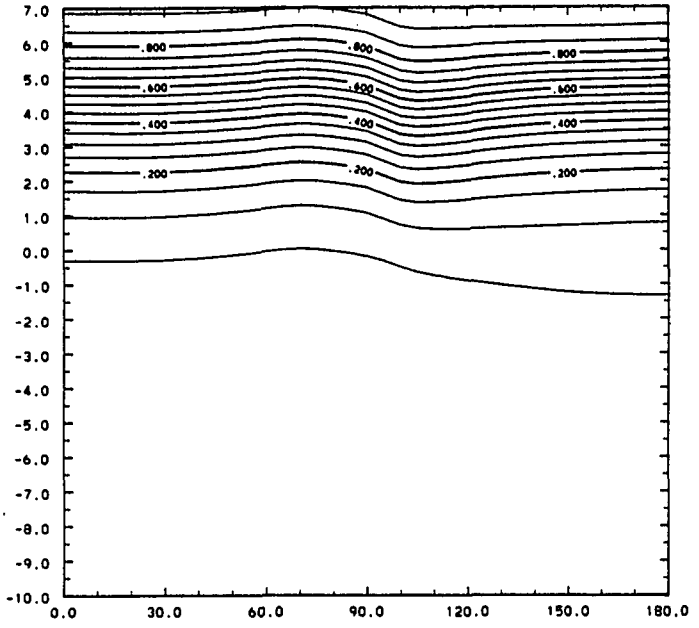
CONTOUR PLOTS FOR TWO-DIMENSIONAL CASES

Appendix C.1 LO EUV Case

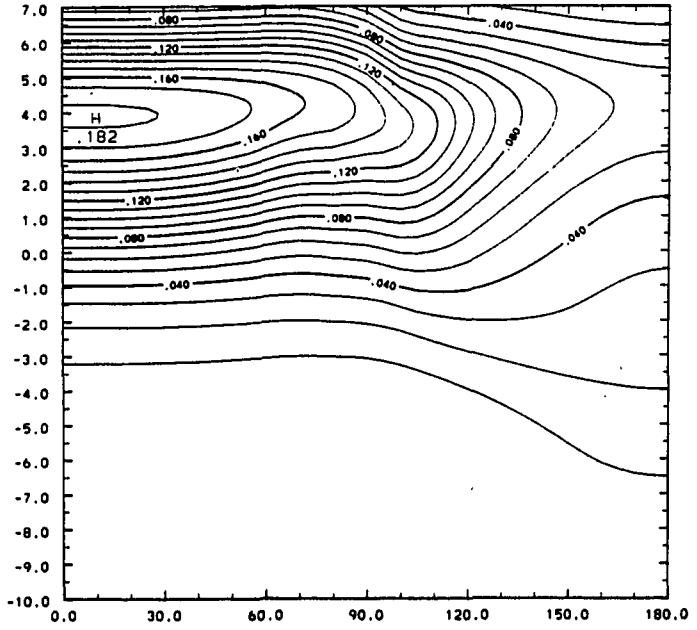




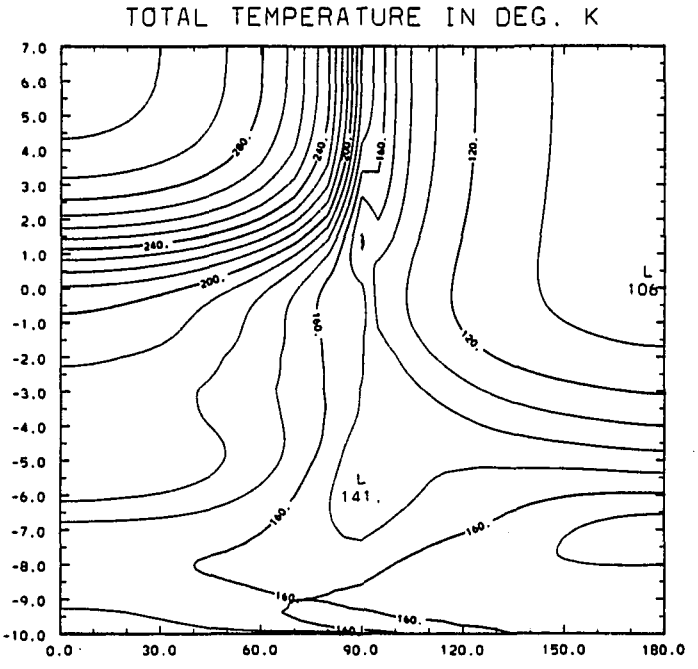
FRACTIONAL NUMBER DENSITY FOR O

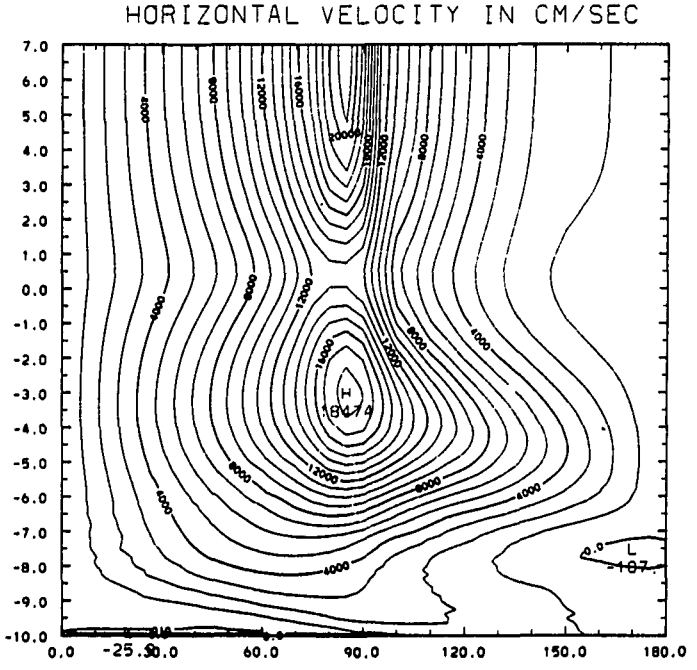


FRACTIONAL NUMBER DENSITY FOR CO

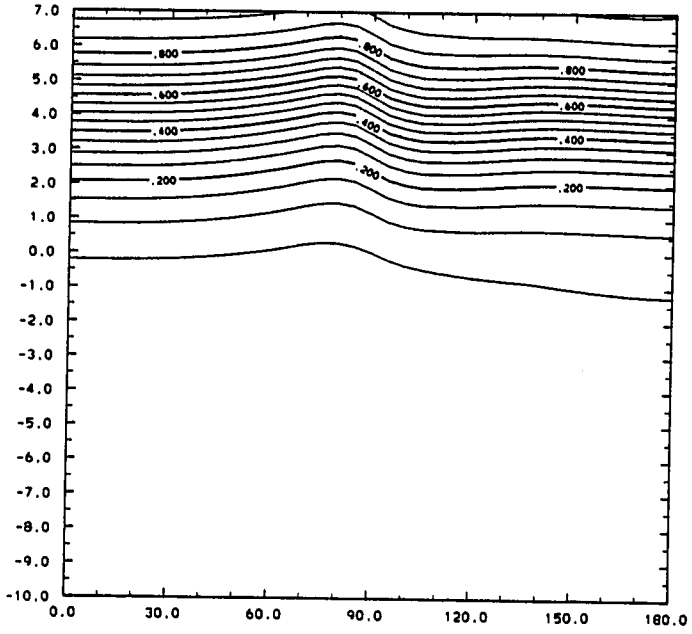


Appendix C.2 MED EUV Case

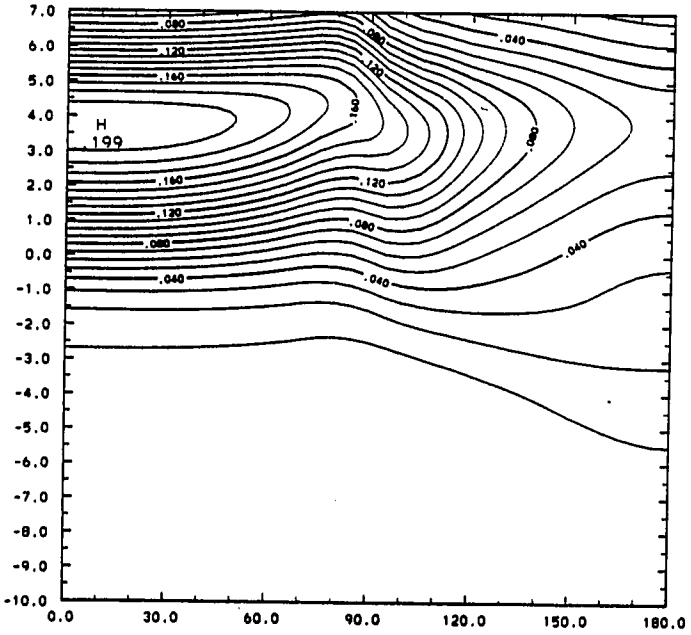




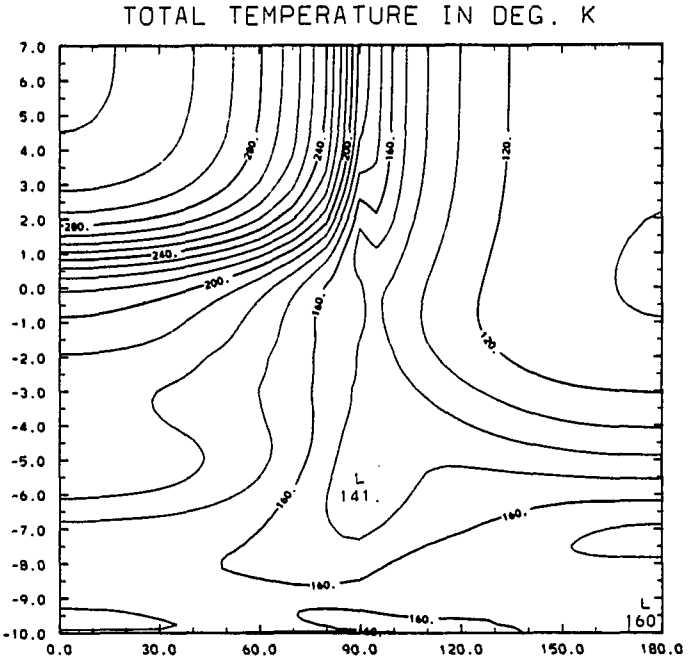
FRACTIONAL NUMBER DENSITY FOR O

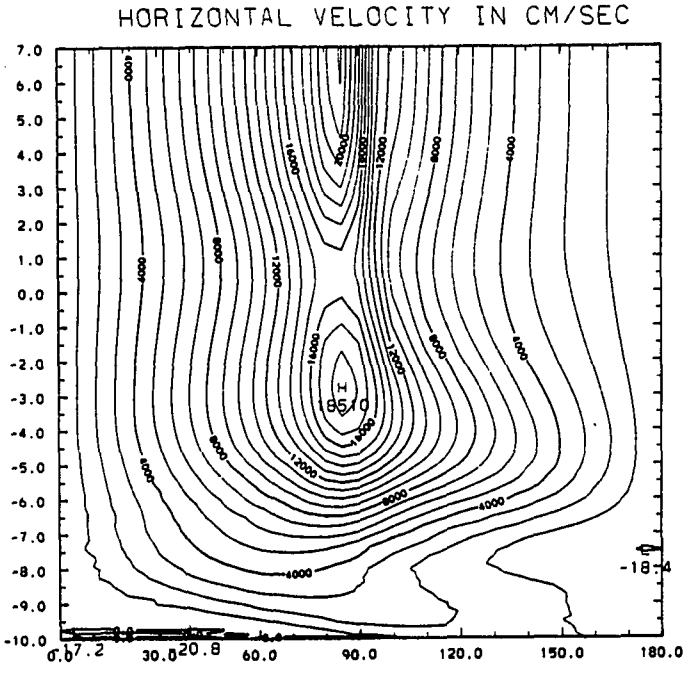


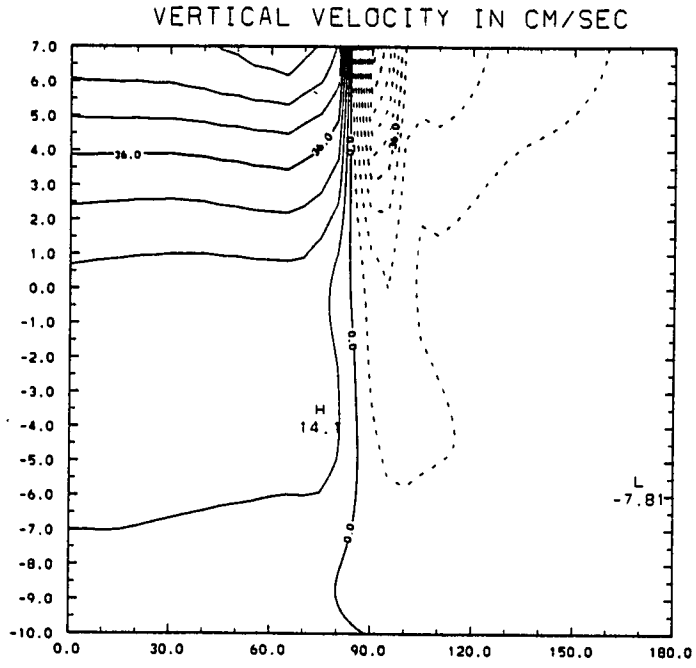
FRACTIONAL NUMBER DENSITY FOR CO

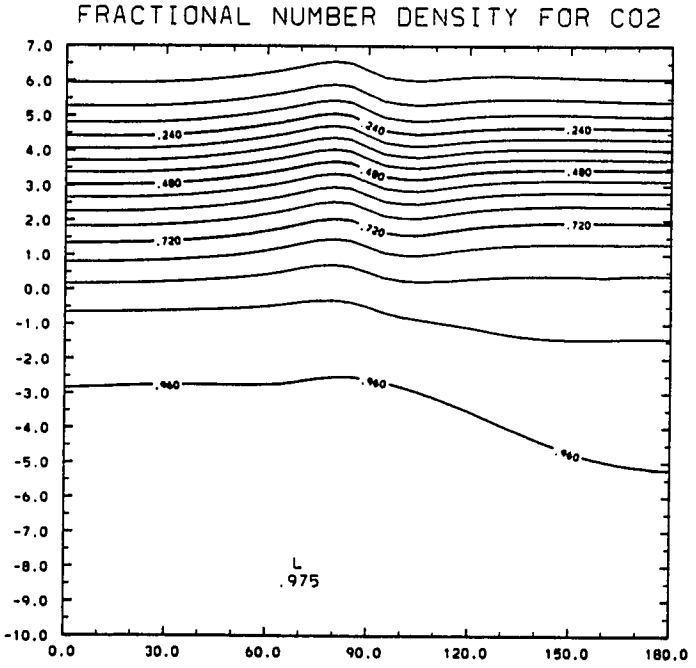


Appendix C.3 Best EUV Case

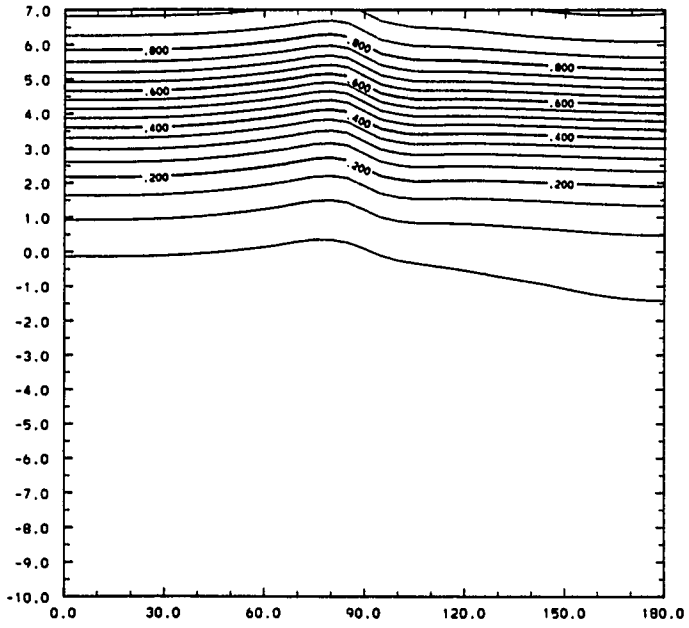




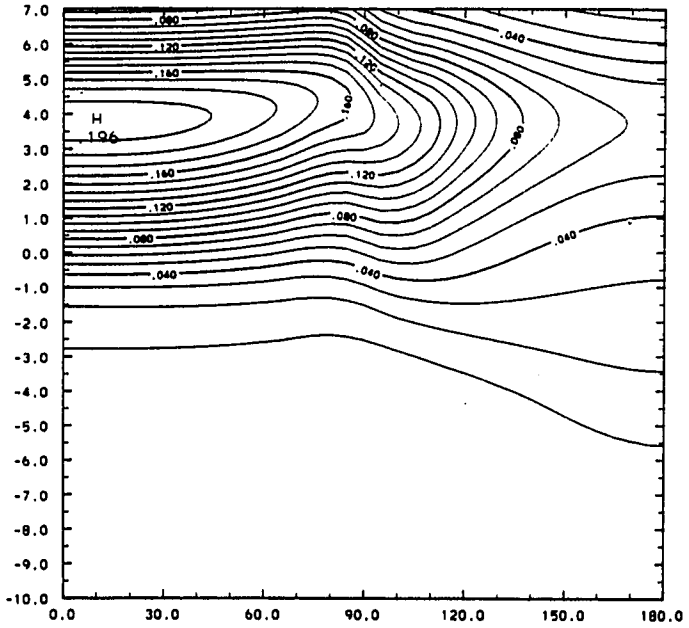

VERTICAL VELOCITY IN CM/SEC
7.0
6.0
5.0
4.0
3.0
2.0
1.0
0.0
-1.0
-2.0
-3.0
-4.0
-5.0
-6.0
-7.0
-8.0
-9.0
-10.0
0.0
30.0
60.0
90.0
120.0
150.0
180.0
H
14.1
L
-7.81


FRACTIONAL NUMBER DENSITY FOR CO2
7.0
6.0
5.0
4.0
3.0
2.0
1.0
0.0
-1.0
-2.0
-3.0
-4.0
-5.0
-6.0
-7.0
-8.0
-9.0
-10.0
0.0
30.0
60.0
90.0
120.0
150.0
180.0
.240
.480
.720
.960
L
.975

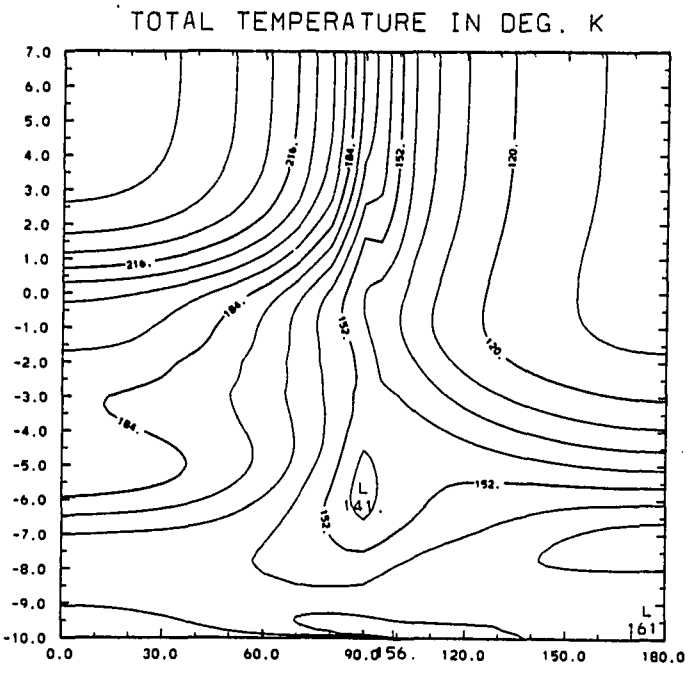
FRACTIONAL NUMBER DENSITY FOR O

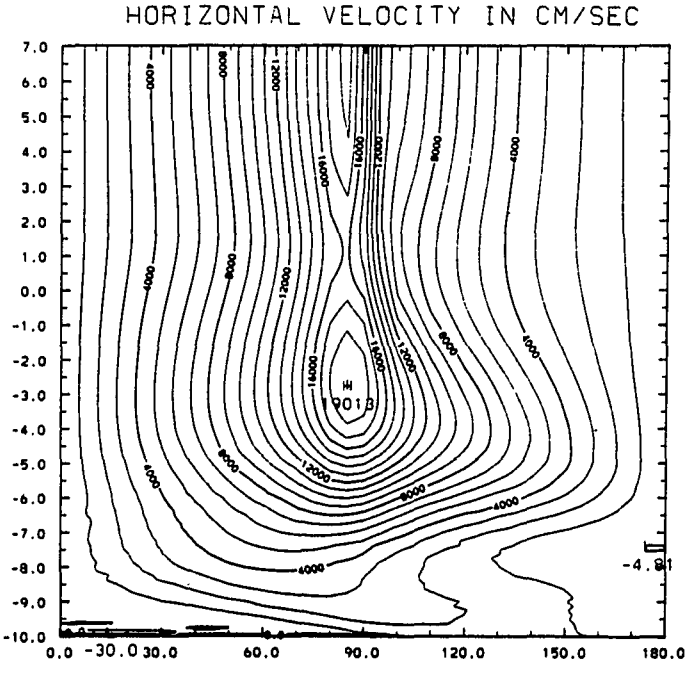


FRACTIONAL NUMBER DENSITY FOR CO

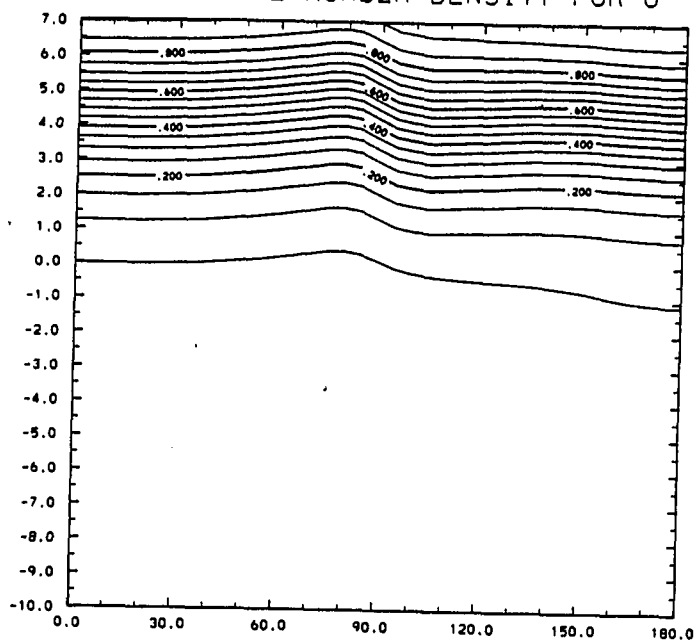


Appendix C.4 Solar Minimum Case

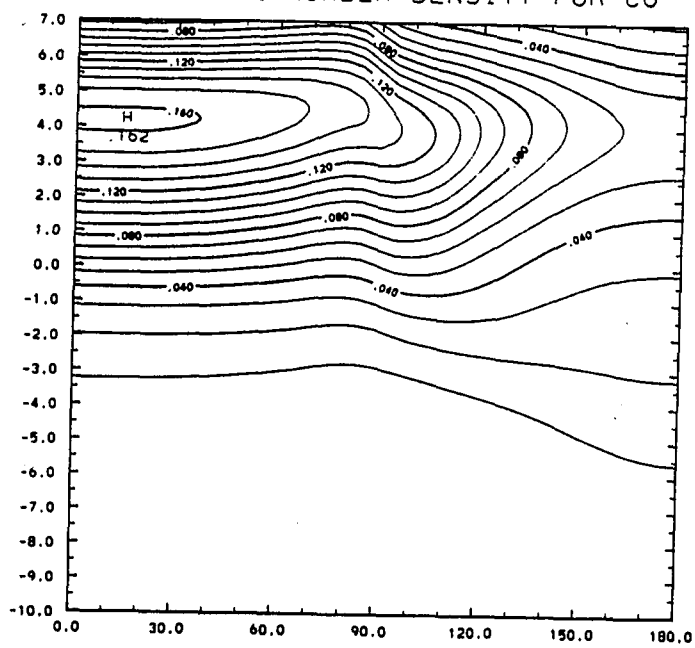




FRACTIONAL NUMBER DENSITY FOR O



FRACTIONAL NUMBER DENSITY FOR CO



APPENDIX D

DERIVATION OF HELIUM MOLECULAR DIFFUSION TERM

The equation for determining CO and O concentrations (or mass mixing ratios) was derived for a log-pressure coordinate system (including nonlinear advection terms) in Dickinson and Ridley (1972). The molecular diffusion term from this coupled continuity-diffusion equation is given below, according to Dickinson and Ridley (1975):

$$e^{z}\tau^{-1}\frac{\partial}{\partial z}\left[\frac{m}{m_{CO_2}}\left(\frac{T_{00}}{T}\right)^{0.25}\underline{\alpha}^{-1}\,\underline{L}\,\underline{\psi}\right] \qquad (D.1)$$

where:

z = $\log_e(p_0/p)$

p_0 = 5×10^{-6} mbar

H_0 = near scale height

τ = diffusion time scale $(p_0/H_0^2/p_{00}\,D_0)$

m = mean mass

m_{CO_2} = CO_2 mean meass (44)

T_{00} = 273°K (at STP for Earth)

T = temperature

$\underline{\psi}$ = mass mixing ratio vector for CO_2 (i = 3), CO (i = 2) and O (i = 1)

The "binary mixture" (with CO_2 derived indirectly) requires that an "effective" molecular diffusion coefficient matrix ($\underline{\alpha}^{-1}$) be defined. $\underline{L}$ is a diffusive operator matrix which applies to the mass mixing ratios ($\underline{\psi}$) defined above. The designated scaling factors incorporated will be re-examined shortly.

The derivation of a He equation now requires that four species and their mutual interaction be addressed. $\underline{\psi}$ now corresponds to O (i = 1), CO (i = 2), He (i = 3) and CO_2 (i = 4). Recall the matrix $\underline{\alpha}$ varies as the inverse of the mutual diffusion coefficients (see Dickinson and Ridley, 1975), now according to:

$$\alpha_{11} = -[\phi_{14} + (\phi_{12} - \phi_{14})\psi_2 + \underbrace{(\phi_{13} - \phi_{14})\psi_3}_{\delta_{11}}]$$

$$\alpha_{12} = (\phi_{12} - \phi_{14})\psi_1$$

$$\alpha_{13} = (\phi_{13} - \phi_{14})\psi_1$$

$$\alpha_{21} = (\phi_{21} - \phi_{24})\psi_2$$

$$\alpha_{22} = -[\phi_{24} + (\phi_{21} - \phi_{24})\psi_1 + \underbrace{(\phi_{23} - \phi_{24})\psi_3}_{\delta_{22}}]$$

$$\alpha_{23} = (\phi_{23} - \phi_{24})\psi_2$$

$$\alpha_{31} = \underbrace{(\phi_{31} - \phi_{34})\psi_3}_{\delta_{31}}$$

$$\alpha_{32} = \underbrace{(\phi_{32} - \phi_{34})\psi_3}_{\delta_{32}}$$

$$\alpha_{33} = -[\phi_{34} + (\phi_{31} - \phi_{34})\psi_1 + (\phi_{32} - \phi_{34})\psi_2] \qquad (D.2)$$

where:

$$\phi_{ij} = \frac{D}{D_{ij}} \frac{m_{CO_2}}{m_j} \qquad (D.3)$$

The δ_{ij}" terms are underscored above, and represent those which are nonlinear and second order. The "D_{ij}" are the mutual diffusion coefficients for gases i and j. "D" is a characteristic diffusion coefficient with the same temperature and pressure dependence as D_{ij}, i.e.,

$$D = D_0\left(\frac{P_{00}}{p}\right)\left(\frac{T}{T_{00}}\right)^{1.75} \qquad (D.4)$$

($P_{00} = 10^6$ dyne/cm^2, $T_{00} = 273$°K at STP, $D_0 = 0.2$ cm^2/sec). STP values of D_{ij} (involving He) are given below, according to Mason and Marrero (1970):

Molecules	Coefficient (cm^2/sec^{-1})
He-O	0.8670
He-CO	0.6195
He-CO_2	0.5129

CO_2, CO, and O mutual diffusion coefficients are those used in Table 1 of Dickinson and Ridley (1972).

The $\underline{\alpha}$-array (Dickinson and Ridley, 1975) is now written as $\alpha(0) + \delta$, where δ is small. This is consistent with the assumption that $\psi_3 << \psi_1$ and ψ_2, for which He is a minor species. The array can be simplified by means of a binomial expansion in order to retain first order terms:

$$\underline{\alpha}^{-1'} = [\underline{\alpha}(0) + \underline{\delta}]^{-1} = \underline{\alpha}^{-1}(0) - \underline{\alpha}(0)^{-1}\,\underline{\delta}\,\underline{\alpha}^{-1}(0) \qquad (D.5)$$

Then $\underline{\alpha}^{-1}(0) = \underline{\beta}$ where det $= (\alpha_{11}\alpha_{22} - \alpha_{12}\alpha_{21})$ giving:

$$\beta_{11} = \alpha_{22}/\det$$

$$\beta_{12} = -\alpha_{12}/\det$$

$$\beta_{13} = (\alpha_{12}\alpha_{23} - \alpha_{22}\alpha_{13})/(\alpha_{33}\det)$$

$$\beta_{21} = -\alpha_{21}/\det$$

$$\beta_{22} = \alpha_{11}/\det$$

$$\beta_{23} = (\alpha_{21}\alpha_{13} - \alpha_{11}\alpha_{23})/(\alpha_{33}\det)$$

$$\beta_{31} = 0$$

$$\beta_{32} = 0$$

$$\beta_{33} = 1/\alpha_{33} \qquad (D.6)$$

The resulting third vector component (for He), neglecting second order terms, appears as follows:

$$\beta_{33}[-(C_{11}L_{11}\psi_1 + C_{22}L_{22}\psi_2) + L_{33}\psi_3] \qquad (D.7)$$

where

$$C_{11} = \delta_{31}\beta_{11} + \delta_{32}\beta_{21}$$

$$C_{22} = \delta_{31}\beta_{12} + \delta_{32}\beta_{22}$$

$$L_{ii} = \frac{\partial}{\partial z} - \left(1 - \frac{1}{m}\left(m_i - \frac{dm}{dz}\right)\right) \qquad (D.8)$$

The molecular diffusion term is now given:

$$e^{z_\uparrow - 1}\frac{\partial}{\partial z}\left[\frac{m}{m_{CO_2}}\left(\frac{T_{00}}{T}\right)^{0.25}\beta_{33}\langle-(C_{11}L_{11}\psi_1 + C_{22}L_{22}\psi_2) + L_{33}\psi_3\rangle\right] \qquad (D.9)$$

BIBLIOGRAPHY

BIBLIOGRAPHY

Anderson, D. E. Jr., The Mariner 5 Ultraviolet Spectrometer Experiment: Analysis of Hydrogen Lyman-alpha Data, J. Geophys. Res., 81, 1213-1216, 1976.

Apruzese, J. P., D. F. Strobel and M. R. Schoeberl, Parameterization of IR Cooling in a Middle Atmosphere Dynamics Model. 2. Non-LTE Radiative Transfer and the Globally Averaged Temperature of the Mesosphere and Lower Thermosphere, J. Geophys. Res., 89, 4917-4926, 1984.

Banks, P. M. and G. Kockarts, Aeronomy, Academic Press, New York, 1973.

Barth, C. A., J. B. Pierce, K. K. Kelly, L. Wallace and W. G. Fastie, Ultraviolet Emission Observed Near Venus from Mariner 5, Science, 158, 1675-1678, 2967.

Bauer, S. J. and H. A. Taylor, Modulation of Venus Ion Densities Associated with Solar Variations, Geophys. Res. Lett., 8, 840-842, 1981.

Belton, M. J. S., D. M. Hunten and R. M. Goody, Quantitative Spectroscopy of Venus in the Region 8000-11000 A., in The Atmospheres of Venus and Mars, J. C. Brandt and M. C. McElroy, Eds., New York, Gordon and Breach, 69-98, 1968.

Bertaux, J. L., J. Blamont, M. Marcelin, V. G. Kurt, N. N. Romanova and A. S. Smirnow, Lyman-alpha Observations of Venera 9 and 10. I. The Nonthermal Hydrogen Population in the Exosphere of Venus, Planet. Space Sci., 26, 817-831, 1978.

Bougher, S. W., The Ultraviolet Night Airglow of Venus--Morphology and Implications, Masters Thesis, The University of Colorado, 1980.

_____, T. E. Cravens, A. F. Nagy, R. G. Roble and E. C. Ridley, A Finite Difference Model of the Venus Thermospheric Circulation, EOS, 62, 318, 1981.

Brinton, H. C., H. A. Taylor, Jr., H. B. Niemann, H. G. Mayr, A. F. Nagy, T. E. Cravens and D. F. Strobel, Venus Nighttime Hydrogen Bulge, Geophys. Res. Lett., 7, 865-868, 1980.

Broadfoot, A. L., S. Kumar, M. J. S. Belton and M. B. McElroy, Ultraviolet Observations of Venus from Mariner 10: Preliminary Results, Science, 183, 1315-1318, 1974.

Cairns, E. B. and J. A. R. Samson, Absorption and Photionization Cross Sections of CO_2, CO, Ar, and He at Intense Solar Emission Lines, J. Geophys. Res., 70, 99, 1965.

_____ and _____, Total Absorption Cross Sections of CO and CO_2 in the Region 550-200Å, J. Opt. Soc. Am., 56, 526, 1966.

Center, R. E., Vibrational Relaxation of CO_2 by O Atoms, J. Chem. Phys., 59, 3523-3527, 1973.

Chamberlain, J. W., Theory of Planetary Atmospheres: An Introduction to Their Physics and Chemistry, International Geophysics Series, Vol. 23, Academic Press, 1978.

Chapman, S. and T. G. Cowling, The Mathematical Theory of Nonuniform Gases, Cambridge University Press, 423 pp., 1970.

Colegrove, F. D., F. J. Johnson and W. B. Hanson, Atmospheric Composition in the Lower Thermosphere, J. Geophys. Res., 7, 2227-2235, 1966.

Connes, P., J. Connes, W. S. Benedict and L. D. Kaplan, Traces of HCL and HF in the Atmosphere of Venus, Astrophys. J., 152, 731-743, 1967.

Cook, G. R., P. H. Metzger and M. Ogawa, Photoionization and Absorption Coefficients of CO in the 600 to 1000Å Region, Can. J. Phys., 43, 1706, 1965.

_____, _____ and _____, Absorption, Photoionization and Fluorescence of CO_2, J. Chem. Phys., 44, 2935, 1966.

Cramp, J. H. W. and J. D. Lambert, Vibrational Relaxation of CO_2 ($\nu 3$) by O atoms, Chem. Phys. Lett., 22, 146-149, 1973.

Cravens, T. E., A. J. Kliore, J. U. Kozyra and A. F. Nagy, The Ionispheric Peak on the Venus Dayside, J. Geophys. Res., 86, 11323-11329, 1981.

_____ and A. F. Nagy, Aeronomy of the Inner Planets, Rev. of Geophys. and Space Phys., 21, 263-273, 1983.

Dalgarno, A., R. J. W. Henry and A. L. Stewart, The Photoionization of Atomic Oxygen, Planet. Space Sci., 12, 235-246, 1964.

Dickinson, R. E., Circulation and the Thermal Structure of the Venusian Thermosphere, J. Atmos. Sci., 28, 885-894, 1971.

_____, Infrared Radiative Heating and Cooling in the Venusian Mesosphere. I. Global Mean Radiative Equilibrium J. Atmos. Sci., 29, 1531-1556, 1972.

_____, Infrared Radiative Emission in the Venusian Mesosphere, J. Atmos. Sci., 33, 290-303, 1976.

_____, Venus Mesosphere and Thermosphere Temperature Structure: Global Mean Radiative and Conductive Equilibrium, Icarus, 27, 479-493, 1976.

_____ and E. C. Ridley, A Numerical Solution for the Composition of a Steady Subsolar-to-Antisolar Circulation with Application to Venus, J. Atmos. Sci., 29, 1557-1570, 1972.

_____ and _____, A Numerical Model for the Dynamics and Composition of the Venusian Thermosphere, J. Atmos. Sci., 32, 1219-1231, 1975.

_____ and _____, Venus Mesosphere and Thermosphere Temperature Structure. II. Day-Night Variations, Icarus, 30, 163-178, 1977.

_____, _____ and R. G. Roble, Meridional Circulation in the Thermosphere. I. Equinox Conditions, J. Atmos. Sci., 32, 1737-1754, 1975.

_____, _____ , and _____, Meridional Circulation in the Thermosphere. II. Solstice Conditions, J. Atmos., Sci., 34, 178-192, 1977.

_____, _____, and _____, A Three-Dimensional General Circulation Model of the Thermosphere, J. Geophys. Res., 86, 1499-1512, 1981.

_____, _____ and _____, Thermospheric General Circulation with Coupled Dynamics and Composition, J. Atmos. Sci., 41, 205-219, 1984.

Donnelly, R. F. and J. H. Pope, NOAA Technical Report, ERL 276-SEL 25, U.S. Government Printing Office, Washingon, D.C., 1973.

Feldman, P. D., H. W. Moos, J. T. Clarke, and A. L. Lane, Identification of the Ultraviolet Nightglow from Venus, Nature, London 279, 221, 1979.

Fox, J. L. and A. Dalgarno, Ionization, Luminosity and Heating of the Upper Atmosphere of Mars, J. Geophys. Res., 84, 7315-7331, 1979.

_____ and _____, Ionization Luminosity and Heating of the Upper Atmosphere of Venus, J. Geophys. Res., 86, 629-639, 1981.

Gerard, J. C., A. I. F. Stewart and S. W. Bougher, The Altitude Distribution of the Venus Ultraviolet Nightglow and Implications on Vertical Transport, Geophys. Res. Lett., 8, 633-636, 1981.

Gierasch, P. J. and R. M. Goody, The Effect of Dust on the Temperature of the Martian Atmosphere, J. Atmos., Sci., 29, 400-402, 1971.

Gordiets, B. F., Yu. N. Kulikov, M. N. Markov, and M. Ya Marov, Numerical Modelling of the Thermospheric Heat Budget, J. Geophys. Res., 87, 4504-4515, 1982.

_____ and _____, On the Mechanisms of the Cooling of the Nightside Thermosphere of Venus, COSPAR, June 22-July 6, 1984, Graz, Austria.

Hedin, A. E., J. E. Salah, J. V. Evans, C. A. Reber, G. P. Newton, N. W. Spencer, D. C. Kayser, C. Alcayde, P. Bauer, L. Cogger, and J. P. McClure, A Global Thermospheric Model Based on Mass Spectrometer and Incoherent Scatter Data, MSIS I, N_2 Density and Temperature, J. Geophys. Res., 82, 2139, 1977a.

_____, C. A. Reber, G. P. Newton, N. W. Spencer, H. C. Brinton, H. G. Mayr, and W. E. Potter, A Global Thermospheric Model Based on Mass Spectrometer and Incoherent Scatter Data, MSIS 2, Composition, J. Geophys. Res., 82, 2148, 1977b.

_____, H. B. Niemann, W. T. Kasprazak and A. Seiff, Global Empirical Model of the Venus Thermosphere, J. Geophys. Res., 88, 73-83, 1983a.

_____, _____ and ___, Progress on Thermospheric Modelling and Recommendations for Venus, private communication, 1983b.

Heroux, L. and H. E. Hinteregger, Aeronomical Reference Spectrum for Solar UV below 2000Å, J. Geophys. Res., 83, 5305-5308, 1978.

Hinteregger, H. E., The Extreme Ultraviolet Solar Spectrum and its Variation During a Solar Cycle, Ann. Geophys., 26, 547-554, 1970.

_____, EUV Fluxes in the Solar Spectrum Below 2000Å, J. Atmos. Terr. Phys., 38, 791-806, 1976.

Holton, J. R., An Introduction to Dynamic Meteorology, International Geophysics Series, Vol. 16, Academic Press, New York, 1972.

_____, The Role of Gravity Wave Induced Drag and Diffusion in the Momentum Budget of the Mesosphere, J. Atmos. Sci., 39, 791-799, 1982.

_____, The Influence of Gravity Wave Breaking on the General Circulation of the Middle Atmosphere, J. Atmos. Sci., 40, 2497-2507, 1983.

_____ and W. M. Wehrbein, A Numerical Model of the Zonal Mean Circulation of the Middle Atmosphere, Pure Appl. Geophys., 118, 284-306, 1980.

Hunten, D. M., Energetics of Thermospheric Eddy Transport, J. Geophys. Res., 79, 2533-2534, 1974.

Izakov, M. N., Effect of Turbulence on the Thermal Regime of Planetary Thermospheres, Kosmich Issled., 16, 403, 1978.

Johnson, F. S. and B. Gottlieb, Eddy Mixing and Circulation at Ionospheric Levels, Planet. Space Sci., 18, 1707-1718, 1970.

Keating, G. M., J. Y. Nicholson and L. R. Lake, Venus Upper Atmosphere Structure, J. Geophys. Res., 85, 7941, 1980.

_____ et al., VIRA Models of Venus Neutral Upper Atmosphere Structure and Composition, presented at Workshop III, Venus Atmosphere and Ionosphere, 25th Plenary Meeting of COSPAR, Graz, Austria, 28 June 1984.

Kockarts, G., Nitric Oxide Cooling in the Terrestrial Thermosphere, Geophys. Res. Lett., 7, 137, 1980.

Krasnopolsky, V. A., A. A. Krysko, V. N. Rogachev, and V. A. Parshev, Spectroscopy of the Venus Night Airglow from the Venera-9, 10 Orbiters, Cosmic Res., 14, 789-795, 1976.

Kumar,. S., A. L. Broadfoot, Helium 584-A Airglow Emission from Venus: Mariner 10 Observations, Geophys. Res. Lett., 2, 357-360, 1975.

Kurt, V. G., S. B. Dostovalow and E. K. Sheffer, The Venus Far Ultraviolet Observations with Venera 4, J. Atmos. Sci., 25, 668-671, 1968.

Lawrence, G. M., C. A. Barth and V. Argabright, Excitation of the Venus Night Airglow, Science, 195, 573-574, 1977.

Lee, L. C., R. W. Carlson, D. L. Judge and M. Agawa, Vacuum Ultraviolet Fluorescence from Photodissociation Fragments of CO and CO_2, J. Chem. Phys., 63, 3987-3995, 1975.

Lindzen, R. S., Tides and Gravity Waves in the Upper Atmosphere, in Mesospheric Models and Related Experiments, D. Fiocco, ed., D. Riedel, Hingham, Mass., 1971.

_____, Turbulence and Stress Owing to Gravity Wave and Tidal Breakdown, J. Geophys. Res., 86, 9707-9714, 1981.

Liu, S. C. and T. M. Donahue, The Aeronomy of the Upper Atmosphere of Venus, Icarus, 24, 148-156, 1975.

Nagy, A. F., T. E. Cravens, S. G. Smith, H. A. Taylor, Jr. and H. C. Brinton, Model Calculations of the Dayside Ionosphere of Venus: Ionic Composition, J. Geophys. Res., 85, 7795-7801, 1980.

Niemann, H. B., W. T. Kasprazak, A. E. Hedin, D. M. Hunten, and N. W. Spencer, Mass Spectrometric Measurements of the Neutral Gas Composition of the Thermosphere and Exosphere of Venus, J. Geophys. Res., 85, 7817-7827, 1980.

_____, R. E. Hartle, A. E. Hedin, W. T. Kasprazak, N. W. Spencer, D. M. Hunten and G. R. Carrigan, Venus Upper Atmosphere Neutral Gas Composition: First Observations of the Diurnal Variations, Science, 205, 54-56, 1979.

Massie, S. T., D. M. Hunten and D. T. Sowell, Day and Night Models of the Venus Thermosphere, J. Geophys. Res., 88, 3955-3969, 1983.

Mason, E. A. and T. R. Marrero, The Diffusion of Atoms and Molecules, Adv. Atmospheric and Molecular Physics, 6, 155-232, Academic Press, New York, 1970.

Matsuno, T., A Quasi One-Dimensional Model of the Middle Atmosphere Circulation Interacting with Internal Gravity Waves, J. Meteor. Soc. Japan, 60, 215-226, 1982.

Mayr, H. G. and H. Volland, Theoretical Model for the Latitude Dependence of the Thermospheric Annual and Semiannual Variations, J. Geophys. Res., 77, 6774-6790, 1972.

_____, I. Harris, R. E. Harris and W. R. Hoegy, Diffusion Model for the Upper Atmosphere of Venus, J. Geophys. Res., 83, 4411-4416, 1978.

_____, _____ and N. W. Spencer, Some Properties of the Upper Atmosphere Dynamics, Rev. Geophys. and Space Phys., 16, 539-565, 1978.

_____, _____, H. B. Niemann, H. C. Brinton, N. W. Spencer, H. A. Taylor, Jr., R. E. Hartle, W. R. Hoegy, D. M. Hunten, Dynamic Properties of the Thermosphere Inferred From Pioneer Venus Mass Spectrometer Measurements, J. Geophys. Res., 85, 7841-7847, 1980.

_____, _____, D. R. Stevens-Rayburn, H. B. Niemann, H. A. Taylor, Jr., R. E. Hartle and H. Volland, On the Diurnal Variations in the Temperature and Composition: A Three-Dimensional Model with Superrotation, COSPAR, June 22-July 6, 1984.

McElroy, M. B. and J. C. Brandt, The Atmospheres of Venus and Mars, 1968.

_____ and McConnell, J. C., Dissociation of CO_2 in the Martian Atmosphere, J. Atmos. Sci., 28, 879-884, 1971.

_____, T. Y. Kong and Y. L. Yung, Photochemistry and Evolution of Mars' Atmosphere: A Viking Perspective, J. Geophys. Res., 82, 4379-4388, 1977.

Moroz, V. I., The CO_2 Bands and Some Optical Properties of the Atmosphere over Venus, Sov. Astron.-A. J., 11, 653-661, 1968.

Roble, R. G., R. E. Dickinson and E. C. Ridley, Seasonal and Solar Cycle Variations of the Zonal Mean Circulation of the Thermosphere, J. Geophys. Res., 82, 5493-5504, 1977.

_____, _____ and _____, Global Circulation and Temperature Structure of Thermosphere with High Latitude Plasma Convection, J. Geophys. Res., 87, 1599-1614, 1982.

Rodriguez, J. M., M. J. Prather, and M. B. McElroy, Hydrogen on Venus: Exospheric Distribution and Escape, submitted to J. Geophys. Res., 1984.

Rottman, G. J., and H. W. Moos, The Ultraviolet (1200-1900Å) Spectrum of Venus, J. Geophys. Res. 78, 8033-8048, 1973.

Rusch, D. W. and T. E. Cravens, A Model of the Neutral and Ion Nitrogen Chemistry in the Daytime Thermosphere of Venus, Geophys. Res. Lett., 6, 791-794, 1979.

Russell, C. T., R. C. Elphic and J. A. Slavin, Initial Pioneer Venus Magnetic Field Results: Dayside Observations, Science, 203, 745-748, 1979a.

_____, _____ and _____, Initial Pioneer Venus Magnetic Field Results: Nightside Observations, Science, 205, 114-116, 1979b.

Schoeberl, M. R. and D. F. Strobel, The Zonally Averaged Circulation of the Middle Atmosphere, J. Atmos. Sci., 35, 577-591, 1978.

Schubert, G., C. Covey, A. Del Genio, L. S. Elson, G. Keating, A. Seiff, R. E. Young, J. Apt, C. C. Counselman III, A. J. Kliore, S. S. Limaye, H. E. Revercomb, L. A. Sromovsky, V. E. Suomi, F. Taylor, R. Woo and U. von Zahn, Structure and Circu-

lation of the Venus Atmosphere, J. Geophys. Res., 85, 8007-8025, 1980.

_____, General Circulation and the Dynamical State of the Venus Atmosphere, in Venus, Ch. 21, 681-765, University of Arizona Press, Tucson, Arizona, 1983.

_____ and R. L. Walterscheid, Propagation of Small-Scale Acoustic-Gravity Waves in the Venus Atmosphere, J. Atmos. Sci., 41, 1202-1213, 1984.

Seiff, A., D. B. Kirk, R. E. Young, S. C. Sommer, R. C. Blanchard, J. T. Findley and G. M. Kelly, Thermal Contrasts in the Atmosphere of Venus: Initial Appraisal from Pioneer Venus Probe Data, Science, 205, 46-49, 1979.

_____, _____, _____, R. C. Blanchard, J. T. Findley, G. M. Kelly and S. C. Sommer, Measurements of the Thermal Structure and Thermal Contrasts in the Atmosphere of Venus and Related Dynamical Observations: Results from the Four Pioneer Venus Probes, J. Geophys. Res., 85, 7903-7933, 1980.

_____ and D. B. Kirk, Structure of the Venus Mesosphere and Lower Thermosphere from Measurements during Entry of the Pioneer Venus Probes, Icarus, 49, 49-70, 1982a.

_____, Dynamical Implications of the Observed Thermal Contrasts in Venus' Upper Thermosphere, Icarus, 51, 574-592, 1982b.

_____, Thermal Structure of the Atmosphere of Venus, in Venus, Ch. 11, 215-279, University of Arizona Press, Tucson, Arizona, 1983.

Sharma, R. D. and R. M. Nadile, Carbon Dioxide (ν2) Radiance Results Using a New Non-Equilibrium Model, AFGL,TR-81-0064, 1981.

Shemansky, D. E., CO_2 Extinction Coefficient 1700-3000Å, J. Chem. Phys., 56, 1582-1587, 1972.

Shimizu, M., Atmospheric Mixing in the Upper Atmospheres of Jupiter and Venus, J. Geophys. Res., 79, 5311-5313, 1974.

Simpson, C. J. S. M., P. D. Gait, J. M. Simmie, The Vibrational Deactivation of the Bending Mode of CO_2 by O_2 and N_2, Chem. Phys. Lett., 47, 133-136, 1977.

Stair, A. T. Jr., Atmospheric Emission Spectra (1.43-16 μm) of the Earth's Limb (SPIRE), Technical Digest Topical Meeting on Atmospheric Spectroscopy, Optical Society of America, Keystone, Colorado, 1978.

Stewart, A. I. F., Design and Operation of the Pioneer Venus Orbiter Ultraviolet Spectrometer, IEEE Trans. Geosci. Remote Sensing, GE-18, 65, 1980.

_____, A. Barth, C. W. Hord, A. L. Lane, Mariner 9 Ultraviolet Spectrometer Experiment: Structure of Mars Upper Atmosphere, Icarus, 469-474, 1972.

_____, D. E. Anderson, Jr., L. E. Esposito and C. A. Barth, Ultraviolet Spectroscopy of Venus: Initial Results from the Pioneer Venus Orbiter, Science, 203, 777, 1979.

_____ and C. A. Barth, Ultraviolet Night Airglow of Venus, Science, 205, 59, 1979.

_____, J. C. Gerard, D. W. Rusch, and S. W. Bougher, Morphology of the Venus Ultraviolet Night Airglow, J. Geophys. Res., 85, 7861, 1980.

Taylor, F. W., D. M. Hunten and L. V. Ksanfomaliti, The Thermal Balance of the Middle and Upper Atmosphere of Venus, in Venus, Ch. 20, 650-680, University of Arizona Press, Tucson, Arizona, 1983.

Taylor, H. A., H. C. Brinton, H. B. Niemann, H. G. Mayr, R. E. Hartle, A. Barnes and J. Larson, In Situ Results on the Variation of Neutral Atmospheric Hydrogen at Venus, presented to VIRA Workshop, COSPAR, Graz, Austria, June 1984. Submitted for publication in Adv. Space Res.

Taylor, R. L., Energy Transfer Processes in the Stratosphere, Can. J. Chem., 52, 1436, 1974.

Torr, M. R., D. G. Torr, R. A. Ong and H. E. Hinteregger, Ionization Frequencies for Major Thermospheric Constituents as a Function of Solar Cycle 21, Geophys. Res. Lett., 6, 771-774, 1979.

_____, _____ and H. E. Hinteregger, Solar Flux Variability in the Schumann-Runge Continuum as a Function of Solar Cycle 21, J. Geophys. Res., 85, 6063-6068, 1980.

_____, _____ and P. G. Richards, The Solar Ultraviolet Heating Efficiency of the Midlatitude Thermosphere, Geophys. Res. Lett., 7, 373-376, 1980b.

_____, P. G. Richards and D. G. Torr, A New Determination of the Ultraviolet Heating Efficiency of the Thermosphere, J. Geophys. Res., 85, 6815-6826, 1980c.

von Zahn, U., K. H. Fricke, H. J. Hoffmann and J. Pelka, Venus: Eddy Coefficients in the Thermosphere and the Inferred Helium Constant of the Lower Atmosphere, Geophys. Res. Lett., 6, 337, 1979a.

_____, D. Krankowsky, K. Mauersberger, A. O. Nier and D. M. Hunten, Venus Thermosphere: In Situ Composition Measurements, the Temperature Profile, and the Homopause Altitude, Science, 203, 768-770, 1979b.

_____, K. H. Fricke, D. M. Hunten, D. Krankowsky, K. Mauersberger and A. O., Nier, The Upper Atmosphere of Venus During Morning Conditions, J. Geophys. Res., 85, 7829-7840, 1980.

_____, S. Kumar, H. B. Niemann and R. Prinn, Composition of the Venus Atmosphere, in Venus, Ch. 13, 299-430, University of Arizona Press, Tucson, Arizona, 1983.

Waltersheid, R. L., Dynamical Cooling Induced by Dissipating Internal Gravity Waves, Geophys. Res. Lett., 8, 1235-1238, 1981.

Washington W. M. and D. L. Williamson, A Description of the NCAR Global Circulation Models, in Methods in Computational Physics, Vol. 17, General Circulation Models of the Atmosphere, J. Chang, ed., 111-172, Academic Press, New York, 1977.

Watson, W. S., D. T. Stewart, A. B. Gardner, M. J. Lynch, The Photoabsorption Coefficients of CO and CO_2 in the Region 350-650Å, Res. Notes Planet. Space Sci., 23, 384-386, 1975.

Wehrbein, W. M. and C. B. Leovy, An Accurate Radiative Heating and Cooling Algorithm for Use in A Dynamical Model of the Middle Atmosphere, J. Atmos. Sci., 39, 1532-1544, 1982.

Weinstock, J., Theoretical Relation Between Momentum Deposition and Diffusion Caused by Gravity Waves, Geophys. Res. Lett., 9, 863-865, 1982a.

_____, Nonlinear Theory of Gravity Waves: Momentum Deposition, Generalized Rayleigh Friction, and Diffusion, J. Atmos. Sci., 39, 1698-1710, 1982b.

_____, Heat Flux Induced by Gravity Waves, Geophys. Res. Lett., 10, 165-167, 1983.

White, O. R., The Solar Output and its Variation, Colorado Association University Press, Boulder, Colorado, 1977.

Widing, K. G., J. D. Purcell and G. D. Sandlin, The UV Continuum 1450-2100Å and the Problem of the Solar Temperature Minimum, Solar Phys., 12, 52, 1970.

Yung, Y. L. and W. B. DeMore, Photochemistry of the Stratosphere of Venus: Implications for Atmospheric Evolution, Icarus, 51, 199-247, 1982.